# The Phase Structure and Rheological Properties of Surfactant Solutions via Dissipative Particle Dynamics
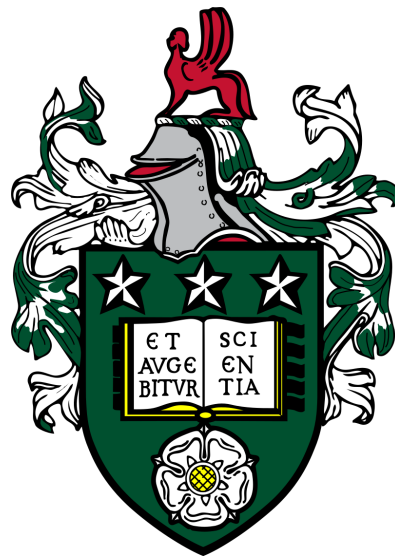
Rachel Louise Hendrikse

The University of Leeds

School of Computing &

School of Chemical and Process Engineering

Submitted in accordance with the requirements for the degree of

Doctor of Philosophy

February 2022

The candidate confirms that the work submitted is their own and that appropriate credit has been given where reference has been made to the work of others.

This copy has been supplied on the understanding that it is copyright material and that no quotation from the thesis may be published without proper acknowledgement.

Acknowledgements

Abstract

This thesis presents a study of anionic surfactant solutions via experimental and simulation methods. The surfactants studied in this work are some of the most common ionic surfactants used in consumer products. Therefore understanding and predicting their behaviour, as a function of concentration, is crucial to the manufacturing of these products. Surfactant solutions can take the form of different 'mesophases' depending on the concentration, which all show widely different properties as a result of molecular self-assembly in solution. The simulation methods used in this work contribute to understanding the behaviour of fluids on the macro-scale, by simulating the individual molecules in solution.

Experimental analysis in this work makes use of techniques such as polarised optical microscopy (POM), rheological measurements, Raman spectroscopy and dynamic light scattering (DLS). These experiments were performed not only to establish the phase behaviour of the surfactant solutions, but also to uncover aspects of the structure at different concentrations. These results are then compared with simulations which are performed for similar systems. For example, Raman spectroscopy is used to show that the conformation of molecules is influenced by structural changes within the fluid, which is later found to be reproducible using simulation.

The simulation technique of dissipative particle dynamics (DPD) is used in this work for studying the equilibrium phase behaviour of solutions at room temperature. Following an establishment of the equilibrium behaviour, a study is performed investigating the effect of the application of shear to these solutions.

From these simulations we can also calculate a viscosity *vs.* shear rate profile for comparison with experimental results. A small selection of equilibrium molecular dynamics (MD) simulations are performed, in order to demonstrate that the simplifications made in performing DPD simulations *vs.* MD simulations have minimal impact on the final results.

Table of Contents

List of Figures

List of Tables

Chapter 1

Introduction

Surfactants are present in many everyday products, such as detergents, shampoos, paints and foods. When the concentration of surfactant molecules in solution is above a critical concentration, the molecules can self-assemble into mesophases. This self-assembly behaviour is driven by the amphiphilic nature of the surfactant molecules. The structure of these mesophases varies, depending on conditions such as the temperature and concentration. Typically mesophases include: micellar, hexagonal, bi-continuous cubic, and lamellar solutions. The structure of these phases will be discussed in greater detail in Chapter 2 of this thesis. Different mesophases have different properties due to their different structures, in particular they tend to have extremely different rheological properties, which will be a topic of interest in this work. Understanding the rheological properties of a surfactant solution for a given set of conditions (*e.g.* for a given concentration and temperature) is key to the manufacturing process of surfactant containing products. The equilibrium phases of surfactant solutions have been studied across literature, for a variety of different surfactant types, using a variety of experimental and numerical methods. This work will make use of different simulation and experimental techniques, in order to investigate the phase behaviour and rheological properties of surfactant solutions.

The particular surfactants of interest in this work are alkyl ethoxysulphates (AES), which are common anionic surfactants. The AES in this work is supplied

by Proctor and Gamble, and is a common component in a number of their products, including laundry detergent, household cleaning products and personal care products. These surfactants molecules have chemical structure $CH_3(CH_2)_x(OCH_2CH_2)_nOSO_3Na$ where x and n take integer values. Typically, in the AES used in commercial products, there is a distribution of x and n. However, in published research, focus is normally on monodisperse systems (fixed x and n). In particular, the surfactant molecule described by $x = 11$ and $n = 0$ has the name sodium dodecyl sulphate (or sodium lauryl sulphate), and its behaviour at low concentration is a relatively well researched topic, using both experimental and simulation techniques. However, molecules of increasing n are less frequently modelled, as are systems of higher concentration.

The modelling of surfactant systems is usually undertaken with the use of a microscale or mesoscale technique. In these methods the individual surfactant molecules are modelled, in order to understand how the structure on the atomistic scale effects the fluid on the macroscopic scale. Simulation in this manner can aid in the understanding some of the phenomena observed in experiments. The most commonly used simulation method, on this scale, for general systems is that of molecular dynamics (MD). MD has historically been used to model the atomistic behaviour of a wide variety of different systems, including surfactant systems. However, for surfactant systems, the time scales required for the self-assembly process of the molecules starts to become unobtainable. This method is time consuming, and it is difficult to reach both the large length scales and time scales due to the computational effort involved. This led to the development of dissipative particle dynamics (DPD). DPD is a mesoscale simulation technique, which uses soft interaction potentials between large, coarse grained molecules to reproduce liquid behaviour. DPD has the benefit of being able to reach time and length scales that were previously unobtainable by traditional MD methods. DPD has been applied to studying the phase behaviour of a variety of systems, as well as being used to study the rheological properties of simple and complex fluids. However,

the application of DPD to ionic surfactant systems is only a recent development. The traditional way of modelling the electrostatic force in MD cannot be directly applied to DPD systems, and so the best method of calculating the Coulombic force for ionic molecules is still an open area of research.

The aim of this work is to study the equilibrium and rheological behaviour of AES-like molecules, using DPD. This work focuses on behaviour specifically at room temperature, with the effect of varying concentration and number of ethoxy groups n, being the main variables of investigation. An understanding of the effect that both concentration and n has, is valuable for the manufacture of surfactant containing products. The ability to predict the effect varying n has on various solution properties, enables for easier development and fine-tuning of commercial products.

The first stage of this work is to confirm that DPD can accurately reproduce the correct phase behaviour for these systems, since there is relatively little work published using DPD for these types of surfactants. Experimentally, we first establish the phase diagram of a commercial AES product, as a function of it's varying concentration. DPD can then be used to simulate the same AES product, which contains a polydisperse distribution of molecules with a varying number of ethoxy groups n. The DPD results are compared with experimental data to confirm the validity of the DPD method for studying the phase diagram. Following this, we investigate the effect of varying n for monodisperse solutions. In particular the location of the phase boundaries, and the types of mesophases that are produced for a given value of n, are of interest in this study.

Following the establishment of a phase diagram, as a function of concentration and n, the individual mesophase structures can be analysed in greater detail. The structure of surfactant solutions can be difficult to study experimentally, and there is often discrepancy between different experimental techniques. This makes computational study an attractive alternative to studying surfactant solutions. In particular, in this work, we find that the micellar, hexagonal and lamellar phases

dominate the phase diagram, and therefore their structures are investigated in detail using DPD. For the micellar solutions the micelle shape and size are of particular interest. Micellar shape and size changes are typically difficult to quantify experimentally, however these changes can effect bulk behaviour, such as the viscosity. For the liquid crystal phases, the structure can be primarily quantified by their periodicity, which has also been shown to influence overall bulk properties and behaviour. Therefore, the effect that variation of n and concentration has on the periodicity of the liquid crystal phases is studied in this work.

Next we turn to studying the effect that concentration and degree of ethoxylation has on the individual molecular shape, as opposed to the self-assembled structures discussed thus far. An interesting question is to whether a coarse-grained simulation method, such as DPD, can capture conformational changes which result from mesophase transitions. Typically this has not been investigated in existing literature, because it is assumed that any conformational behaviour would be lost as a result of coarse-graining. We begin by experimentally studying the conformational changes that AES molecules undergo, as a result of variation of concentration (and therefore phase transitions), by means of Raman spectroscopy. We then compare this with the results obtained via DPD, to try and understand if any information can be gained from studying such quantities via coarse-grained simulation. Conformational changes can play a role in understanding overall bulk behaviour. However, typically molecules which are large and complex, such as surfactants, are once again difficult to study experimentally.

Next we turn our attention to the rheology of surfactant solutions. Surfactant solutions typically possess a complex rhological profile, depending on which mesophase they are residing in. The viscosity *vs.* shear rate behaviour of AES is measured experimentally. While this plays a part in establishing the phase diagram, it also enables us to investigate whether DPD can be used to recreate the correct viscosity-shear rate profiles. Simulations are performed using DPD, in which shear is applied to the surfactant solution structures, at varying shear rates.

From this we can not only calculate viscosity, but also study the effect that shear has on the mesophase structures.

A final aspect of this work turns to MD simulations. As already discussed, MD is more time consuming than DPD, and the time scales required for the self-assembly of molecules starts to become unreachable. However, one of the drawbacks of DPD simulations, is that it is often unknown the extent to which the coarse-graining has on the final results. Therefore we perform additional MD simulations which aim confirm whether the parameters calculated in this work are affected by the coarse-graining performed. Here we focus on the micellar phase only due to the computational cost involved for these simulations. Therefore, in particular, we focus on the effect coarse-graining has on the shape of the micelles, as well as the individual molecules.

In summary, the aims of this project can be reduced to the following key questions:

- What effect does the degree of ethoxylation n have on the phase diagram? This includes which mesophases, in particular, are produced through self-assembly, and at what concentrations do transitions to different mesophases occur?

- How does the value of n and the concentration affect the mesophase structure? Of particular interest are aspects of the structure that are typically difficult to measure experimentally.

- Does transition between mesophases have an effect on the conformation of AES molecules? If so, can DPD capture this despite the coarse-graining procedure?

- Can the rheology of different mesophases be captured using DPD, including the viscosity *vs.* shear rate profile? Can we use DPD shearing simulations to understand what is happening to a complex fluid when subject to a shear force?

- Is there any evidence that the coarse-graining performed for DPD simulations influences the results calculated? Therefore, would different results would be obtained via molecular dynamics simulations?

This thesis is structured as follows. Chapter 2 begins with a detailed discussion on the different mesophases that can form for surfactant solutions with varying concentration and temperature. Chapter 3 then presents an overview of the different simulation methods that can be used to model surfactant solutions, before going into detail about the simulation methods used in this work.

Chapters 4 and 5 provide experimentally obtained information about AES solutions, in order for a comparison with the simulated results in later chapters. In Chapter 4, the phase diagram for AES is established, as well as the rheological behaviour of the different mesophases. Chapter 5 provides information about how the molecular shape is effected by the phase changes, by means of Raman Spectroscopy measurements. These measurements also help to confirm the boundries between the different mesophases, as a function of their concentration.

Chapters 6 and 7 then present detailed investigations using the DPD simulation method. Chapter 8 presents a small selection of MD results, studying the the surfactant solutions in the low concentration region. This allows for a direct comparison of similar parameters, calculated from the two different simulation methods, for the same system.

The DPD simulations are all performed using the DL_MESO [26] simulation package, while the MD simulations are performed using LAMMPS [27]. The simulations are performed using two different HPC services. The first is the Tier 3 University of Leeds service 'ARC' (Advanced Research Computing). While additional support for simulations was provided by the Tier 2 service 'CSD3' (Cambridge Service for Data-Driven Discovery). The CSD3 service provided just over 3 million CPU hours in order to produce the results presented in this thesis.

Chapter 2

Surfactants

Surfactants are typically molecules that are amphiphilic, meaning that they contain both hydrophobic ('*tail*') and hydrophilic ('*head*') parts [28]. Usually the tail of an amphiphile is composed of one or two hydrocarbon chains [29], and an illustration of this structure is shown in Fig. 2.1. The head is either an ionic or nonionic group, and surfactants are often classified according to their head group: nonionic, anionic, cationic or amphoteric.

Surfactants are also typically defined as materials that, at low concentrations, lower the surface tension (or interfacial tension) between either two liquids, a gas and a liquid, or between a liquid and a solid. This is, in fact, where the word 'surfactant' originates from; as a contraction of the phrase 'surface active agent'. When surfactant is added to a solvent, such as water, it has the effect of decreasing the surface tension up to a critical value of the concentration, a value which is given the name of the 'critical micelle concentration' (CMC). Above the CMC, the surface tension will no longer decrease and remains constant, however, surfactant molecules begin to self-assemble into micelles [30]. A micelle is an aggregate of

Hydrophilic head

Hydrophobic tail
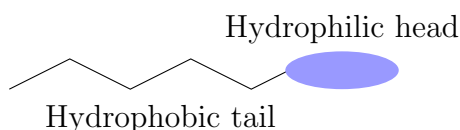
Figure 2.1: Simple illustration of the amphiphilic nature of surfactant molecules.
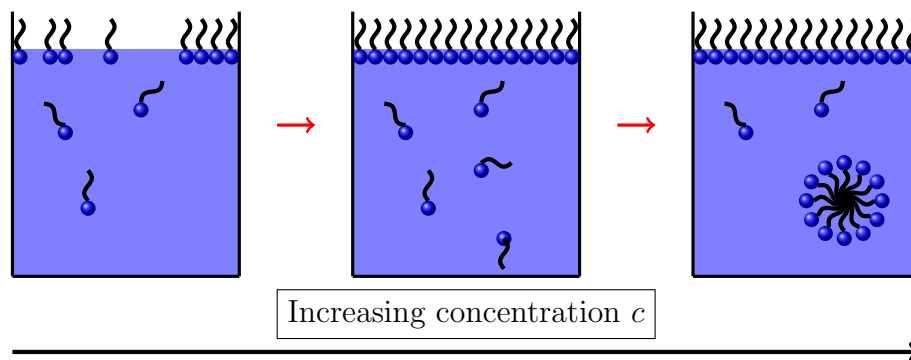
Figure 2.2: The effect of increasing concentration in a surfactant solution. Micelles do not form until the solution is above a critical concentration (CMC) such that the interface is saturated with molecules.

(a) Spherical

(b) Worm-like
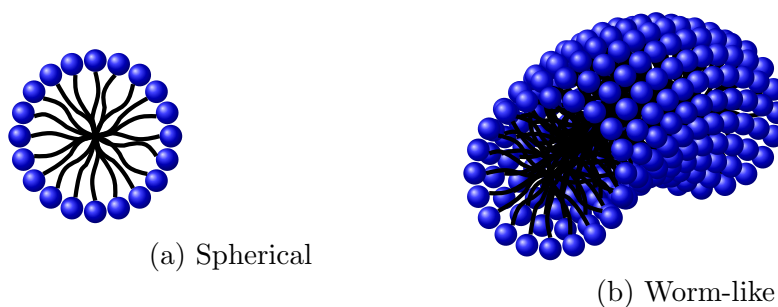
Figure 2.3: Illustration of micelle shapes.

the surfactant dispersed in solution. This process is illustrated in Fig. 2.2. The value of the CMC is different for each surfactant, as is the number of monomers which make up the micelle. This aggregation is a result of the amphiphilic nature of the molecules, and the tendency for a system to organise itself in a way that will minimise its free energy [31]. The initial types of micelles that form are approximately spherical in shape, with the hydrocarbon tails directed towards the centre. At higher concentrations these spherical aggregates can often grow to long, rod-like micelles, particularly for nonionic surfactants. Spherical and rod-like (or 'worm-like') micelles are illustrated in Fig. 2.3.

Higher values of surfactant concentration will result in the self-assembly of surfactant molecules into crystal-like structures, often referred to as being different 'mesophases' of the solution. A material that forms liquid crystal phases upon the addition of a solvent is given the name 'lyotropic'. The lyotropic phases can be categorised into three main types: lamellar, hexagonal and cubic. The structure of these phases is shown in Fig. 2.4. In the lamellar structure, the surfactant

(a) Lamellar

(b) Bicontinuous Cubic
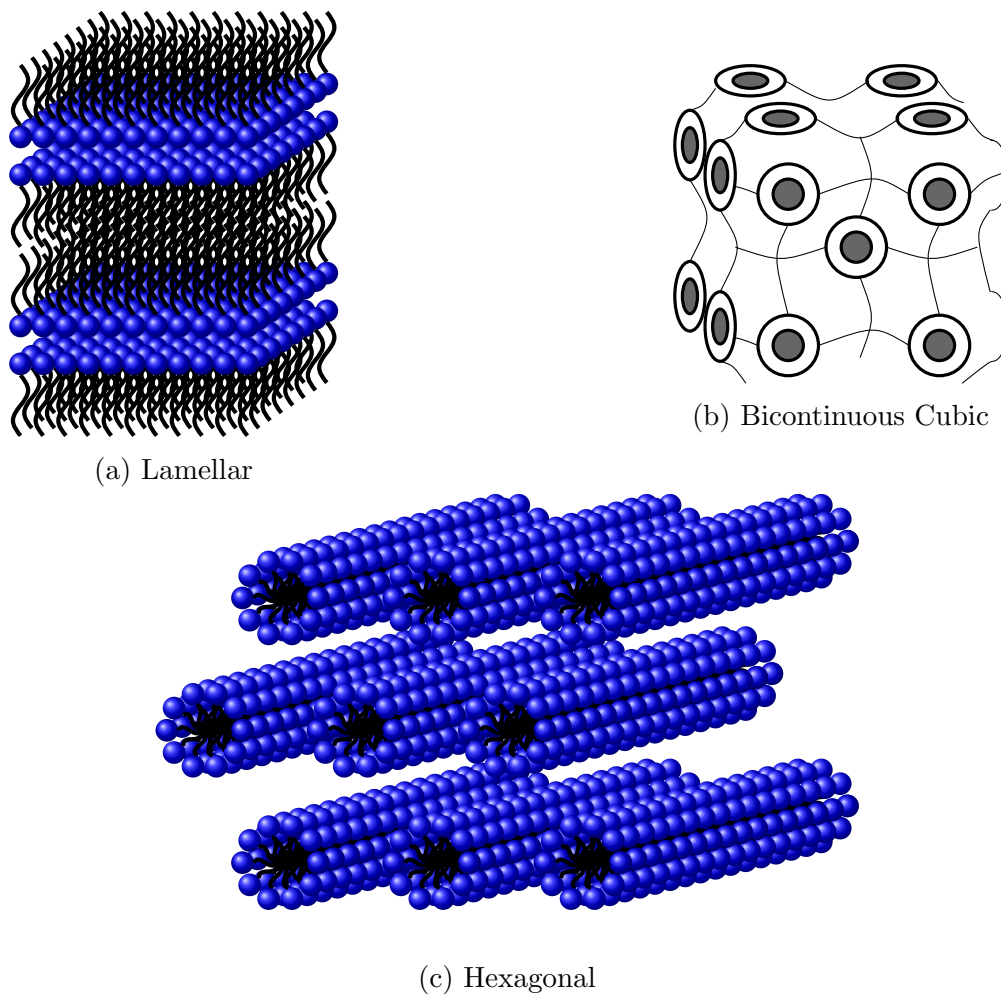
(c) Hexagonal

Figure 2.4: Illustration of different lyotropic liquid crystal phases.

molecules are arranged in bilayers separated by water layers. The layers extend over large distances, of the order of microns or more [32]. The hexagonal phase consists of long cylindrical rods of molecules arranged on a hexagonal lattice. There are two different kinds of cubic phase. One phase (that typically forms between the lamellar and hexagonal phase) is called the bicontinuous phase, and this is one of the most complicated phases. It consists of rod-like surfactant structures forming extended networks [33]. The other (which forms between the hexagonal phase and micellar solutions) is called the micellar cubic phase. In this phase the molecules arrange themselves into micelles, which then organise to form a cubic lattice [34]. The particular mesophase formed by the surfactant solution is also dependant on its temperature, as well as its concentration. In particular there is a critical temperature required for the formation of the discussed structures, called

45
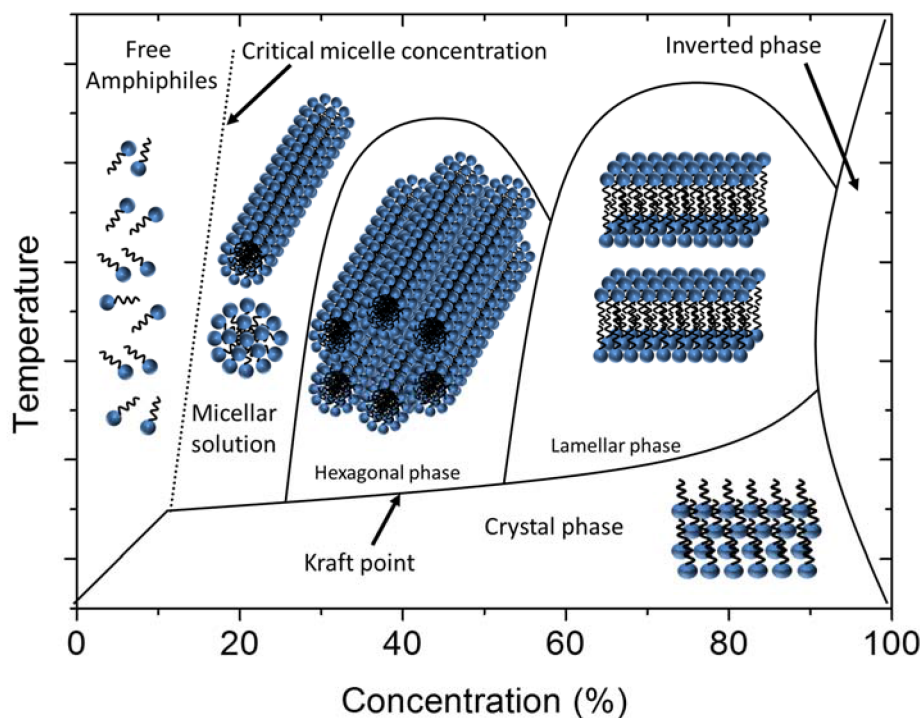
Figure 2.5: Image taken from Dierking and Al-Zangana (2018) [1], illustrating a typical equilibrium phase diagram.

the Kraft temperature. Below the Krafft temperature the surfactant molecules remain in crystalline form, even in an aqueous solution. In general, the mesophase formed by single-chain ionic surfactants tends to be most dependant on variation of the concentration, while for many non-ionic surfactants temperature is a more important variable [35]. A phase diagram provides information on what particular phase a solution will be in under a given set of equilibrium conditions. A typical example of a phase diagram for surfactant systems is presented in Fig. 2.5. Note that the Kraft temperature increases as the concentration of the surfactant molecules increases in solution [34].

This chapter will continue by first discussing the formation and structure of the expected phases in more detail, initially covering the micellar phase in Section 2.1, before moving onto the lyotropic crystalline phases in Section 2.2. Following this, the AES systems that are to be studied in this work are described, and what phase behaviour is expected from similar systems in Section 2.3.

46

2.1 Micelles

Micelles begin to form when the surfactant concentration is above the CMC. These spherical aggregates are dynamic and are continuously formed and broken down in solution. The micelles dissociate into monomers and reaggregate into micelles continuously [36]. This is an important consideration when experimentally studying the micelles, as the method for measuring the micelle must take place over a time period that captures the micelle before reorganisation occurs. There can be considered to be two relaxation processes (and associated time scales) for micelles. The first τ_1 being the relatively fast exchange of monomers between the micelles and bulk solution, and the second being the slower relaxation time τ_2 related to the complete micelle dissociation. The relaxation process τ_1 occurs on the time scale of microseconds, while τ_2 on milliseconds [36]. In fact it is shown by Oh and Shah [36] that for molecules formed by sodium dodecyl sulphate (anionic surfactant with chemical formula $CH_3(CH_2)_{11}SO_4Na$), the relaxation time τ_2 can vary strongly depending on the solution concentration (ranging from 0.005s – 10s), implying an optimum concentration at which the micelles are most stable. The spontaneous self-assembly of molecules into micelles is driven by the aim of a minimal free energy. The free energy of the system decreases when the hydrocarbon/water contact area is minimised, leading to the enclosure of the hydrocarbon chain inside the micelle [37].

A typical parameter for characterising micellar solutions is the aggregation number of the system. The aggregation number of a micelle is defined as the number of surfactant molecules per micelle. The aggregation number of a system is not a single value but usually takes the form of a distribution, from which a mean aggregation number N_{agg} can be calculated. A typical size distribution for micellar solutions is shown in Fig. 2.6.

Micelles formed from ionic surfactants are more complicated due to the fact that the micelles will have a net charge. This causes the ions to gather at the surface of the micelle due to electrostatic attraction. This behaviour was first
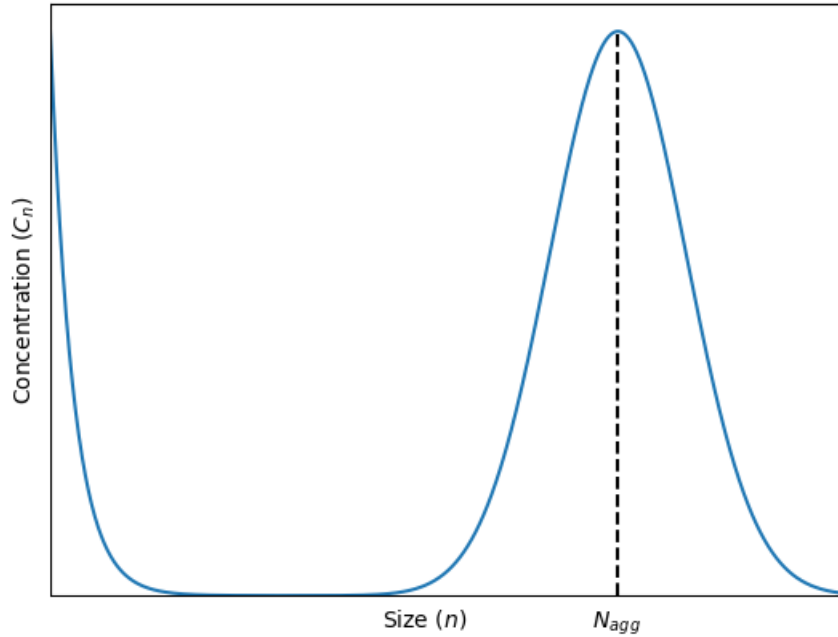
Figure 2.6: Typical micelle size distribution, where C_n is the number of aggregates of size n. The initial decay is the monomer distribution *i.e.* the monomers that do not belong to micelles. The Gaussian peak at higher n is a representation of monomers belonging to micelles, with the distribution of micelles having mean aggregation number N_{agg}.

described by the the electrical double layer (EDL) model, originally developed by Helmholtz [38] and since expanded on by numerous others [39–41] to create Gouy–Chapman–Stern theory. A representation of the structure of an ionic micelle and the EDL model, as described by Gouy–Chapman–Stern theory, is presented in Fig. 2.7. At the centre of the micelle there is a hydrophobic core, made of the hydrocarbon chains, surrounded by the charged head group of the molecule. The double layer model then consists of the Stern layer, which is a layer of ions strongly-bound to the charged micelle surface. Following this is an outer layer of loosely associated mobile ions (diffuse layer). The Stern layer is a concentric shell with $(1 - \alpha)N$ counterions, where α is the degree of ionisation (also referred to as the apparent degree of counterion dissociation [42]) and N is the aggregation number. The electrical double layer, due to the formation of the counterion layers, results in electrostatic screening of the charged micelle [2,31]. The zeta potential is a measure of the strength of the electrostatic potential at the 'slip plane' between particle and solution. The slip plane can be understood as the point at which the
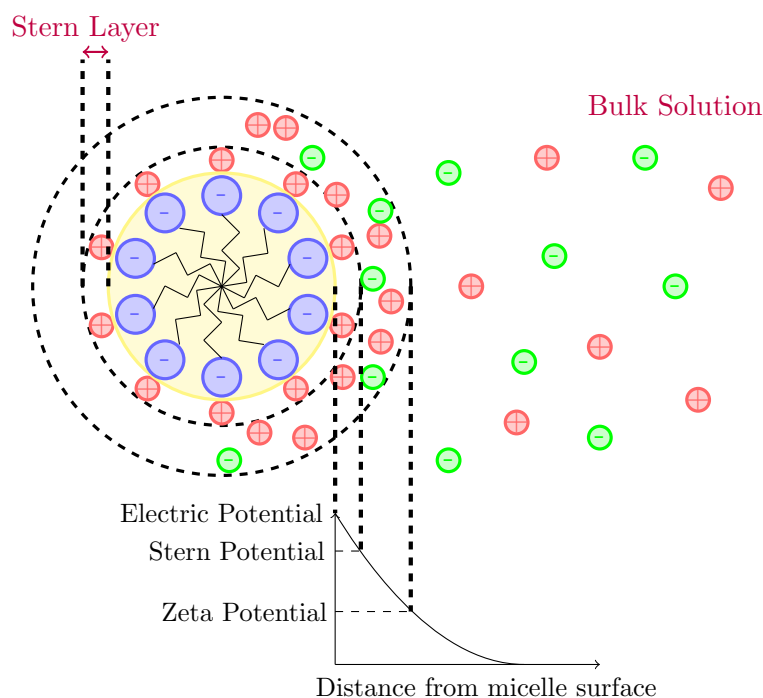
Figure 2.7: Representation of the electrical double layer of ionic micelles. Figure adapted from Lombardo [2].

cluster of charges at the surface of the micelle ends, and transition into solution begins. A commonly used length scale is the Debye length λ_D. This is the distance from the particle at which the electrostatic potential falls by $1/e$, and can be considered as a measure of a micelle's net electrostatic effect in solution, and how far its electrostatic impact persists. Of course solutions containing a large and/or high number of micelles will lead to an overlap of these EDLs, leading to further complication [43]. Despite the electrostatic screening (sometimes also called the 'Debye screening') of the charged micelles, the electrostatic force persists over a relatively large distance, such that there can be strong intermicellar interactions due to the charges.

At high concentrations in the micellar region, 'micellar cubic' phases can sometimes form. This occurs when a large number of micelles have formed, and the aggregates organise themselves onto a cubic lattice [2,44,45], in order to maximise their spacing. This organisation is shown in Fig. 2.8. There have been a variety of different cubic structures observed for the micellar cubic phase, including Pm3n, IM3m and Fm3m space groups [44,46,47]. Micellar cubic phases are isotropic [45],
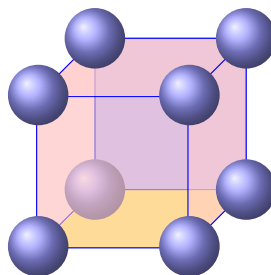
Figure 2.8: Structure of micellar cubic mesophases. Spherical micelles organise themselves onto a cubic lattice.

and therefore like other micellar phases are unable to be identified using polarising microscopy, a technique that will be discussed and applied in Chapter 4, but are distinguishable from standard micellar solutions by their relatively high viscosity [44, 45].

2.2 Liquid Crystals

At increasing concentrations, spherical micelles can transform in to rod-like micelles. When the concentration is further increased, this can cause rod-like micelles to orientate and pack themselves into a hexagonal structure, called the hexagonal mesophase. Further increase in concentration often results in the transition to the neat layered structure of the lamellar phase. For some surfactants, there can be a cubic phase occurring between the hexagonal and lamellar phases, although this is often only within a narrow concentration range or is absent. This section will provide more detail about these lyotropic liquid crystals and their structure.

2.2.1 Lamellar Phase

In the lamellar phase, surfactant molecules are aligned in a bilayer structure which extends over large distances. These layers can slide over each other if an external force, such as shear, is applied, allowing the solution to flow like a liquid. While the lamellar phase is viscous relative to the micellar phase, it is typically one of the least viscous lyotropic liquid crystal structures. The structure of the lamellar phase is anisotropic, and therefore visible when placed between crossed polarisers.
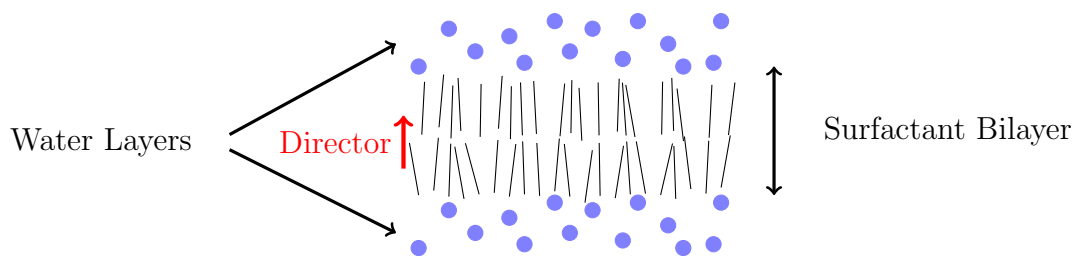
Figure 2.9: Meaning of the unit vector the 'director', which describes the average direction of the surfactant molecules, and thus provides a parameter with which to describe the orientation of the lamellar phase.

This, therefore, is a common and useful method for detecting the existence of this mesophase.

The lamellar phase can be characterised by the periodicity of the layers, referred to as the d-spacing. This value includes the thickness of the bilayer and its associated water layer. This d-spacing value is frequently calculated from experiments using small angle X-ray scattering (SAXS) [15, 48, 49]. The d-spacing that the lamellar layers form at for a given surfactant molecule depends on a variety of factors, including the temperature [50, 51] and the concentration [49, 50, 52]. Furthermore, different types of surfactants can follow different concentration *vs.* d-spacing relationships. It is commonly found using SAXS that the d-spacing decreases with increasing surfactant concentration [49, 50, 53, 54], however there are rare occasions that the opposite behaviour has been found for different surfactant types [55].

The molecules in the lamellar phase are aligned approximately in the same direction. In order to describe this orientation, a unit vector called the director can be introduced, which is described in Fig. 2.9. The director can be defined as the average direction of the long molecular axes of all molecules in the liquid crystal. Therefore, an individual molecule may vary in its degree of alignment with the director.
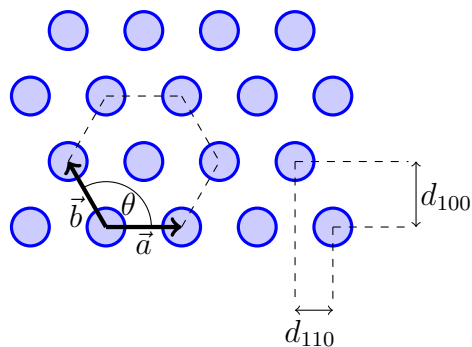
Figure 2.10: Representation of the unit cell of the hexagonal lattice, formed by hexagonal mesophase, in which $|\vec{a}| = |\vec{b}|$ and $\theta = 120°$. For the hexagonal phase there are two d-spacings, d_{100} and d_{110}, which can be measured by experimental techniques in order to determine the inter-rod spacing $a = |\vec{a}| = |\vec{b}|$, using that $a = 2d_{100}/\sqrt{3}$ and $a = 2d_{110}$ for a hexagonal lattice.

2.2.2 Hexagonal Phase

The hexagonal mesophase consists of indefinitely long cylindrical micelles, which become aligned to form a two-dimensional hexagonal lattice. The space in-between the surfactant rods is filled with water molecules. This phase is viscous in comparison to the lamellar phase, but not relative to cubic phase. Similarly to the previously discussed lamellar phase, when the hexagonal phase is observed by polarised microscopy, textures can be seen due to the long-range orientational order, aiding in its identification.

The structure of this phase can be characterised by the spacing between the rods, a, as illustrated in Fig. 2.10. The spacing between these rods has been shown to be dependant on factors such as the concentration [24, 25, 49, 50] and temperature [50, 51].

2.2.3 Bicontinuous Cubic Phases

The structure of the bicontinuous cubic phase is more complex than that of the lamellar and hexagonal phases, and therefore the least well understood of the liquid crystalline structures. While the lamellar phase consists of a one-dimensional stacking of bilayers, and the hexagonal phase is based on two-dimensional stacking of micellar rods, the cubic phase shows periodicity in all three dimensions.

Typically authors may divide the cubic phases into two different groups: (1) cubic structures that are continuous with respect to both the water and hydrocarbon components; and (2) those that are discontinuous in their hydrocarbon regions but continuous in their water regions [56]. The micellar cubic phase, as discussed in Section 2.1, would be an example of the type 2 cubic phases. The first type of cubic phases are usually called 'bicontinuous', since they are continuous in both water and hydrocarbon regions. As the second type has already been discussed in previous sections, the type 1, bicontinous phases are the focus of this section.

The bicontinuous cubic phase structure as shown in Fig. 2.4b is just one of the accepted forms that the structure can take (also identifiable as space group Im3m). However, the structure presented is theoretically the most likely form of the cubic phase when it appears in between a lamellar and hexagonal phase, while other types exist in other parts of the phase diagram [57]. In existing literature, to be discussed in Section 2.3, it is found that for the surfactants of study in this work, the region between the hexagonal and lamellar phases is the most likely concentration range in which the cubic phase may be observed. Other potential bicontinuous cubic structures that are of note include those that can be described as two networks of rods, mutually intertwined and unconnected (space groups Ia3d and Pn3m) [57, 58]. These were among the first of the cubic phases that were identified and the structure established [58]. There are numerous reviews that discuss the other forms that the cubic region can take in much greater detail [35, 56–58], due to their structural complexity. Finally, it is worth mentioning that experimentally determining the form of a cubic phase is difficult and, whilst their presence can be inferred from experimental results, the exact structure that they take can be open to debate.

2.3   Alkyl ethoxysulphates (AES)

Alkyl ethoxysulphates (AES) are common anionic surfactants, and will be the primary surfactant used for experimental study in this thesis. Commercial AES is

usually a mixture which consists of an alkyl chain of between 12 and 16 carbon units joined to an ethylene oxide (EO) chain of between 1 to 8 EO units, terminated by a sulphate group. Chemical structure is of the form $CH_3(CH_2)_x(OCH_2CH_2)_nOSO_3Na$ [59]. The type of AES to be used in this work is provided by Proctor and Gamble, and the distribution of x and n is illustrated in Table 2.1. This type of AES can also be referred to as AE1S, as a result of the average degree of ethoxylation being approximately 1 (actual value 1.03). The AES is provided in the form of a paste made up of 70% surfactant and 30% water.

It is much more common for research across literature to focus on monodisperse, as opposed to polydisperse, solutions. As part of the analysis of the phase behaviour of AE1S, we will compare with the equilibrium phases formed by monodisperse solutions of molecules similar to AES (*i.e.* solutions in which x and n do not take the form of a distribution). Therefore, we will now, in the remainder of this section, review the published phase diagrams, as found by other researchers. For example, sodium lauryl ether sulphate (SLES) (also sometimes called sodium laureth sulphate) is the name given to the molecule in which $x = 11$, but still with variable ethoxylation n. Sometimes n is specified in the name of the molecule, for example laureth-2 sulphate. The molecule that is defined by $x = 11$ and $n = 0$ is given the name sodium dodecyl sulphate (SDS) (or sometimes sodium lauryl sulphate). To our knowledge there is no existing published phase diagram for AE1S, which is therefore investigated in Chapter 4. However there is work published by Li *et al.* (2016) [15] studying the molecularly similar AE3S. As this is expected to be similar to AE1S, we will also review their reported phase diagram to allow for a comparison with the results reported in Chapter 4.

The simulation aspect of this research will have particular interest on the effect of introducing ethylene oxide (EO) into the hydrophobic chain. For example, it has been shown that for AES type molecules the Krafft point changes (the minimum temperature at which a surfactant can form micelles), as a function of both hydrocarbon chain length n and number of OCH_2CH_2 groups x [60]. In other

research it has been found that, for SLES molecules, the addition of EO groups leads to higher micellar aggregation numbers, perhaps due to dispersing the charges in the head-group, thus weakening the electrostatic repulsion [61]. Zhang *et al.* [62] analyse the effect of varying the EO groups on the rheology of different ionic and nonionic surfactants, finding that they can greatly effect the rheological behaviour, including the relationship between the viscosity and the shear rate.

Ethoxylation	AES (%)
0	49.0
1	24.0
2	13.0
3	7.0
4	4.0
5	2.0
6	1.0
7	0.0

Chain length	AES (%)
C12	67
C13	0
C14	26
C15	0
C16	6

Table 2.1: Information on the distribution of chain lengths in AES.

2.3.1   Equilibrium Phase Diagrams

2.3.1.1   AE3S

In the work of Li *et al.* (2016) [15], researchers investigate AE3S solutions at room temperature, by using polarising optical microscopy and small angle X-ray diffraction. They find that mesophases micellar, hexagonal, cubic and lamellar form with increasing AE3S concentration. A summary of the phase boundaries found are shown in Table 2.2. It is of note that the cubic range that appears is relatively narrow, so it is uncertain whether an equivalent phase will form for AE1S. It is also reported that there is a multiphase micellar-hexagonal region, which is primarily identified by polarising optical microscopy images. Typically these regions where two phases are thought to co-exist are difficult to identify, so this will be a boundary of interest when studying the phase diagram of AE1S.

Mesophase	Concentration Range (wt. %)	Viscosity Range (Pa· s)
Micellar	$0 - 40$	$0 - 10$
Micellar/Hexagonal	$40 - 45$	$10 - 100$
Hexagonal	$45 - 80$	$200 - 1000$
Cubic	$80 - 90$	$200 - 1000$
Lamellar	$90 - 100$	$10 - 100$

Table 2.2: A summary of the phase boundaries found by Li *et al.* (2016) [15] for AE3S solutions at 25°C. Also listed is an estimate for the range the mesophase viscosities fall within, for each of the different mesophases. Note that the concentrations are given as a percentage of the 70% AES paste, not as a percentage of surfactant that the solutions contain.

2.3.1.2   Sodium Dodecyl Sulphate (SDS)

SDS is an extremely commonly studied anionic surfactant, particularly in the relatively low concentration range of the micellar phase. However, the high concentration regions are less well studied. The extremely commonly referenced [63, 64] phase diagram, as found by Kékicheff *et al.* [3] via differential calorimetric measurements, for SDS solutions is shown in Fig. 2.11. At lower temperatures, this phase diagram predicts that the mesophases can coexist with parts of hydrated crystal within the solution (which are labelled as C_2), which they refer to as a coagel. Note that according to this phase diagram, at our planned temperature of study ($\approx 25°C$), we are on the edge of a phase boundary above around 40 wt.%. This phase diagram also indicates that the lamellar phase should never form under equilibrium conditions at room temperature, for any value of surfactant concentration. Despite the phase diagram found by Kékicheff *et al.* [3] being widely cited, other researchers have reported different findings, particularly with regard to the composition of the phase at room temperature between around 40 wt.% and 60 wt.%. Guo [65] reports that at 20°C, the following regions are found with varying concentration: above 0.2wt.% micelles exist with spherical structure; concentration above 1.6 wt.% micelles have a rod/cylinder structure; concentration above ≈ 40 wt.% shows a single phase of the hexagonal liquid crystal. Other well known investigations of SDS around room temperature include the work of McDonald and Peel [66]. As part of their work they study samples of constant concentration, and

Figure 2.11: The phase diagram for SDS/water mixtures as determined by Kékicheff *et al.* [3]. Structures are labelled as: H_α, Hexagonal phase; M_α, two dimensional monoclinc phase; R_α, rhombohedral phase; Q_α, cubic phase; T_α, tetragonal phase; L_α, lamellar phase. C refers to SDS hydrates, where the subscript refers to the number of molecules associated with each SDS molecule in the hydrate.

vary the temperature to investigate phase transitions in the phase diagram. They report that there are phase transitions at $\approx 22°$C, for the samples 50 wt.% and 60wt.%, indicating the formation of the hexagonal phase. Meanwhile the transitions above $31°$C, in those containing 70, 75 and 80 wt.%, indicate the formation of lamellar phase. Leigh *et al.* [24], however, disputed the findings of McDonald and Peel [66] in the finding of a lamellar phase at ambient temperatures, stating that they did not find evidence of a lamellar phase at any of the concentrations trialled, for temperatures below 320K (around $47°$C). For measurements taken at 313K, they do however agree that the phase in the 40–60% concentration range can be attributed to being hexagonal (with decreasing unit cell size with increasing concentration). Conversely, in recent research, Bahadur *et al.* [67] report that SDS 58 wt.% at room temperature results in a gel phase due to random jamming of the lamellar structured entities. Is observed that the equilibrated SDS gel shows a lamellar structure similar to that in powder SDS. The lamellar thickness in the gel

57

phase is estimated to be 4.6nm, compared with 3.9nm in the powder phase (SDS systems crystallize with lamellar structures [68, 69]). All of the above discussed research leads to a complicated view of the SDS phase diagram, particularly at room temperature.

In the process of producing a phase diagram, such as the one shown in Fig. 2.11, generally a researcher will take a concentration sample, and gradually increase or decrease the temperature, in order to obtain the equilibrium phase at a selection of temperatures, doing so for a variety of different samples at a variety of concentrations. An interesting note is that Kékicheff et $al.$ [3] report their coagel solution states are dependant on their thermal hysteresis. For example, if the heating rate chosen is too fast, then phase jumps can be missed in the process of gradual heating, indicating that the system does not reach thermodynamic equilibrium between each transition. This is because the liquid crystalline phases can take a very long time to form. It has been noted [70] that isoplethal methods (constant composition) such as these are less ideal than performing isothermal (constant temperature) experiments, and therefore can lead to uncertainties and errors, but are more often performed because they are more practical.

2.3.1.3 Sodium Lauryl Ether Sulphate (SLES)

SLES is the case in which the surfactant molecules are defined by $x = 11$ with variable n. The more specific case in which $x = 11$ and $n = 3$ will from now on be referred to as SLE_3S. Poulos et $al.$ [4] use penetration experiments to establish an approximate phase diagram for SLE_3S surfactant solutions, with their findings shown in Fig. 2.12. Similar research also investigating the dissolution of SL_3S confirms this order of phase transition [71]. The small-angle neutron scattering pattern, found by Poulos et $al.$ [4], of the initial SLE_3S/water phase with 72 wt.% confirms lamellar phase with repeat distance $d = 43.9$Å.
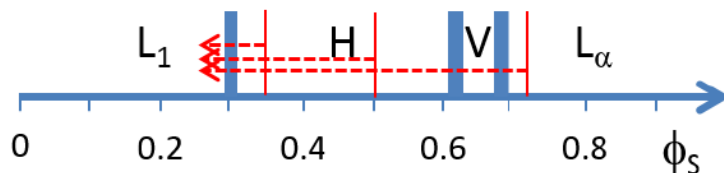
Figure 2.12: Approximate phase diagram of the SLE_3S surfactant, as determined by Poulos *et al.* [4]. Initial phase is a paste containing 72% volume fraction surfactant in water. When dissolving, an initially lamellar phase (L_α) transforms into a cubic phase (V), a hexagonal phase (H), and finally an isotropic micellar phase (L_1). ϕ_S is the volume fraction of surfactant in solution.

2.4 Summary

This chapter has provided an overview of surfactant solutions, and the structures mesophase can form at different concentrations. Although surfactant solutions can also undergo a phase change as a result of changing temperature, this work will be primarily concerned with the phase behaviour at room temperature (defined in this work as 25°C). In particular, this work will be interested in the phase behaviour of systems described by the chemical formula $CH_3(CH_2)_x(OCH_2CH_2)_nOSO_3Na$, which, in most commercial applications, comes with varying x and n.

There is generally a lack of literature reporting the phase diagrams of simple, single surfactant systems. Most literature reports the phase behaviour of mixtures consisting of two or more surfactant types, meaning that available existing experimental data is limited. An exception to this is the special case in which $x = 11$ and $n = 0$, which has the name sodium dodecyl sulphate (SDS). Therefore the phase behaviour for the molecular distribution described in Table 2.1 will be presented in Chapter 4.

Chapter 3

Simulation Methods

3.1 Overview

There are many different approaches to simulating surfactant phase formation. Generally, we can split the study of the behaviour of fluids into different approaches which consider different length scales, including: quantum mechanical, atomistic, mesoscopic and continuum mechanics. With increasing length scale, simulations are able to access longer time scales, however, this has the trade off of neglecting more of the finer atomistic details. The different length and time scales represented by different simulation methods is illustrated in Fig. 3.1. There is often a compromise between the desire to reach high accuracy, *vs.* the desire to simulate large systems for a long time.

Quantum mechanical (QM) methods, which include the treatment of the quantum nature of electrons and nuclei, are computationally very demanding. It often isn't feasible to study a system's time evolution with this level of detail [72], except for very small scale systems. Therefore, for many applications that require simulating a large number of atoms, the simulations are scaled up to a more atomistic level. Atomistic approaches include molecular dynamics (MD) simulations [73–85]. In these methods the atoms in a molecular chain are individually modelled, being represented as bonded point masses. The atoms in the simulation are allowed to interact via a set of forces (defined by a set of potentials) for a period of time.
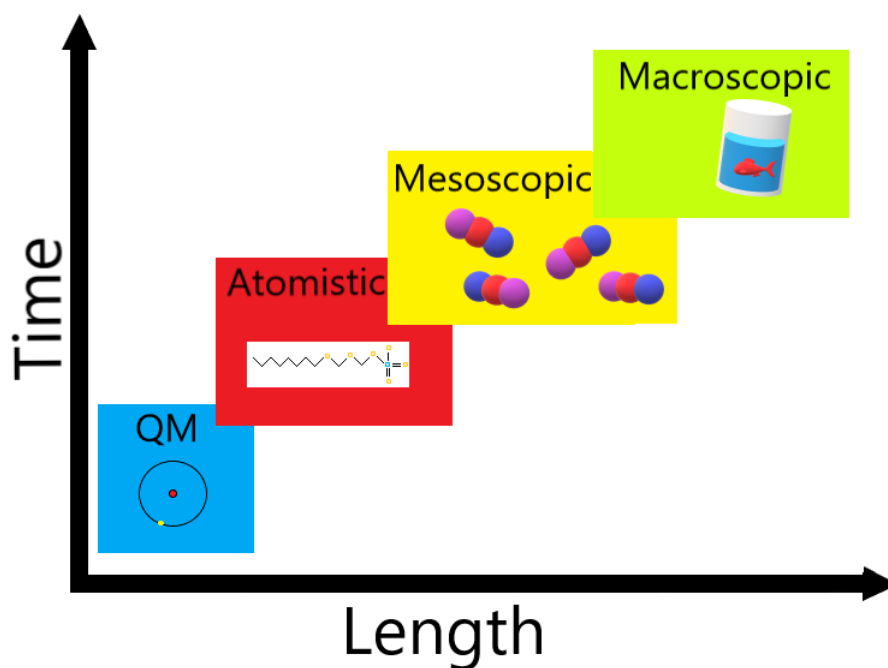
Figure 3.1: An illustration of the different simulation methods, and the differences in the time and length scales they are able to access.

Newton's equations of motion are solved for each atom, therefore these simulations can be very expensive computationally. Hence, MD simulations have only been possible for studying micelle formation in recent years, due to the long timescales involved in micelle aggregation, requiring enormous computational resources. MD simulations contain a variety of parameters that need to be obtained in order to correctly model the interaction potentials, and these parameters are often obtained via full quantum mechanical simulations [14, 72] or from experiment [86].

On a larger length scale we move to coarse grain models. In these models a number of atoms are grouped together, instead of being modelled individually. This reduces the number of calculations that need to be performed per iteration. One such method is coarse-grained molecular dynamics [76–81], which is the far more common method of choice for surfactant systems (as opposed to all-atom molecular dynamics [80, 82–85]), due to the long chain nature of surfactant molecules.

Other coarse grained methods include Monte Carlo methods [87–93], which rely on random sampling in order to obtain the equilibrium molecular configurations for solutions. Monte Carlo methods have been one of the most widely used methods to

study surfactant self-assembly processes, owing to their fast computational speed, and the fact that they can be used with relative ease to calculate characteristics for a solution, such as critical micelle concentration and micelle size. In these simplified models, the molecules can either be confined to a lattice [87–90], or be free to move in continuous space [91–93], with earlier calculations taking place on lattices. Although the simulation progresses forward via time steps, these time steps do not correlate directly with real time, and therefore MC methods can't be used to calculate dynamical properties, such as transport coefficients and rheological properties, like MD methods can. Therefore MC methods are unsuitable for our purposes. However, such methods have still been useful for many years in predicting equilibrium properties of simple surfactant solutions. For example, lattice Monte Carlo simulation was the first simulation method to predict a drop in free monomer concentration (the concentration of molecules not belonging to aggregates) above the CMC value, which is seen experimentally but not predicted by theory [89].

Next, we will move onto mesoscale modelling. Mesoscale modelling is intended to be the bridge between the atomistic methods discussed and the macroscale. Even when coarse graining is applied to the MD, we are still generally unable to reach long time and length scales, hence the need for the development of other numerical models, in order to enable the calculation of dynamical properties. Mesoscopic methods include lattice-Boltzmann [94, 95] and lattice gas automaton [95, 96]. Although these methods have been applied to polymer systems, their main disadvantage comes from the restriction of the particles to a lattice. Another mesoscale modelling method that has become popular for surfactant systems is dissipative particle dynamics (DPD) simulations [97–101]. DPD is distinctly different from lattice-Boltzmann and lattice gas automaton models, as the particles are allowed to interact in continuous space. This method involves the grouping of atoms in a similar way to the coarse grain modelling in MD, except the sites involved in these simulations typically cover more atoms than sites in the coarse

grain MD models. The forces in DPD simulations are also modelled differently to those in MD, further enhancing computational speed, as much longer time steps can be taken relative to MD simulations. The longer time steps, combined with the larger particle size, makes DPD a much more attractive method than MD for simulating hydrodynamics.

The macroscale is the most coarse-grained scale, in which continuum-based calculations are performed, for example with the use of computational fluid dynamics (CFD) [102–104]. At this level, the solution is modelled as a field quantity and therefore there are challenges in trying to capture small-scale phenomena in a large-scale simulation. These methods rely on using constitutive equations in order to capture the microscopic details of the fluid, as the length scale is too large for the modelling of the phenomena themselves. This limits the molecular complexity that can be captured in the simulation. Such constitutive material models can be derived from experimental observations [105–107]. As we aim to uncover some of the molecular physics that leads to explanations of phase formation behaviour this method is not suitable for our purposes.

For our calculations DPD is the ideal simulation method, due to its ability to capture the phase formation by modelling the individual molecules, while being computationally efficient. From modelling of the fluid structure, we can calculate a variety of parameters that would normally have to be found via experiments. As well as comparing how well the DPD method makes predictions when compared with data obtained experimentally, we will also perform a small selection of MD simulations. This will allow us to analyse how the method of coarse graining affects the phase formation in the simulation. The DPD method can also be used to calculate and predict properties such as the viscosity as a function of the shear rate. This means we can find a constitutive relationship between the viscosity and shear rate, without the need for experiments.

In the next two sections we will discuss the mechanics of how the DPD and MD simulations work, as well as how they are linked.

3.2 Molecular Dynamics

3.2.1 Forces and General Algorithm

Molecular dynamics uses classical mechanics to model molecular systems, and atoms are modelled as single spherical particles with an assigned radius. Quantum-mechanical properties of systems are entirely neglected. The potential energy can be calculated by summing energies that arise from a variety of different interactions:

$$E_{\text{Pot}} = \underbrace{E_{\text{LJ}} + E_{\text{electrostatic}}}_{\text{non-bonded}} + \underbrace{E_{\text{bond}} + E_{\text{angle}} + E_{\text{tor}}}_{\text{bonded}} \tag{3.1}$$

where the above terms will be explained in this section. The energies can be categorised into those that come from bonds between atoms in a molecule and non-bonded interactions between all atoms in the system.

The energy between two neutral, non-bonded atoms comes from a combination of the Pauli repulsion, due to overlapping electron orbitals, and van der Waals attraction. It is most commonly modelled by the Lennard-Jones potential [108, 109], or alternatively the Buckingham potential [110], which was proposed as a simplification of the Lennard-Jones potential. The Lennard-Jones potential takes the form

$$E_{\text{LJ}} = 4\epsilon \left[\left(\frac{\sigma}{r_{ij}} \right)^{12} - \left(\frac{\sigma}{r_{ij}} \right)^6 \right] \tag{3.2}$$

where r_{ij} is the distance between the two centres of atoms i and j, with two parameters to be chosen: the diameter σ and the well depth ϵ. An alternative to E_{LJ} in Eq. 3.1, is the Buckingham potential, given by:

$$E_{\text{Buck}} = A \exp\left(-Br_{ij}\right) - \frac{C}{r_{ij}^6} \tag{3.3}$$

where A, B and C are positive constants. The first term on the RHS is the repulsive term and the second term is the attractive term.

The electrostatic potential energy $E_{\text{electrostatic}}$ between a pair of atoms with

charges q_i and q_j is given by:

$$E_{\text{electrostatic}} = \frac{q_i q_j}{4\pi\epsilon_0 r_{ij}}. \tag{3.4}$$

The electrostatic force is the term that usually causes the most difficulty, as it leads to the most computationally expensive part of the calculation. Therefore, in literature, it is far more common to find research using non-ionic molecules, as opposed to ionic. This is due to the long-range nature of the Coulombic force, compared with the other contributions which are relatively short-range. Since the Coulombic force is so long range, it isn't realistic to apply a cut-off in the same way that can be applied to the Lennard-Jones force. A typical method for dealing with the ionic contributions makes use of the Ewald summation method [111–113]. In this method, the interaction illustrated in Eq. 3.4 is divided into two parts consisting of a short-range contribution and a long-range contribution. The short-range part is calculated in real space, while the long-range part is calculated in reciprocal space by making use of a Fourier transform [114]. This method is much quicker than performing the direct summation. An adaptation of the traditional Ewald method are Particle-Particle-Particle-Mesh (PPPM) [115] methods. Both Ewald and PPPM split the calculation into the short- and long-range parts. In PPPM, the long-range interaction parts are calculated by use of a mesh. The charge density is mapped onto a discrete, finely spaced mesh throughout the domain, and then fast Fourier transforms (FFTs) can be used to solve Poisson's equation on the mesh, and then interpolate electric fields on the mesh points back to the atoms [116]. While the two methods are very similar, the PPPM method is much more efficient, due to how it solves the reciprocal space part of the calculation. The traditional Ewald summation method scales as $N^{3/2}$, where N is the number of atoms in the system. The PPPM solver scales as $N \log N$, due to the FFTs [112]. More information on the implementation of the two algorithms can be found in Pollock and Glosli [117].

So far the discussed energies come from non-bonded interactions. We will now discuss the remaining interactions, which arise from bonded interactions. For two

atoms that are covalently bonded, there is an optimum separation distance between the two. When the two atoms are separated by this distance, the bond energy is zero. When their distance strays from this optimal distance the bond energy is non zero. The bond energy can be represented by a harmonic potential [118]

$$E_{\text{bond}} = \frac{1}{2}k_{ij}(r_{ij} - r_{ij}^0)^2,$$ (3.5)

where k_{ij} is a spring constant, r_{ij} is the distance between the two atoms, and r_{ij}^0 is the optimal distance between the two atoms. This energy can be thought of as the stretching energy. The bond energy can be represented in other different ways, such as the Morse potential for diatomic molecules [119].

The potential energy that comes with bond angle flexing is given by [118]

$$E_{\text{angle}} = \frac{1}{2}k_{ijk}(\theta_{ijk} - \theta_{ijk}^0)^2,$$ (3.6)

where k_{ijk} is a force constant, θ_{ijk} is the bond angle between the two atoms i and k about j, and θ_{ijk}^0 is the equilibrium bond angle between the two atoms. This energy can be thought of as the bending energy.

The torsion angle θ_{t} is the angle between the planes formed by the first three and last three atoms of four consecutively bonded atoms. The torsion angle energy is periodic, and can be given by [118]

$$E_{\text{tor}} = A(1 + \cos{(m\theta_{\text{t}} - \phi)})$$ (3.7)

where A, m and ϕ are constant values.

From the expression for the potential energy (Eq. 3.1), an expression for the force can be found using $f = -\nabla E_{\text{Pot}}$. The trajectories of the molecules are found by solving Newton's equations of motion

$$\mathbf{f}_i = m\frac{d\mathbf{v}_i}{dt},$$ (3.8)

$$\frac{d\mathbf{r}_i}{dt} = \mathbf{v}_i \tag{3.9}$$

for each particle. These equations are typically integrated using the velocity-Verlet algorithm [120], which is a mathematically equivalent, but more computationally efficient, implementation of the originally proposed Verlet algorithm [121]. The velocity-Verlet algorithm is normally implemented, in order to advance from time t to $t + \Delta t$, as follows.

1. Create velocities $\mathbf{v}_i$ at an intermediate time $t + \frac{1}{2}\Delta t$, using $\mathbf{v}_i(t + \frac{1}{2}\Delta t) = \mathbf{v}_i(t) + \frac{1}{2}\Delta t \mathbf{a}_i(t)$.

2. Update the positions at $t + \Delta t$, using the intermediate velocity calculated in the previous step, by $\mathbf{r}_i(t + \Delta t) = \mathbf{r}_i(t) + \Delta t \mathbf{v}_i(t + \Delta t)$

3. Evaluate the forces, and thus calculate an acceleration $\mathbf{a}_i(t + \frac{1}{2}\Delta t)$ at the new time step, using $\mathbf{r}_i(t + \Delta t)$.

4. Calculate the fully advanced velocity using $\mathbf{v}_i(t + \Delta t) = \mathbf{v}_i(t + \frac{1}{2}\Delta t) + \frac{1}{2}\Delta t \mathbf{a}_i(t + \Delta t)$

Note that the acceleration $\mathbf{a}_i(t + \Delta t)$ is calculated from the interaction potential using $\mathbf{r}_i(t + \Delta t)$. This algorithm assumes that the acceleration $\mathbf{a}_i(t + \Delta t)$ only depends on the position $\mathbf{r}_i(t + \Delta t)$, and does not depend on the velocity $\mathbf{v}_i(t + \Delta t)$.

There are a number of constants in the discussed equations that must be defined. In the context of molecular modelling, a force field refers to the parameter sets used in the above equations in order to calculate the potential energy E_{Pot} of a system. These parameters are often found from experiments [86] or calculations using quantum mechanics [14, 72] (or a combination of both). There have been a large number of different force field models that have been developed, often for specific molecule types. Some examples include the Martini force field [122], which is specifically for coarse-grained models. Initially it was developed for the simulation of lipids, but has since been extended to other molecules. This force field involves a mapping of four heavy atoms to one coarse-grained interaction

site. Other general force fields for all-atom simulations include the Dreiding [123] and GROMOS [86] force fields. One of the popular models for water is the SPC model [124].

MD simulations are often begun from a random initial configuration of particles within the domain. The domain is usually a cubic system with periodic boundary conditions. This allows for the simulation of a relatively small number of atoms to function as if it is a part of a larger system, hopefully producing results that are representative of the bulk material. Therefore it is important to consider the minimum size of the system that must be simulated for this to be true. This is particularly important for simulations trying to reproduce systems with large features or periodicity. Clearly, the number of interactions per iteration increases greatly with increasing number of particles N in the simulation. However, in practice, usually a cut-off is applied at a defined separation between particles. Beyond this cut-off (for forces other than the electrostatic force) it is taken that the force is negligibly small and can be considered to be zero. This allows more efficiency in computing the forces, since all atom pairs need no longer be considered. For the electrostatic force a cut-off of this form induces too much error, due to its long range nature and required more careful consideration, as previously discussed.

With increasing iterations the molecules will arrange themselves in order to decrease the repulsion forces when equilibrium is reached. The time step Δt has to be very small (on the order of femtoseconds), and thus reaching large time scales with this simulation method is difficult (a discussion on methods for determining the correct time step to use in MD simulations can be found in Choe and Kim (2000) [125]). In theory, a variety of properties can be analysed using the simulation method, including the viscosity and diffusion coefficients. However, due to the relatively long time scales needed for the self assembly of amphiphilic molecules into their micellar or liquid crystal phases, this method is difficult to use for analysing such systems. Typically, if MD is to be used, the phase is pre-arranged into something close to its equilibrium phase and the simulation begins

from there. This is opposed to the ideal scenario of beginning from a completely random initial configuration of molecules and atoms. Also, due to the high molecular weight of surfactant molecules, the molecule is often coarse-grained in order to reduce computational effort.

In summary, the procedure for a molecular dynamics simulation is as follows:

1. Give atoms an initial position and velocity.

2. Calculate the forces on each of the atoms.

3. Using a discretised version of Newton's equations and an adequately small time step Δt, find a set of updated positions and velocities for the atoms in the domain *e.g.* using the velocity-Verlet algorithm.

4. Apply temperature control (*i.e.* adjust the atoms velocities to remain at a fixed temperature).

5. Move into the new set of positions and update the time step $t = t + \Delta t$.

6. Repeat for as long as required.

The different algorithms that can be used in order to apply temperature control will be described in the following section. The stopping criteria for a MD simulation varies depending on the author and the system being simulated. There is no real universally accepted stopping criteria for MD simulations [126]. Although sometimes a stopping criteria is defined based on convergence of system parameters, such as the potential energy [127] or average root mean square (RMS) [128].

3.2.2 Thermostats

If the particles in the simulation interact by a pair-wise potential only, and the total number of particles N and the volume V are also kept constant, then the MD simulations are said to be performed in the microcanonical (NVE) ensemble. In these simulations, the total energy E is conserved. However, by application of a

thermostat (temperature control), other ensembles can be produced. For example, the canonical NVT ensemble is produced in a simulation in which the number of particles N, volume V, and temperature T are fixed. The isothermal–isobaric (NPT) ensemble is produced when the number of particles N, pressure P, and temperature T are conserved [5]. The NPT thermostat is considered to be the closest thermostat to one replicating laboratory conditions (*e.g.* with the substance open to ambient temperature and pressure).

There are many different types of thermostat that have been developed in order to produce these conditions [129–132]. One simple idea is to re-scale the velocities of the particles in each time step, in order to maintain constant temperature. This is called the Berendsen [129] thermostat. The instantaneous temperature of the system is calculated by making use of the average kinetic energy of the system:

$$k_{\mathrm{B}}T = \frac{1}{N} \sum_{i,\alpha} m v_{i,\alpha}^2 \qquad (3.10)$$

where N is the number of degrees of freedom and $v_{i,\alpha}$ is the component of the velocity of atom i, such that $\alpha = x, y, z$. However, this thermostat is not Galilean invariant, and since momentum is not locally conserved, this thermostat does not conserve hydrodynamics [5].

One commonly used thermostat was developed by Anderson [130], in order to maintain constant temperature. This thermostat operates by randomly selecting an atom or molecule in the system, and assigning a new velocity (that is given by Maxwell–Boltzmann statistics) for the given temperature. A downside of this thermostat is that it does not preserve hydrodynamics. Lowe [131] proposed an adaptation of the Anderson thermostat that does preserve hydrodynamics. This thermostat functions by changing the velocities of particle pairs, rather than acting on single particles. Similarly to in the Anderson thermostat, the velocity of the particle pair is replaced by a velocity taken from a Maxwell distribution. However, while the magnitude of the velocity of each of the particles in a given pair is changed by the same amount, the velocity kick is applied in opposite directions. This means

that the sum of the velocity vector of the combined pair remains the same before and after the kick. Therefore keeping the momentum the same and conserving the total momentum. For each particle, the velocity is exchanged for a new velocity (drawn from a Maxwell distribution) with a probability given by $\Gamma \Delta t$, where Γ is a 'bath' collision frequency. The viscosity is predicted by Lowe to have viscosity $\eta \propto \Gamma$.

Another important thermostat is the Nosé-Hoover thermostat [132]. This thermostat aims to control the temperature by introducing a new internal degree of freedom into the Hamiltonian. This extra degree of freedom is to represent a heat bath, in such a way that the temperature and average kinetic energy of the molecules are fixed. Adding this coupling changes the equations of motion and introduces an additional variable controlling the weight of that coupling, α [5]:

$$F = \frac{d\mathbf{p}}{dt} = -\nabla E_{\text{Pot}} - \alpha \mathbf{p} \qquad (3.11)$$

where $\mathbf{p}$ is the momentum of the particle and coupling α is calculated by

$$\frac{d\alpha}{dt} = \frac{1}{t_{\text{S}}}(T - T_0) \qquad (3.12)$$

where t_{S} is the thermostat coupling parameter, controlling energy transfer back and forth from the thermostat, T is an instantaneously calculated system temperature and T_0 is a system target temperature.

3.3 Dissipative Particle Dynamics (DPD)

The method of DPD was first introduced by Hoogerbrugge and Koelman [133], and has been developed by many other contributors since [17, 101, 134–136]. This section will outline how DPD works, and highlight some of the important contributions that have been made by other researchers during its development.

3.3.1 Forces and General Algorithm

This section will discuss the principles of the DPD method. Following the descriptions given by Groot and Warren (1997) [134] and Sato (2011) [137] we first discuss the general DPD approach for a simple set of non-bonded particles.

A DPD simulation box generally consists of cubic, continuous space, with periodic boundary conditions in every direction. The box is filled with an ensemble of beads $i = 1, ..., N$. The DPD method groups atoms in a molecular chain into a packet or a 'bead'. Each of these beads has a localised mass, with a continuous spatial position and velocity. The position of these beads are updated discretely with advancement in time. Due to the fact that the beads don't have hard sphere bounds, the beads can overlap with each other, which is one of the factors aiding the quick equilibration time of the method. The time evolution of the beads is governed by Newton's equations of motion, as in MD. However, the forces involved are represented differently to those in MD.

The force that acts on bead i from non-bonded beads can be written as

$$\mathbf{f}_i = \sum_{j \neq i} (\mathbf{F}_{ij}^{\mathrm{C}} + \mathbf{F}_{ij}^{\mathrm{D}} + \mathbf{F}_{ij}^{\mathrm{R}}) \tag{3.13}$$

where $\mathbf{F}_{ij}$ are the forces acting on bead i by bead j. The total force being made up of a conservative force $\mathbf{F}_{ij}^{\mathrm{C}}$, a dissipative force $\mathbf{F}_{ij}^{\mathrm{D}}$, and a random force $\mathbf{F}_{ij}^{\mathrm{R}}$. The conservative force is repulsive and given by

$$F_{ij}^{\mathrm{C}} = \begin{cases} a_{ij}(1 - \frac{r_{ij}}{r_{\mathrm{C}}})\hat{\mathbf{r}}_{ij} & \text{for } r_{ij} < r_{\mathrm{C}} \\ 0 & \text{for } r_{ij} \geq r_{\mathrm{C}} \end{cases} \tag{3.14}$$

where a_{ij} is the maximum repulsion between beads i and j, r_{C} is a specified cut-off radius, $\mathbf{r}_{ij} = \mathbf{r}_i - \mathbf{r}_j$, $r_{ij} = |\mathbf{r}_{ij}|$, $\hat{\mathbf{r}}_{ij} = \mathbf{r}_{ij}/|\mathbf{r}_{ij}|$. The conservative force gives beads a chemical identity with the constant a_{ij}. In particular, this is the parameter that varies between hydrophilic and hydrophobic beads.

The dissipative (or drag) force $\mathbf{F}_{ij}^{\mathrm{D}}$ and random force $\mathbf{F}_{ij}^{\mathrm{R}}$ are given by

$$\mathbf{F}_{ij}^{\mathrm{D}} = -\gamma\omega^{\mathrm{D}}(r_{ij})(\hat{\mathbf{r}}_{ij} \cdot \mathbf{v}_{ij})\hat{\mathbf{r}}_{ij}, \tag{3.15}$$

$$\mathbf{F}_{ij}^{\mathrm{R}} = \sigma\omega^{\mathrm{R}}(r_{ij})\zeta_{ij}\hat{\mathbf{r}}_{ij}\Delta t^{-1/2}, \tag{3.16}$$

where ω^{D} and ω^{R} are r dependent weight functions that vanish for $r_{\mathrm{C}} < r$, γ is a friction coefficient, σ is the noise amplitude, $\mathbf{v}_{ij} = \mathbf{v}_i - \mathbf{v}_j$, $\zeta_{ij}(t)$ is a randomly fluctuating Gaussian variable, with zero mean and unit variance. Note that the dissipative force is dependant on not only the separation between the beads, but also on the relative velocity of the beads. The dissipative force is often also referred to as the drag or friction force, due to the fact that as the two beads move near each other, a slowly moving bead would receive momentum from a faster bead, and a faster bead would be slowed down by interaction with the bead. This interaction contributes to the viscosity of the fluid. The random force can be interpreted as the result of atomic collisions that occur in a real fluid (similar to Brownian motion).

It was shown by Espanol and Warren [135] that one of the weight functions, either ω^{D} or ω^{R}, can be chosen arbitrarily, and this fixes the other weight function. This is in order to satisfy the fluctuation-dissipation theorem. The relationship between the two functions is shown to be

$$\omega^{\mathrm{D}} = [\omega^{\mathrm{R}}]^2 \tag{3.17}$$

and the relationship between the amplitudes is

$$\sigma^2 = 2\gamma k_{\mathrm{B}}T. \tag{3.18}$$

The dissipative and random forces together form a thermostat, which keeps the mean temperature of the system constant. In practice the most commonly chosen

function for ω^D is

$$\omega^D = \begin{cases} (1 - \frac{r_{ij}}{r_C})^2 & \text{for } r_{ij} < r_C, \\ 0 & \text{for } r_{ij} \geq r_C. \end{cases} \qquad (3.19)$$

It is suggested by Groot and Warren (1997) [134] to use a modified version of the velocity-Verlet algorithm to discretise Newton's equations of motion, as opposed to the standard velocity-Verlet integration. This is because the force in DPD depends on the velocity between beads $\mathbf{v}_{ij}$, whereas in standard velocity-Verlet the force is assumed to be independent of $\mathbf{v}_{ij}$. This has become the standard integration method for DPD. The adapted velocity-Verlet algorithm is as follows:

1. Find an updated position for the positions at time $t + \Delta t$ using $\mathbf{r}_i(t + \Delta t) = \mathbf{r}_i(t) + \Delta t \mathbf{v}_i(t) + \frac{1}{2}(\Delta t)^2 \mathbf{a}_i(t)$.

2. Find an intermediate value for the velocity $\tilde{\mathbf{v}}_i(t + \Delta t) = \mathbf{v}_i(t) + \lambda \Delta t \mathbf{a}_i(t)$.

3. Calculate the forces between the beads, and hence calculate a value for the acceleration at the new time step, using both the position $\mathbf{r}_i(t + \Delta t)$ and intermediate velocity $\tilde{\mathbf{v}}_i(t + \Delta t)$.

4. Calculate the final updated velocity at the new time step using the original and new acceleration, $\mathbf{v}_i(t + \Delta t) = \mathbf{v}_i(t) + \frac{1}{2}\Delta t(\mathbf{a}_i(t) + \mathbf{a}_i(t + \Delta t))$.

The variable factor λ is also introduced as a parameter to be chosen. Groot and Warren (1997) [134] choose to use $\lambda = 0.5$ in their work, along with $\Delta t = 0.04$, but also later investigate varying λ and conclude that a higher value can be used which means a higher time step could be used. As within MD, the simulation can begin with the molecules randomly placed. Once we move forward in time, the beads will arrange themselves in order to decrease the repulsion forces when equilibrium is reached. This is how equilibrium behaviour can be investigated. If the force were independent of velocity, the actual velocity-Verlet algorithm, as described in Section 3.2, would be recovered for $\lambda = 0.5$. However, as the force does depend on velocity, the intermediate velocity needs to be used in order to find an updated value for the acceleration.

In order to use DPD to model polymer systems, an additional force is introduced to Eq. 3.13 in order to 'bond' together a chain of beads to replicate a long chain polymer. This has the form of a simple harmonic spring force [97]

$$F_i^{\mathrm{S}} = \sum_j C(r_{ij} - l_0)\hat{\mathbf{r}}_{ij}, \qquad (3.20)$$

where the sum runs over all of the beads which are directly connected (*i.e.* those that are chemically bonded) to bead i. C is the spring constant and l_0 is an unstretched bond length. Another possible additional force is one which takes into account the hydrocarbon chain stiffness. A common choice for a potential for such an addition could take the form [97]

$$U(i-1, i, i+1) = K(1 - \cos(\theta - \theta_0)) \qquad (3.21)$$

where the angle θ is defined as the scalar product of the two bonds connecting beads $i-1$, i and i, $i+1$ (in other words the angle between adjoining bonds), K is a bending constant, and θ_0 is a preferred, equilibrium angle. However, in this work we will take the potential to be the slightly more simple form [17]

$$U = \frac{1}{2}K(\theta - \theta_0)^2 \qquad (3.22)$$

which simply comes from a Taylor expansion of $(1 - \cos(\theta - \theta_0))$ when $(\theta - \theta_0)$ is small.

3.3.2 Electrostatic interactions

As is the case in MD simulations, there is difficulty in application of the DPD method to molecules with charges. For all of DPD interactions currently discussed, the interactions vanish when the distance between two beads exceed the cutoff radius r_{C}. However, long range electrostatic interactions cannot be treated in a similar way. Long range electrostatic interactions have been dealt with in MD

simulations by Ewald summation methods, as discussed in Section 3.2. However, that approach models the atoms as point charges, and application of this in DPD would lead to problems. Due to the soft repulsions used in DPD, in which the beads are allowed to overlap, as opposed to the hard repulsion forces of the Lennard Jones potential, this would lead to artificial ionic pair formation.

One of the earliest examples of using DPD to model ionic surfactants is that of Groot (2003) [101], who proposes a way to work electrostatic interactions into the DPD method. In this method they tried to prevent artificial ion-pair formation by solving the electrostatic field locally on a lattice, and smearing the charge on a DPD bead out over a number of the nearest grid points. An alternative method builds on this idea of charge smearing and is suggested by Gonzalez-Melchor *et al.* (2006) [138]. The electrostatic interactions are calculated using the standard Ewald sum method. Charge distributions of the exponential form are used on DPD beads, in order to prevent artificial ionic pair formation. Other forms of charge shearing have been investigated, for example Warren *et al.* (2013) [139] investigate using Gaussian smearing. A comparison of different smearing methods is discussed in Warren and Vlasov (2014) [139].

3.3.3 Unit Conversion

Most work using DPD is usually presented in reduced DPD units, in which the unit of length is the particle size $r_C = 1$, the unit of mass is the particle mass $m = 1$, and the unit of energy is defined by setting $k_B T = 1$. One method of converting the units used in DPD to real units, is by matching the density of water in the simulation to a known experimental value, and therefore a value for r_C can be obtained in real units.

The parameterisation used in this work, presented by Anderson *et al.* (2018) [17], groups two molecules together to form the water bead in the simulation. Therefore, the mass of one DPD bead of water m is the mass of two water molecules; in real units this is $m = 5.98 \times 10^{-26}$kg. A typical choice for the

number density ρ of beads in the simulation box, and the one used in this thesis, is defined by $\rho r_{\mathrm{C}}^3 = 3$. The reason for this choice is due to the work of Groot and Warren [134], and this will be discussed in Section 3.3.4.

Use that the number density $\rho = \rho_{\mathrm{m}}/m$ where ρ_{m} is the mass density, producing relation for r_{C}:

$$r_{\mathrm{C}} = \left(\frac{3m}{\rho_{\mathrm{m}}}\right)^{1/3}. \tag{3.23}$$

Using that the density of water at room temperature is ≈ 1000 kg/m³, this finds a value for r_{C} in real units to be $r_{\mathrm{C}} \approx 5.65 \times 10^{-10}$m.

The standard time scale used in DPD simulations results from setting $k_{\mathrm{B}}T = 1$. Making use of the relation

$$\frac{1}{2}m\langle v^2 \rangle = \frac{3}{2}k_{\mathrm{B}}T \tag{3.24}$$

this means that, by using $m = 1$, $\langle v_{\mathrm{DPD}}^2 \rangle = 3$ in DPD units. By saying that: the distance in real units $d_{\mathrm{Real}} = d_{\mathrm{DPD}}r_{\mathrm{C}}$; time in real units $t_{\mathrm{Real}} = t_{\mathrm{DPD}}\tau_{\mathrm{C}}$; and $v_{\mathrm{DPD}} = d_{\mathrm{DPD}}/t_{\mathrm{DPD}}$, we can show that using the relationship in real units yields

$$\frac{m}{2}\left\langle \left(\frac{d_{\mathrm{DPD}}r_{\mathrm{C}}}{t_{\mathrm{DPD}}\tau_{\mathrm{C}}}\right)^2 \right\rangle = \frac{3}{2}k_{\mathrm{B}}T \tag{3.25}$$

$$\left(\frac{r_{\mathrm{C}}}{\tau_{\mathrm{C}}}\right)^2 m\left\langle \left(\frac{d_{\mathrm{DPD}}}{t_{\mathrm{DPD}}}\right)^2 \right\rangle = 3k_{\mathrm{B}}T \tag{3.26}$$

$$\left(\frac{r_{\mathrm{C}}}{\tau_{\mathrm{C}}}\right)^2 = \frac{k_{\mathrm{B}}T}{m}. \tag{3.27}$$

Using $k_{\mathrm{B}}T = 4.11 \times 10^{-21}$J at room temperature, and the previously calculated values of $r_{\mathrm{C}} = 5.65 \times 10^{-10}$m and $m = 5.98 \times 10^{-26}$kg, finds a value for the time scale of $\tau_{\mathrm{C}} = 2.16 \times 10^{-12}$s.

The above base units can be used to find conversions from DPD units into real units for other quantities that will be useful throughout this thesis. Viscosity has dimensions [mass/length]/[time] this means that conversation into real units $\eta = 1$ DPD units $= 4.5 \times 10^{-5}$ kg/(m· s).

3.3.4   The Conservative Repulsion Parameter

The choice for the values of the conservative repulsion parameters a_{ij} in equation 3.14 are clearly crucial to making sure that the model will produce the right phase behaviour. The values of a_{ij} essentially define the chemical species of a bead. A typical choice for a_{ij} comes from trying to match the compressibility of the liquid with that found experimentally. Following the derivation from Groot and Warren (1997) [134], the compressibility is given by

$$\kappa^{-1} = \frac{1}{nk_{\mathrm{B}}T\kappa_T} = \frac{1}{k_{\mathrm{B}}T}\left(\frac{\partial p}{\partial \rho}\right)_T, \tag{3.28}$$

where κ_T is the isothermal compressibility. Groot and Warren define the pressure, using the virial theorem [140], as

$$p = \rho k_{\mathrm{B}}T + \frac{1}{3V}\left\langle \sum_{j>i}(\mathbf{r}_i - \mathbf{r}_j)\cdot \mathbf{F}_{ij}^{\mathrm{C}}\right\rangle, \tag{3.29}$$

and they are able to determine via simulation that

$$p = \rho k_{\mathrm{B}}T + \alpha a \rho^2 \tag{3.30}$$

where $\alpha = 0.101 r_{\mathrm{C}}^4$, is a good approximation for the pressure, provided a sufficiently high density ($\rho > 2/r_{\mathrm{C}}^3$). This now implies that the compressibility of water is now able to be calculated by (and setting $r_{\mathrm{C}} = 1$)

$$\kappa^{-1} \approx 1 + 0.2\frac{a\rho}{k_{\mathrm{B}}T}. \tag{3.31}$$

This expression now means that experimental compressibilities can be used, in order to obtain conservative force parameters for bulk fluids. For example, authors will often to choose to match to the compressibility of water. At 300K, water is determined experimentally to have the value $\kappa^{-1} = 15.9835$, generating the typical

parameterisation:

$$a_{ij} = \frac{75k_{\mathrm{B}}T}{\rho} \qquad (3.32)$$

where it is very common to choose $\rho = 3$ due to Groot and Warren finding that this is one of the lowest possible densities where the scaling relation still holds. Choosing a lower density is optimal as the number of interactions (and therefore computational effort) increases with increasing density. The above derivation only holds if one DPD bead corresponds to one water molecule. The relation was later corrected by Groot and Rabone (2001) [141] so that

$$a_{ij} = \frac{75N_{\mathrm{m}}k_{\mathrm{B}}T}{\rho} \qquad (3.33)$$

where N_{m} is the number of water molecules per bead, however many researchers still use the incorrect first version, despite having a bead mapping numbers where $N_{\mathrm{m}} \neq 1$.

However other researchers, such as Anderson $et\ al.$ (2017) [16], argue that matching the compressibility is irrelevant, arguing that what really matters is that density fluctuations should be relatively insignificant above the DPD length scale. They also argue that the above method can suffer from unrealistic artefacts, due to the coarse-graining procedure, at high values of a_{ij}. In the follow up paper Anderson $et\ al.$ (2018) [17], it is argued that for the choice of number density $\rho r_{\mathrm{C}}^3 = 3$, and for $a_{ij} \geq O(10)$, the DPD fluid can be regarded as being thermodynamically incompressible on length scales larger than r_{C}.

It is from the work of Anderson $et\ al.$ (2017) [16] and Anderson $et\ al.$ (2018) [17] that we will take our parameters for DPD simulations. The authors argue that thermodynamic properties of the system are expected to be largely determined by the value of $a_{ij}(R_{ij}^{\mathrm{C}})^3$ (where R_{ij}^{C} is the cut-off for interactions between beads i and j) . Generally other researchers often choose $R_{ij}^{\mathrm{C}} \equiv r_{\mathrm{C}} = 1$, so that all interactions have the same cut-off length, and the difference in bead species is defined entirely by the choices of a_{ij}. However, this would be an unsatisfactory method if the beads
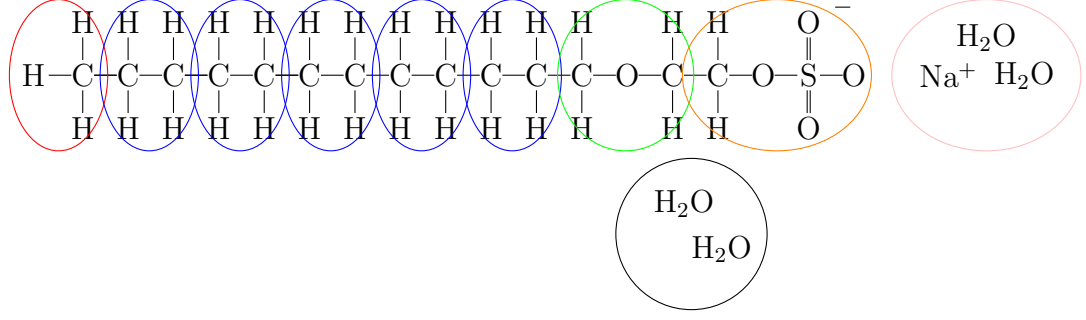
Figure 3.2: Illustration of the coarse graining used in the DPD simulations, where the number of [CH$_2$OCH$_2$] beads is varied.

were to have different numbers of atoms such that they cannot be assumed to have the same molar volumes for different bead types. Sometimes it is impractical to force the discretisation to fulfil this criteria. Therefore Anderson *et al.* (2018) [17] choose to separately specify both a_{ij} and R_{ij}^C for a pair of beads, and use the values of the self-repulsion cutoffs $(R_{ii}^C)^3$ in order to capture the differences in the beads' molar volumes. They assign the value of $(R_{ij}^C)^3$ for different beads, in proportion to the molar volume of the fragment of the molecule the bead is representing. The molar volume of water is used as a reference and is defined as $(R_{ij}^C)^3 = r_C^3 = 1$. They define the values of a_{ij} by using a combination of mutual solubilities, partition coefficients, and liquid density matching [16]. When extending to ionic molecules, they chose a_{ij} such that $a_{ij}(R_{ij}^C)^3 = 25$ is satisfied [17] when dealing with the interaction between either two ionic molecules, or one ionic molecule and a water molecule. In order to calculate the cut-off between two different types of beads the simple rule is applied: $R_{ij}^C = \frac{1}{2}(R_{ii}^C + R_{jj}^C)$. The full set of a_{ij} and R_{ij}^C parameters to be used in our simulations is shown in Table 3.1, and the coarse graining used is illustrated in Fig. 3.2.

In order to model the electrostatic pair potential between charged beads, the authors use Slater-type charge smearing, in which the Coulombic potential between two charged beads i and j is given by:

$$E_{\text{electrostatic}} = \frac{\Gamma q_i q_j}{4\pi r_{ij}}[1 - (1 + \beta^* r_{ij})e^{-2\beta^* r_{ij}}] \tag{3.34}$$

bead i	bead j	a_{ij}	R_{ij}^{C}
H_2O	H_2O	25.0	1.0000
H_2O	CH_2CH_2	45.0	1.0370
H_2O	CH_3	45.0	0.9775
H_2O	$CH_2OSO_3^{-1}$	17.9	1.1170
H_2O	CH_2OCH_2	24.0	1.0580
H_2O	Na^+	25.0	1.0000
CH_2CH_2	CH_2CH_2	22.0	1.0740
CH_2CH_2	CH_3	23.0	1.0145
CH_2CH_2	$CH_2OSO_3^{-1}$	28.5	1.1540
CH_2CH_2	CH_2OCH_2	28.5	1.0950
CH_2CH_2	Na^+	45.0	1.0370
CH_3	CH_3	24.0	0.9550
CH_3	$CH_2OSO_3^{-1}$	28.5	1.0945
CH_3	CH_2OCH_2	28.5	1.0355
CH_3	Na^+	45.0	0.9775
$CH_2OSO_3^{-1}$	$CH_2OSO_3^{-1}$	13.3	1.2340
$CH_2OSO_3^{-1}$	CH_2OCH_2	25.5	1.1750
$CH_2OSO_3^{-1}$	Na^+	17.9	1.1170
CH_2OCH_2	CH_2OCH_2	25.5	1.1160
CH_2OCH_2	Na^+	24.0	1.0580
Na^+	Na^+	25.0	1.0000

Table 3.1: Values for parameters a_{ij} and R_{ij}^{C} to be used in this study, taken from the research of Anderson *et al.* (2017) [16] and Anderson *et al.* (2018) [17].

where r_{ij} is the bead separation, q_i and q_j are the charges, $\Gamma = e^2/(k_\mathrm{B}T\epsilon_0\epsilon_r r_\mathrm{C})$ is a dimensionless electrostatic coupling parameter, and $\beta^* = 0.929 r_\mathrm{C}^{-1}$ is the tuneable Slater parameter. Ewald summation methods can then be used to implement this calculation, and this is the method which we will also use in our simulations. Other choices of parameters that we adopt from their research include: spring constant $C = 150$ (DPD units) in Eq. 3.20; bending constant $K = 5$ (DPD units) and equilibrium angle $\theta_0 = 180°$ in Eq. 3.22. Choice of bond lengths in Eq. 3.20 are set according to the number of heavy atoms n_i and n_j in the bonded beads, calculated as $l_0 = 0.1(n_i + n_j) - 0.01$. The origin of this choice stems from the fact that it will result in $l_0 = 0.39$ for bonds between beads that each contain two heavy atoms $e.g.$ between two (CH_2CH_2) beads. For the parameters adopted in Anderson [16] the resulting bond length during simulation has an average location at $l = 0.445 r_\mathrm{C}$ or 2.52Å in real units. This is approximately equivalent to the distance between three carbon atoms in an alkyl chain.

3.3.5 Other Parameters

Other choices, in order to complete the expressions for forces, need to be made for friction coefficient γ and noise amplitude σ. As the two are related, only one independent choice needs to be made. It is extremely common across published DPD research to make the choice of $\gamma = 4.5$, and the time step $\Delta t = 0.04$ [98, 142]. For the choice of time step, a compromise must be made between computational efficiency with choosing as large a time step as possible, but also maintaining the stability of the simulation. These parameter choices stem from the early work of Groot and Warren [134], in which they find that for $\sigma = 3$, a time step of $\Delta t = 0.04$ results in deviations in temperature of 2% (when using the velocity-Verlet integration scheme), which is deemed as an acceptable compromise.

Sometimes researchers will use a slightly lower time step in their simulations in order to improve on this temperature control [17, 143], but most researchers in recent work still make the choice of $\gamma = 4.5$. In the initial simulations in this

work we adopt the parameter choice of Anderson [17] who use $\Delta t = 0.01$, and the standard choice for the noise amplitude $\sigma = 3$. However, later the parameter σ becomes irrelevant as we apply a thermostat to the equations, which will be discussed in Section 3.3.6.

3.3.6 Schmidt number and Thermostats

Traditionally, DPD doesn't require a thermostat to keep the temperature in check. Instead it uses the dissipative and random forces as the system thermostat. The dissipative force parameter γ is one way that the dynamic viscosity μ can be controlled. However, the relationship between γ and μ is fairly complex. For example, if the conservative forces are neglected, Marsh [136] showed that the expression for the dynamic viscosity μ takes the form

$$\mu \approx \frac{45 k_{\mathrm{B}} T}{4 \pi \gamma r_{\mathrm{C}}^3} + \frac{2 \pi \gamma \rho^2 r_{\mathrm{C}}^5}{1575}. \tag{3.35}$$

This expression is fairly complicated, even without the addition of the conservative and electrostatic forces. When converted into real units, this viscosity is extremely low compared to what would be expected for fluids. Using standard DPD and varying γ, it would be fairly difficult to obtain a realistic viscosity for a fluid. It is also suggested that a large γ may result in difficulty in controlling the temperature of the system and the time step may need to be reduced [144].

Another point of interest is the Schmidt number Sc. The Schmidt number is defined as the ratio of kinematic viscosity ν and mass diffusivity D: $\mathrm{Sc} \equiv \frac{\nu}{D} = \frac{\mu}{\rho D}$. Similarly as above, Marsh [136] showed that the expression for the self diffusion coefficient takes the form

$$D \approx \frac{45 k_{\mathrm{B}} T}{2 \pi \gamma \rho r_{\mathrm{C}}^3} \tag{3.36}$$

leading to an expression for the Schmidt number

$$\mathrm{Sc} \approx \frac{1}{2} + \frac{(2 \pi \gamma r_{\mathrm{C}}^4)^2}{70875 k_{\mathrm{B}} T}. \tag{3.37}$$

The typical choices used in DPD for the dissipative force parameter γ and dissipative force cutoff r_C generates a fluid with an unrealistically small Schmidt number (on the order of ≈ 1). The Schmidt number could also be increased by increasing r_C, however this also increases the number of calculations per iteration, and thus computational expense. This low Schmidt number is suitable for gases, but too small for liquids, which have Schmidt numbers around 1000. There are a variety of ways to raise Schmidt number, such as increasing γ and r_C from their usual choices of $\gamma = 4.5$ and $r_C \approx 1$, but both of these methods decrease computational efficiency.

One way around the confusing relationship between γ and μ, is to use a different pairwise thermostat. Two that are of note for DPD systems are the Lowe-Andersen [131] and Stoyanov-Groot [5] thermostats. Both of these thermostats implement temperature control using a similar method. The Lowe-Andersen thermostat is discussed in the context of MD simulations in Section 3.2.2, where we also discuss the Nosé-Hoover thermostat. The Stoyanov-Groot thermostat was specifically developed for DPD particle systems, and is a combination of the Lowe-Anderson thermostat and a thermostat that is similar to the Nosé-Hoover thermostat, coupled in parallel. The Nosé-Hoover thermostat is adapted to be one that acts on pairs of beads (as the Lowe-Andersen thermostat does), rather than individual beads. The Nosé-Hoover thermostat is adapted and implemented by applying a thermostating force on pairs of beads i and j within a cutoff distance r_C:

$$F_{ij} = \alpha \psi(r_{ij}/r_C)(1 - T/T_0)[(\mathbf{v}_i - \mathbf{v}_j) \cdot \mathbf{e}_{ij}]\mathbf{e}_{ij} \tag{3.38}$$

where α is a thermostat coupling parameter, ψ is a smearing function such that $4\pi \int_0^1 \psi(r)r^2 dr = 1$ and $\psi(r) = 0$ for $1 \leq r$, $r_{ij} = |\mathbf{r}_{ij}|$ is the distance between beads i and j, r_C is the cut-off radius, T is the instantaneous temperature value, T_0 is the predefined temperature for the system, $\mathbf{v}_i$ is the velocity of bead i, and $\mathbf{e}_{ij} = \mathbf{r}_{ij}/|\mathbf{r}_{ij}|$ is a unit vector in the direction of $\mathbf{r}_{ij}$. Unlike the α in the standard Nosé-Hoover algorithm described in Eq. 3.2.2, the coupling parameter remains

constant throughout the simulation.

With the Stoyanov-Groot thermostat, for each pair of beads that is selected, we choose between the Nosé-Hoover thermostat and the Lowe-Anderson thermostat with probability $P = \Gamma \Delta t$ (where Δt is the integration time step and Γ is the Lowe-Andersen exchange frequency, as discussed in Section 3.2.2). In extreme cases of the probability P, the original two thermostats can be recovered. When $P = 0$, then the thermostat functions entirely as the pairwise variation of the Nosé-Hoover thermostat. When $P = 1$, this produces the Lowe-Andersen thermostat. When P is low, the resulting simulation has a high diffusion coefficient and low viscosity, and when P is high the liquid will have low diffusion coefficient and high viscosity.

In summary, in both the Lowe-Anderson thermostat and the Stoyanov-Groot thermostat a random selection of bead pairs are selected to have their relative velocities replaced with values from a Maxwell-Boltzmann distribution, for the required temperature. The Stoyanov thermostat also applies additional forces based on instantaneous temperatures to other bead pairs. Both of these thermostats require a choice of a collision frequency Γ, while the Stoyanov-Groot thermostat also requires the choice of additional parameter α. The fluid viscosity is thought to be linearly proportional to the choice of parameter Γ. The diffusivity is $\propto 1/\Gamma$, meaning that the Schmidt number ends up being $\propto \Gamma^2$. This relationship is confirmed by simulations performed by Stoyanov and Groot [5], with their results shown in Fig. 3.3.

There is no consensus in literature about how important the Schmidt number is in simulations, and the impact it has on results, although it is a topic of interest [134]. For example, Symeonidis et al. [145] perform DPD simulations modelling polymer chains and applying the Lowe-Andersen thermostat with varying choices of Γ in order to vary the Schmidt number. They find that when no shear is applied, the effect of varying Sc is minimal on the value for the radius of gyration R_g. However, when shear is applied using Less-Edwards boundary conditions, there is a large difference in the value of R_g found at different Γ values. However, one
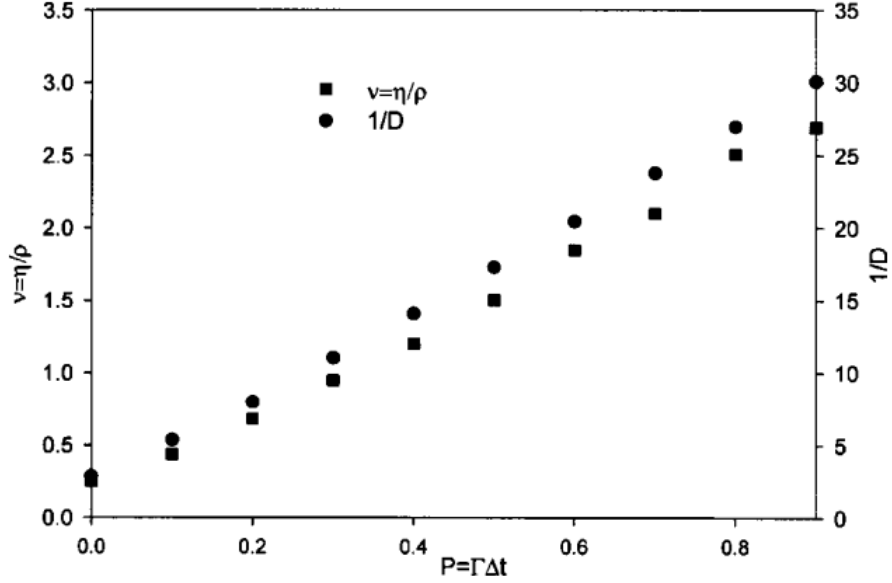
Figure 3.3: Figure showing the relationship between probability $P = \Gamma\Delta t$ and the viscosity η for DPD simulations conducted using Stoyanov-Groot [5] thermostat. Also shown is the relationship between P and the inverse of the diffusion coefficient $1/D$. The fact that these two relationships are linearly proportional means that the Schmidt number will be $\propto \Gamma^2$ [5].

study investigating the effect of the Schmidt number on the rheology of macro-molecules, simulated using DPD, finds that the Schmidt number is unimportant in determining the rheology [146].

3.3.7   Implementing Shear Flow

There are a number of different ways in which shear flow can be induced in a DPD simulation, and a number of different methods for calculating the viscosity. Methods for calculating the shear viscosity can broadly be categorised into two types: equilibrium and non-equilibrium methods. A typical equilibrium method makes use of Green–Kubo relations [147, 148], which used auto-correlation functions (ACF), which calculates the shear viscosity as:

$$\eta(t) = \frac{V}{k_{\mathrm{B}}T} \int_0^\infty \langle \sigma(n)\sigma(n+t) \rangle_n dt \tag{3.39}$$

where σ are the off-diagonal components of the stress tensor, V is the simulation volume, k_{B} is the Boltzmann constant and T is the temperature. The tensor

consists of nine components σ_{ij} which define the state of stress at a point inside the simulation box, however only the off diagonal components are used in the viscosity calculation. The method of calculating the stress tensor will be discussed in the following section. The angular brackets indicate an average over different starting times n or time origins. This integrand decays to zero in the limit of a long t. This method is most useful for Newtonian fluids. For non-Newtonian fluids the method will produce a value for the zero shear viscosity (the theoretical viscosity of a material when it is effectively at rest). However, this method is often hampered by the noisy tail of the ACF given by Eq. 3.39.

In order to investigate fluids that are expected to exhibit non-Newtonian behaviour, other methods are required. One such method is a non-equilibrium method, by using Lees-Edwards boundary conditions [6]. Lees-Edwards boundary conditions are an adaptation of standard periodic boundary conditions for inducing shear flow. The introduction of a shear strain into the simulation allows for investigation of the effect this has on the viscosity, for Newtonian fluids. This method works by giving a periodic domain a velocity that is proportional to the domain's vertical position, when compared with the centre domain, as is illustrated in Fig. 3.4. As a bead in the simulation box moves through the boundary at either the top or the bottom of the box, it has its velocity and tangential position changed. This generates a generate a linear velocity profile over the box domain, and we can obtain a constant shear rate for the system.

3.4   Shear Viscosity for Liquid Crystals

For an isotropic fluid, the shear viscosity can be simply calculated using the stress (or pressure) tensor and the applied shear rate. For a shear flow defined as application of a velocity field such that $\mathbf{v} = v_x(y)\hat{\mathbf{x}}$, there is only one non-zero off-diagonal term in the stress tensor: σ_{xy} (or the equivalent σ_{yx}). Using that the shear rate is
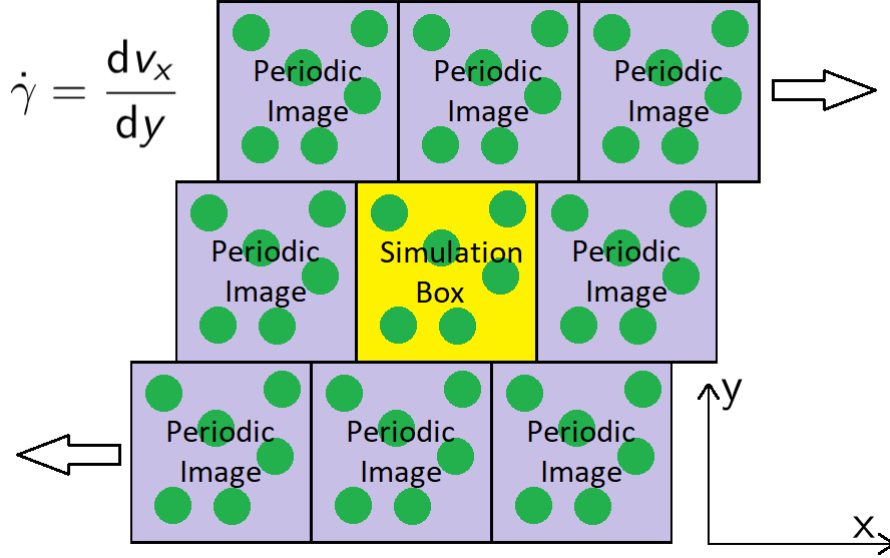
Figure 3.4: Illustration of Lees-Edwards boundary conditions [6] for shear flow. The shear rate $\dot{\gamma}$ can be calculated using the velocity v_x of the box.

given by $\frac{\partial v_x}{\partial y}$, the viscosity can be calculated using

$$\sigma_{xy} = -\eta \frac{\partial v_x}{\partial y}, \tag{3.40}$$

where the viscosity can vary for a variety of fluids depending on the magnitude of the shear rate applied. This stress tensor can be calculated using the Irving-Kirkwood definition [149] for a system by summing components of pairwise forces and vectors between bead pairs and by averaging over a large number of time steps. The stress tensor is therefore calculated using

$$\sigma_{\alpha\beta} = \sum_i (m_i v_{i,\alpha} v_{i,\beta} + \sum_{j>i} F_{ij,\alpha} r_{ij,\beta}), \tag{3.41}$$

where α and β represent the x, y, and z directions, and the sum in i is over all beads in the system. Although as noted above, only the component defined by $\alpha = x$ and $\beta = y$ is needed to calculate the viscosity.

However, for a nematic or a smectic liquid crystal, there are effectively 3 different shear viscosity coefficients to be considered, depending on the direction of shear flow. Miesowicz viscosity coefficients η_1, η_2, or η_3 are defined by the shear
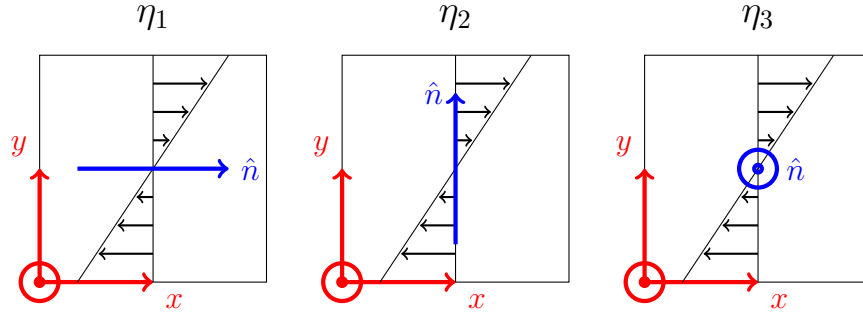
Figure 3.5: Definition of the Miesowicz viscosity coefficients η_1, η_2, and η_3. Measurement of the coefficients η_i involved orientating the director of the liquid crystal $\hat{n}$ relative to the flow velocity.

viscosities of the fluid in the nematic phase when the director lies along the x, y, or z axis, respectively. An illustration of the definition of η_1, η_2, and η_3 relative to the director is shown in Fig. 3.5. These were first measured experimentally by Miesowicz [150, 151], by aligning the director of the sample using an external magnetic field and measuring the viscosities using an oscillating plate viscometer. An electric field could also be used in place of the magnetic field. A summary of the three viscosities in relation to the flow velocity $\mathbf{v}$ [152] follows:

- η_1 is when director $\mathbf{n}$ is parallel to flow velocity;

- η_2 is when $\mathbf{n}$ is parallel to the velocity gradient;

- η_3 is when $\mathbf{n}$ is orthogonal to both the flow and the velocity gradient.

Note that other authors often use slightly different definitions of which coefficient η_i corresponds to which direction. Consider a nematic liquid crystal which has a director $\mathbf{n}$ that can be considered as a function of two angles θ and ϕ:

$$\mathbf{n} = (\cos\theta\cos\phi, \cos\theta\sin\phi, \sin\theta) \tag{3.42}$$

where angles θ and ϕ are defined in Fig. 3.6. The viscosity is a combination of the three Miesowicz viscosities as well as a fourth η_{12}, which cannot be visualised in the usual way, but is related to a stretch deformation [152]. It can be found
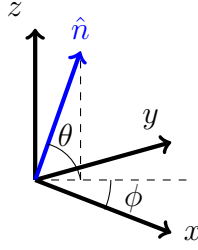
Figure 3.6: Definition of angles used in Eqs. 3.42 and 3.43 for the director of the liquid crystal $\hat{n}$.

that the expression for the apparent viscosity becomes [152]

$$\eta(\theta, \phi) = \eta_1 \cos^2 \theta \cos^2 \phi + \eta_2 \sin^2 \theta + \eta_3 \sin^2 \phi \cos^2 \theta + \frac{1}{4}\eta_{12} \sin^2 2\theta \cos^2 \phi. \quad (3.43)$$

Clearly the apparent viscosity depends on the alignment of the director with respect to the directions of shear and the velocity gradient. However, there is still a use for classical shear flow viscometers in order to assess such systems. Generally a change in the orientation of the director is induced under application of shear. In general, nematic crystals under shear will have a director that is parallel to the velocity, so a conventional shear rheometer will give a good approximation for η_1. In a smectic crystal such as the lamellar phase, there is generally a preference to form the layers in one of two orientations. When the lamellar layers are stacked in the direction of the velocity gradient, this is usually referred to as the parallel oriented lamellar phase (η_2). When the lamellar layers are stacked in the velocity gradient-neutral plane, and since the orientation of the director is perpendicular to the velocity gradient, this orientation is referred as the perpendicular orientation (η_3). These two orientations are illustrated in Fig. 3.7. For SLE$_3$S surfactant/water, which is molecularly very similar to AES, textures viewed under a polarised optical microscope indicate a parallel orientated alignment of the lamellar phase under shear [4]. Similarly, orientation of the liquid crystal phase has been found for the hexagonal mesophase, generally with the rods of the hexagonal crystal in alignment with the flow direction [153]. Further discussion of the experimental evidence for the alignment of the mesophases is provided in Chapter
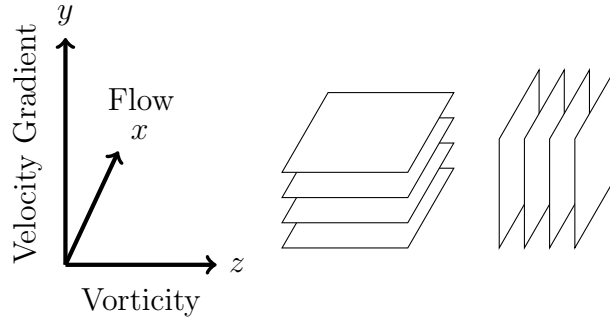
Figure 3.7: Meaning of the parallel and perpendicular orientations of the lamellar phase under the application of shear. Figure adapted from Ref [7].

4.

For the purpose of calculating a Schmidt number, we need to not only calculate a value for the viscosity η, but also for the diffusivity D. There are two common ways to calculate the diffusion coefficient. One method uses mean squared displacement, so that D is calculated using [154]

$$D = \frac{\langle (\mathbf{r}(t) - \mathbf{r}_0)^2 \rangle}{2td} \tag{3.44}$$

where $\mathbf{r}$ is the position of the bead, $\mathbf{r}_0$ is the initial position at time $t = 0$, t is time, d is the number of dimensions of the simulation box, and the angled brackets indicate an average over all beads. The diffusion coefficient can also be calculated using the velocity auto-correlation function [154], in a similar way that the zero-shear viscosity can be calculated using Eq. 3.39. In this case D can be calculated as

$$D = \frac{1}{d} \int_0^\infty \langle \mathbf{v}(n) \cdot \mathbf{v}(n + t) \rangle_n dt \tag{3.45}$$

where $\mathbf{v}$ is the velocity vector and the angled brackets indicate an average over all different starting positions, as in Eq. 3.39.

3.5 Effect of Periodic Boundary Conditions on Lyotropic Crystal Phases

3.5.1 Lamellar Phase

The lamellar phase can form within the simulation box in an orientation that creates a d-spacing value that minimises the potential energy of the box, and therefore is as close to the equilibrium d-spacing as possible. However, the nature of the finite size of the box and the periodic boundary conditions imposes some constraints on the orientations that the layers can form at, and therefore the available d-spacing values for the layers to take. Opposite sides of the boxes must match due to the periodic boundary conditions. This means, for example, for the two box sides in the $x - y$ plane, the surfactant layers must pass through the same x and y coordinates for the surfaces located at both $z = 0$ and $z = L$. This leads to a constraint on the angle that the layers can form at, and is illustrated in 2-dimensions in Fig. 3.8. The imposition of the constraints in 3-dimensions leads to the condition that the d-spacing layers must form to satisfy

$$\left(\frac{d}{L}\right)^2 (\kappa_1^2 + \kappa_2^2 + \kappa_3^2) = 1 \tag{3.46}$$

where κ_i are integers related to the number of layers that have formed in dimension i. Further derivation of this expression can be found in Appendix A.

3.5.2 Hexagonal Phase

The effect of boundary conditions on the hexagonal phase is more complicated due to the extra dimension of the structure (*i.e.* two dimensions as opposed to one in the lamellar phase). Consider the formation of a lattice in a 2-dimensional case, which forms in a square domain with periodic boundary conditions. An example of a unit cell that would satisfy these boundary conditions is shown in Fig. 3.9,
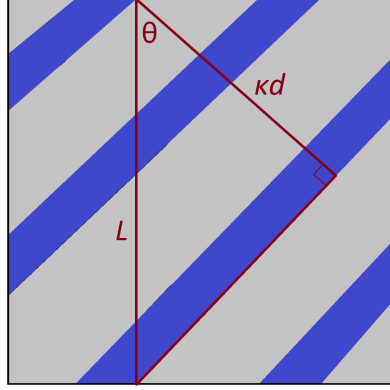
Figure 3.8: Illustration of the formation of repeated lamellar layers in the simulation box. A triangle illustrates the constraint that the periodic boundary conditions impose. The vertical line of this triangle has a length the same as box size L. A second line has length κd, where κ is an integer related to the number of layer repeats it passes though, and d is the spacing between the repeated layers. This line is normal to the periodic layers in the box and is in the same direction as the director for the molecules. These lines can form a right angled triangle such that $L \cos \theta = \kappa d$.

and the unit cell must form in such a way to satisfy equations

$$
\begin{aligned}
I_1 \vec{a} + I_2 \vec{b} &= \begin{bmatrix} L \\ 0 \end{bmatrix}, \\
I_3 \vec{a} + I_4 \vec{b} &= \begin{bmatrix} 0 \\ L \end{bmatrix},
\end{aligned}
\tag{3.47}
$$

where I_i are integers, in order to satisfy the boundary conditions. In order to be considered a perfect hexagonal lattice, this would require $|\vec{a}| = |\vec{b}|$. However, the formation of the unit cell is restricted by these boundary conditions, and the hexagonal lattice tends to form in a stretched/obscured way in order to meet these conditions. In the perfect hexagonal lattice described in Fig. 2.10, there is just one inter-rod spacing value, as the nearest six neighbours to any lattice point are all of equal distance away. However, for the situation described in Fig. 3.9 there can be up to three independent distances for the nearest neighbour spacing, described by the length of vectors $|\vec{a}|$, $|\vec{b}|$ and $|\vec{a} + \vec{b}|$. Therefore an average inter-rod spacing r, can be calculated as an average of these three distances. It will be discussed later in Chapter 7, why in the case of the simulations carried out in this work, it is not
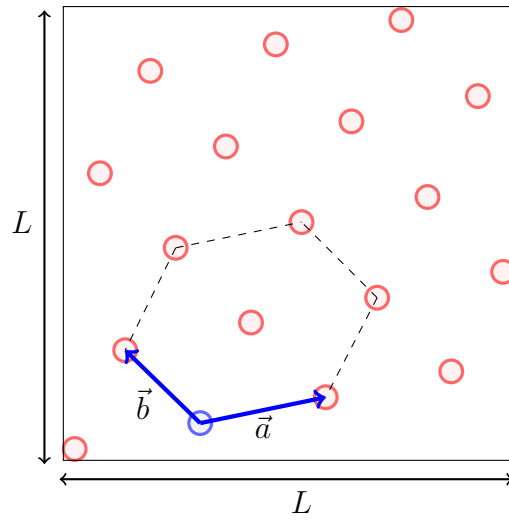
Figure 3.9: Formation of a lattice inside a 2-dimensional box, with periodic boundary conditions.

necessary to extend the above description to three dimensions.

Chapter 4

Experimental AES Phase Diagram and Rheology

As discussed in Chapter 2, there is no known published phase diagram for AE1S. There are also no known published rheological studies, detailing the relationship between the applied shear rate and the solution viscosity, as a function of composition. Therefore, this chapter will look to identify the mesophases formed by AES/water solutions, and identify the location of the phase boundaries, by a combination of polarising optical microscopy and rheological measurements. The results of these measurements will allow for a comparison with computational studies in later chapters.

There are many different experimental methods which can be used in order to determine the mesophase that forms for a surfactant solution at a given temperature and concentration. It is most often the case that a combination of different experimental techniques are used, in order to determine the phase diagram. One popular experimental method is through polarising optical microscopy (POM) [15, 155, 156], which uses plane-polarised light to observe structures that are birefringent (*i.e.* structures that are anisotropic). Structures that can be identified via this method include the hexagonal and lamellar phases, however this method cannot be used to identify the micellar and cubic phases, because they

are optically isotropic and do not give textures. In order to distinguish between the cubic and micellar phases, it is sometimes possible to use the fact that they have enormous difference in viscosities [155]. Other methods that could be used to identify the mesophase that has formed include small-angle neutron scattering [157–159], light scattering experiments [157, 158], small angle X-ray scattering [156, 160], NMR [161], and Raman spectroscopy [162].

4.1 Materials

The homogeneous samples for these measurements were prepared by mixing a controlled amount of surfactant with deionised water to create the desired concentration, and leaving the sample to stand at room temperature.

The AES paste used for creating the samples consists of 70% AES, and is supplied by Procter & Gamble. However, the concentration will be presented as a weight percentage (wt.%) of AES, as opposed to a percentage of the paste, as is done by some researchers [15]. Rheological measurements on micellar solutions formed by sodium dodecyl sulphate (SDS) are also performed in Section 4.3.2. The SDS (99+%) was purchased from Sigma-Aldrich.

Samples were created across the full concentration range obtainable via the AES paste (0-70 wt.%). For SDS solutions, samples are created in the micellar region (0-20 wt.%). Solutions that went on to form micellar solutions were left to equilibrate for at least 2 weeks before measurement, all other samples at higher concentrations were allowed to stand for at least 12 weeks before rheological measurements were performed. Microscopy imaging took place a significant time later than the rheological measurements, due to a lack of access to experimental facilities during the Covid-19 university shutdown. Therefore, the optical microscopy images reported in this chapter were performed on samples that were left to stand for at least 12 months. Samples were stored in sealed containers, in order to prevent drying or contamination.
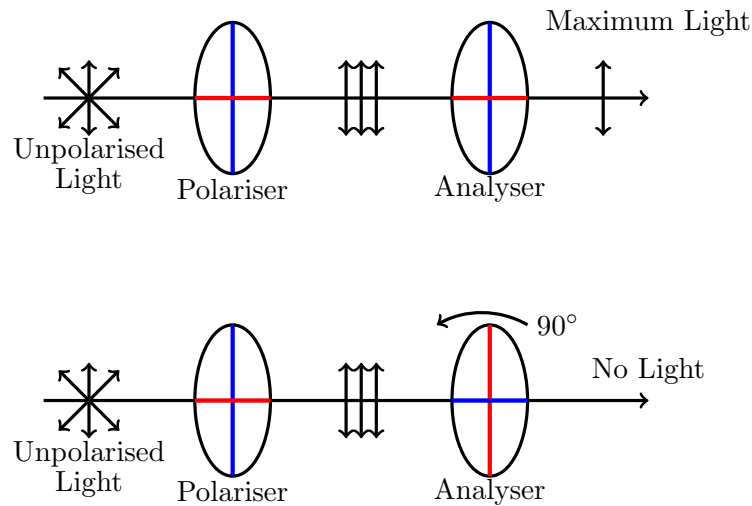
Figure 4.1: Illustration of polarised light. Once the ordinary light passes through the polariser, it is only oscillating in one direction, and therefore the analyser must also be orientated in the same direction in order for the light to pass.

4.2 Polarised optical microscopy (POM)

4.2.1 Background

Polarised optical microscopy uses plane-polarised light to observe structures that are birefringent. Normal sources of light are unpolarised and have electric field oscillating in all directions (perpendicular to the direction of propagation). If the electric field oscillates in one direction only, it is referred to as plane polarised light. Something that polarises light is referred to as a polariser. The principle of polarised light is illustrated in Fig. 4.1. When a second polariser (analyser) is added, the light can only travel through it fully if it is orientated in the same way as the polarised light. If the analyser is placed 90° to the polarised light, beyond the analyser no light will get through.

If a crystal is placed between the polariser and analyser, as the light enters the crystal it will be split into two rays with different velocities vibrating perpendicular to each other [163]. One of these rays is called the ordinary-ray (O-ray) and one the extraordinary-ray (E-ray). The ordinary- and the extraordinary- rays become out-of-phase once they exit the material. These two rays are then recombined with constructive and destructive interference when they pass through the analyser

[164]. Polarisation colours result from the interference of the two waves, and the angle between the polariser and analyser can be varied to extract information about materials.

The light that enters the crystal after passing through the polariser is only split when the material is anisotropic and the material contains a range of refractive indices. Isotropic materials, such as cubic crystals and micellar solutions, only have one refractive index and therefore do not act as beam splitters. Therefore, since POM relies on analysing the interference of the split beams as they are recombined through the analyser, no information can be gained by looking at isotropic materials.

4.2.2 AES Phase Identification

This section will look at identifying the phases formed by use of POM. In order to visualise the textures, a thin layer of pre-equilibrated sample is viewed under crossed polarisers. The process for achieving this thin sample is to squeeze a small amount of sample between two glass slides. However, this can inadvertently apply a degree of shear to the sample, and the application of shear force can influence the phase taken. To avoid this, we apply as small an amount of sample as possible to the glass slide, and apply as little force as possible to flatten. While one could then leave the sample on the prepared slide to equilibrate after being prepared, there could then be an influence from the exposed boundary with the air, such as sample evaporation, which may alter the phase. Hence we chose to not do this, and simply try and prepare the sample in a way which applies as little force as possible to the sample that is to be imaged.

A summary of the different textures identified for different AES concentrations is shown in Table 4.1, and the corresponding approximate phase boundaries in Fig. 4.2. Concentrations 6.9, 13.2 and 20.1% exhibit no textures, indicating the existence of an isotropic solution. Qualitatively the viscosity of these solutions is relatively low, therefore they will be assigned to the micellar phase. Quantitative

rheology measurements in Section 4.3 will confirm this. There then exists a large hexagonal region for samples of concentrations from 28% up to 58.6%, which are identifiable from their marble/smoke-like [165, 166] or mosaic [71, 166] textures. A sample of 59.9% displays a transition to lamellar phases, which is identifiable from a more streaked like texture [166]. Further increase in concentration continues to display lamellar textures. A selection of microscopy images at different concentrations is shown in Fig. 4.3. An interesting observation is that the lamellar phases also display a high degree of alignment at solution/air boundaries, as illustrated in Fig. 4.4. This helps provide an extra point of identification between the hexagonal and lamellar phases.

Sample Concentration (wt.%)	Appearance
6.9	No Textures
13.2	No Textures
20.1	No Textures
28.0	Hexagonal
34.7	Hexagonal
41.3	Hexagonal
49.7	Hexagonal
52.1	Hexagonal
58.6	Hexagonal
59.9	Lamellar
63.1	Lamellar
70	Lamellar

Table 4.1: Identification of the mesophases formed by AES/water solutions at room temperature. Phases identified using POM.
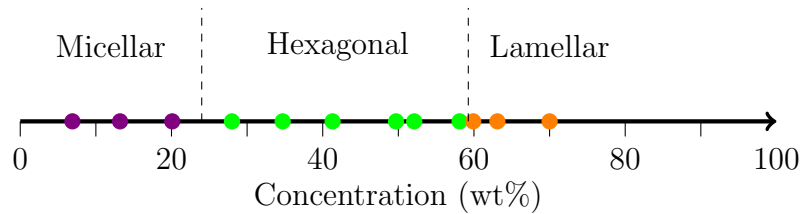
Figure 4.2: Phase boundaries of AES solutions at room temperature, identified by POM imaging.

Identifying the phases of solutions at concentration boundaries can be difficult due to potential inhomogeneities in the solution sample. This is particularly true for very viscous phases where dissolution is slow, and different portions of the
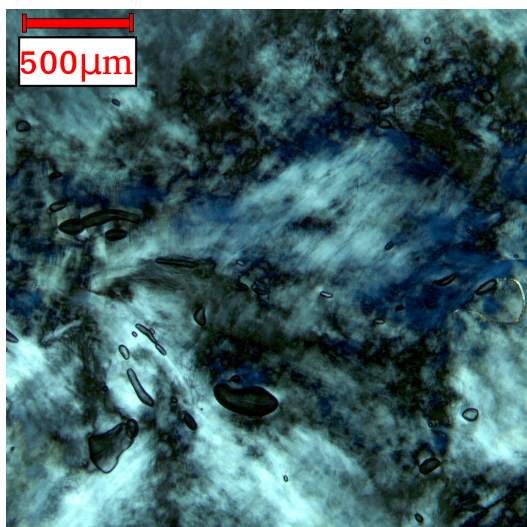
(a) $c = 41.3$wt.%
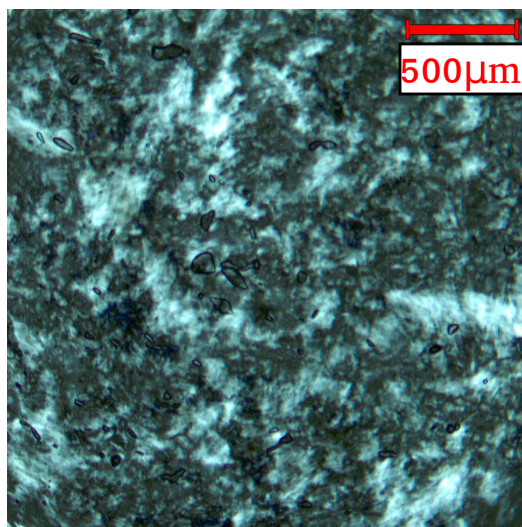
(b) $c = 52.1$wt.%
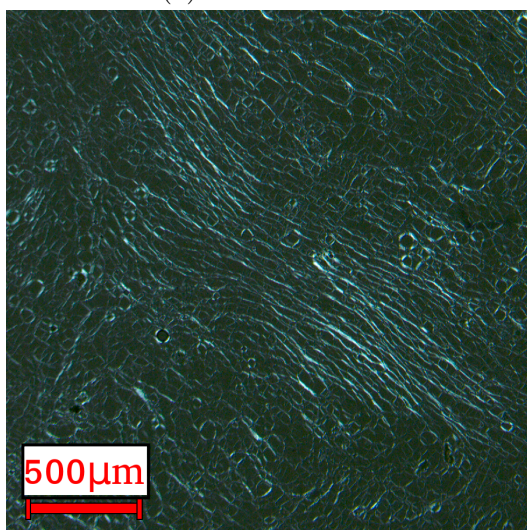
(c) $c = 59.9$wt.%
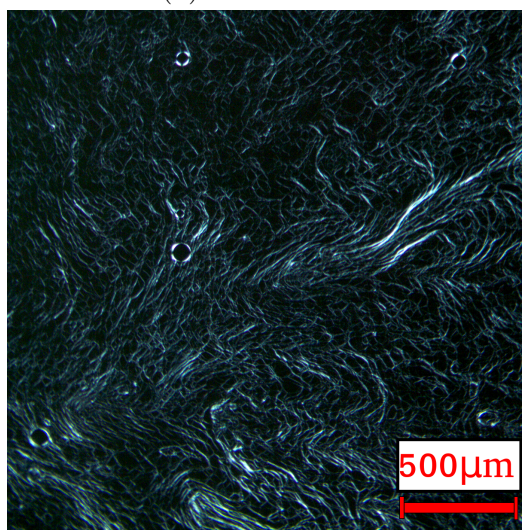
(d) $c = 70$wt.%

Figure 4.3: POM images at 5x magnification of a variety of AES solutions at different concentrations c. Phases identified as hexagonal (a and b) and lamellar (c and d).
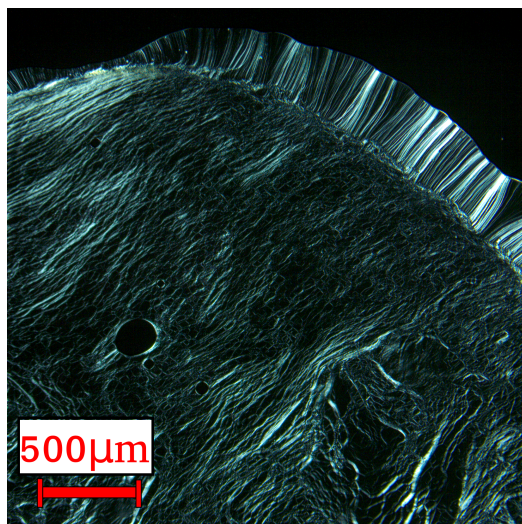
Figure 4.4: POM images at 5x magnification of a sample at concentration $c = 63.1$wt.%. Phase is identified at this concentration as lamellar. The region of this image that is completely black is where no solution is present. There is increased phase alignment of the lamellar phase at the phase boundary between the bulk surfactant and the interface with the air.

sample could be residing at slightly different concentrations, and therefore slightly different phases. However, our samples were allowed to equilibrate for between 12 and 24 months before POM imaging, so it is unlikely that further equilibration time would improve homogeneity. Furthermore, repeated microscopy images were taken from different parts of the sample to confirm conclusions. For AES/water solutions, identifying the boundary between the hexagonal and lamellar phases is the most tricky. For some surfactants a cubic phase can exist in between the two phases [4, 15], and for AE3S this is discussed in Section 2.3. This makes the identification of the phase boundary easier, however, no cubic phase is identified for AE1S/water solutions at room temperature. Originally, the samples in the region where a cubic phase would be expected to exist were prepared at 52.1%, with the next sample concentration at 63.1%. In order to attempt to locate any potential cubic phase, additional samples at interim concentrations were created. As a concentration of 58.6% was identified to have a hexagonal phase, this narrows the window for any potential cubic phase to just 1.3%, making it unlikely that it has been missed. Otherwise, the location of the phase boundaries identified is reasonably similar between AE1S and AE3S.

101

An alternative method to investigating the phases formed by AES/water solutions would be to conduct a penetration scan experiment [4, 167, 168]. In this experiment, a concentrated amount of surfactant is placed in a capillary tube and placed in contact with pure water, creating an interface between the two. Then, POM images of the surfactant-water interface are taken at short time intervals, in order to observe phase formation as a function of composition. This produces layers of different mesophases as the concentration varies between the two samples. This method has its benefits, including the fact that it is quicker due to not having to wait for fully equilibrated samples for imaging. It also removes the homogeneity uncertainty problem, as discussed above. However, it is more difficult to gauge an estimate for the location of the phase boundaries using this method. Quantitative information on the phase boundaries can only be obtained if the local composition along the tube can be determined, for example by refractive index measurements [169]. Therefore, this isn't a method that has been explored in this research.

4.3   Rheology

Rheological measurements can aid in phase identification, because different mesophases are expected to have different viscosity ranges. Solutions containing spherical micelles are generally of low viscosity [170, 171]. If the micelles start to become less spherical at increased concentrations (*i.e.* more rod like), there can be an increase in the viscosity of the solution [171], although the solution still has relatively low viscosity when compared to liquid crystal phases. When the concentration reaches high enough levels, these elongated micellar rods can align into an hexagonal phase, which results in a large increase in value for the viscosity. Lamellar phases on the other hand generally have a lower viscosity value than the cubic and hexagonal phases, due to the layered nature of the system [172]. Cubic phases usually have the highest viscosity values of all liquid crystal phases, however no cubic phases are identified for this system using POM imaging.

4.3.1 Background

There are two basic types of flow, these being shear flow and extensional flow. In the study of shear flow, fluids are subject to a simple shear stress field, causing components to shear past one another. In extensional flow, fluid components flow away or toward each other. Shear flows are much easier to study, and are most easily measured on a rotational rheometer [173]. These are the types of flow we will be measuring.

The shear viscosity η, also referred to as the apparent viscosity, is defined as the shear stress τ experienced by the fluid, divided by the shear rate $\dot{\gamma}$

$$\eta = \frac{\tau}{\dot{\gamma}}. \tag{4.1}$$

This is also how viscometers or rheometers calculate the viscosity. There are a number of different types of viscometer, but by far the most common is the rotational viscometer. These viscometers work by immersing a rotating spindle into a fluid, and measuring how much torque is required to turn the spindle. The spindle applies stress to the fluid, and then from use of Eq. 4.1 a viscosity can be calculated. The shape of the spindle can take many forms. A cone-plate/plate-plate configuration can also be used for applying the shear stress. Some of the different types of geometries used in viscometers are illustrated in Fig. 4.5. Different spindle types are more (or less) appropriate, depending on the fluid to be measured. The cone-plate geometry usually consists of a lower, temperature controlled plate and an upper rotating cone of a very shallow angle. A small amount of sample is placed in between the two plates, and the cone is brought down to make contact with the sample. This set up has the benefit that a uniform shear rate is generated across the entire sample. Another benefit is that, as the sample is small, temperature equilibration is rapid. The plate-plate configuration is very similar, but it does not generate a uniform shear rate. In the concentric cylinder configuration, the sample is poured into an outer 'cup', and the inner cylinder lowered into the sample. This
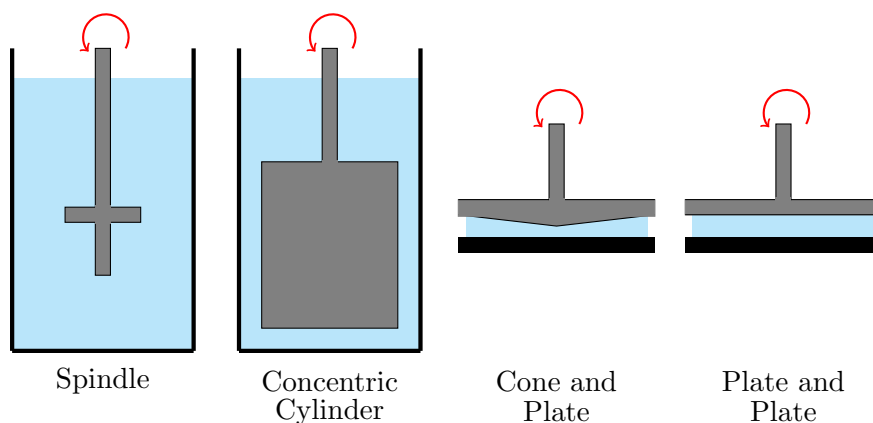
Figure 4.5: Illustration of different kinds of rotational geometries that can be used to measure viscosity using a rheometer.

geometry is useful for solutions that would struggle to be loaded into the cone-plate geometry (*e.g.* solutions with such low viscosity that they would run out of the edges of the cone-plate/plate-plate system), although a much larger sample size is usually required. In this work the low-viscosity solutions (likely to correspond to the micellar phase) are measured using the concentric cylinder system, while the higher viscosity samples are measured using the cone-plate geometry.

Generally, fluids can be classified into two different types depending on Eq. 4.1: either Newtonian fluids or non-Newtonian fluids. When the viscosity η that is calculated is independent of the shear rate $\dot{\gamma}$, at a given temperature, these fluids are called Newtonian, as they obey Newton's law of viscosity. However, it is more common that fluids exhibit non-Newtonian behaviour, meaning that their viscosity is dependent on their shear rate. Among non-Newtonian fluids, we can also classify into shear-thinning and shear-thickening fluids. That is fluids that have a decrease in viscosity with increasing shear, and those that have an increase. Examples of shear-thickening fluids are cornstarch in water and nanoparticles dispersed in a polymer solution. Examples of shear-thinning fluid are paints and polymer solutions. It should be noted that fluid viscosity, even for a Newtonian fluid, is generally still dependant on the pressure and temperature, with viscosity usually increasing with increased pressure and decreasing temperature.

Shear flow can be illustrated as layers of fluid sliding over one another with
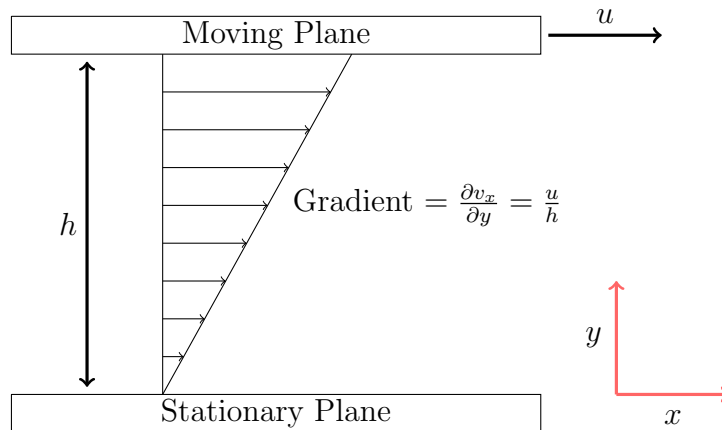
Figure 4.6: Illustration of Couette flow using two infinite flat plates. The upper plate is being moved in the x direction with velocity u while the bottom plate is stationary. This creates a linear velocity profile between the two plates. The x component of the velocity of a fluid element at height h in the y direction can be calculated as $v_x = yu/h$.

each layer moving at a different speed, such that there is a velocity profile across the domain. A simple case of illustrating shear flow is Couette flow, as illustrated in Fig. 4.6. In this case a fluid is trapped in between two parallel plates, where one plate is moved with a velocity relative to the other. In this set up the shear rate $\dot{\gamma}$ is simply the velocity of the wall u divided by the plate separation h *i.e.*

$$\dot{\gamma} = \frac{u}{h} = \frac{\mathrm{d}v_x}{\mathrm{d}y}.$$

(4.2)

This Couette flow can be induced in the geometries illustrated in Fig. 4.5.

For most fluids, the effect of shear-thinning is reversible, and the fluid will eventually return to its original viscosity when the shearing force is removed. When this recovery process is time dependent, the fluid is considered to be thixotropic [173] (note that thixotropic materials are always shear-thinning). Thixotropic materials usually exhibit this behaviour because there are time dependent microstructural rearrangements occurring in the fluid following the application of shear.

The following section will discuss the rheological behaviour that is expected for surfactant systems similar to AES/water solutions. Discussion will split into dealing with the micellar phase and the liquid crystal phases separately, due to

their differing behaviour.

4.3.2 Micellar Solutions

4.3.2.1 Overview of Empirical Rheology Models for Micellar Solutions

For micellar systems, changes in the solution viscosity are expected to be most influenced by changes in the shape of micellar aggregates, the number of micelles formed and/or due to micellar interactions [174–177]. AES is structurally very similar to SDS. Therefore, the rheology of monodisperse SDS/water systems is expected to be very similar to that of polydisperse AES/water systems. The micellar phase of SDS/water systems has been found by other researchers to be Newtonian, with an increasing viscosity with increasing concentration within this region [175, 176]. A number of reasons for this increase in viscosity have been suggested by different researchers. It is most often suggested that for SDS solutions, the size and shape of the SDS micelles changes very little, and therefore the strong repulsive intermicellar interactions play a large role in the measured increase in the viscosity [175–177].

There have been a number of theoretical attempts to connect the viscosity of micellar solutions to the concentration. For example, early relations include the Einstein equation [178]

$$\eta = \eta_{\mathrm{w}}(1 + 2.5\Phi) \tag{4.3}$$

where η_{w} is water viscosity and Φ is the volume fraction of surfactant. This relation is applicable if the micelles were to behave as single spherical and noninteracting particles. At infinite dilution (where these interaction between micelles are minimised), the viscosity is expected to be mostly sensitive to the shape and size of the micelles in the solution. At very low concentrations (below $\approx 0.2\%$), Eastoe *et al.* [174] confirm that this relationship correctly describes the viscosity of surfactant solutions with Na^+ counterions. Therefore, this indicates spherical micelles at least at very low concentrations. Alternatively, there is Batchelor's corrected

equation, that also considers two-body hydrodynamic interaction between hard spheres, given as:

$$\eta = \eta_{\text{w}}(1 + 2.5\Phi + 6.2\Phi^2). \tag{4.4}$$

Montalvo [175] finds for SDS micelles in solution that the data does not appear to fit either Eq. 4.3 or Eq. 4.4 beyond very low concentrations, suggesting that higher-order terms to these equations should be expected, due to strong repulsive intermicellar interactions, that become more important at higher concentrations.

Arguably the most popular equation for describing the viscosity of rigid and spherical particles is the Mooney equation [179]:

$$\eta = \eta_{\text{w}} \exp \frac{2.5\Phi}{1 - Q\Phi} \tag{4.5}$$

where Q is an inter-particle parameter in the range $1.35 < Q < 1.91$. Note that for dilute solutions as $\Phi \to 0$, Eq. 4.5 is the same as Eq. 4.3. The Mooney equation was then generalised to the form [180]

$$\eta = \eta_{\text{w}} \exp \frac{K\Phi}{1 - Q\Phi} \tag{4.6}$$

where K is a shape factor that varies from $2.5 < K < 5$ and Q varies between $0.6 < Q < 2.1$. The choice of $K = 2.5$ theoretically correlates to what is expected for spherical particles, while deviation from this would indicate prolate or oblate shapes. However, it is theorised that very high values of $K \approx 5$ can also arise from electroviscous effects from the presence of charge on the surface of dispersed particles [180]. In the Mooney equation, the hydrodynamic effects of particle collisions have been neglected, and these effects become important as concentration increases [181]. In order to take into account the mutual interaction of particles and their collisions, Vand [182] derived the theoretical formula

$$\eta = \eta_w \exp\left(\frac{v\Phi + r(k - g)\Phi^2}{1 - Q\Phi}\right) \tag{4.7}$$

where g and k are shape factors, Q is the hydrodynamic interaction constant, and r is the collision time parameter, which indicates how long particles are involved in collisions. For rigid, non-solvated spheres without mutual interactions and Brownian motion, the theoretical values of $g = 2.5$, $k = 3.175$, $Q = 0.609$ and $r = 4$ are derived. As r is representing the proportion of time spent by particles in a collision, its value will be reduced for particles of decreased size due to Brownian motion, or particles with repulsive forces [181]. However, generally the parameters in other non-theoretical cases are not known. Fitting to Eq. 4.7, in order to find exact values for the parameters, may be relatively difficult compared to previous equations discussed, due to the increased number of parameters (leading to overfitting).

4.3.2.2   Measurements for AES Rheology for Micellar Solutions

Viscosity measurements in the AES micellar phase were made for concentrations 7, 11, 13, 17, 20 AES wt.%. Measurements were also made for a range of SDS solutions with concentrations 5, 10, 15, 20 wt.%, as well as for pure water. Although the viscosity of SDS micellar solutions has been reported by other authors [175, 183], they are repeated here to allow for a direct comparison with AES solutions, measured using the same procedure and equipment. Measurements were performed at 25°C using the Anton Paar Physica MCR301 Rheometer and 27mm concentric cylinder geometry (as illustrated in Fig. 4.5).

The readings were made in the largest shear-rate-range that the equipment would allow for each sample. The limiting factor on the lower bound for the shear rate is due to torque that can be measured (minimum torque = 0.1 µNm) by the Anton Paar Rheometer. At higher shear rates, there can be an influence of secondary flows, and Couette flow can no longer be assumed, placing an upper bound on what can be measured. A logarithmic step-wise ramp method was used in order to gradually increase the shear rate, starting at a shear rate of $0.01\mathrm{s}^{-1}$ (although in every case the shear rate had to reach higher values before a large

enough torque value was measured for viscosity calculation). Once the shear rate had reached 100s^{-1} the results were repeated in order to check for thixotropic behaviour, but the results were found to be independent of past shearing.

A plot of the calculated viscosity against shear rate is shown in Fig. 4.7, and it can be seen that in the shear rates trialled, the solutions exhibit Newtonian behaviour. Newtonian behaviour indicates that the micelles are maintaining approximately the same size and shape with application of shear, as any change in micelle size would be expected to have an influence on the viscosity value. A plot of the calculated viscosity η against surfactant concentration c is shown in Fig. 4.8. The relationship between η and c, for SDS, is in excellent agreement with values measured by other authors [175, 183]. Fitting to Eq. 4.6 is performed by assuming that the volume fraction Φ and weight fractions are approximately equivalent. A fit to the parameters in Eq. 4.6 is performed using a least squares to fitting method, using a Python script. The viscosity increases non linearly with increasing concentration for both AES and SDS systems, with the AES solutions having a viscosity of higher magnitude than the SDS systems. In particular, the viscosity difference between the two systems is most noticeable at higher surfactant concentrations. The larger viscosity of AES solutions may be in part due to an increase in the micelle size, due to the average length of an AES molecule being approximately one ethoxylation unit (OCH_2CH_2) longer. If we assume that the micelles are spherical with a radius close to the length of one surfactant molecule, this would increase the size of an AES micelle by $2(OCH_2CH_2)$, relative to an SDS micelle.

Fits are also obtained to Eqs. 4.4 and 4.5, as well as Eq. 4.6, with the results for this shown in Fig. 4.9. Eq. 4.4 is shown to be a poor fit to the data, in agreement with what is found by Montalvo [175] for SDS solutions. This is to be expected, as Eq. 4.4 is not expected to be valid beyond very low concentrations. Eq. 4.5 provides a more reasonable fit to the data, however a much better fit is obtained when Eq. 4.6 is used and K is allowed to deviate from 2.5. The parameters obtained
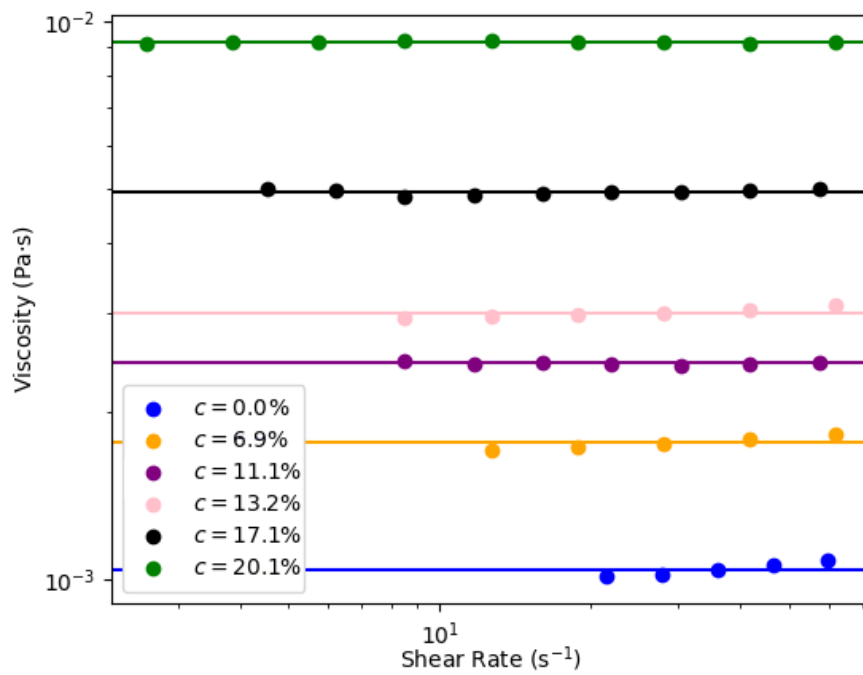
(a) AES solutions
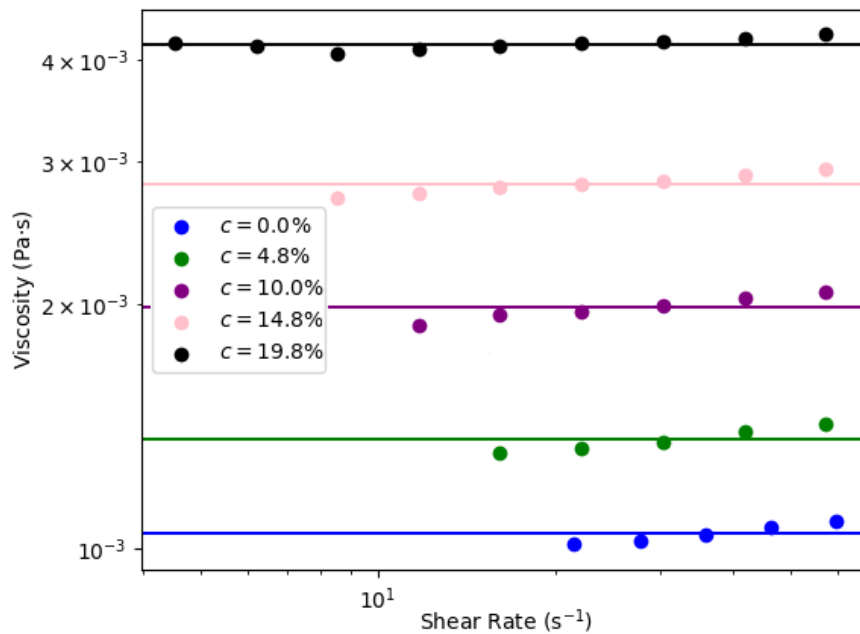
(b) SDS solutions

Figure 4.7: Calculated viscosity against shear rate for a range of (a) AES and (b) SDS solutions in the micellar mesophase, for a variety of concentrations c. Solutions display Newtonian behaviour.
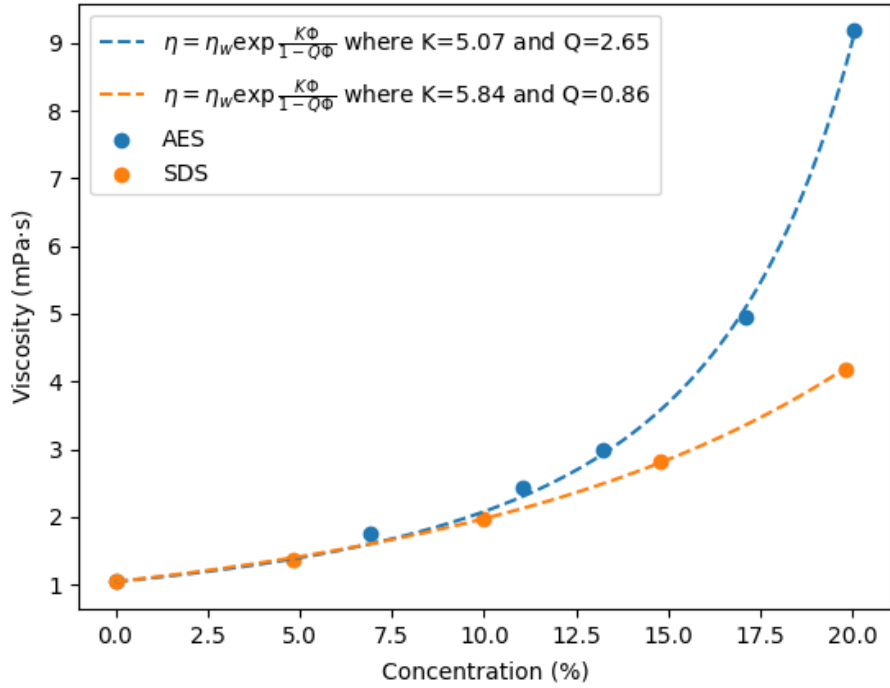
Figure 4.8: Plots of calculated viscosity (mPa·s) against concentration (wt.%) for AES and SDS solutions. The solutions are fitted using Eq. 4.6. Error bars are calculated as the standard deviation of the results obtained from varying shear rates (Fig. 4.7), but are smaller than the symbol size so are not visible.

from fitting Eq. 4.6 to the data are: $K = 5.07$ and $Q = 2.65$ (AES); $K = 5.84$ and $Q = 0.86$ (SDS), indicating that the viscosity of the solution cannot be modelled as non-interacting hard spheres (which requires $K = 2.50$). This is likely to be because of a combination of non-spherical micelles (as we are considering relatively high concentrations) and/or interactions between those micelles. In order to investigate whether the effect is caused by micellar interaction, the data was fit using Eq. 4.7. Guettari [181] find that fitting to micelles in an AOT/water/isooctane system (where AOT is sodium bis(2-ethylhexyl) sulfoccinate) requires a value for the interaction time that is much higher than the theoretical value $r = 4$, as a result of attractive forces dominating the interaction. If we use theoretically derived values for spherical particles $g = 2.5$, $k = 3.175$ and $Q = 0.609$, and allow r to be a fitting parameter, values for r are found to be $r = 52.6$ (AES) and $r = 28.6$ (SDS). This could indicate that it is micellar interactions playing a role in increasing the viscosity.

Although a number of theoretical equations can provide adequate fits to the
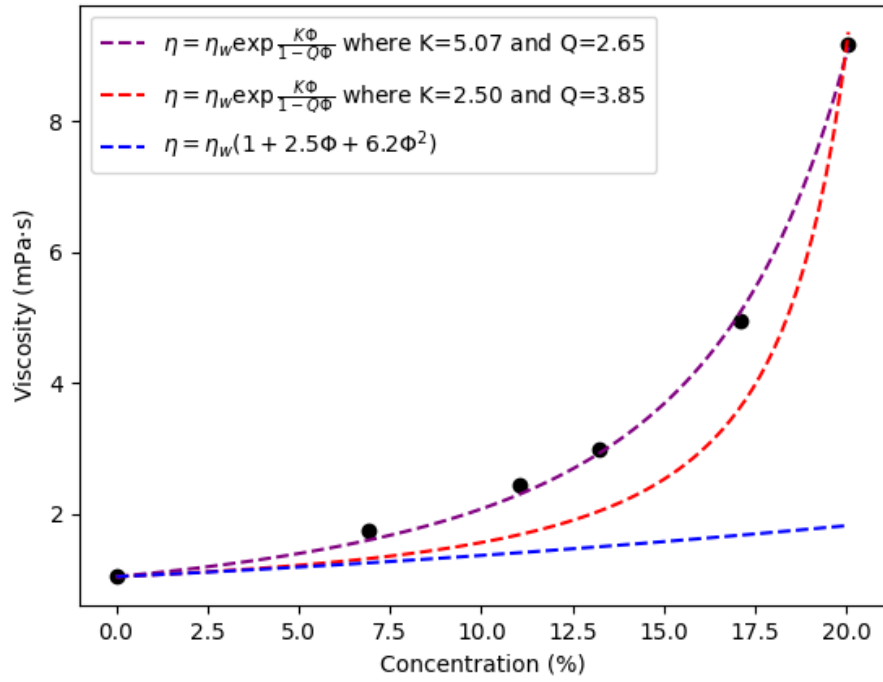
(a) AES solutions
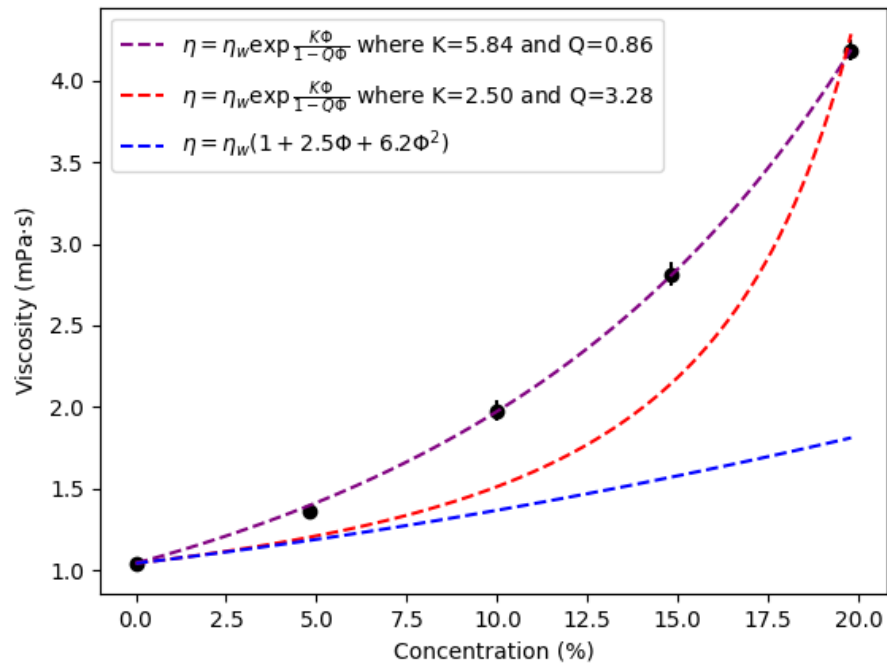
(b) SDS solutions

Figure 4.9: Plots of calculated viscosity (mPa·s) against concentration (wt.%) for AES and SDS solutions: (a) AES and (b) SDS solutions fitted with Eqs. 4.4, 4.5, 4.6. Error bars are calculated as the standard deviation of the results obtained from varying shear rates (Fig. 4.7), but are smaller than the symbol size so are not visible.

experimental data, it is unclear from these fits alone, what the causes the increasing viscosity. While the theoretical equations discussed can account for non-spherical micelles, most of the theoretically derived equations assume that the micellar shape and size does not change much with increasing concentration. It is more likely that the shape factor is concentration dependant, with micelles deviating from spherical shape upon increasing concentration. Also most exclude considerations of intermicellar interactions, in particular electrostatic interactions. The fits obtained using equations that assume spherical shape and neglect interactions are in general poor beyond extremely low concentrations. At the beginning of this section it was proposed that an increase in viscosity was likely due to an increase in the number of micelles, the shape of those micelles, or as a result of intermicellar interactions. The effect of varying the concentration on the micellar shape and size will be discussed in the following chapter.

4.3.3   Lyotropic Liquid Crystals

4.3.3.1   Overview of Rheology for Lyotropic Liquid Crystals

The non-micellar mesophases of surfactant/water systems produce extremely different rheological behaviour when compared with the micellar case. They possess a viscosity value many orders of magnitude larger than that of micellar systems, while also displaying a more complex viscosity *vs.* shear rate relationship, which is expected to be shear-thinning and time-dependent [15, 175, 184–188]. The behaviour of the liquid crystals formed by surfactant/water systems is less well studied than the micellar region, due to this extra level of complication.

While liquid crystals generally maintain their ordered structure under application of shear, lamellar and hexagonal solutions can enter the flowing state. For example, the bilayers of the lamellar phase can slide over one another under the influence of a shear force, and similarly in the hexagonal phase the rods can slide past one another. Both the hexagonal [153, 189–191] and lamellar [7, 192–194] phases have been shown to exhibit phase orientation under the application of

shear. This is briefly mentioned in Section 3.4, as evidence for why we can focus on one orientation for our simulations. For example it is shown that for SLE$_3$S surfactant/water systems, there is a parallel-orientated alignment of the lamellar phase under shear [4], in the shear range that the authors researched. Experimental research suggests that for some systems, there is a transition from the parallel orientation to the perpendicular orientation at very high shear rate [192, 193, 195]. Such behaviour has also been found using MD [7]. It is suggested that a potential reason for the the shear-induced orientation transition is the smaller viscosity in the perpendicular lamellar phase [7, 195]. However, this high shear rate behaviour doesn't appear for all lamellar systems, and for many systems the parallel orientation can be shown to persist from both low to high shear rates [194]. For other systems, there can be a transition for the parallel bilayers to vesicles at high shear rates (also often referred to as 'onions') [185]. In the range of shear rates to be studied in this research, generally the experimental evidence suggests that we can assume that the phase maintains parallel orientation of the lamellar bilayers.

The hexagonal phase generally has a viscosity higher than that of the lamellar phase. Experimental research also shows shear alignment of the hexagonal structure [153, 189–191]. For example, Richering *et al.* [153] investigate the rheological properties of an hexagonal phase formed by nonionic surfactant. The hexagonal solutions exhibit shear-thinning, and under shear two different alignments can be obtained: either an in-shear-plane orientation or an out-of-shear-plane 'log-rolling' orientation. An illustration of these two alignments is shown in Fig. 4.10. When shear is applied to the solutions, the hexagonal phase first aligns perpendicular to the direction of shear flow at short shearing time, and then and eventually parallel to the flow direction at long shearing time. This alignment of the hexagonal rods along the flow direction is the most common orientation that has been found by other researchers [189–191]. For a hexagonal phase in which the rods are along the flow direction, there can also be orientation of the hexagonal structure in the plane perpendicular to the shear flow. Suppose that Couette flow is induced by applying
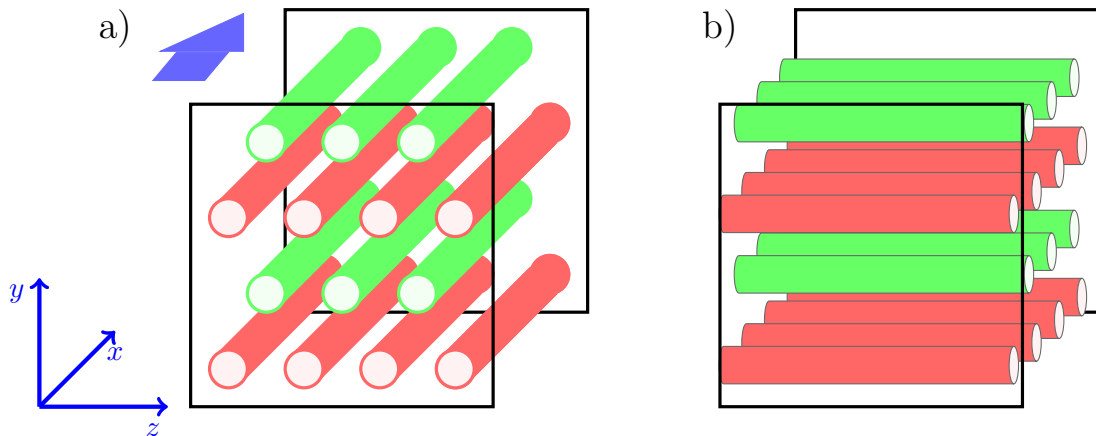
Figure 4.10: If shear flow is induced in the x direction by shearing using the $x - z$ plane, the rods in the hexagonal phase align in either in an (a) in-shear-plane or an (b) out-of-shear-plane 'log-rolling' orientation .
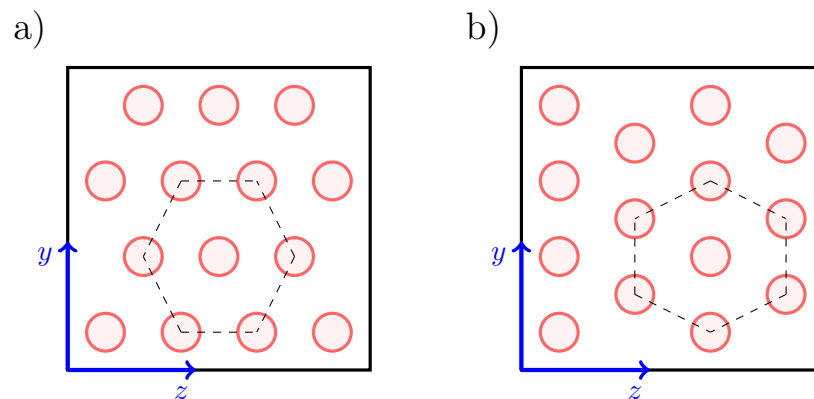
Figure 4.11: If shear flow is induced in the x direction by shearing using the $x - z$ plane, rods in the hexagonal phase tend to align along the x-axis. The perpendicular plane ($y - z$ plane), experimentally, takes one of the two orientations that are given the name parallel (a) or perpendicular (b).

shear to the x-z plane in the x direction, so that the hexagonal rods are aligned along the x-axis. Figure 4.11 illustrates the two possible orientations of the unit cell. It is most often found that at room temperature the orientation described as *parallel* forms [189, 191]. It has been shown that at very high temperatures, the orientation can change such that a *perpendicular* orientation forms [189], however in all of our work we will be at temperatures in the range such that we can assume parallel alignment.

The shear thinning behaviour of these systems is often able to be fit to one of

the following similar models for polymers under shear flow. The Cross model [105]:

$$\eta = \eta_\infty + \frac{\eta_0 - \eta_\infty}{1 + \alpha\dot{\gamma}^{(1-n)}} \qquad (4.8)$$

where η_∞ is the infinite shear viscosity, η_0 is the zero shear viscosity, α is a constant, n is the power law index. When $\alpha\dot{\gamma}^{(1-n)} \gg 1$, Eq. 4.8 becomes the Sisko equation [106]:

$$\eta = \eta_\infty + K\dot{\gamma}^{(n-1)} \qquad (4.9)$$

where K is the consistency index. When we do not see the effects of plateau to the infinite shear viscosity we can simplify further to just the power law relationship:

$$\eta = K\dot{\gamma}^{(n-1)} \qquad (4.10)$$

When solutions follow this relationship, a plot of η *vs.* γ on a log-log scale would appear linear with gradient $(n-1)$. It is most common to use Eq. 4.10 for fitting for surfactant systems [185–188]. However, the Sisko equation can be used [196] when the plateau to η_∞ can be observed, and the Cross model [197] when the crystal displays a plateau to zero shear viscosity η_0. The approximate flow curves that these equations model are illustrated in Fig. 4.12. There can be variations on the fitted parameters K and n between different surfactants, as well as from changing surfactant chain length [196], concentration [185, 187, 188, 198] or temperature [187, 188, 198].

The structures formed in lyotropic liquid crystals have, however, often been shown to exhibit viscoelastic behaviour [15, 175, 185, 187, 196, 197], and a number of authors have reported plastic behaviour by some lyotropic liquid crystal phases [175, 186, 188]. In this case, the solutions initially behave like a solid by being resistant to flow, and requiring a minimum yield stress to start flowing. This means that the concept of a zero shear viscosity doesn't exist, with the fluid having an ever increasing viscosity as the shear rate approaches zero. In these fluids the yield stress can be estimated by extrapolating shear rate $\dot{\gamma} \to 0$, in plots of shear
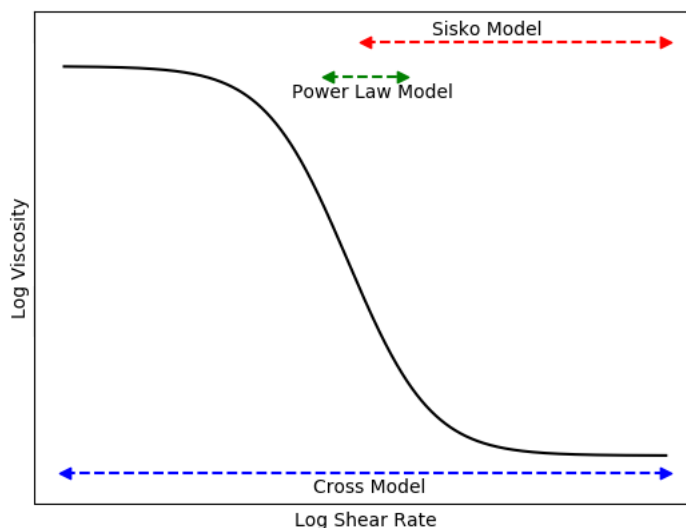
Figure 4.12: Illustration of a flow curve and the models that can be used for fitting to its shape.

stress *vs.* shear rate. This is more commonly observed in the lamellar phases as opposed to the hexagonal phases [197]. The yield stress is difficult to obtain as a true material constant, due to the fact that the value found can be dependent on the measurement technique employed, of which there are many. There is no universal method for determining yield stress, and there is usually a preference for different methods across different industries [199]. While the yield stress can be considered as an engineering reality, it does not have a clear scientific meaning since it is a manifestation of strong viscoelasticity [200].

The spacing between the periodic components of the lamellar and hexagonal phases are expected to play roles in their rheology. For example, it is concluded by Ichihara *et al.* [201] that the viscosity of lamellar gels was in part controlled by the layer-to-layer interactions between bilayers. Measurements revealed that an increased NaCl concentration resulted in a decreased d-spacing caused by the screening of electrostatic repulsion between lamellar bilayers. This decreased layer separation increased the layer-to-layer interactions, leading to increased viscosity. Given that a number of authors have found a dependence of the lamellar d-spacing and hexagonal inter-rod values on surfactant concentration [24, 25, 50, 53, 55], one might expect that the viscosity of the lyotropic phases is directly influenced by concentration of surfactant molecules. The exact relationship between the con-

centration and viscosity found experimentally is not clear. Most often it is found that an increase in the surfactant concentration leads to an increase in the viscosity [188], whilst it is found by others that the viscosity for a particular phase is at its maximum in the middle of the concentration range [202]. Other authors have found that the viscosity of the hexagonal and lamellar phases vary only slightly as a function of the composition [184], relative to the viscosity changes that are induced by a phase transition. Therefore it is possible that the relationship between the concentration and viscosity for a given phase is surfactant specific.

The rheological behaviour of lyotropic liquid crystals has been shown to be strongly dependent on shear history [184, 196]. Versluis and van de Pas [196] vary the number of ethylene oxide units in anionic surfactant chains forming lamellar layers, and find that the samples with the largest number of EO (ethylene oxide) units show the most noticeable shear/time history. With the first up-curve (the viscosity *vs.* shear rate profile produced when starting from a low shear rate and increasing) resulting in lower viscosity values than those produced from subsequent down (starting from high shear rate and decreasing) and up-curves. This indicates a change in the microstructure due to the shear history. The fitted values of K and n also therefore change. The values of index n decreases for fits to curves after the initial first shearing cycle, while values for K increase. Values for K are also higher for shorter chains, while n is lower. Gallegos *et al.* [185] show that for lamellar systems, there is an initial growth of viscosity, which is due to viscoelasticity, followed by a decrease in viscosity to a steady-state value. These results are explained by the partial alignment of the lamellar layers, and then finally, total alignment when an equilibrium viscosity is reached.

Clearly, it is important to take into account the shear history of a fluid when finding a viscosity *vs.* shear relationship, as well as making sure the structure has been allowed sufficient time under a given shear stress to reach its equilibrium structure. The most common protocol for analysing the rheology of a system involves making shear rate or shear stress ramps (as in flow curves). However, a

viscosity value taken from a flow curve is likely to be biased by previous shear rates applied in the ramp. One alternative way to study the rheology of the systems would be to perform measurements of steady state viscosities. However, for highly viscoelastic samples, the measurement of steady state values at low shear rates can be extremely time consuming and can be a challenge from an experimental point of view [200].

4.3.3.2 Measurements for AES Rheology for Lyotropic Liquid Crystals

Due to the fact that the rheological behaviour of these phases is expected to be dependant on the shear history, initial measurements are taken without pre-shear treatment, which is similar to the protocol taken by other researchers [184, 201]. Shearing is performed using an Anton Paar Physica MCR301 Rheometer, as was performed for the micellar solutions. Due to the higher viscosity of the lamellar and hexagonal phases, a cone and plate geometry was used (diameter of the upper plate 75mm, 1° angle, measuring gap 1 mm).

In order to investigate the time dependant behaviour of the solutions, constant shear rate experiments were performed. The calculated viscosity can then be plotted as a function of time. An illustration of the time dependant viscosity of a 63.1% AES solution, which is expected to be in the lamellar phase (based on POM imaging), is shown in Fig. 4.13. This run begins at a shear rate of $\dot{\gamma} = 0.001\text{s}^{-1}$, which is maintained for a 20 minute period. After this period the shear rate is increased to $\dot{\gamma} = 0.01\text{s}^{-1}$, and following further 20 minute equilibration periods to $\dot{\gamma} = 0.1\text{s}^{-1}$ and then $\dot{\gamma} = 1.00\text{s}^{-1}$. It is clear that it is the initial shearing run that has the most time dependant viscosity. This increasing viscosity in the initial shearing stage at low shear rate is expected to be due to the existence of a yield stress as a manifestation of viscoelasticity, and is observed by other researchers in similar systems [185]. For subsequent increases in the shear rate, the calculated viscosity decreases as a function of time, and it is expected that this is due to the phase becoming increasingly aligned due to the application of

shear. With increasing shear rate, shear alignment is induced more quickly. The alignment induced at higher shear rates has an effect on the viscosity when the sample is returned back down to reduced shear rates. Upon returning to the lower shear rate $\dot{\gamma} = 0.10\text{s}^{-1}$ from $\dot{\gamma} = 1.00\text{s}^{-1}$, the viscosity is approximately time independent and is lower in value. This indicates that full shear alignment of the lamellar phase has taken place.

When the initial shear rate chosen is larger, we can miss the behaviour that provides evidence for a yield stress. For example, the time dependant viscosity found from shearing a 70% AES solution, which is also expected to be lamellar, is shown in Fig. 4.14. The sample is initially sheared at $\dot{\gamma} = 0.10\text{s}^{-1}$, and while the sample takes a relatively long time to induce alignment, there is no increase in the viscosity as a function of time at any point. The shear rate is then increased to $\dot{\gamma} = 1.00\text{s}^{-1}$, and sheared until it reaches an approximately constant viscosity. The shear rate is increased again to $\dot{\gamma} = 5.00\text{s}^{-1}$. For each of these jumps to higher shear rates the equilibration time to reach a constant viscosity is relatively short compared to the initial run. Similar time dependant behaviour under steady shear is found for phases that exist in the hexagonal phase, an example of which is shown in Fig. 4.15.

Obviously the downside to studying the solutions using steady shear measurements is that it is very time consuming. Long periods of time are needed to find steady-state viscosities at low shear rates. Rheological behaviour can also be investigated by making steady-shear measurements and ramping the shear rate up and down, producing flow curves. Repeated cycles should highlight any thixotropic behaviours of the fluid, in particular the behaviour that is as a result of shear alignment of the crystal phases. If alignment was induced as a result of the initial up-curve run (due to long shearing time and high shear rates used), then any further up-down cycles should produce the same calculated viscosities as the induced alignment is maintained. The effect of this on a 34.6% AES concentration sample which, based on the POM images, is expected to be in the hexagonal phase, is
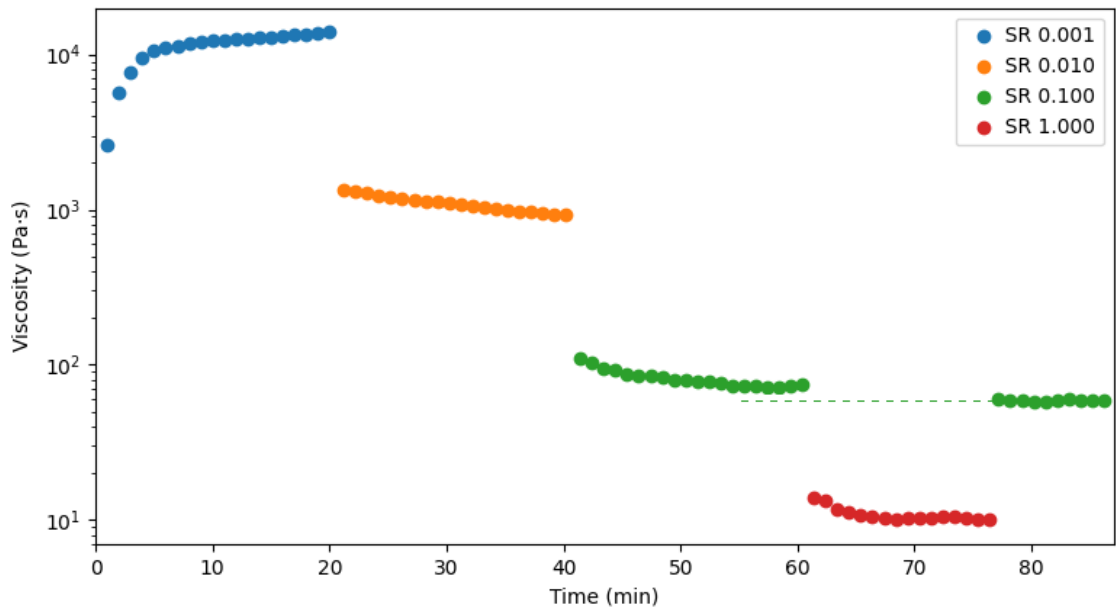
Figure 4.13: Steady state shear measurements of 63.1% AES solution. Shearing begins at a shear rate of $0.001s^{-1}$, and is gradually increased at 20 minute intervals to $\dot{\gamma} = 0.01s^{-1}$, $\dot{\gamma} = 0.1s^{-1}$ and $\dot{\gamma} = 1s^{-1}$, before being returned to $\dot{\gamma} = 0.1s^{-1}$. Each data point corresponds to a measurement made over a period of 60s.
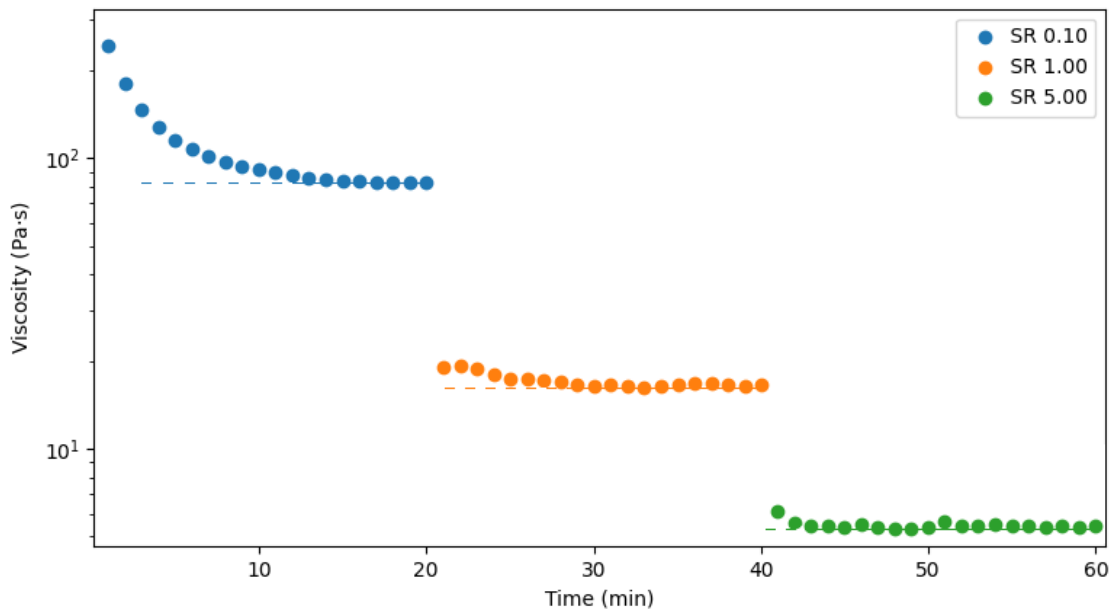
Figure 4.14: Steady state shear measurements of 70.0% AES solution. Shearing begins at a shear rate of $\dot{\gamma} = 0.1s^{-1}$, and is increased at 20 minute intervals to $\dot{\gamma} = 1.00s^{-1}$ and $\dot{\gamma} = 5.00s^{-1}$. Each data point corresponds to a measurement made over a period of 60s.
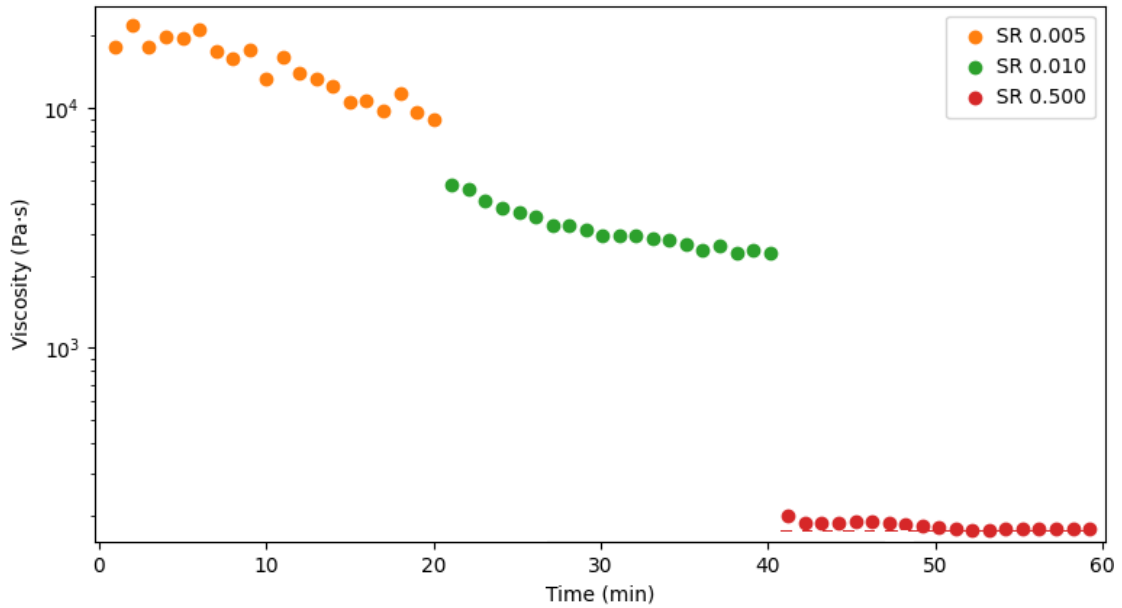
Figure 4.15: Steady state shear measurements of 41.3% AES solution. Shearing begins at a shear rate of $\dot{\gamma} = 0.05\text{s}^{-1}$, and is increased at 20 minute intervals to $\dot{\gamma} = 0.01\text{s}^{-1}$ and $\dot{\gamma} = 0.50\text{s}^{-1}$. Each data point corresponds to a measurement made over a period of 60s.

shown in Fig. 4.16. It is clear from Fig. 4.16 that the results from the initial up run are vastly different from subsequent shear cycles. The initial ramp up of the shear rate from $\dot{\gamma} = 0.001\text{s}^{-1}$ to $\dot{\gamma} = 1\text{s}^{-1}$ induces alignment in the liquid crystal that is maintained when the sample is returned to lower shear rates. As we have chosen to perform our DPD simulations using liquid crystal phases that are aligned in the shear direction, the rheological behaviour found in these is most likely to be comparable to results produced once shear alignment has been induced, rather than the initial up-curves, in which there is not yet full alignment.

Viscosity *vs.* shear rate flow curves are obtained from measurements on a variety of concentrations in the range 20-70%. Based on the POM images, this range is expected to cover the hexagonal and lamellar mesophases. The viscosity *vs.* shear rate curves for a selection of concentrations is shown in Fig. 4.17. The curves shown are those that are obtained following previous up-down ramp cycles. Consecutive up-down cycles are performed until approximately consistent flow curves are achieved. The 28.0, 34.6 and 41.3% concentrations are thought to correspond to hexagonal phases, while concentrations 63.1 and 70.0% are lamellar.
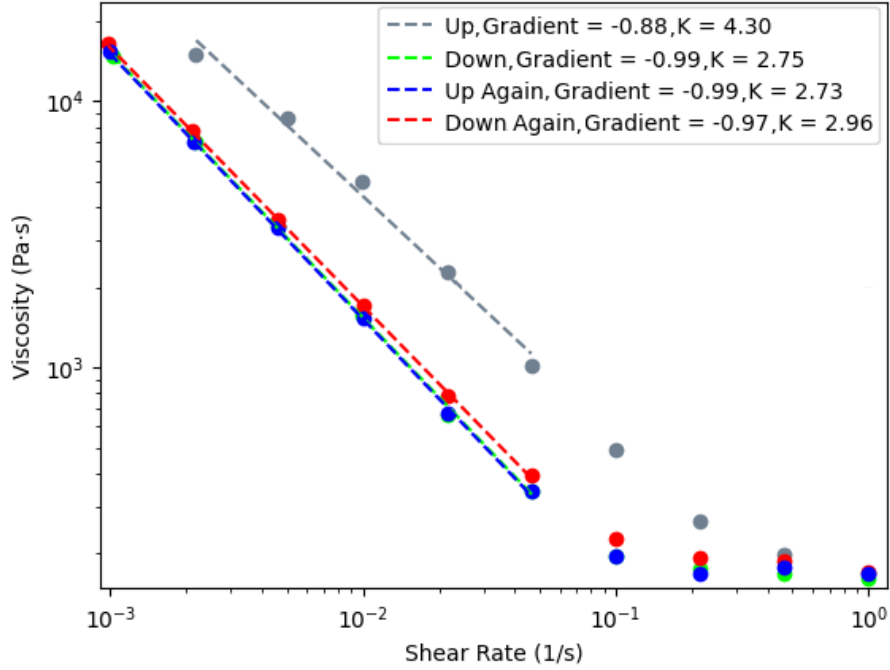
Figure 4.16: Steady-shear measurements of a 34.6% AES concentration sample. Each data point is measured at a constant shear rate, for a duration of 60s. Measurements are started at a shear rate of $\dot{\gamma} = 0.001\text{s}^{-1}$ and gradually increased to a maximum of $\dot{\gamma} = 1\text{s}^{-1}$ (grey). They are then ramped back down (green), followed by another cycle of increase (blue) and decreasing (red) shear rates. Linear fits are obtained using Eq. 4.10. The gradient provides the value of $(n-1)$.

At no concentration trialled in the shear rate range used do we observe a plateau to zero-shear viscosity. It is of note that two of the larger hexagonal phases plateau at high shear rates within this range, while the lamellar cases continue to decrease at high $\dot{\gamma}$. It is likely that the lamellar phase would also plateau at shear rates $10\text{s}^{-1} < \dot{\gamma}$, as has been observed in other lamellar systems [196]. The viscosity *vs.* shear behaviour is consistent with that found by other authors of other lamellar and hexagonal systems [175, 184, 185, 188]. The behaviour of the 28.0% concentration is somewhere in between the behaviour of the other samples, with the change in gradient at higher shear rates indicating a potential plateau at shear rates higher than those trialled.

In the shear rate range where the relationship of η *vs.* $\dot{\gamma}$ can be fit by a power law relationship given by Eq. 4.10, values for K and $(n-1)$ can be obtained. Table 4.2 shows the fits obtained for a variety of concentrations. The results obtained for a 58.6% sample are also included, which is not plotted in Fig. 4.17. The
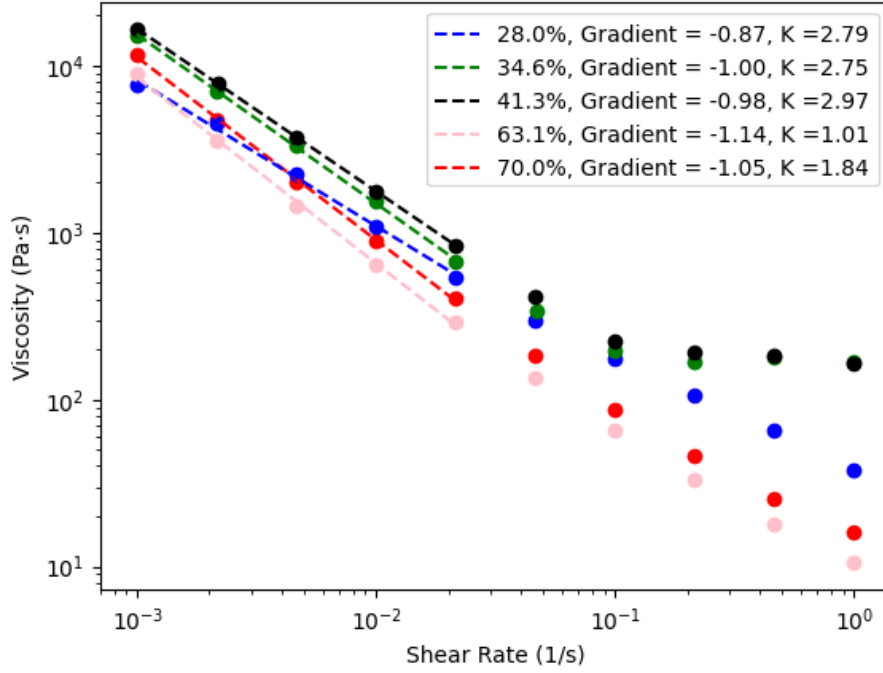
Figure 4.17: Steady-shear measurements of samples with AES concentrations 28.0, 34.6, 41.3, 63.1 and 70.0%. Fits shown are performed in the approximately linear region that can be fitted using Eq. 4.10. The gradient provides a value for $(n-1)$ in Eq. 4.10. Based on POM imaging, the solutions were assigned to the hexagonal (28.0%, 34.6%, 41.3%) and lamellar (63.1%, 70.0%) phases.

value of $(n-1)$ is indicative of how the sample responds to the application of shear. The gradient $(n-1)$ of these two phases are found to be largely similar, while the decreased viscosity of the fluid in transition from hexagonal to lamellar is highlighted by the change in the value of K. The relative consistency of the flow index n with varying concentration has been observed in similar systems [188], even when the value of K changes considerably. For other liquid crystal systems, the value of $(n-1)$ can vary considerably, depending on the surfactant, although usually takes a value in the range $-1.3 < (n-1) < -0.4$ [175, 184, 185, 188, 196], which is consistent with what is found for AES systems.

The 58.6% concentration is indicated by POM measurements to be on the edge of the hexagonal region, where interpreting the textures can become more difficult. This sample is incredibly viscous, and therefore it becomes very difficult to measure the rheology, particularly at lower shear rates. The measurements obtained for this sample are shown in Fig. 4.18, but are not particularly reliable, due to the large fluctuations in the values obtained for the viscosity. While the other samples are

Concentration (%)	$(n-1)$	K
28.0	-0.87	2.79
34.6	-1.00	2.75
41.3	-0.98	2.97
58.6	-0.38	5.29
63.1	-1.14	1.01
70.0	-1.05	1.84

Table 4.2: Values obtained by applying power law given in Eq. 4.10 to viscosity *vs.* shear rate curves for different concentrations of AES (wt. %) in solution. Fits are performed to curves that are obtained from approximately aligned lyotropic crystal phases. For concentration 58.6%, the data is fitted in the shear rate range $\dot{\gamma} = 0.02 - 0.05 \text{s}^{-1}$. All other concentrations are fitted in the range $\dot{\gamma} = 0.001 - 0.05 \text{s}^{-1}$.

able to be fit as a power-law fluid using Eq. 4.10, in the approximate shear rate range of $\dot{\gamma} = 0.001 \text{s}^{-1}$ to $\dot{\gamma} = 0.05 \text{s}^{-1}$, the 58.6% solution can only be measured consistently at shear rates above $\dot{\gamma} \approx 0.02 \text{s}^{-1}$. At lower shear rates the solution is expected to be above viscosity values that are out of range of the rheometer. As there is the possibility that this viscosity is being measured in a range where the viscosity has plateaued (or is plateauing), the values obtained for n and K may not be comparable with other values obtained from other concentrations (explaining why the values for 58.6% in Table 4.2 are very different to the values for other concentrations). However, due to the fact that upon transition to a lamellar phase we would expect a noticeable drop in the viscosity, the large magnitude of the viscosity indicates that at this concentration the phase transition has not taken place, and at 58.6% we still have a hexagonal phase.

The differing behaviour of the 28% concentration when compared with the other two higher hexagonal concentrations, could be a reflection of the fact that the sample is on the boundary between the micellar and hexagonal phases. It is possible that this sample is undergoing a shear induced phase change, or is a mixture of a micellar/hexagonal phase. POM imaging at this concentration indicates the existence of the hexagonal phase, and the relatively high viscosity of the solution at this concentration when compared with the viscosities of micellar solutions helps confirm this. However, qualitatively it can be observed from handling of the solution, that it possesses a relatively low viscosity when compared with the other
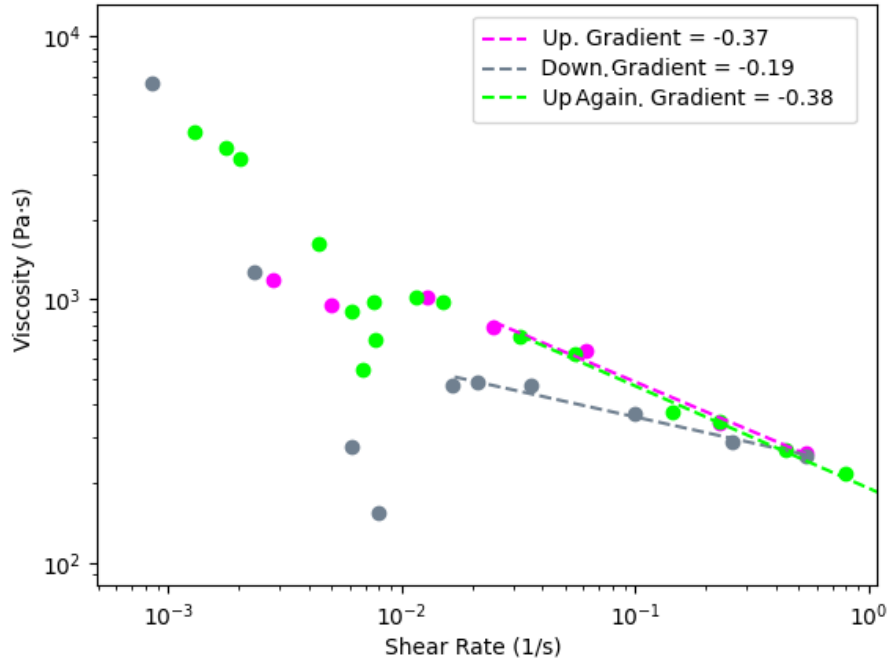
Figure 4.18: Steady-shear measurements of samples with AES concentration 58.6%. Fits shown are performed in the approximately linear region, fitted using Eq. 4.10. The gradient provides a value for $(n-1)$ in Eq. 4.10. Based on POM imaging, this solution belongs to the hexagonal phase, but is practically difficult to measure due to its high viscosity.

hexagonal phase solutions. This is partially indicated in Fig. 4.17 by its smaller viscosity at $\dot{\gamma} = 0.001\text{s}^{-1}$, and its shallower gradient in the line of best fit, which when extrapolated to lower shear rates highlights its increasingly low viscosity at small shear rates. It could be that the hexagonal phase at this concentration is unstable and poorly formed, with increasing stability and structure under the influence of shear. It is worth considering the point made in Section 4.2.2, that to some degree some shear has to be applied to the sample, in order to produce the POM images. This will be discussed in greater detail in Chapter 7, when the solution at this concentration can be analysed in greater detail, with the aid of simulation results.

4.4 Summary

The aim of this chapter was to investigate the phases formed by AES/water solutions at room temperature, as well as establish the rheological behaviour of the

different phases. POM imaging finds evidence of micellar, hexagonal, and lamellar phases. The phase boundary between the micellar and hexagonal phase exists somewhere between 20.1 and 28.0%, while the hexagonal/lamellar boundary is between 58.6 and 59.9%, based on this imaging. The boundary between the micellar and hexagonal phase is confirmed by the difference in the rheology of the solution at 20.1% and 28.0%, as the solution displays a transition from Newtonian with low viscosity, to shear-thinning with higher viscosity. The transition to a lamellar phase is also confirmed by a drop in the magnitude of the viscosity from the hexagonal phase.

In general, the solutions appear to have an increase in viscosity with composition, within their respective phases. Analysis of the samples on the edge of the hexagonal phase are the most difficult. In particular the 58.6% sample becomes difficult to measure, because of its high viscosity, whilst the 28.0% sample displays slightly different shear thinning behaviour compared to samples from the middle of the hexagonal region. The high viscosity of the 58.6% sample can cause problems from a manufacturing point of view. Commercial products often contain surfactants in a micellar concentration range. The high viscosity at intermediate concentrations between the lamellar paste and the micellar concentrations, means the mixing and dissolution process required to create these products is more challenging.

The following chapter will study the effect the phase change has on the shape of the molecules in the solution, using Raman spectroscopy. This will also aid in confirming the phase boundaries, as established in this chapter.

Chapter 5

Changes in Molecular Shape

The effect of varying the concentration of AES molecules in solution is discussed in Chapter 4. The influence the concentration has on the phase structure is discussed, and estimates for the location of the phase boundaries is obtained through a combination of POM imaging, and rheological measurements. The process of a phase change is likely to have an influence on the shape of the individual molecules. This is one of the aspects that will be analysed in DPD simulations. Therefore, this chapter will look at experimentally obtaining information about the shape molecules take, depending on the phase of the solution, in order for a comparison.

Two of the most common methods to assess conformational changes experimentally are infrared (IR) spectroscopy and Raman spectroscopy. The technique of Raman spectroscopy is used in this work for analysing AES systems under equilibrium conditions. Raman spectroscopy is selected as it displays advantages over IR for systems containing water molecules, which will be discussed further later in this chapter.

This chapter will begin with how the conformational changes of the molecules will be characterised throughout this chapter, using the definition of *trans* and *gauche* conformations of the molecule. Following this, the experimental technique of Raman spectroscopy is described, how its application to AES systems can aid in understanding these conformational changes, and discussing the limitations of what can be gained by experimental methods.

5.1 Conformational Changes

The surfactant molecules can undergo conformational changes due to phase and concentration changes of the solution. This is because the shape of the molecule in solution is influenced by the other molecules around it. Conformational changes refer to different ways of bending/twisting the same molecule, without breaking bonds. It is expected that structured phases will lead to less twisted or 'curved' molecules in solution. The surfactant AES molecules are primarily made up of long hydrocarbon chains, and so this is a natural starting place for analysis of the Raman spectrum. Analysis in computation requires the calculation of the dihedral angles.

Consider a chain of carbon-carbon single bonds labelled $..., i-1, i, i+1, ...$ The rotational angle of bond i is defined as the angle between two planes. The first plane is defined by bonds $i-1$ and i, and the second plane by bonds i and $i+1$. The angle between these planes illustrated in Figure 5.1 [9]. If we define that bond i is described by vector $\mathbf{u}_i$, for a series of three consecutive bonds, this can be calculated mathematically as

$$\cos\theta = \frac{(\mathbf{u}_1 \times \mathbf{u}_2) \cdot (\mathbf{u}_2 \times \mathbf{u}_3)}{|\mathbf{u}_1 \times \mathbf{u}_2| \, |\mathbf{u}_2 \times \mathbf{u}_3|} \tag{5.1}$$

$$\sin\theta = \frac{\mathbf{u}_2 \cdot ((\mathbf{u}_1 \times \mathbf{u}_2) \times (\mathbf{u}_2 \times \mathbf{u}_3))}{|\mathbf{u}_2| \, |\mathbf{u}_1 \times \mathbf{u}_2| \, |\mathbf{u}_2 \times \mathbf{u}_3|}. \tag{5.2}$$

Special cases of this angle θ include: $\theta = 180°$, $\theta = +60°$ and $\theta = -60°$ which are the *trans*, *gauche*$^+$ and *gauche*$^-$ conformations. Figure 5.2 illustrates the difference between a *trans* and *gauche* state.
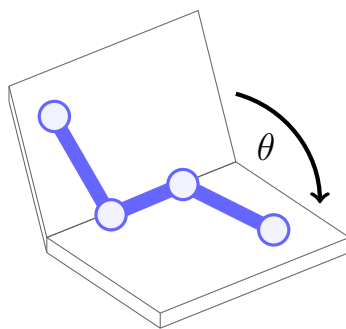
Figure 5.1: Illustration of the meaning of angle θ in Eqs. 5.1 and 5.2 [8].
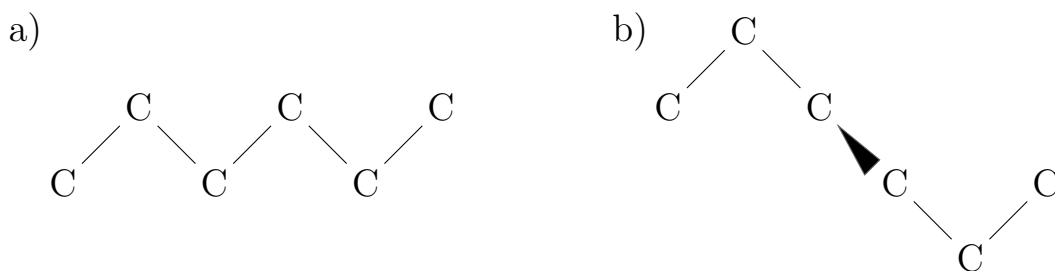
Figure 5.2: Illustration of the (a) *trans* state, and (b) the introduction of a *gauche* dihedral angle. The thicker bond symbol represents a bond pointed out of the paper towards the reader. Illustration adapted from Sperling (2015) [9].

5.2 Raman Spectroscopy

5.2.1 Overview

This section will discuss the background of Raman Spectroscopy, and its application to mesophase forming systems such as AES solutions. Raman scattering occurs when light interacts with molecular vibrations, and while most of our analysis will be on liquid systems, this technique can also be used to study gas and solid phases.

5.2.1.1 Principles of the Method

There are three different types of spectroscopy, including: absorption spectroscopy, in which a substance absorbs some electromagnetic radiation (*e.g.* IR and NMR); emission spectroscopy, in which a substance emits rather than absorbs (*e.g.* luminescence); and scatter spectroscopy, in which we measure the amount of light that a substance scatters at different wavelengths. Raman spectroscopy is a form

of scatter spectroscopy.

Most of the time when a photon interacts with a material and is scattered, it does so elastically (the energy of the photons remains the same before and after scattering). This is called Rayleigh scattering. However, a small percentage of time the incident photons interact in a way that leads to energy being lost or gained by the scattered photons; meaning that the scattered photons also have a different frequency to the incident photons. Raman scattering can be classified into two types depending on if the energy is lost or gained: Stokes Raman scattering and anti-Stokes Raman scattering. In Stokes Raman scattering, an electron is excited from the ground level and falls to a higher vibrational level than its initial level. Therefore, Stokes scattered light has less energy than the incident light. In anti-Stokes scattering, an electron is excited and then falls to a lower level than its initial level. This means there is an energy transfer to the scattered photon, so the scattered light has more energy than the incident light. The value of the change in energy depends on the frequency of vibration of the molecule. If it is high frequency the energy change is significant. If it is low frequency the energy change is small. Rayleigh scattering, Stokes and anti-Stokes scatter is illustrated in Fig. 5.3.

In order to analyse the results from these experiments, the intensity of this scattered light *vs.* frequency shift is plotted for the sample. The Rayleigh scattered light is removed using a filter. Using this spectrum, different frequencies correspond to the energy levels of different functional group vibrations. Therefore the location of the peaks in the spectrum at different frequency values, helps us work out which functional groups are present in the solution. The value of the intensity is largely proportional to the number of those vibrational groups in the solution. Therefore a change in the abundance of a given vibrational mode in a solution is reflected in the change in intensity.

We will now briefly discuss why Raman spectroscopy is the more ideal choice for our system, as opposed to the equally common spectral method of IR. Ra-
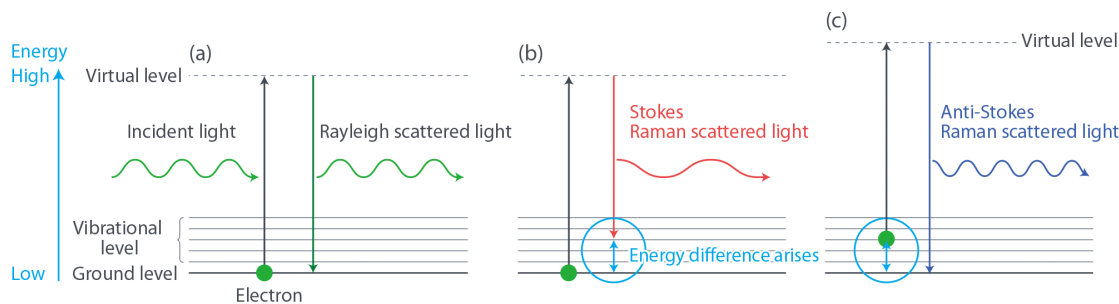
Figure 5.3: An illustration of the Rayleigh scattering, Stokes and anti-Stokes scattering processes [10].

man spectroscopy depends on a change in polarisability of a molecule, whereas IR spectroscopy depends on a change in the dipole moment. The magnitude of the scattered Raman intensity for a given bond correlates with polarisability of the molecule. Vibrations that involve polar bonds (*e.g.* C-O , N-O , O-H) are relatively weak Raman scatterers, while neutral bonds (*e.g.* C-C , C-H , C=C) have large changes in polarisability during a vibration, and therefore are strong scatterers. This makes Raman spectroscopy ideal for studying surfactant molecules in solution. In contrast, in IR spectroscopy, the dipole moment is not similarly affected such that while vibrations involving neutral bonds are strong Raman scatterers, they are weak in IR. It is usually the case that bonds that have large Raman intensities often have weak IR intensities, and vice versa. IR interacts very strongly with water molecules, with these vibrational modes being so large that they usually obscure other vibrational modes in the sample. This means that IR is unsuited for studying AES solutions, due to its weak scattering of C-H bonds and strong scattering of O-H bonds, which would dominate the spectra.

5.2.1.2 Analysing the Spectra

As already mentioned, the Raman shift in the spectra is different for different vibrational modes in the sample. These different vibrations can be caused by different bonds and different kinds of vibrations for each of those bonds. For example, CH_2 components in the hydrocarbon chain can produce multiple peaks in the spectra, for different kinds of vibrations. These include stretching, bending
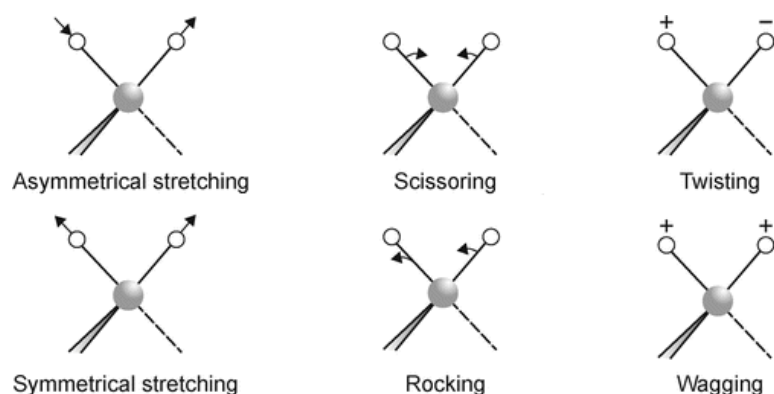
Figure 5.4: Illustration of the different kinds of vibrations for CH_2 that show up in Raman Spectra. Figure taken from Zaharescu and Mocioiu [11].

(or scissoring), twisting, rocking, and wagging, amongst others. An illustration of the different movements involved for CH_2 is shown in Fig. 5.4, and the frequency peaks corresponding to each of these modes will manifest at different locations.

Vibrations manifest as curves with the shape of a Gaussian or Lorentzian. Theoretically, the concentration of a vibrational mode is represented by the area of the curve, rather than the absolute peak height, due to interactions that can lead to broadening. While it would be best to analyse these bands by considering their integrated area, authors will very often consider peak heights (from either curve fits or simply the raw data), because of complications in resolving overlapping curves [203], even in recent research [204]. Also generally, it is most common to calculate the ratio of two of the peaks within the spectra, to monitor changes. This is because the absolute intensity of the spectra can vary between measurements, whereas the internal ratio between two peaks should not change. However, while there is usefulness in the ratios for characterising the environmental state of a system, this ratio can not necessarily be considered a quantitative measure of lateral order [205] unless we can be certain of the origin of the peaks involved.

5.2.1.3 Conformational Changes

As previously mentioned, Raman spectroscopy can be used to analyse any conformational changes that may occur in the molecules in solution. The Raman technique is particularly suited to studying the conformation of the hydrocarbon chain

portion of the surfactants and has been used extensively by researchers [206–209]. In n-alkanes with up to around 18 carbon atoms, the all-trans configuration is the most stable [210] (meaning that the hydrocarbon chain is made up of entirely *trans* dihedral angles). With increasing numbers of gauche dihedral angles in the hydrocarbon chain, the potential energy increases. While the *gauche* conformation in a hydrocarbon chain is less energetically favoured than the *trans* conformation [9], they are present in solution because small amounts of energy are sufficient to overcome the energy barrier between a *trans* and *gauche* conformation. It has been shown using Raman spectroscopy, that the ratio between *gauche* and *trans* segments can show an abrupt change under a phase change [211], as the *trans* conformation becomes more energetically favourable at higher concentrations, as the energy barriers become harder to overcome.

For AES molecules, the bands that appear in Raman spectra with the largest intensity are from the O-H bonds of water at 3000–3800cm^{-1}, and from C-H stretching modes between 2800–3000cm^{-1}. There are also a number of medium-size peaks of interest in the region from 900–1800cm^{-1}. There are other peaks of smaller magnitude in other regions, but these are subject to larger amounts of noise and become more difficult to analyse. An illustration of the raw intensity data produced during a Raman spectroscopy reading, without background removal, is shown in Fig. 5.5. It is hoped that by comparing the ratios of peak intensities, in-particular *trans* to *gauche* ratios, this can aid in identifying conformational changes in the different mesophases. In turn, this should also aid in identifying the locations of the phase boundaries.

5.2.2 Curve Fitting and Peak Locations

Along with peak height ratios to categorise phase change, discontinuities can also be observed in the location of peak frequency and full width half maxima (FWHM) of curves [212]. Obviously, this relates back to our discussion about using the peak area rather than the absolute intensity for analysis, as the FWHM and peak height
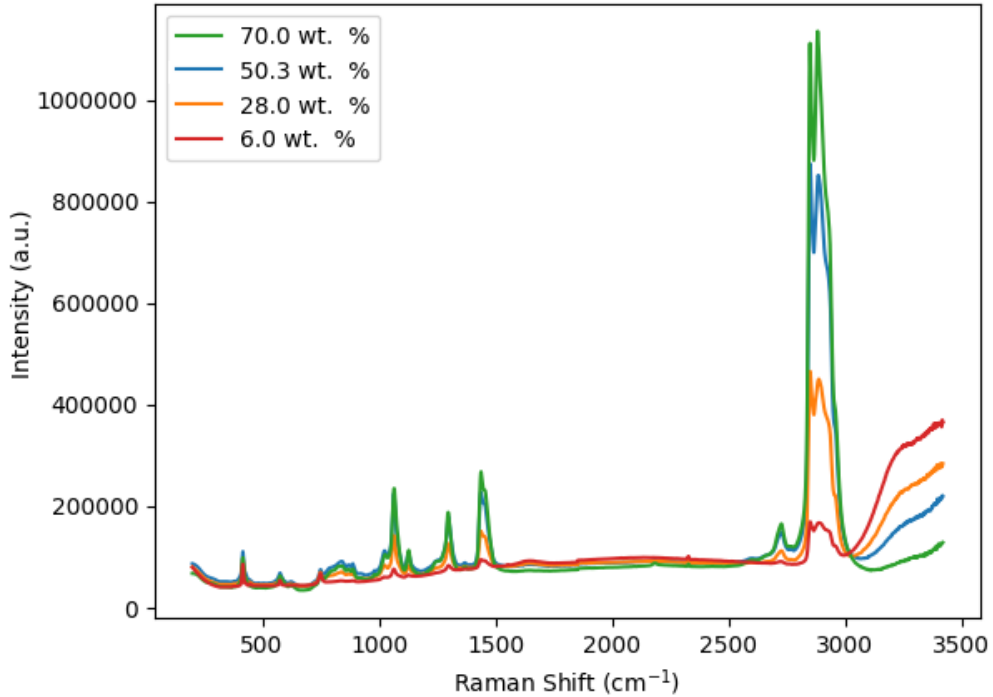
Figure 5.5: Examples of raw data taken by Raman spectroscopy for a variety of concentrations. Background removal has not been applied.

are related to the area of a sub-band.

When bands are resolved into their individual sub-bands by curve fitting techniques, they are normally fit to either Gaussian [213] or Lorentzian [203, 211, 214] distributions. Raman spectroscopy is based on exciting molecules from a ground state to a first excited state from the absorption of energy from a laser. The excited molecules rapidly return to the ground state after a few picoseconds, and this relaxation is called the lifetime τ_a. The shape of the curve of the vibration is related to this lifetime τ_a. At first, all of the excited molecules vibrate coherently together, but after some time, motion and slight differences in vibrational frequencies randomise this over time. The time over which the molecules vibrate coherently has lifetime τ_c. It is the relationship between this τ_a and τ_c that dictate what shape curve we end up with. In solids $\tau_c \gg \tau_a$, because the molecule's environment is not in motion *i.e.* the excited molecule relaxes before incoherence becomes a factor. This results in a Gaussian profile for the vibration. However, in a gas $\tau_c \ll \tau_a$, and the resulting line shape is Lorentzian. Liquids sit somewhere between these two extremes, so the profiles can have features of both Gaussian

135

and Lorentzian curve shape. We will therefore use the most simple curve fitting procedure that combines both the Lorentzian and Gaussian shapes. The Gaussian-Lorentzian (G-L) profile can be represented as $f(x) = AG + (1 - A)L$, where G and L are Gaussian and Lorentzian profiles respectively, and A is the fraction of Gaussian curve ($0 \leqslant A \leqslant 1$) [215].

Difficulties arrive with curve fitting when there are many overlapping modes in the same region and at this point fitting curves becomes tricky or impossible. The difficulty in fitting increases as the number of modes in the fit increases, and there can be less confidence in the reproducibility of the fits. For this reason, researchers will often choose to still compare peak intensities instead of doing curve decomposition.

While peak positions could be obtained simply as the location (cm^{-1}) of the maximum intensity, the shift values as obtained from experiment are discretised to the nearest integer. As the shift in the peaks is relatively small, this often provides little information about the movements of the peak due to concentration changes. Therefore, more precise values for the peak location are obtained by fitting a Gaussian to the top portion of the peak (usually $\approx 90\%$ of the maximum intensity) and taking the location from this fitted curve.

5.2.3   Background Removal and Peak Scaling

The largest source of uncertainty in our results for the peak frequency positions and height ratios is likely to be due to variability in the spectral background, and difficulty in removing the background. There is no standardised method for background removal, posing challenges in making comparisons with the results of other researchers. Kint *et al.* [216] make the same observation, and choose the method of defining linear baselines between certain ranges. For example, a linear baseline is defined within the regions from: 3200 to 2500 for C-H stretching bands; and $3850cm^{-1}$ to $3100cm^{-1}$ for OH stretching bands. Others use different methods, *e.g.* Vogel [211] choose to use a Lorentzian profile to fit the background. As there

is, in general, a lack of consensus among researchers on the best baseline removal method, we compare different baseline removal methods for different regions of the spectrum. For the modes producing larger peak intensities, the exact choice of baseline is less relevant, becoming more relevant when the peak is smaller.

Another issue is that of peak height scaling. Even with a suitable background removal method, the absolute height of the peaks is subject to change between measurements, while the absolute ratios between the peaks should not change. It is also common by other researchers to use an additive to the solution in order to scale the intensities, or to find another peak within the spectrum that is assumed not to change. Both of these methods have their flaws, and therefore it is usually safer to compare peak ratios within the spectra, rather than attempting to scale all peak heights to one reference peak.

5.2.4 Results and Analysis

5.2.4.1 Baseline Removal in Region 900–1800cm^{-1}

There are a number of vibrational modes from different bonds within this region, some of which overlap. The peaks produced by an AES solution is shown in Fig. 5.6. These can broadly be separated into four distinct regions: 1000–1200 (dominated by C-C stretching), 1200–1400 (dominated by CH_2 twisting), 1400–1520 (dominated by CH_2 scissoring), and 1520–1800 (O-H bending). Each of these regions are potentially overlapping, making a baseline fit difficult. One approach would be to choose to treat the entire range as overlapping peaks and fit a curved or linear baseline to the whole region. This is what is defined as 'Baseline 1' in Fig. 5.6. Alternatively one could choose to fit a baseline to each sub-region individually, using the edges of each region. This is what is illustrated by 'Baseline 2' in Fig. 5.6. We will analyse our results using both baseline choices, in order to verify that the choice of baseline fitting does not impact the results of the analysis of the intensity changes. In the following sections, we will analyse each of these distinct regions individually.
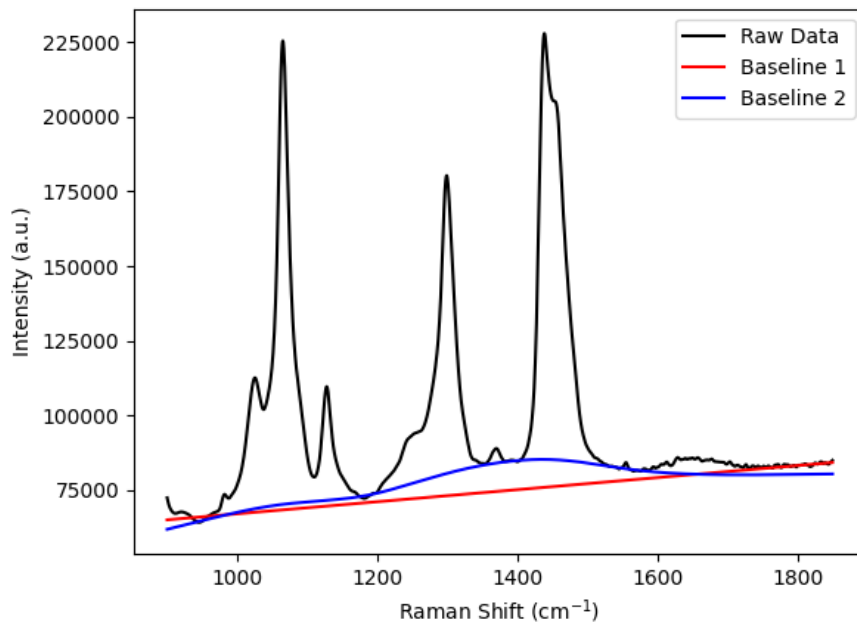
(a) Raw data fitted with different baselines.
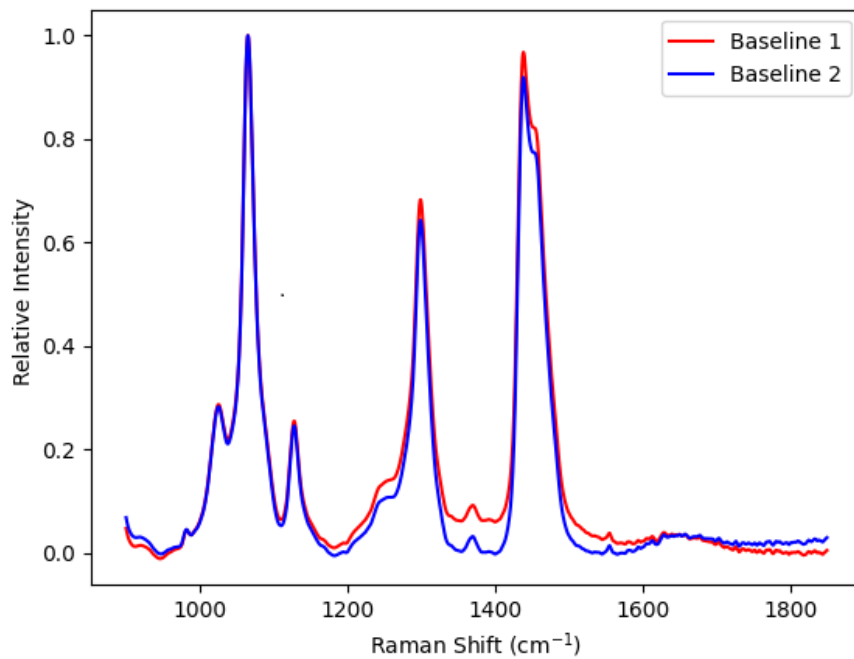
(b) Raw data minus baselines. Plot scaled to the largest peak.

Figure 5.6: Baseline fitting in the region 900–1800cm^{-1}. Example shown for solution with concentration $c = 67$ wt.% AES.
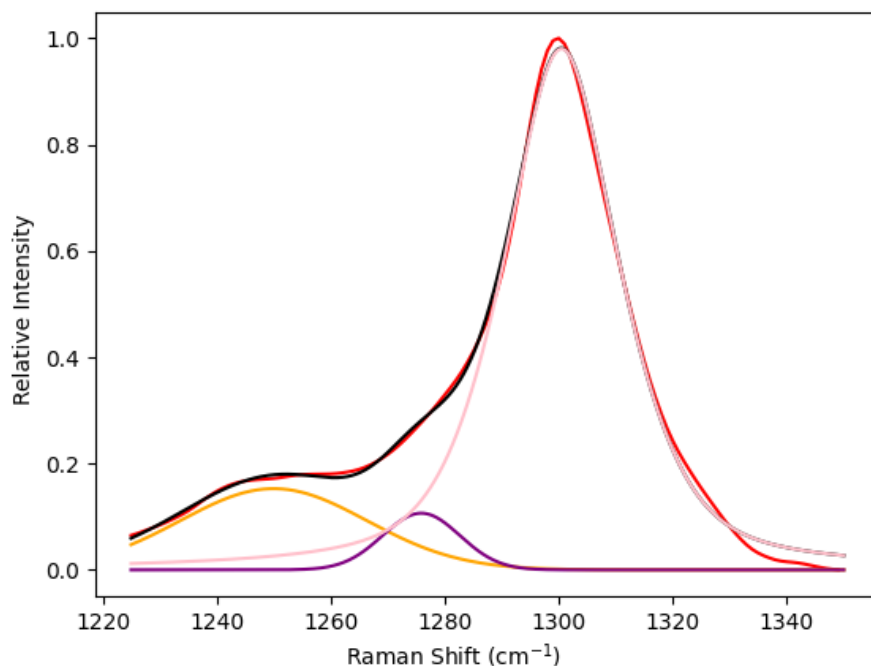
Figure 5.7: Three modal curve decomposition (illustrated by the black curve) in the region 1220–1350cm^{-1} (raw data shown in red). Example is given to intensity data using the baseline removal method baseline 2, as illustrated in Fig. 5.6. Similar fits are obtained using the linear baseline fit (baseline 1). Concentration sample = 67%

5.2.4.2 Modes in Region 1200–1400cm^{-1}

An example of what is found for AES molecules in the region 1200–1400cm^{-1} is shown in Fig. 5.7, along with a three modal decomposition. At least three curves are required to provide a reasonable fit to the data, however, we will discuss how it is expected that there are more underlying modes in the spectra.

The region is dominated by a peak at 1295cm^{-1}, which is related to CH$_2$ twisting in the hydrocarbon chain [217–219]. Quantum mechanical simulations by Tarazona *et al.* [220] on *n*-alkanes reveal that C-C stretching of primarily *trans* conformers produces peaks at around 1250cm^{-1}, while *gauche* conformers introduce peaks at higher frequencies at around 1260–1280cm^{-1}. Conversely, studies looking at molecules containing (OCH$_2$CH$_2$)$_n$ components report twisting CH$_2$ modes at around 1280cm^{-1} (*trans-trans-trans* and *trans-gauche-trans* conformations in the OCCO chain) and 1245cm^{-1} (*trans-gauche-trans* and *gauche-gauche-gauche*) conformations [221,222]. The number of overlapping peaks in this region makes curve

decomposition very difficult, with a greater number of modes than that shown in Fig. 5.7 usually producing inconsistent results.

Other peaks in this region may include a vibration at around 1300cm^{-1}, related to SO$_4$ stretch [218]. While this would be expected to overlap with the proposed CH$_2$ twisting peak, the SO$_4$ mode is expected to be weak in comparison, so that the CH$_2$ twisting mode dominates [223]. The CH$_2$ twisting mode at $\approx$ 1300cm^{-1} has been found to be moderately sensitive to chain conformation, with Kint *et al.* [216] finding band narrowing. These changes are suggested to indicate increased conformational order. This is supported by Tarazona *et al.* [220], whose quantum mechanical calculations show that consecutive *trans* bonds produces a narrow band in the CH$_2$ twisting peak, whereas conformations containing a mixture of *trans* and *gauche* produce broad spectral responses. However, the overall integrated intensity of the band is shown to be largely conformer independent, which confirms what is suggested from experimental results by Strobl and Hagedom [224], that the integration of the intensity of this band could be used as a reference for studying intensity changes in other parts of the spectrum. We will use this invariance to compare with other peak ratios in other regions in later sections. For our results for AES solutions, the width of the peak at 1300cm^{-1} is found to be largely concentration independent, and no band narrowing is found. Therefore we can approximately say that the maximum intensity of the peak at I(1300)$\propto$ area of the curve. Therefore, we will assume that the intensity is largely conformation independent, instead of needing to rely on an integration from curve decomposition.

5.2.4.3 Modes in Regions 3000–3425 cm^{-1}

It is also possible to analyse the changes in water molecules when surfactants are present [225, 226], as there is an O-H stretching band appearing at 3000–3800cm^{-1}. This band is inhomogeneously broad and is usually fitted as a number of overlapping component subbands related to different O-H vibrational modes.

For example, one possible fit places sub-bands at: 3041, 3232, 3430, 3557, and 3635cm^{-1} [227]. Due to limitations in our equipment, we only have access to measuring a proportion of this band, with equipment measuring up to 3425cm^{-1}. Without access to the full range of the band, resolving into sub-bands for analysis is difficult. Therefore we will not make use of this region for analysing the effect of varying concentration on the solutions. However, there is close proximity between the bands produced from CH_2 and CH_3 stretching in the 2800–3000cm^{-1} range and this water peak. There can be considerable overlap between these two regions, so we can't completely ignore the bands produced from the water molecules, particularly at low concentrations. Generally, however, we can approximate the fit of the water vibrations in this region using only a two-curve fit. There are other vibrational modes as a result of O-H bonds, for example, OH bending modes appearing at 1581 and 1641cm^{-1}, but these modes are very weak and only appear with very low intensity [228]. Therefore they are of limited use for our analysis due to the noise that they will contain.

5.2.4.4 Modes in Region 2800–3000cm^{-1}

While it was first the bands appearing from C-C stretching that were shown to be correlated with the *trans/gauche* ratios, it has also been shown that the C-H stretching vibrations can give some information on the order or disordered state of hydrocarbon chains [229]. Peak ratios in this region have been found to be sensitive to the physical state of a system, and thus can provide estimates on the degree of chain conformation.

In the 2800–3000cm^{-1} region, this broad band has historically been thought to be made up of four individual sub-band contributions, attributed to CH_3 and CH_2 symmetric and asymmetric stretching. Assignments of band peaks in similar molecules (sodium lauryl sulphate [230], sodium dodecyl sulphate [231, 232] and other hydrocarbon chains [233]) often place peaks at approximately: 2850cm^{-1} (CH_2 symmetric), 2880cm^{-1} (CH_2 asymmetric), 2873cm^{-1} (CH_3 symmetric) ,

2955cm^{-1} (CH_3 asymmetric) [232]. However, sometimes in other molecules, the peaks manifest in slightly different locations. For example, Kint *et al.* [216] investigate dimyristoylphosphatidylcholine (DMPC) using Raman at different temperatures and concentrations. DMPC undergoes a phase change from micelles, to a gel phase, to a lamellar phase, with increasing concentration. They find bands at 2853, 2883, 2935 and 2960cm^{-1}. The bands are shown to be sensitive to the alkyl chain order/disorder and show abrupt changes at lipid phase transitions.

However, generally, it has been difficult to exactly assign these peaks to their specific origins, and the assignments as discussed above have been challenged in more recent years. In particular, it has been difficult to experimentally attribute which parts are a result of *gauche* vibrations *vs.* those from *trans* vibrations. It would be useful to be able to effectively categorise the origin of these peaks, for a more quantitative assessment of the degree of change in the conformation of the molecules. Some researchers have started to suppose that this region can be decomposed into more than four modes. This has been assisted by developments in computational and theoretical research [234, 235]. For example in alkane chains, Shemouratov *et al.* [234] assign 2848 and 2881cm^{-1} to the symmetric and antisymmetric stretching vibrations of the CH_2 group in the *trans*-conformers. The *gauche*-conformers are assigned to frequencies at 2876 and 2925cm^{-1}. Peaks at 2938 and 2962cm^{-1} are assigned to the symmetric and antisymmetric vibrations of CH_3. There are also several overtone spectral features, with the most peaked at 2900 and 2940cm^{-1} and corresponding to the overtones of the deformation vibrations of the CH_2 groups.

For AES in this region, we find a large region of overlapping peaks corresponding to the CH_2 and CH_3 modes, as expected. However, since these overlap with the later O-H vibrations at higher wavelengths, this makes complex baseline removal difficult. Therefore in this region, we adopt the linear baseline technique similar to Kint *et al.* [216], in which we fit a straight line to the distribution in range $2200–2300 \text{cm}^{-1}$, as in this range there are not any expected or identified
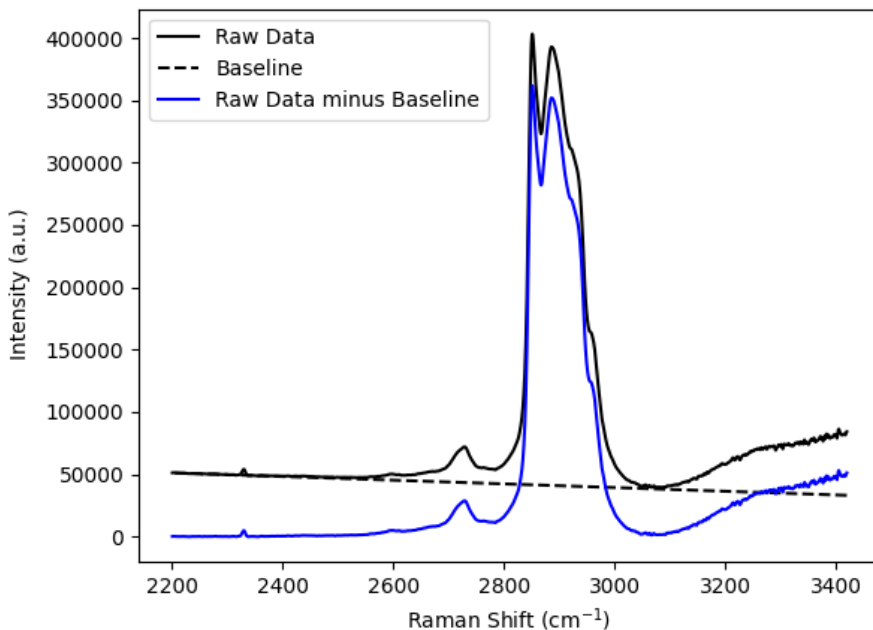
Figure 5.8: Linear baseline fitting for the overlapping CH modes in the region 2800–3000cm^{-1} and OH modes in the 3000–3400cm^{-1} region. Concentration $c = 67$wt.%.

peaks in the spectrum. This can then be extrapolated as the baseline fit over the 2300–3400cm^{-1} range. An illustration of the baseline removal in this region is shown in Fig. 5.8.

Intensity Ratios

The location of the peaks we find in this region are almost identical to that of Kint *et al.* [216]. These authors find that the ratio of their I(2883)/I(2935) increases with concentration, with different behaviour in different phase regions. The most drastic increase is seen in the micellar region, until the solution undergoes phase change and enters a gel phase, during which the gradient of the relationship between I(2883)/I(2935) and concentration greatly decreases. There is another abrupt jump upon phase transition from gel to lamellar. Based on the suggestion of the location of the underlying *gauche* and *trans* peaks by Shemouratov *et al.* [234], this behaviour would be expected for an increase in *trans* conformations with increasing concentration. This is because the I(2935) peak would be mainly expected to be dominated by the antisymmetric CH$_2$ *gauche* vibrations, and I(2883) mainly from antisymmetric CH$_2$ *trans* vibrations. While

143

Kint *et al.* [216] do not also report the ratio of I(2850)/I(2935), similar behaviour should be expected for this ratio based on similar reasoning. The results obtained for AES solutions for these ratios is shown in Fig. 5.9. Also plotted is the ratio I(2850)/I(2883), which remains approximately constant, as expected as these two peaks in the spectra are dominated by *trans* vibrational modes. Note that in all plots the error bars are calculated as the standard error $\sigma_x = \sigma/\sqrt{S}$ where σ is the standard deviation of multiple readings S. The changes in the ratios I(2883)/I(2935) and I(2850)/I(2935) are consistent with an increase in *trans* modes with concentration, as well as being consistent with what is found by Kint *et al.* [216]. The jump in the value of the ratio between phases is less pronounced than that found by Kint *et al.* [216], but the behaviour within each phase region is broadly the same. The *trans/gauche* ratio that these intensity ratios are presumed to represent, show the greatest change within the micellar and lamellar mesophases, while only there is only a moderate effect of increasing concentration within the hexagonal range. There is no identifiable change in the intensity ratios that could indicate an additional, unique phase in between the hexagonal and lamellar phases (*e.g.* a cubic phase). Rather the ratios would indicate a simple transition from hexagonal to lamellar phase.

Based on the suggested positions of the *gauche* and *trans* component modes, there are a variety of other changes in the peaks that would be seen if there were an increase in *trans* conformations. The peak at 2960cm^{-1} is assigned to CH$_3$ modes, which are expected to be less sensitive to chain conformation than CH$_2$ modes in the middle of the chain. Therefore the peak at 2960cm^{-1} could be considered approximately invariant relative to the CH$_2$ modes. This means that the height of the peaks at 2850cm^{-1} and 2880cm^{-1} would be expected to grow in relation to this shoulder peak at 2960cm^{-1}. This has been found by other researchers. For example Hadri *et al.* [236], who plot the ratios I(2883)/I(2940) and I(2883)/I(2962) for a nonionic surfactant, finding this to be the case. A plot of the ratio I(2850)/I(2960) is shown in Fig. 5.10, as well as a comparison with the ratio I(2850)/I(2930). It
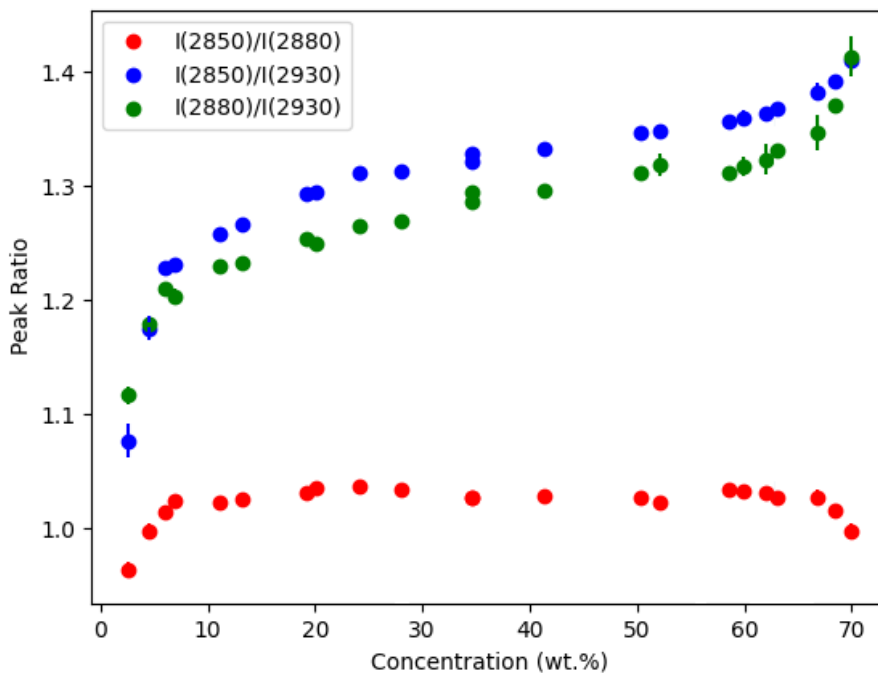
Figure 5.9: Ratio of intensities in the region 2800–3000cm^{-1} with increasing concentration. The error bars are calculated as the standard error $\sigma_x = \sigma/\sqrt{S}$ where σ is the standard deviation of multiple readings S.

can be seen that I(2850)/I(2960) increases with similar behaviour as compared to I(2850)/I(2880) and I(2850)/I(2930), however, the magnitude of the ratio changes much more greatly. This may be due to a lack of obscuring from *gauche* mode peaks in intensity at I(2960), thus enabling I(2850)/I(2960) to better capture the increase in the I(2850) mode. However, we still reach a similar conclusion, that there is little change in the number of *trans* modes in the hexagonal region, when compared with the lamellar and micellar cases. Once again, there is no suggestion of an additional region in between the hexagonal and lamellar phases.

A comparison can be made with the peak located at 1300cm^{-1}, which is assumed to be approximately conformation invariant. Plots of I(2850)/I(1300) and I(2930)/I(1300) are shown in Fig. 5.11. Recall that the peak at I(2850) is expected to be almost entirely dominated by *trans* and that I(2930) is made up of *trans* and *gauche* modes. While it may seem counter-intuitive that the ratios of both of these peaks are increasing, this can be explained by the fact that the trans peak has a larger proportionality constant than that of the gauche peak. To explain this, consider that the peak at 2850cm^{-1} can be represented by I(2850)= AcN_T,
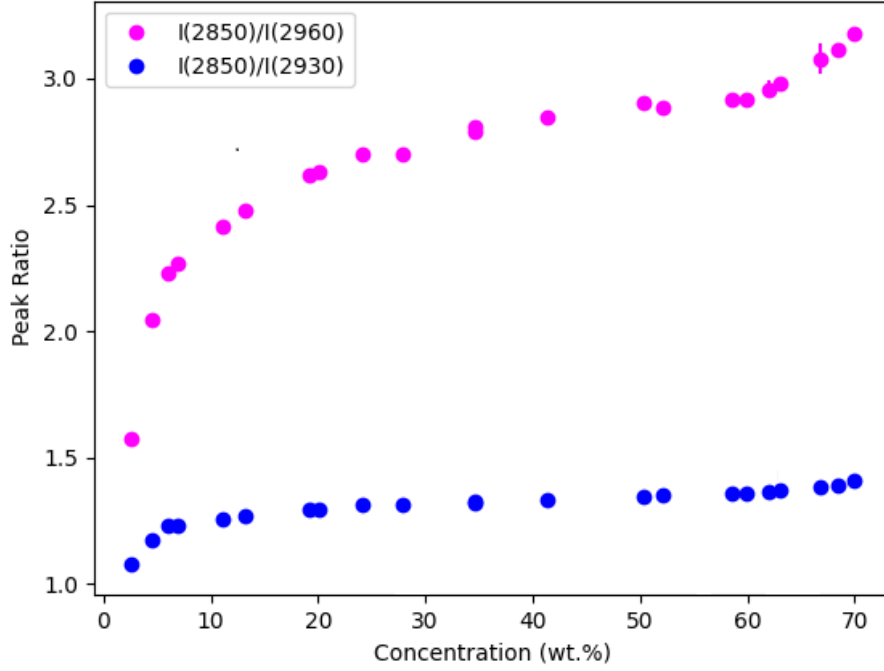
Figure 5.10: Comparison of the change in ratios I(2850)/I(2930) and I(2850)/I(2960) with increasing concentration. The error bars are calculated as the standard error $\sigma_x = \sigma/\sqrt{S}$ where σ is the standard deviation of multiple readings S.

where A is a constant, $0 < c < 1$ is the concentration of surfactant molecules and N_T is the fraction of surfactant molecules in the *trans* conformation. Similarly, I(2930)= $c(BN_T + CN_G)$ where B and C are constants and N_G is the number of *gauche* configurations. If N_T is increasing and N_G decreasing, then the ratio of I(2850)/I(2930) shown in Fig. 5.10 , will always increase no matter the value of constants A, B, C. If we assume that I(1300)= Dc, where D is a constant, and therefore I(1300) is independent of conformation. For the ratio I(2850)/I(1300) $= (A/D)N_T$, that is, it is proportional to the number of *trans* configurations. For the ratio I(2930)/I(1300)= $(BN_T + CN_G)/D$, if N_T is increasing with increasing concentration (so that N_G is decreasing), then I(2930)/I(1300) will increase if $C < B$ and decrease if $B < C$. Based on this reasoning, the ratio I(2850)/I(1300) should provide the best estimate for the change in the number of *trans* configurations in the solution.

In Fig. 5.11 there are three distinct regions that can be identified, which are interpreted as corresponding to the micellar, hexagonal, and lamellar phases.
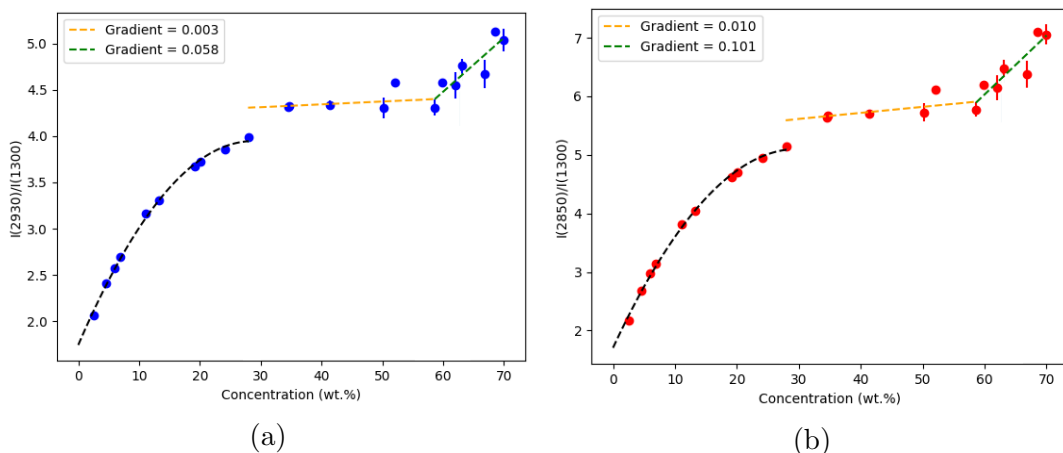
Figure 5.11: Plot of intensity ratios (a) I(2930)/I(1300) and (b) I(2850)/I(1300). Ratios calculated using linear fit baselines for both regions. The error bars are calculated as the standard error $\sigma_x = \sigma/\sqrt{S}$ where σ is the standard deviation of multiple readings S.

Each region is fitted differently, and it is observed that the hexagonal and lamellar regions display approximately linear relationships.

Peak Positions

Besides intensity ratio changes, there could also be a variety of changes seen in the location of the peak maximum, due to changes in the size of contributing modes from overlapping peaks. For example, it would be reasonable for there to be a downward shift in the peak position at around 2850cm^{-1}, as this peak grows with increasing *trans* modes, and the influence from the overlapping *gauche* mode at 2876cm^{-1} becomes less significant. This behaviour has been seen by other researchers such as, Plastin *et al.* [204], who study the micelle formation in solutions of sodium octanoate. They find a peak with position around 2860cm^{-1}, where the peak position decreases with increasing concentration. They attribute this to the change in conformation of the hydrocarbon tails during micelle formation, suggesting that the *trans* formation is more common in micelles than in free monomers, as the molecules in micelles are 'straightened'. They suggest that this behaviour comes about because the *trans* conformations contributing to the peak, have a frequency lower than in *gauche* conformations which is consistent with the assignment of *trans* and *gauche* modes by Shemouratov *et al.* [234]. Therefore, a
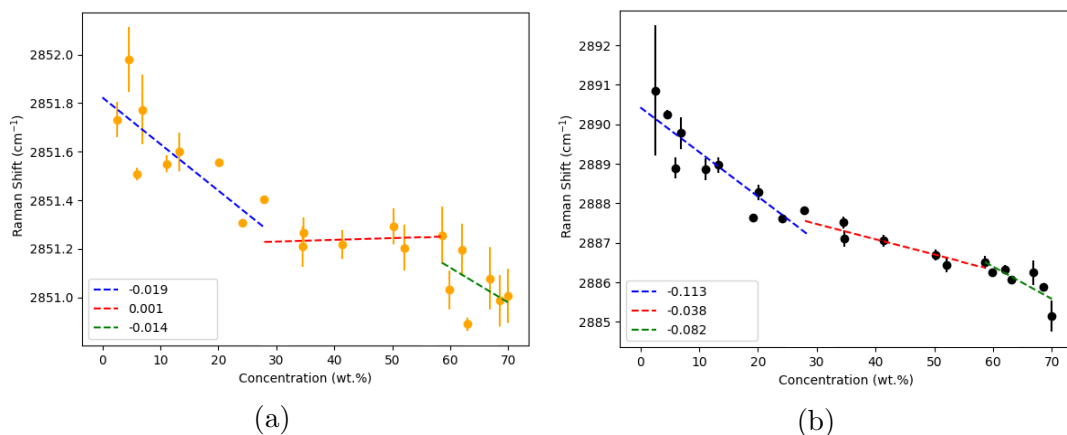
Figure 5.12: Position of peaks in the region (a) 2850cm^{-1} and (b) 2880cm^{-1}. The error bars are calculated as the standard error $\sigma_x = \sigma/\sqrt{S}$ where σ is the standard deviation of multiple readings S.

decrease in the frequency at around 2860cm^{-1} indicates an increase of the fraction of surfactants in the *trans* conformation, and, consequently, micelle formation.

A plot of this peak for AES solutions is shown in Fig. 5.12a. This is similar to the behaviour seen by Plastin *et al.* [204] for this peak during micelle formation. The change in position of the primarily *trans* 2880cm^{-1} peak would be difficult to suggest, as it is expected to overlap with *gauche* modes on either side. However, the location of our peak for AES within this region is located at a slightly higher location than the 2880cm^{-1} expected, with a position of around 2890cm^{-1} at low concentrations in the micellar phase. This slightly higher location may be manifesting due to overlap with neighbouring peaks at higher locations. Therefore it might be reasonable to expect to see movement from 2890cm^{-1} towards 2880cm^{-1}, as the *trans* peak begins to dominate over adjacent modes. The behaviour of this peak is shown in Fig. 5.12a. While both the position of the 2850 and 2880cm^{-1} peaks increase or decrease as expected, a more obvious behavioural difference between mesophases is found from the position of the 2850cm^{-1} peak, perhaps due to a greater level of obscuring from multiple underlying modes of the 2880cm^{-1} peak. The position of the 2880cm^{-1} peak once again indicates that there is an increase in *trans* modes with increasing concentration within the micellar and lamellar phases, with minimal change within the hexagonal phase.
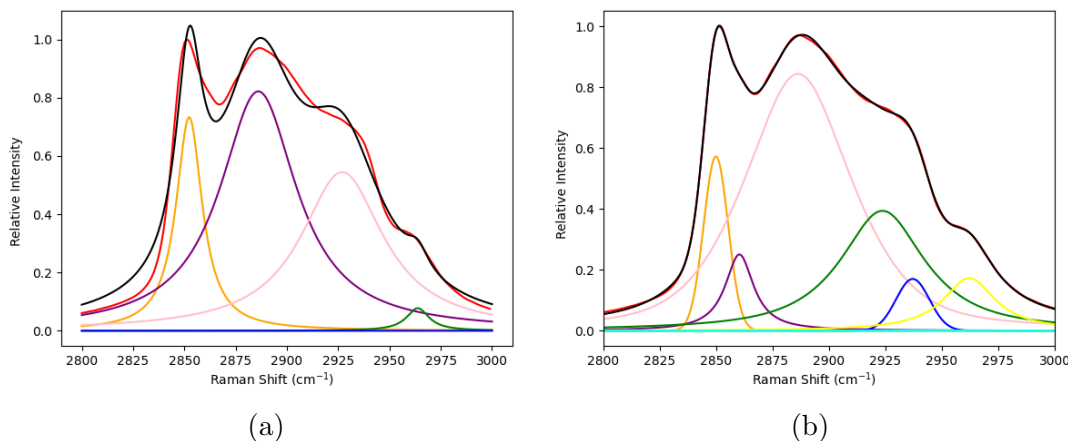
Figure 5.13: Comparison of curve decomposition in the region 2800–3000cm^{-1}, for a number of (a) four or (b) six modes. Intensity is scaled by the intensity of the peak located at approximately 2850cm^{-1}. Raw data is shown in red, fitted curve is shown in black. Concentration sample = 67%. Other peaks show the curves used in the fits.

Curve Decomposition

While it is most common to model this range with a decomposition of four curves, it has been shown how it is likely that this region is actually made up of a greater number of components. However, fitting an increasing number of modes becomes tricky with increasing fitting parameters, and we run the risk of over fitting. A comparison of fitting peaks using four *vs.* six curves is shown in Fig. 5.13. The peaks for the six mode fit are located around the same approximate positions as those suggested by Shemouratov *et al.* [234]. We also allow for the fitting of two additional curves with maximums centred at around 3250cm^{-1} and 3460cm^{-1}, that stem from the overlapping contribution from the O-H bonds in water molecules. The influence of the water curves on the CH vibrational modes is shown in Fig. 5.14. At low surfactant concentration levels, the water curve begins to overlap with the CH vibrational modes and taking the water modes into account in curve fitting becomes important. It can be seen that we obtain a much better fit with the six curves, in particular, there is a slight shoulder in the peak of the spectrum at 2850cm^{-1}, which is much better fit with the addition of another curve at around 2860cm^{-1}. The asymmetry of this peak has been seen in the Raman spectra of lyotropic liquid crystals in other works [237], however, its exact origin is uncertain.
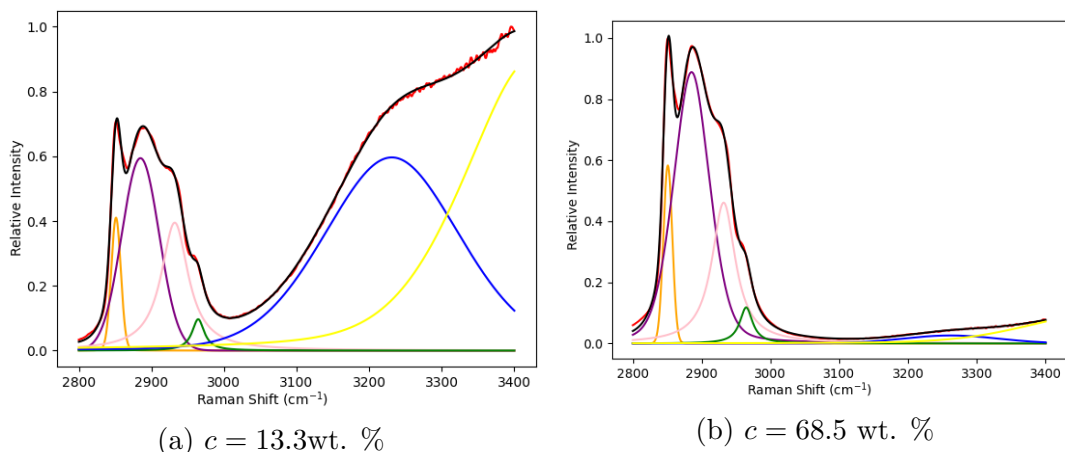
Figure 5.14: Curve decomposition including the influence of the water vibrational peaks in region 2800–3400cm^{-1}. Examples are shown for two different concentrations c. Intensity is scaled to the largest peak in the domain for plotting. In the region 2800–3000cm^{-1} the four curve fitting is shown.

While there is a greater match to the raw data from the fit consisting of six modes as opposed to four modes, the six mode fit displays greater variability and it is more difficult to obtain consistent fits between spectra corresponding to the same concentration. Therefore we will instead study the effect of increasing concentration in the curve decomposition from four peaks in the 2800–3400cm^{-1} region. Results of the ratio of peak at 2850 and 2930cm^{-1}are shown in 5.15. Note that concentrations below 10 wt.% are not shown, due to increased difficulty fitting at lower concentrations. Although the fitted curves are likely to be representing multiple vibration nodes, it is thought that the fitted curves fitted at around 2850 and 2890cm^{-1} are dominated by *trans* configurations, while the curve at 2930cm^{-1} is influenced by *gauche* modes. Broadly similar behaviour is found from these fitted curves, to what is found by peak intensity ratios in Fig. 5.9. Although, the size of the error bars illustrates the greater variability in using results from curve fits as opposed to the intensity data shown in Fig. 5.9. Smaller changes are seen in the ratio of the areas rather than the ratio of the maximum intensity, reflected in the smaller gradients, which is similar to what is shown by other researchers [203].
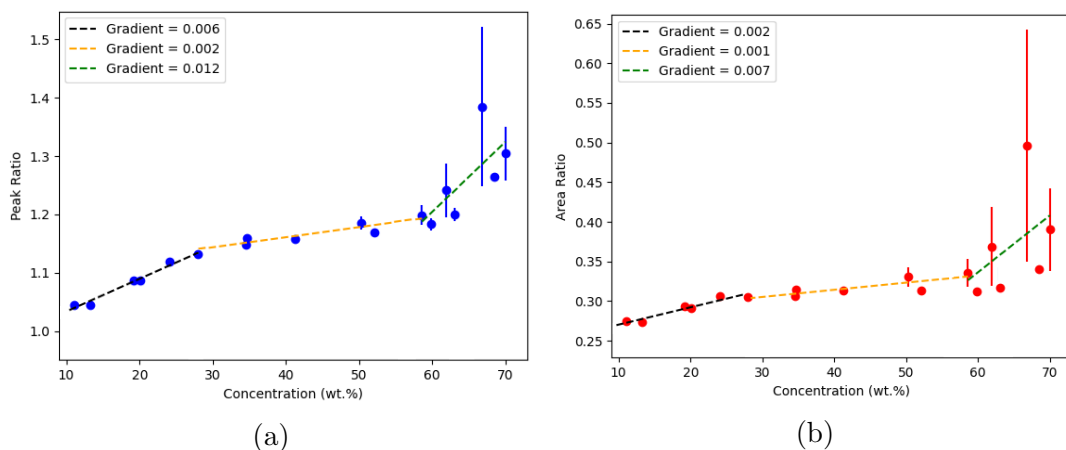
Figure 5.15: Ratio of fitted curves shown in Fig. 5.14 located at 2850cm^{-1} and 2930cm^{-1}. Shown is the ratio of the (a) maximum peak intensity and ratio of the (b) areas under the curves.

5.2.4.5 Modes in Region 1000–1150cm^{-1}

In hydrocarbon chains, it is usually found that three Raman bands appear in the region of 1000–1150cm^{-1}. Two bands appear at around 1060cm^{-1} and 1130cm^{-1}, which can be assigned to C-C stretching of *trans* segments. Another band appears at around 1080cm^{-1} which is assigned to C-C stretching modes of *gauche* segments, and this region has been widely used for monitoring conformational changes [203, 206, 211, 229, 238]. The ratio of these peaks can be used to evaluate the average number of *trans* bonds appearing in solution. These peaks can also undergo frequency shifts as a result of the phase change [206]. In SDS molecules, some authors attribute part of the peak at around 1080cm^{-1} to being the result of symmetrical stretching of SO_3, Picqart [206] considers this and argues that there is likely significant obscuring of the C-C stretching modes from SO_3 stretching in this region.

A further added complication in this region is that it is highly likely there are a number of hidden contributions from C-O bonds. For example polyethylene oxide $H(OCH_2CH_2)_nOH$ shows Raman peaks in aqueous solution at around 1040, 1060, 1120 and 1140cm^{-1}, all corresponding to C-O-C modes [221]. Similarly placed bands are reported in the spectra of $CH_3OCH_2CH_2OCH_3$ [222] and poly(ethylene glycol) [239]. Despite this being the most common spectral range for analysing the
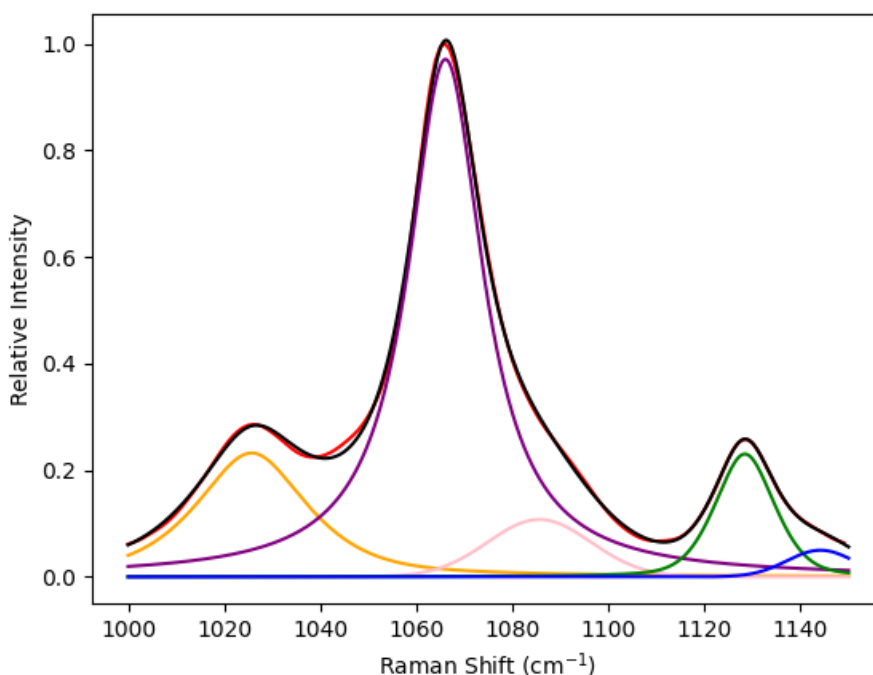
Figure 5.16: Five modal curve decomposition (black curve) in the region 1000–1150cm^{-1} (raw data shown in red). Example is given to fit using the intensity data using the linear fit baseline removal method (baseline 1). Similar fits are obtained using the closer baseline fit (baseline 2). Note that the baselines are shown in Fig. 5.6. Concentration $c = 67\%$.

trans/gauche ratio in hydrocarbon chains, this is difficult for AES like molecules, due to the number of overlapping peaks expected in the region.

An example of what is found in the vibrational spectra for AES solutions is shown in Fig. 5.16, along with a five curve modal decomposition. However, it is expected that there are actually more than five underlying modes contributing to the spectrum, but the modes are too small to accurately fit to the spectra.

Peaks are clearly identifiable at approximately 1025, 1066, and 1128 cm^{-1}. There also appears to be at least one peak around 1085cm^{-1}, explaining the apparent asymmetry of the curve centred at 1060cm^{-1}. The peaks 1066 and 1128cm^{-1} can primarily be considered originating from C-C *trans* vibrational modes, with underlying C-O modes. The 1085cm^{-1} bulge is expected to partially originate from overlapping modes related to C-C *gauche* and SO$_3$ vibrations. The peak centred at around 1025cm^{-1} doesn't seem to appear in the Raman Spectra of SDS of other researchers [206], leading us to conclude that the peak is related to the ethoxyl

groups (OCH_2CH_2) in the AES molecules, however specific assignment of its exact mode is difficult. Underlying this spectra are expected modes from different C-O vibrations, making curve decomposition difficult.

If the peaks in the region were entirely from C-C stretching modes, then we might expect that we could get an idea of the *trans-gauche* transition from the position of the 1066cm^{-1} peak. There would be an expected peak shift from higher to lower with increasing number of *trans* modes. A plot of this peak position is shown in Fig. 5.17 where it is shown that the opposite behaviour is seen with increasing concentration. This suggests that contribution to the spectra from C-O related bonds as well as vibrations in the head group are significant, and can't be ignored in the curve decomposition.
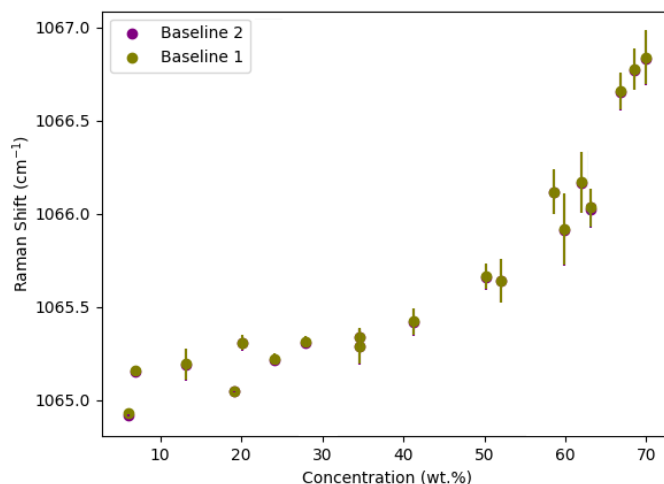
Figure 5.17: Position of intensity peak at around 1060cm^{-1} against increasing concentration. The error bars are calculated as the standard error $\sigma_x = \sigma/\sqrt{S}$ where σ is the standard deviation of multiple readings S.

Analysis of the curve decomposition shown in Fig. 5.16 supports the idea that there is another mode contributing to the peak at 1060cm^{-1}. The positions of the fitted curves at approximately 1060cm^{-1} and 1080cm^{-1} are shown in Fig. 5.18. There is a slight movement of the fitted curve at 1060cm^{-1} towards higher frequencies, while the peak at approximately 1080cm^{-1} dramatically shifts to lower frequencies at higher concentrations. Particularly the 1080cm^{-1} curve shifts with the greatest intensity once we enter what we believe to be the lamellar phase. Indicating that this movement is trying to compensate for the existence of a peak
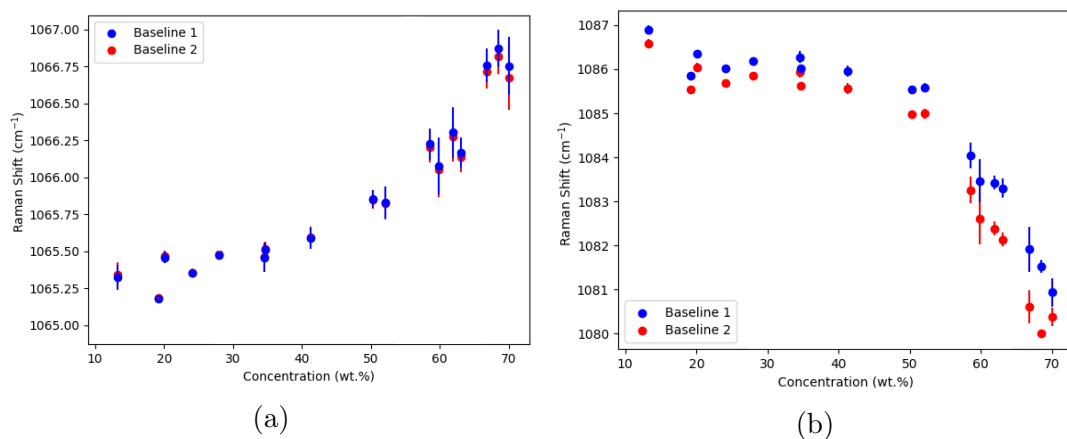
Figure 5.18: Position of fitted curves shown in Fig. 5.16 located at (a) 1060cm^{-1} and (b) 1080cm^{-1} against increasing concentration of AES. The error bars are calculated as the standard error $\sigma_x = \sigma/\sqrt{S}$ where σ is the standard deviation of multiple readings S.

in the range 1060–1080cm^{-1}. However attempts at trying to fit a peak in this range struggle to be consistent between different spectra. The ratio of the fitted curve at 1060cm^{-1} to 1080cm^{-1} is shown in Fig. 5.19. This ratio would be expected to correspond to the ratio of *trans/gauche* conformations. In the micellar and hexagonal phase ranges, this ratio behaves in a way that is consistent with that found from *trans/gauche* ratios in the 2800–3000m^{-1} region. However, once the solution enters the presumed lamellar phase, the plot deviates from this behaviour. It is presumed that the missing peak in the frequency range 1060–1080cm^{-1} is the head group vibrational mode corresponding to SO$_3$ vibrations, that undergoes dramatic change under lamellar phase transition.

5.2.4.6 Modes in Other Regions

Further peaks that come from vibrations related to the hydrocarbon chain include: 1440cm^{-1} (CH$_2$ scissoring), 890cm^{-1} (CH$_3$ rocking), 830cm^{-1} (CC stretching), 720cm^{-1} (CH$_2$ rocking) [217–219]. In the region 700-1000cm^{-1} there are is a huge number of contributing modes that are mostly medium or weak in strength [221, 222]. Therefore we will not attempt to analyse this region, due to the difficulties in separating out any peaks. There are also a number of S-O weak/medium bending modes in the 400–650cm^{-1} region [223], which we will not attempt to discuss.
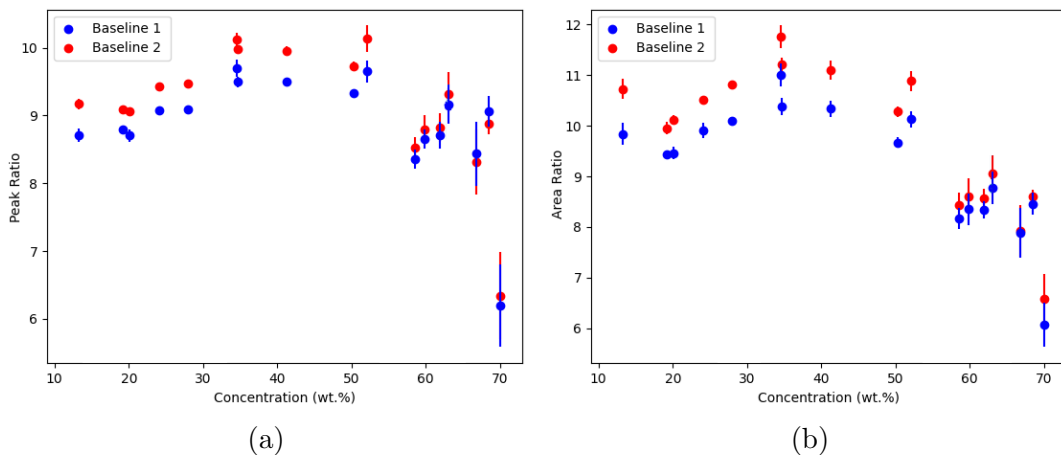
Figure 5.19: Ratio of fitted curves shown in Fig. 5.16 located at 1060cm^{-1} and 1080cm^{-1}. Shown is the ratio of the (a) maximum peak intensity and (b) areas under the curves. The error bars are calculated as the standard error $\sigma_x = \sigma/\sqrt{S}$ where σ is the standard deviation of multiple readings S. The error bars are calculated as the standard error $\sigma_x = \sigma/\sqrt{S}$ where σ is the standard deviation of multiple readings S.

We find that the CH_2 scissoring band presents two components, a main band at 1440cm^{-1} and a shoulder at 1460cm^{-1}. The shoulder at around 1460cm^{-1} is usually attributed to the CH_3 mode [236]. These modes have been shown to be sensitive to phase structural changes, having been shown to change with temperature and concentration *e.g.* a decrease in frequency separation of the two components with increasing concentration [216]. However, how these changes relate directly to the conformational shape is not well known. Furthermore, there is most likely at least one peak of unknown origin in this band, with curve decomposition requiring at least one additional curve to obtain a reasonable fit. This is shown in Fig. 5.20 Therefore, we will not analyse this region for evidence of conformational changes.

5.2.4.7 Summary

In this section, we have analysed how the number of *trans* and *gauche* modes in the hydrophobic chain of AES molecules varies with increasing concentration, using Raman spectroscopy. By analysing peaks originating from a variety of vibrational modes, we have established a clear link between the increase in the number of molecules in the *trans* conformation with increasing concentration. There
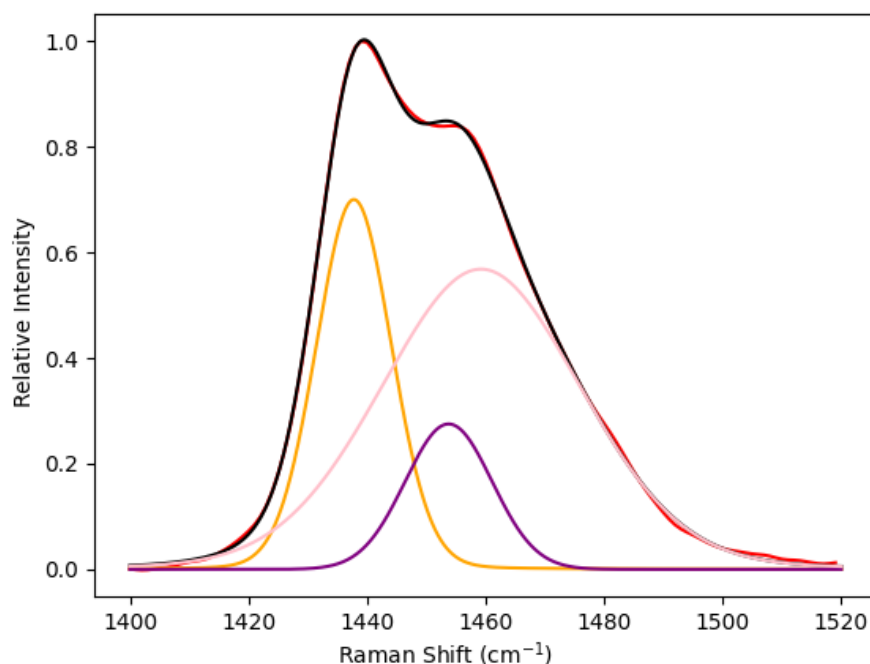
Figure 5.20: Three modal curve decomposition (illustrated by the black curve) in the region 1400–1520cm^{-1} (raw data shown in red). Example is given to intensity data using the baseline removal method baseline 2, as illustrated in Fig. 5.6. Similar fits are obtained using the linear baseline fit (baseline 1). Concentration $c = 67\%$.

are differences in the effect of increasing concentration for each of the different mesophases. In the micellar region, increasing concentration appears to have a relatively large effect on the number of *trans* bonds compared to the lyotropic phases. The lamellar phase also shows an increase in *trans* conformations, while the number in the hexagonal phase shows little change with increasing concentration.

It is shown in this section how it can be difficult to be certain of the origin and meaning of the peaks found in Raman spectra. Often we rely on the research of others looking at similar molecules, or from computational research, in order to assign peaks to different vibrational modes. It can also be difficult to be sure that a curve seen in the spectra can be completely assigned to a particular vibrational node, because there may be underlying vibrations with smaller intensity obscuring the spectra.

It was hoped that these Raman spectroscopy experiments could help provide

verification for the location of the phase boundaries. While peak ratios can help distinguish between the micellar, hexagonal and lamellar phases, there is nothing in our analysis to suggest the existence of a unique cubic phase between the hexagonal and lamellar mesophases, in agreement with the POM and rheological measurements in the previous chapter. From the data presented in this chapter, a boundary between the hexagonal and lamellar phases would be placed at approximately ≈ 60 wt. %, which is in good agreement with that determined in the previous chapter. In many cases there is an abrupt change in the Raman results at a concentration located in the range between the 28% and 35%. If this were due to a phase change between the micellar and hexagonal phases, this would place the phase boundary slightly higher than that identified in the previous chapter, in which POM imaging identified the 28% sample as belonging to the hexagonal phase. This raised the query as the exact nature of the solution at this concentration. This will be investigated in more detail in subsequent chapters.

Chapter 6

Micellar Phase

AES and SDS micellar solutions experimentally exhibit Newtonian behaviour, as presented in Section 4.3.2. Increasing the concentration of the solution increases the viscosity, with a nonlinear relationship. However, it is not necessarily clear whether this viscosity increase is due to changes in the micellar shape or size, or due to increased interaction between the micelles, potentially due to electrostatic effects. Therefore, it would be beneficial to experimentally investigate the effect of increasing surfactant concentration on the size and shape of micelles. This can be performed via a variety of experimental techniques. One of the most simple methods is dynamic light scattering (DLS). DLS measurements are non-invasive, relatively quick, and involve very little sample preparation. This chapter will begin by detailing the DLS method, followed by its application to studying micelle formation in AES and SDS systems. There are limitations to what can be gained from DLS measurements, which will be discussed later in the chapter. Section 6.2 then moves onto discussing other experimental methods, which have been used by other researchers, to study SDS micelle size and shape, and how this compares with the data obtained via DLS measurements.

The next section of this chapter, Section 6.3, presents a DPD study of the formation of micellar solutions. The aim of this study is firstly to confirm that DPD reproduces a micellar solution that is in reasonable agreement with what is found experimentally. Secondly, it also aims to investigate the effect on the micelles of

varying ethoxylation n in the surfactant molecule, as described by the chemical formula $CH_3(CH_2)_x(OCH_2CH_2)_nOSO_3Na$. Simulations are also performed in which a distribution of n is used, which represents the distribution of n in AES as described by Table 2.1. This DPD section is split into two main parts, the first being a study of the solutions as they form under equilibrium conditions (Section 6.3.1), which includes the aims discussed thus far. Following this, Section 6.4 moves onto using DPD in order to obtain viscosity measurements from the simulations, as well as discussing the effect of applying shear to the simulation boxes, and what impact this has on the shape of the micelles. The obtained viscosity measurements for the SDS and AES solutions can be compared with those presented in Chapter 4.

6.1 Dynamic Light Scattering (DLS)

The interaction of light with substances can be used to obtain information about structure. A technique that works well for solutions of relatively low concentration is dynamic light scattering (DLS). DLS can be used for measuring the size and size distribution of particles in the submicron region. These experiments monitor fluctuations in scattered light as a function of time, in order to find this information. This section will briefly summarise the DLS method. Specifically, the measurements are performed in this work using the Malvern Zetasizer Nano ZS 2, and so this section contains a summary of technical information from Malvern Instruments [240, 241].

This experimental method is based on the effect of incident electromagnetic radiation on a molecule. When electromagnetic radiation is incident on a molecule, it will induce an oscillating dipole. This oscillating dipole will re-emit the electromagnetic radiation at the same wavelength as the incident radiation (elastic scattering), however the wave will be scattered in a different direction (so long as the particles are small compared to the incident radiations wavelength). As the particles are undergoing random, Brownian motion, this causes laser light to be scattered at different intensities. It is from the analysis of the intensity fluctuations

that the velocity of the Brownian motion of the particles can be found. Larger particles will be slower, and smaller faster, because they are given greater kicks from the solvent molecules. The initial information calculated is a value for the diffusion coefficient D of a scattered particle.

Intensity of the scattered light fluctuates as a function of time, due to the constant motion of the particles in solution. The intensity recorded during the experiment is usually analysed in terms of the intensity auto-correlation function

$$G(\tau) = \frac{\langle I(t)I(t+\tau)\rangle}{\langle I(t)\rangle^2} \tag{6.1}$$

where I is the intensity and τ is the delay time. This autocorrelation function decays starting from zero delay time ($\tau = 0$). If the solution consists of monodisperse particles, Eq. 6.1 is an exponential decay of the form

$$G(\tau) = A[1 + B\exp(-2\Gamma\tau)] \tag{6.2}$$

where A is the baseline, B is the intercept,

$$\Gamma = Dq^2 \tag{6.3}$$

where D is the translational diffusion coefficient and

$$q = \frac{4\pi n}{\lambda_{\mathrm{W}}}\sin\frac{\theta}{2} \tag{6.4}$$

where n is the refractive index of the dispersant (water), λ_{W} is the wavelength of the laser and θ is the scattering angle. However, if the solution is polydisperse, the decay of the auto-correlation function can have a variety of contributing exponential decays from particles of different sizes. Faster dynamics due to smaller particles lead to faster decorrelation of the scattered intensity. In this case the decay can be represented as a sum of exponential decays.

An estimate for the mean hydrodynamic diameter d for spherical particles in di-

160

lute suspensions, can be found from the calculated transitional diffusion coefficient D using the Stokes-Einstein relationship

$$D = \frac{k_B T}{3\pi\eta d} \tag{6.5}$$

where k_B is Boltzmann's constant, T is temperature, and η is the viscosity of the solvent. As a result of this method, the value that is found for d will depend on not only the size of the particle core, but will also measure the layer of ions surrounding the micelle. The measurement will also be influenced by the surface structure of the micelles. Uneven micelle surface, with protruding monomers in different directions, will affect the diffusion coefficient of a micelle and slow it down, resulting in a larger estimate for the hydrodynamic radius.

The data output from a DLS experiment using Malvern Zetasizer Nano ZS 2, is the intensity distribution of particle sizes. This intensity distribution is weighted by the scattering intensity of each particle fraction. This scattering intensity is proportional to the molecular mass m of a particle squared, while the mass is proportional to the volume, resulting in $I \propto m^2 \propto d^6$. Therefore, the presence of large particles in the solution can dominate the intensity distribution, which can produce initially misleading results. Therefore, it is often desirable to convert the intensity distribution data into volume or number distributions instead, using Mie theory [242, 243]. However, there are a number of assumptions that are made in order to convert from an intensity distribution to a volume or mass distribution. These include: all particles are spherical; the particles are homogenous and similar density; the optical properties of the particles are known (the refractive index); and that there is no error in the intensity distribution. An example of the micelle sizes found from using different distributions by Martina *et al.* [18] is shown in Table 6.1. Notice that two peaks are identified in the intensity distribution, while there is only one in the volume distribution and the number distribution. There are often additional peaks corresponding to large particle sizes in the intensity distribution, that become insignificantly small in the volume and number distributions. Also

Distribution	Size
Intensity Peaks	4.210 ± 1.104
	119.1 ± 43.00
Volume Peak	3.46 ± 0.7105
Number Peak	3.012 ± 0.4651

Table 6.1: Data obtained by Martina *et al.* [18] for an SDS solution with a concentration of 0.01M ($\approx$ 0.3wt.%). Sizes in nm.

note how the peak located at 4.2nm in the intensity distribution shifts its location in the corresponding number and volume distributions.

6.1.1 Background of measuring SDS using DLS

DLS can be used to ascertain information about the size and polydispersity of micelles in solution, and has been applied by other researchers to SDS solutions in particular [18, 244–247]. The CMC value for SDS is around 8.2mM (0.24wt.%) [248], above which DLS can be used to find information about the size of the micelles that form.

However, for SDS micelles, the application of DLS is complicated, due to the layer of charges surrounding the micelle. For example, Ali *et al.* (2013) [246] find that, at a temperature of 298K and concentration of 0.05M (1.5%), SDS solutions exhibit a DLS peak diameter of 1.54nm. This is smaller than the diameter of 4.2nm, reported by Martina [18] (shown in Table 6.1) for a concentration of 0.01M (0.3wt.%). As the location of this peak should indicate the size of the SDS micelle, this would imply a counter-intuitive conclusion that the SDS micelles are decreasing in size, with increasing concentration. Similarly, Mehta *et al.* [245] and Ali *et al.* (2017) [247] report similar decreases in the position of the intensity peak with increasing SDS concentration in aqueous solution.

The results as reported above are not what might be expected. The reported SDS results would indicate a decrease in the micellar size with increasing concentration, and that the micelle size is much smaller than is expected. The length of an SDS molecule is expected to be around 2nm, so a theoretical estimate for the diameter a spherical micelle consisting of SDS molecules would be around 4nm.

These results are also in contradiction with results reported from experimental methods such as small angle X-ray scattering, which find micelle diameters of around 4-5nm [249] (note that this will be discussed in more detail in Section 6.2). The underestimate in the size of micelles from DLS measurements roots back to an overestimation for the translational diffusion coefficient D, as a result of the ionic nature of SDS, and there are several approaches in published literature to try to explain these results.

One approach is to consider that the calculated value of D in DLS, produces the value for the mutual diffusion coefficient, rather than the micelle diffusion coefficient [12]. That is the total diffusion for all the surfactant components, including contributions from micelles, free surfactant monomers, and free counterions. Consider the contributions to the mutual diffusion coefficient D for a nonionic surfactant to be

$$D = \frac{c_1 D_1 + N_{\text{agg}}{}^2 c_{\text{mic}} D_{\text{mic}}}{c_1 + N_{\text{agg}}{}^2 c_{\text{mic}}} \tag{6.6}$$

where D_1 is the free monomer diffusion coefficient and D_{mic} is the micelle diffusion coefficient, N_{agg} is the aggregation number and the concentration of the species are c_1 and c_{mic}. When we are far above the CMC, the number of free monomers is relatively small so $D \approx D_{\text{mic}}$. For an ionic surfactants, the expression includes contributions for counterions and becomes the much more complicated expression

$$D = \frac{c_1 c_+ D_1 D_+ + q^2 c_1 c_{\text{mic}} D_1 D_{\text{mic}} + N_{\text{agg}}{}^2 c_+ c_{\text{mic}} D_+ D_{\text{mic}}}{c_1 D_1 + c_+ D_+ + (N_{\text{agg}} - q)^2 c_{\text{mic}} D_{\text{mic}}}$$
$$\times \frac{c_1 + c_+ + (N_{\text{agg}} - q)^2 c_{\text{mic}}}{c_1 c_+ + q^2 c_1 c_+ + N_{\text{agg}}{}^2 c_+ c_{\text{mic}}} \tag{6.7}$$

where D_+ and c_+ are the counterion diffusion coefficient and concentration. q is the number of bound counterions to a micelle consisting of N_{agg} surfactant ions. At high concentrations much above the CMC, the expression simplifies to

$$D = \frac{(1 + m - q)D_+ D_{\text{mic}}}{D_+ + (m - q)D_{\text{mic}}}. \tag{6.8}$$

Fig. 6.1 shows the mutual diffusion coefficients calculated theoretically using the expression in Eqs. 6.7 and 6.6 by Sutherland *et al.* [12], substituting in values that are representative. There is a sharp drop as the concentration reaches the CMC for both cases. For ionic micelles the increase in the mutual diffusion coefficient is a result of ionic diffusion. Sutherland *et al.* [12] calculate micelle diffusion coefficients for a variety of sodium alkylsulfonates, via Taylor dispersion methods. They then compare this with the results obtained from DLS experiments, as well as mutual diffusion coefficients from other studies. At surfactant concentrations well above the CMC value, the DLS diffusion coefficients for nonionic surfactant solutions are approximately identical to the micelle and mutual diffusion coefficients. For ionic surfactants, the DLS and mutual diffusion coefficients are identical, but considerably larger than the micelle diffusion coefficient. Their results for SDS molecules are shown in Fig. 6.2. Sutherland *et al.* [12] reach the conclusion that their results suggest that the diffusion coefficients obtained in DLS are actually mutual, rather than micelle, diffusion coefficients. However, it can be found from Eq. 6.7, that at low concentrations (before ionic diffusion dominates) $D \approx D_{\text{mic}}$, proof of which is shown in Appendix B. Therefore, an estimate for D_{mic} could be obtained at low concentrations, by fitting and extrapolating to zero concentration (above the CMC).

Another, more common, approach is by considering the potential effect of inter-micellar interactions [250, 251]. Due to the fact that the micelles are charged, the forces of repulsion between them can be significant. Assuming that an increasing surfactant concentration leads to an increased number of micelles in the solution, which is reasonable given that research suggests that the aggregation number remains approximately constant, there will be a decrease in the average distance between them. This increasing electrostatic force can influence the diffusion of the micelle, making the diffusion coefficient concentration dependant. On the basis of this argument, D is often approximated to take the form (to the first order in the
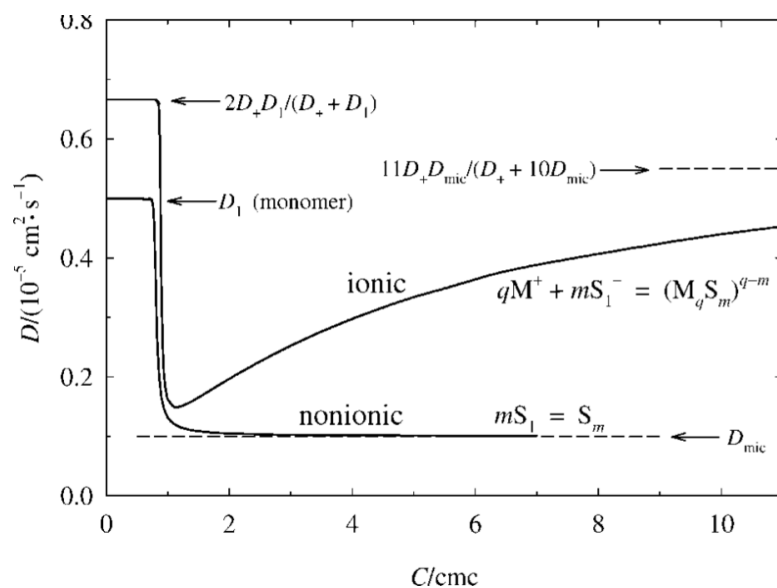
Figure 6.1: Mutual diffusion coefficients D for nonionic surfactants and ionic surfactants using Eqs. 6.7 and 6.6, as calculated by Sutherland *et al.* [12]. Parameters used: $D_{\mathrm{mic}} = 0.1 \times 10^{-5} \mathrm{cm}^2\mathrm{s}^{-1}$, $D_1 = 0.5 \times 10^{-5}\mathrm{cm}^2\mathrm{s}^{-1}$, $D_+ = 1.0 \times 10^{-5}\mathrm{cm}^2\mathrm{s}^{-1}$, $m = 60$ and $q/m = 0.83$.
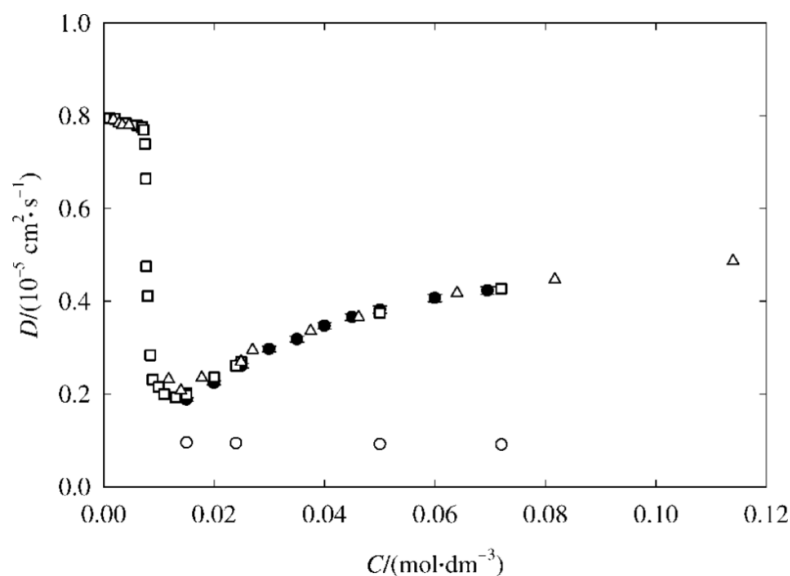
Figure 6.2: Diffusion coefficients as calculated by Sutherland *et al.* [12]. Coefficients given as: DLS (filled circles), mutual (open squares and triangles), and micelle (open circles) diffusion coefficients for aqueous solutions of sodium dodecyl sulphate at 25°C.

165

concentration above CMC, c) [251]

$$D = D_0(1 + k_D(c - c_{\mathrm{CMC}}))$$ (6.9)

where k_{D} is an interaction parameter (usually obtained from fitting to experimental results), and D_0 is the diffusion coefficient at infinite dilution. Using this argument, one should be able to obtain a reasonable estimate D_0, from extrapolation of $c \rightarrow c_{\mathrm{CMC}}$. Crucially, if the micelles interact repulsively (which they are expected to do because of their net charge) then this has the effect of increasing the diffusion coefficient, which has been shown to be what is expected theoretically [252].

It is possible that the effect of the ions in solution results in a combination of the two explanations above. However, in both interpretations, an estimate for the micellar size can be obtained by extrapolating to zero concentration (above the CMC). However, it is likely to be difficult to interpret any changes in size of the micelles at increasing concentrations. Section 6.1.2 will now detail the results of measuring SDS and AES micelles, at a variety of concentrations.

6.1.2   Study using DLS to measure AES and SDS solutions

Measurements are made on SDS and AES aqueous solutions, in the micellar mesophase concentration range. These experiments were performed using Malvern Zetasizer Nano ZS 2. The scattered light is detected at an angle of $173°$, known as back scatter detection. There are several advantages to using back scattering techniques, with one crucial advantage being the treatment of contaminants, such as dust particles. These particles are typically larger in size than the micelles we want to measure. Large particles will mainly scatter in the forward direction, therefore by using back scattering detection, the effects of contaminants can be reduced.

Measurements are made in the approximate concentration range $0 - 20\%$. The samples are prepared using a similar method as discussed in the previous chapter.

However before measurement they are filtered using a syringe filter, in order to remove any contaminants or dust particles. The Malvern Zetasizer software automatically fits a variety of overlapping exponential decays to the autocorrelation function, using Eq. 6.2, and uses Eq. 6.5 to calculate an intensity *vs.* size distribution. An example of the intensity *vs.* size distribution obtained for a selection of concentrations is shown in Fig. 6.3, as well as its conversion into a volume distribution using Mie theory. A peak in the intensity distribution for all solutions above the CMC value is located in the 0.8–4.5nm range. For higher concentrations, there is also a peak at higher size values, ranging from peak location around 10–35nm. However, in the intensity distribution, the magnitude of the scattered light is $I \propto d^6$. Converting into a volume distribution, the volume is $V \propto d^3$. If we convert the peaks found in the 10–35nm intensity distribution to the volume-weighted distribution, they become insignificantly small. This indicates that they are only an insignificantly small contribution to the solution. Therefore peaks located in the 10-35nm size range, will not be analysed further, and the remainder of this section will focus on the peaks in the lower range.

A plot of the location of the peak in the intensity distribution, as well as the corresponding values of the diffusion coefficient using Eq. 6.5, is shown in Fig. 6.4. The peak location is taken from the intensity distributions, as opposed to the number or volume distribution, due to a lack of confidence in the assumptions that have to be made in Mie theory for the conversion. All of the concentrations plotted correspond to solutions above the CMC, where micelle formation is expected to be taking place.

The values for size obtained are significantly lower than what is expected based on the theoretical size of an individual SDS molecule (expected diameter $\approx$ 4nm). Although, the initial increase in the diffusion coefficients, with increasing concentration just beyond the CMC, is consistent with the values found using DLS by Sutherland *et al.* [12], who explain this increase in D to be reflective of the fact that it is a mutual diffusion coefficient influenced by ionic diffusion. Note that
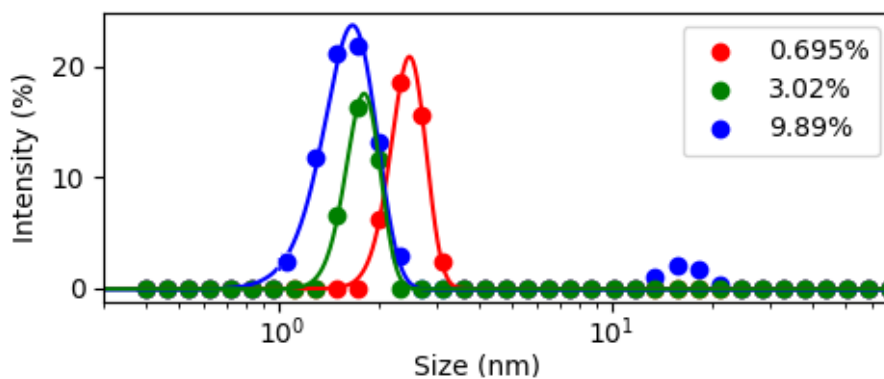
(a) AES Solution
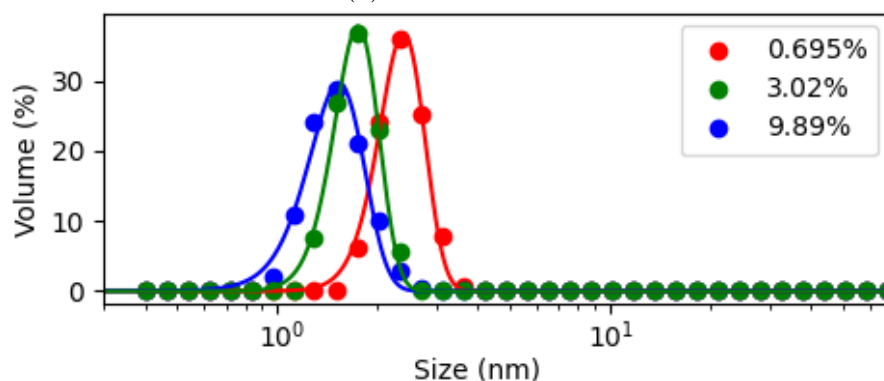
(b) AES Solution
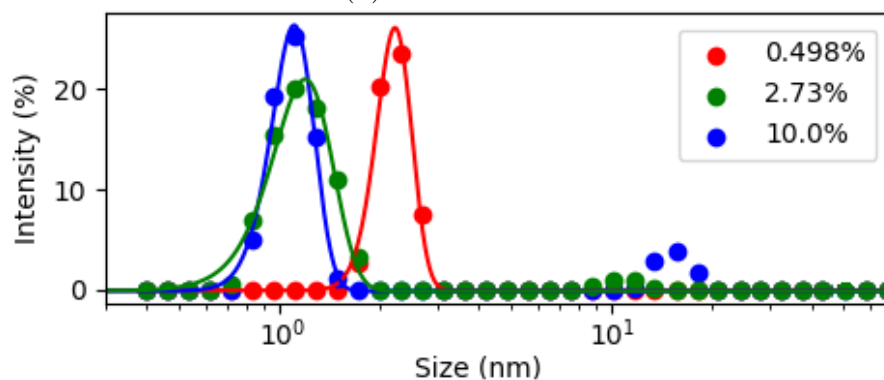
(c) SDS Solution
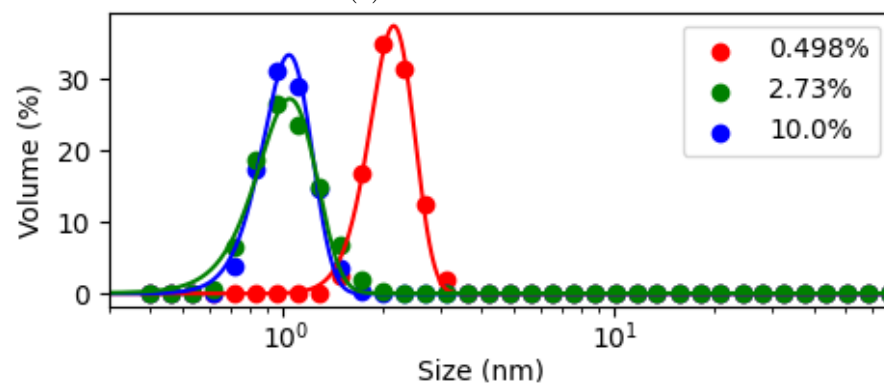
(d) SDS Solution

Figure 6.3: The size data obtained from DLS measurements using the Malvern Zetasizer. Shown are the intensity and corresponding volume distributions for AES and SDS solutions of varying concentration.

these authors only make measurements up to a concentration of around 2%.

The drop off in the diffusion coefficient at higher concentration values ($\approx 10\%$) is not predicted by Eq. 6.7, and could be explained by a couple of different scenarios. First is that the SDS micelle is growing in size, potentially becoming non-spherical and rod-like. An alternative is that the decrease is manifesting due to intrinsic problems with using DLS at higher concentrations. For high concentrations, there may be more inter-particle or inter-micellar interactions, due to closer proximity in solution. In other words, an individual molecule may encounter (or cross paths with) another molecule in solution, altering its diffused distance over the course of a measurement. Therefore, the size calculated from the value of diffusion coefficient would not be indicative of the size of that molecule. Also, at higher concentrations there is also the problem of multiple scattering. A single photon of laser light will scatter off multiple particles before reaching the detector. This would lead to the detection of a less correlated signal, compared to the original signal. This rapid loss of correlation is not the result of particle motion, and thus not related to the particle's size.

When the concentration gets larger, the calculated diffusion coefficients are significantly lower for AES than they are for SDS solutions. However, based on the information available, it is unclear why this is the case. Therefore, we will focus on the lower concentration range, as shown in Fig. 6.5, using the theory for ionic micelles as discussed in the previous section. Eq. 6.9 can be used in order to obtain estimates for the diffusion coefficient at infinite dilution D_0. In Eq. 6.9 the concentration ($c - c_{\mathrm{CMC}}$) corresponds to the concentration above the CMC, therefore Fig. 6.5 shows the diffusion coefficient plotted against the concentration of surfactant in the system, minus the CMC value. Eq. 6.9 is fitted to the data at low concentration values, and extrapolation of ($c - c_{\mathrm{CMC}}) \to 0$ provides an estimate for D_0. This fit is performing using Python, using a least-squares fitting method. The value of the CMC used for SDS is 8.2mM [253] (or 0.24%). It is found that for monodisperse solutions containing increasing ethoxylation n, the value of the
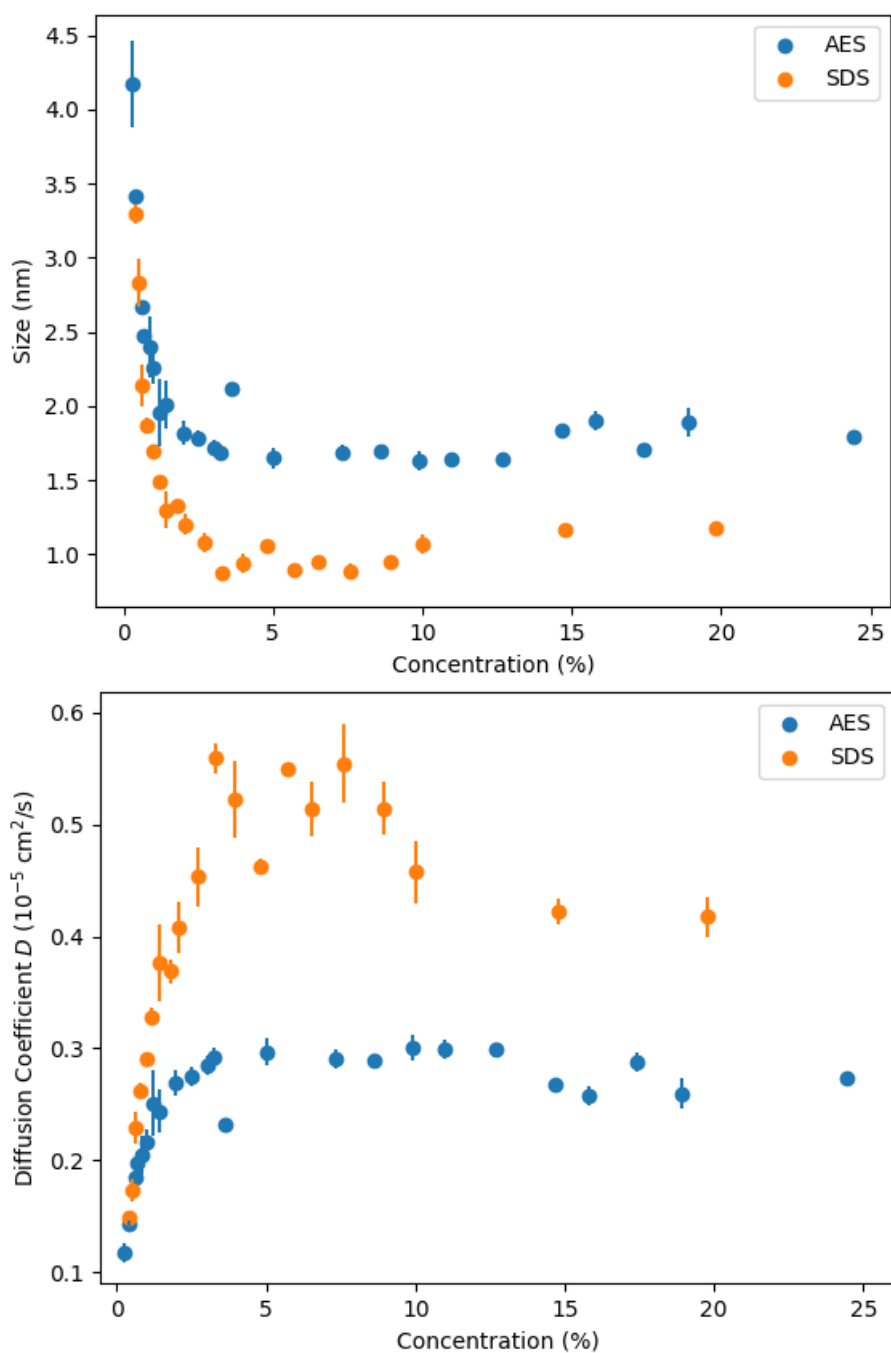
Figure 6.4: Location of peak in the size distribution data obtained from DLS measurements, and the corresponding diffusion coefficient. Data is plotted for a variety of concentrations, of both AES and SDS solutions. Error bars represent the standard deviation in repeated measurements.

CMC drops for $n = 1, 2, 3$ to a constant value of $c_{\text{CMC}} = 0.8$mM [253]. Therefore, as the average ethoxylation of AES is $n \approx 1$, the CMC is estimated to be 0.8mM (or 0.03%).

For SDS micelles the estimate for D_0 from DLS measurements is $D_0 = (0.082 \pm 0.013) \times 10^{-5}$cm^2/s, which corresponds to a hydrodynamic size estimate of $d_{SDS} = 6.0 \pm 1.0$nm. The value obtained for AES is $D_0 = (0.073 \pm 0.009) \times 10^{-5}$cm^2/s, corresponding to a size value of $d_{AES} = 6.75 \pm 0.88$nm. This value of $d_{SDS} = 6.0 \pm 1.0$nm is larger than the theoretical estimate of around 4nm. This could be explained by DLS measuring the hydrodynamic size rather than the size of the micelle core. This means the value would be larger than expected as it would also include a layer of ions around the core, as depicted by Fig. 2.7. The AES micelles are predicted to be larger, as expected due to their longer average molecular length, by around $l \approx 0.75$nm. Estimating that the bond length of C-O is around (1.4 ± 0.1)Å [254], and the bond length of C-C is (1.5 ± 0.1)Å [255], the resulting contribution of $(\text{OCH}_2\text{CH}_2)$ contributes an additional length of around (4.3 ± 0.2)Å (of course the actual length of OCH_2CH_2 will be slightly less than this when taking into account bond angles). Expecting that the micelles grow by $2\times$ this length (which is 0.86nm), this is in good agreement with the growth of the micelle size from SDS micelles to AES micelles.

6.1.3   Conclusion

The technique of DLS could not be used to gain information about how the micelles of SDS or AES change size or shape with varying concentration. Due to likely interactions between micelles, the diffusion coefficient is greatly overestimated, leading to a large under-prediction of the micellar size. At very low concentrations, an estimate for the hydrodynamic size of the micelles can be found by performing a linear fit to the relationship between the diffusion coefficient and concentration, then extrapolating the concentration to zero. This provides size estimates for SDS and AES of $d = 6.0 \pm 1.0$nm and $d = 6.75 \pm 0.88$nm respectively. These over
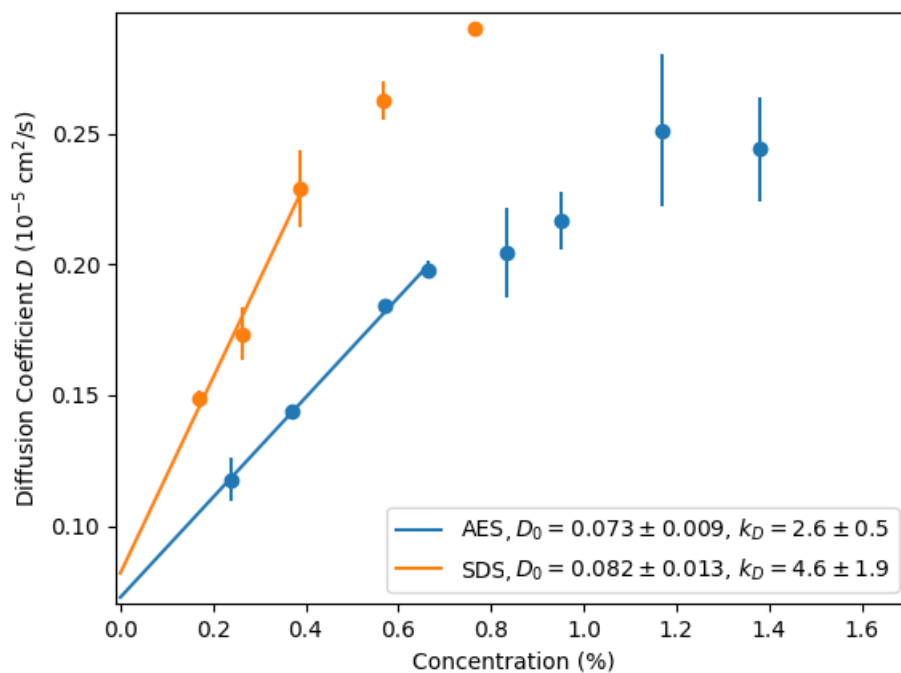
Figure 6.5: The diffusion coefficient plotted against the concentration above the CMC, as determined via DLS measurements. The x-axis is the concentration of surfactant in the system minus the CMC value. The error bars represent the standard deviation in repeated measurements. Eq. 6.9 is used to fit to the linear region of the data at low concentrations, and uncertainties in the fit are obtained by extreme fits through the error bars.

predictions could be explained by the fact that DLS measures a hydrodynamic radius, which would include not only the micelle core, but also an additional layer of ions surrounding the micelle. Additionally, with the knowledge now of how quickly the relationship between the diffusion coefficient and concentration becomes nonlinear, a more accurate estimate may have been obtained by performing more measurements in the very low concentration range.

There are other experimental methods that exist that may be more appropriate for determining the size and shape of ionic micelles in the larger concentration range. This is most commonly conducted for SDS micelles, and the micelles of other variations of ethoxylation n are less commonly reported. The following section will review some of the other experimental methods that can be used to find information about the size and shape of micelles, and present a summary of what is reported in literature for SDS micelles.

6.2 Shape of Micelles

6.2.1 Experimental Methods

As discussed in the previous section, one experimental method to find out information about micelle size is DLS. One of the limitations of DLS is that the method assumes that all particles are spherical and the system is monodisperse [256]. However, due to geometrical packing constraints, the micelles are likely to become increasingly non-spherical as they grow in size [19]. The results obtained via DLS are also affected by electrostatic interactions between the micelles, making a link between the diffusion coefficient obtained, and the size of the micelle difficult. There has been much research dedicated to investigating the shape SDS micelles take using other experimental methods, particularly using small-angle neutron scattering (SANS) [19, 21, 22, 249, 257–259] and small-angle X-ray scattering [244, 260, 261] (SAXS). These methods can provide more detailed information on the structures of particles in solution, despite requiring more complicated procedures [256]. The scattering intensity data that is produced from these experiments, is usually fitted to an ellipsoidal model. The shapes that these models represent for individual micelles are illustrated in Fig. 6.6. It is typical when modelling SDS micelles to use core-shell model ellipsoids. This is simply a model that consists of treating the micelles as two concentric ellipsoids, termed the 'core' and 'shell' components. The core consists of the hydrophobic tails of the surfactants, while the shell consists of the hydrophilic head groups and counter ions [262].

There can be quite a wide variety of different results found for the shape of SDS molecules in literature, particularly for lower concentrations, owing to the difficulty in fitting models to the scattering data. For example, Berr and Jones [249] investigate using SANS for SDS molecules at 0.05M ($\approx$ 1.4wt.%) concentration and room temperature, finding that the data is best fit by the micelles taking an oblate ellipsoid shape, with $b_2 = b_3 = 25.0$Å and $b_1 = 20.3$Å, producing a ratio of $b_1/b_2 = 0.81$. Likewise, Bergstrom and Pedersen [19] attempt a model to their
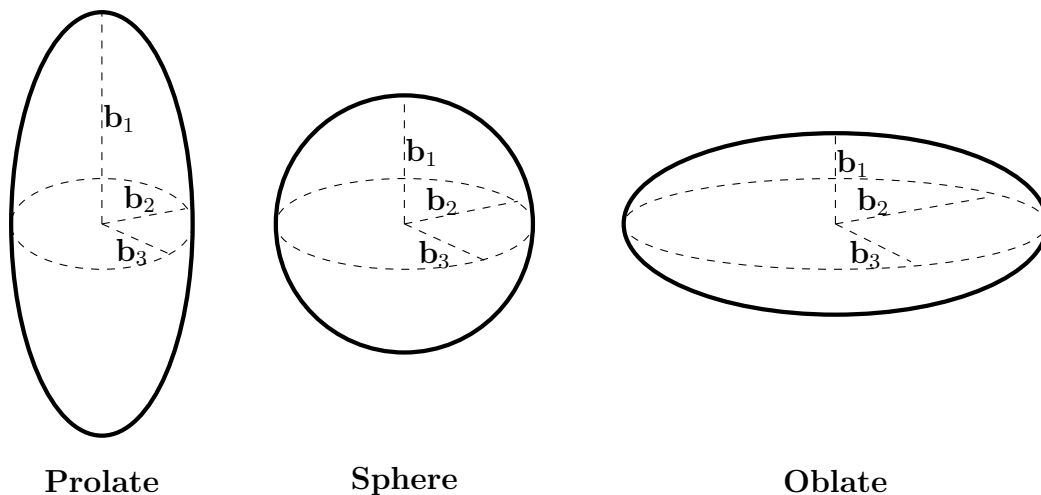
Figure 6.6: An illustration of the different models typically used to fit experimental data, in order to determine the size and shape micelles form in solution.

wt.%	b_1 (Å)	$b_2 = b_3$ (Å)	N_{agg}	b_1/b_2
0.25	8.9	19.9	42	0.45
0.50	11.5	19.8	54	0.56
1.0	12.0	20.4	60	0.59

Table 6.2: A summary of the results of Bergstrom and Pedersen [19]. Results are obtained via SANS data fitted using an oblate ellipsoidal model, for SDS micelles that form at 40.0°C for various concentrations. N_{agg} corresponds to the calculated mean aggregation.

SANS data for monodisperse tri-axial ellipsoids (*i.e.* where $b_2 \neq b_3$), however it was found that $b_2 \approx b_3$, and so the data was reanalysed with a model for which $b_2 = b_3 \neq b_1$. A summary of the results of these oblate ellipsoidal fits are in Table 6.2.

As the concentration increases, there is reasonable amount of experimental evidence to suggest that the micelles start to approach a more spherical form. For example at a concentration of 0.07M ($\approx$ 2wt.%), a SANS study of SDS micelles finds that the micelles are spheres or ellipsoids whose axial ratio is near 1 [257]. With further increasing concentrations, research suggests that the micelles begin to stretch into the prolate form. SANS experiments by Kumar *et al.* [263] in 0.3M SDS solutions ($\approx$ 8.7wt.%) found the best fit to the scattering data using monodisperse, prolate ellipsoidal micelles of radius $b_1 = 33.0$Å and $b_2 = b_3 = 16.7$Å resulting in ratio $b_1/b_2 = 1.98$. Summerton *et al.* [264] find that at 20 wt.% and

Temperature (°C)	b_1 (Å)	$b_2 = b_3$ (Å)	N_{agg}	b_1/b_2
14.0	36.5	18.6	96	1.96
20.0	34.3	18.6	104	1.84
40.0	29.9	18.6	122	1.61
60.0	26.9	18.6	136	1.45

Table 6.3: A summary of the results of Khodaparast *et al.* [20]. Results consist of SANS data analysed using a prolate ellipsoid model, where SDS micelles form at 20 wt.% at various temperatures. N_{agg} is the mean aggregation number.

Concentration (mM)	Concentration (wt%)	b_1/b_2	N_{agg}
71.8	2.1	1.49	83
135	3.9	1.64	91
180	5.2	1.72	99
359	10.4	1.95	108

Table 6.4: Results obtained by Ludwig *et al.* [21]. The SANS data is analysed using a prolate ellipsoid model, where SDS micelles form at 20°C at various concentrations. N_{agg} is the mean aggregation number.

20.0°C, micelles form with an aggregation number $N = 170$ and $b_1/b_2 = 1.8$. Likewise Khodaparast *et al.* [20] also find the micelles take the prolate shape at 20 wt.%, with their results for varying temperatures illustrated in Table 6.3. Ludwig *et al.* [21] also study SDS micelle formation using SANS, finding prolate micelles with varying axial ratios for different concentrations. Their results are illustrated in Table 6.4.

It is worth noting that varying results are not only found between different authors, but also when comparing results from different experimental methods. For example, Gawali [260] investigate SDS micelles at room temperature using both SAXS and SANS, using the core-shell ellipsoid model. For a 10wt.% solution, using SAXS, the authors report a prolate shape with $b_1 = 18.2$Å and $b_2 = b_3 = 13.1$Å, generating a ratio $b_1/b_2 = 1.39$. This contrasts with the results that are found using SANS, reporting values $b_1 = 24.6$Å and $b_2 = b_3 = 15.1$Å, generating a ratio $b_1/b_2 = 1.63$. Interestingly, they also note that both prolate ellipsoid and oblate ellipsoid models can fit the data to a reasonable extent, however only finding slightly better fits using the prolate ellipsoid model.

However, while prolate models appear to be the most common choice at high

Concentration (wt%)	N_{agg}
0.5	58.6
1	65.7
2	84.3
5	91.6
10	104
20	112

Table 6.5: Aggregation numbers reported by Hammouda [22] for SDS micelles, at room temperature with varying concentration, as determined by SANS measurements. N_{agg} is the mean aggregation number.

micellar concentration, not all authors report that prolate models fit the data best. Hammouda [22] also investigate SDS micellar solutions using SANS, and find that their data is best fit by oblate ellipsoids, for micelles formed in the entire concentration range 0.5wt.%–20wt.%. While they obtain their results using an oblate fit, the increase in micellar volume with increasing concentration is consistent with authors using prolate models. The values that they find for the aggregation number N_{agg} with increasing concentration are listed in Table 6.5.

Vass *et al.* [265] discuss the issue of conflicting literature suggesting whether ionic micelles, including SDS micelles, are oblate or prolate. The main source of the problem is that the scattering functions from an oblate or prolate micelle are very similar. From their analysis of SANS data, Vass *et al.* [265] conclude that generally systems could be reasonably fitted by micellar models with both prolate and oblate micelles. In their analysis of the works of others, they conclude that there are some findings that are in agreement, despite researchers sometimes making different ellipsoidal fits. It is concluded that, at sufficiently high ionic surfactant concentration, the aggregates most certainly become elongated structures and that the dimensions of their circular or ellipsoidal cross sections are limited by the length of the hydrocarbon segment of the surfactant. However, at low concentrations, the data can be particularly hard to fit, presumably because the micelle is not particularly stretched in either direction (that is that they are nearly spherical).

It is also interesting to note that, due to long range Coulombic interactions,

charged micelles tend to arrange themselves into an ordered structure, giving rise to a correlation peak in SAXS data. The relationship between this peak and the average separation in micelles is more easily determined at higher concentrations [266]. For SDS micelles at 20% concentration at room temperature, this separation is determined to be 5.7nm [266].

Clearly there are lots of potential sources of error for the discussed experimental calculations, even though they are an improvement over DLS methods. For example, much of the discussed research also uses monodisperse data fits, with these being much simpler and easier to implement when compared to a polydisperse fit. For example, Hassan *et al.* [267] observe that micelles are dynamic, so small shape fluctuations are likely, and will introduce a small polydispersity in the circular cross section. However, these effects would be hard to observe in the scattering data observed, so chose to use the more simple prolate ellipsoidal fit. As illustrated, experimental results are often model dependent, and different conclusions can be made about the micellar size and shape depending on the assumptions and approximations made in analysing the experimental data. The most consistent conclusion for how SDS micelles change with increasing concentration, is that they most certainly grow in volume and likely transform from spherical or nearly spherical micelles to elongated or rod-like micelles. Therefore computational studies can complement experimental research, and help provide more details for understanding the micellar shape changes.

6.2.2 Simulation Methods

This subsection will provide an overview of the two methods that will be used to assess the size and shape of micelles, as found via DPD simulation. Determining the aggregation number via simulations is more straight forward than experimental methods, as the aggregation number can be calculated directly from the simulation results, and no assumptions have to be made about the relationship between the micelle size and the number of molecules contributing to an individual micelle.

Determining the size and shape of the micelle is less straight forward, owing to the difficulty in determining the boundary between the surface of the micelle and the solution, as well as dealing with fluctuations of monomers at the surface of the micelle. One common method for assessing micelle shape and size in simulations is to use the radius of gyration of the micelle, which will be discussed further within this section.

6.2.2.1 Aggregation number

As discussed in Section 2.1, the mean aggregation number N_{agg} is widely used to characterise micellar systems, where N_{agg} is the mean number of molecules per micelle in a solution. In order to calculate N_{agg} individual micelles need to be identified. This is performed by outputting the position of all beads in the simulation box at a set interval, and then analysing each snapshot for the number of aggregates. Clusters are identified by defining a cut-off distance, and molecules that are closer than that distance are said to be in contact with each other and form an aggregate. Only the hydrophobic tail of the molecules is used in this calculation, as they are expected to make up the hydrophobic core of the micelle. The cut-off distance used in all of the calculations to be performed is 1 DPD unit.

In simulations we can also calculate a weighted aggregation number, defined as $N_{\mathrm{W}} = \langle N^2 \rangle / \langle N \rangle$ where $\langle N^2 \rangle = \sum_{N=1}^{\infty} N^2 P_{\mathrm{micelle}}(N)$. Here N is the number of monomers in a given molecule, and P_{micelle} is the probability of finding a monomer existing in a micelle of size N. This can also be described as the number weighted average of the micellar component of the aggregate size distribution. The use of the weighted aggregation number, as opposed to simply the aggregation number, can capture the polydispersity of the system. The difference between the mean aggregation number N_{agg} and the weighted aggregation number N_{W} is illustrated in Fig. 6.7. The different average aggregation numbers (*i.e.* a number average N_{agg} or weighted average N_{W}) correspond to those determined by different experimental techniques [268]. For example, the number average can be obtained via

membrane osmometry [269], while the weighted average is determined via static light scattering measurements [270].
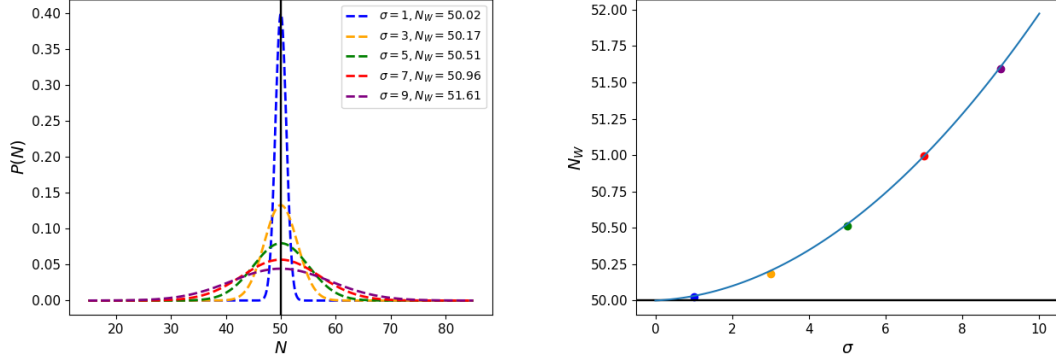
(a) Probability Gaussian distribution $P(N)$ vs. micelle size N for a variety of standard deviation σ values.

(b) Resulting weighted aggregation numbers N_W produced from distributions with different standard deviations σ.

Figure 6.7: Theoretical illustration of the meaning of the weighted aggregation number N_W. All distributions have mean aggregation number value $N_{agg} = 50.0$. With increasing polydispersity (illustrated by increasing standard deviation σ), the weighted aggregation number N_W increasingly deviates from N_{agg}.

6.2.2.2 Geometrical Size and Shape of Micelles

The radius of gyration, R_{G}, is the main parameter that will be used in order to quantify the size of micelles. The value of R_{G} is commonly used in the analysis of simulation results, in order to give information about the size of an object. The radius of gyration for a given micelle is calculated as:

$$R_{\mathrm{G}}^2 = \frac{1}{N} \sum_{k=1}^{N} (\mathbf{r}_k - \mathbf{r}_{\mathrm{COM}})^2 \tag{6.10}$$

where $\mathbf{r}_k$ is the position of a particle in a micelle consisting of N particles and $\mathbf{r}_{\mathrm{COM}}$ is the centre-of-mass for the micelle: $\mathbf{r}_{\mathrm{COM}} = \frac{\sum_i^N m_i \mathbf{r}_i}{\sum_i^N m_i}$.

If spherically-shaped micelles, and constant density, are assumed, there exists a simple relationship between the radius of gyration R_{G} of a micelle and an effective micelle radius R_{S} [271]:

$$R_{\mathrm{S}} = \sqrt{\frac{5}{3}} \langle R_{\mathrm{G}} \rangle. \tag{6.11}$$

The effective radius is linked to the hydrodynamic radius that is measured in DLS techniques. Using DLS measurement techniques, a spherical particle in solution is measured by assuming that it is a body moving through the solution. If the solvent is water, the hydrodynamic radius includes all the ions and water molecules attracted to the micelle. Therefore, if there were no inter-micellar interactions interfering with the results, the value obtained by DLS techniques may be expected to be larger than that obtained obtained in the above equation, as it wouldn't account for this additional layer.

In reality, the micelles are most likely not smooth spheres. Micelles most likely have protrusions from various monomers, resulting in a rough surface. These micelles are likely to be in liquid-like dynamic motion, and the fluctuations most likely result in a spherical micelle when averaged over time [272]. This varying surface shape is one of the reasons that the radius of gyration is most commonly used for analysing micelle shape and size. Compared to other methods for analysing the size, for example a spherioidal fit to the shape of a micelles surface, the radius of gyration is relatively easy to calculate. Fits to the surface of a micelle, for example, are very difficult due to the fluctuations.

When micelles begin to elongate, the relationship given in Eq. 6.11 will no longer hold. However the value of the radius of gyration can still be used to help characterise the shape of the micelle. If we use the fact that the volume of the hydrophobic core is proportional to N (*i.e.* the density remains constant no matter the aggregation number), then spherical micelles will follow the relation $R_{\mathrm{G}} \propto N^{1/3}$. Therefore the value of R_{G}^3/N should be independent of N for spherical micelles. However, rod- and worm-like structures will require a larger power law. For example, Anderson *et al.* [17] use this reasoning to identify the concentration at which the micelles become non-spherical, in an SDS/water system described by DPD. Note that throughout this section, we will use N to denote an aggregation number for a particular micelle, while N_{agg} is used to talk about the mean aggregation number.
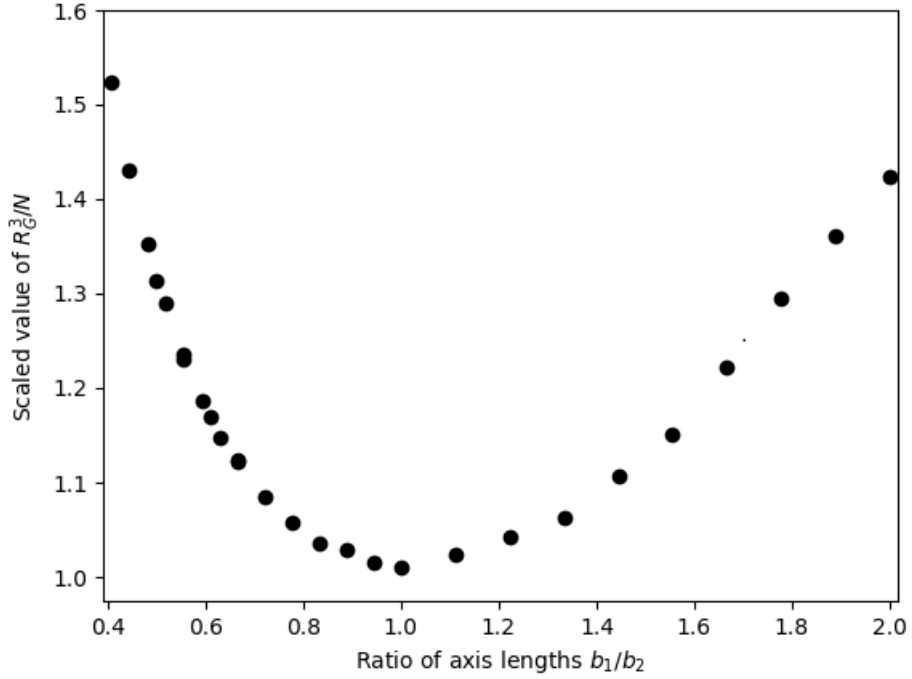
Figure 6.8: Theoretical relationship between R_G^3/N and the ratio of the ellipsoid axis b_1/b_2 (as defined in Fig. 6.6). The plotted value of R_G^3/N is scaled to the value of R_G^3/N for spherical micelles (*i.e.* $b_1/b_2 = 1$). Data points are determined using a Monte Carlo calculation performed in Python.

If we assume that micelles take one of the spheriod shapes illustrated in Fig. 6.6, then we can find the theoretical variation of R_G^3/N for non-spherical micelles. The relationship between R_G^3/N and the ratio of the ellipsoid axis, b_1/b_2, assuming constant density of molecules inside the micelle, is shown in Fig. 6.8. For values in which $b_1/b_2 < 1$ illustrates an oblate structure, while $1 < b_1/b_2$ is a prolate micelle.

6.2.2.3 Geometrical Size and Shape of Molecules

As well as considering the size and shape of the micelles, we can also consider the size and shape of the individual molecules. The radius of gyration can also be used to quantify changes in the molecular shape. In this context, it is defined as the average squared distance of the beads making up the molecule, from its centre of mass. This is in contrast to its previous usage for categorising the shape of the whole micelle. For a single molecule:

$$R_g^2 = \frac{1}{N} \sum_{k=1}^{N} (\mathbf{r}_k - \mathbf{r}_{\text{COM}})^2 \tag{6.12}$$

181

where N is the number of particles in the molecule and r_{COM} is the centre-of-mass for the molecule: $r_{\text{COM}} = \frac{\sum_i^N m_i \mathbf{r}_i}{\sum_i^N m_i}$.

6.3   DPD Simulations

The method of DPD was introduced in Section 3.3, as a simulation technique using coarse-grained particles for modelling complex fluids. The simulation package used in this work for the DPD calculations is DL_MESO [26]. This package is selected as it has been extended for application to ionic systems, while many other available packages are currently not. DPD has been extensively applied to surfactant systems [17, 63, 97, 98, 273–277]. DPD is well suited for application to surfactant systems, as it allows for modelling systems in a way that would not be achievable using traditional MD techniques, due to the length- and time-scales involved. DPD has been shown to be able to reproduce the micellar phase behaviour [63, 98, 273, 274, 276–278], from initial configurations consisting of a random placement of beads in the simulation box.

In early DPD research, the interaction parameters chosen for the beads representing the hydrophobic and hydrophilic behaviour portions of the surfactant molecules generally did not represent any chemical species in particular (*i.e.* there was no link between the interaction parameters and specific molecules to be modelled) [97, 98, 273, 274, 276, 277]. More recently various authors have attempted to generate more specific interaction parameters to correlate to a surfactant molecule in particular [16, 17, 63], including the parameters that will be used in this study [17].

Typically DPD is most often applied to nonionic surfactant systems [97, 98, 273–278], allowing all of the forces between molecules to be modelled using short range forces. DPD is less typically applied to ionic systems [17, 63], such as the anionic surfactant used in this work, due to the complication of introducing the long-range electrostatic force. The introduction of the ionic force into the DPD method is discussed in Section 3.3.2. The introduction of the ionic force into DPD

simulations is still relatively recent, and the best method for its integration is still under consideration.

DPD has also been applied to studying the rheological behaviour of surfactant systems [273–277]. Although simulations which apply shear to measure the viscosity are typically only performed at high shear rates [273, 275, 277, 279], as the simulations suffer from a large amount of noise at decreasing shear rates [273, 279]. Using DPD, shear-thinning behaviour has often been reported for micellar systems [273, 274, 277]. Typically it is observed that micelles can change shape due to the application of shear, in particular spherical micelles can transform into stretched, worm-like micelles under heavy shear [276]. Worm-like micelles can also be broken up into small spherical micelles at high shear rates, leading to lower viscosity [273, 274]. It has been shown in DPD simulations that the application of shear force can stretch a random molecular conformation, to more extended conformations during the shear flow. The surfactant molecules can stretch in length as a result of large applications of shear force [276]. This has the result of meaning that the radius of gyration calculated can be dependent on the shear rate [280].

The purpose of the remainder of this chapter will be to study the results of DPD modelling of the micellar phase, for molecules with SLES like structure. The parameters and the treatment of the electrostatic interactions in this study will be taken from Anderson *et al.* (2018) [17], who only apply them to micellar systems where the ethoxylation value $n = 0$ (in chemical formula $CH_3(CH_2)_x(OCH_2CH_2)_nOSO_3Na$). The only computational studies that could be found investigating micellar solutions of single-component SLES surfactants were two recent studies. Panoukidou *et al.* [281] study SLES in sodium chloride/water solutions using DPD, and Peroukidis *et al.* [282] who study SLE_nS solutions with $n = 1, 2, 3$ using MD simulations. The first part of this investigation will consist of equilibrium simulations, in order to determine the phase behaviour under equilibrium conditions at room temperature. Following this there will be an investigation into whether DPD can be used to study such systems under the influence of a shear

force, as a fluid would be subject to in a rheometer, and if the viscosity can be accurately calculated using DPD for such systems.

6.3.1 Micellar Solution Study

Micellar solutions with concentrations 7%, 10% and 20% are investigated, which is expected to be completely in the micellar range, based on the experimental results shown in Chapter 4. For each concentration trialled, we also run a number of simulations investigating the effect of varying the ethoxylation n in the molecular chain length. For each concentration, four monodisperse simulations are performed (for $n = 0, 1, 2, 3$), as well as a polydisperse case (distribution of n), corresponding to the distribution of chain lengths in AES. However, as the number of molecules corresponding to the higher values of n in Table 2.1 is relatively small, only values up to $n = 3$ in AES are included. The AES distribution case has an average value of $n = 0.76$ in the simulations. The hydrocarbon chains are also simplified, in that only chains with 12 carbon atoms are included (*i.e.* the hydrocarbon chain length is monodisperse). The variation of concentration and n will allow us to understand the effect of this on parameters such as the size and shape of the micelles that form. The concentration is calculated as a percentage of mass weight. As the sodium atoms in the solution are considered to be partially hydrated with two water molecules, this is taken into consideration in the calculation of the concentration.

It has previously been discussed in Chapter 3 that DPD typically does not require the addition of a thermostat for temperature control. This is because the dissipative and random forces act in a way that naturally thermostats the system. However, typical parameter choices for dissipative parameter γ and cut-off r_C (such as the ones used in these simulations) lead to a very low value for the Schmidt number. Possible choices for additional thermostats that can be applied are discussed in Section 3.3.6. One of the draw backs to applying a thermostat in this way is that obtaining the equilibration of the surfactant phases is slower than if no thermostat was applied, reducing the benefit of performing DPD simulations

over other simulation methods. Therefore in this work traditional DPD will first be applied (*i.e.* no additional thermostat), in order to perform the initial equilibration of the surfactant phases at various concentrations. Once the equilibrium phases have been generated, we will switch to using the Stoyanov-Groot thermostat, when shear is applied and the viscosity is calculated. The exact choices of parameters required for the thermostat will be discussed in later sections. The Stoyanov-Groot thermostat is selected due to the large range of different Schmidt numbers that can be generated using this thermostat. This will allow us to investigate the effect of varying the Schmidt number on some of the parameters for the micellar phase under shear.

6.3.1.1 Simulation Set-Up

Cubic boxes are used with periodic boundary conditions in all simulations. The box size used in the following simulations is $L = 50$ in all cases. The large value of L was chosen in order to produce a large number of micelles so that a distribution of micelle sizes would be found. The simulations are initialised by populating the box with a random configuration of molecules and water beads. The number of beads in the box n is chosen to satisfy $\rho = n/L^3 = 3$ (see Section 3.3.4). The coarse graining of the molecules matches that used by Anderson *et al.* (2018) [17] in their investigation of SDS molecules, and is discussed in Section 3.3.4. The choices for the parameters a_{ij} and R_{ij}^{C} are listed in Table 3.1. The cutoff for the dissipative and random forces is assigned to be the maximum value of R_{ij}^{C} used in the system, and the dissipative friction amplitude was set at $\gamma = 4.5$. The energy of the system is governed by setting $k_{\mathrm{B}}T = 1$. The noise amplitude is automatically chosen in DL_MESO [26] in order to satisfy the relationship between noise amplitude σ and dissipative parameter γ, shown in Eq. 3.18. Finally, the time step chosen also matches that used by Anderson *et al.* (2018) [17], with a value of $\Delta t = 0.01$. Based on the work of Groot and Warren [134] a time step of this size should result in artificial temperature fluctuations of less than 1%.

In the work of Anderson *et al.* (2018) [17], the simulations are performed in boxes that contain 500 surfactant monomers. The size of the box and the number of water beads are adjusted in order to achieve the desired concentration at the correct bead density, which is simulated in the concentration range 0.06-23%. It is found by Anderson *et al.* (2018) [17] that at lower concentrations the DPD simulations result in an under prediction of the mean aggregation number N_{agg} for SDS micelles. However, the mean aggregation number grows rapidly at concentrations above about 15%, and the aggregation numbers become more like those found experimentally. For concentrations that are relatively low, this choice in box size would produce a number of micelles, *e.g.* a concentration of about 7% would produce ≈ 10 micelles on average. However, the authors report that by 23% the aggregation number reaches such a large value that on average there are only, on average, two micelles in the simulation box, which appears to result in the continuous coalescence and separation of those two micelles into one large micelle of maximum aggregation number $N = 500$. This work will primarily be concerned with solutions at large concentrations, and therefore larger box sizes of $L = 50$ are used, in order to achieve a greater number of micelles. The case in which $n = 3$ and $c = 7\%$ contains the smallest number of surfactant molecules $N_{\mathrm{s}} = 2265$, while the largest number of surfactant molecules are in the $n = 0$, $c = 20\%$ case where $N_{\mathrm{s}} = 9609$ (full details on the number of surfactant molecules for each simulation case can be found in Appendix C). This will have the draw back of being more computationally expensive, but does mean that a distribution of micelle sizes can be calculated, as well as assessing whether there is any underlying structure in the location and separation of the micelles (*e.g.* micellar cubic phases). Furthermore, the very large aggregation numbers that are found by Anderson *et al.* (2018) [17] at high concentrations are much higher than what is found by equivalent concentrations experimentally [22], and the relatively small box sizes may be one of the causes.

6.3.1.2 Equilibration

Once a micellar simulation is begun from a random configuration of molecules, the formation of the initial micelles is rapid. However, the subsequent increase in the micellar size, and therefore mean aggregation number N_{agg} equilibration takes a considerable amount of time. In order to determine that the micellar solution is fully equilibrated, it is typical to monitor the value of the mean aggregation number of the system N_{agg}, and to state that equilibration has taken place once no further change in N_{agg} is observed, over a defined time period. Anderson *et al.* (2018) [17] perform their simulation in boxes containing 500 surfactant monomers. Equilibrium in N_{agg} is defined as the point at which block averages, where a block is 5000 DPD time units (or 5×10^5 time steps), of the number of micelles fluctuate about a constant value. However, the exact length of time that a system maintains constant N_{agg} before it is considered equilibrated is relatively arbitrary and difficult to define. For example, the plot of N_{agg} over time, for a 7% solution in which $n = 3$, is shown in Fig. 6.9. This simulation contains 2265 surfactant molecules and 350085 water beads. The initial growth in N_{agg} is rapid, with $N_{\mathrm{agg}} = 30.6$ achieved after only 3.5×10^4 time units. However, subsequent growth is very slow. There is also a period in the time range 1.5–2.1×10^5 in which the aggregation number maintains an almost constant value of $N_{\mathrm{agg}} = 35.4$, before jumping to a higher value after increased time. Based on the previously discussed equilibration criteria, one might have assumed that the simulation was fully equilibrated. Therefore in this work each simulation is run for as long as is realistically possible with the computational resources that are available. An example of the final micelles obtained for a 20% case is shown in Fig. 6.10. The majority of the simulations presented in this section are conducted on the HPC system for the University of Leeds [283]. The simulation shown in Fig. 6.9 is performed on 27 processors (splitting the domain into equal cubic boxes of size $3 \times 3 \times 3$). The results are obtained by performing approximately 2.5×10^7 iterations, which requires approximately 52,000 CPU hours. The ARC (Advanced

Research Computing) HPC service at Leeds places a time limit on submitted jobs of 48 hours. While the total running time of the simulation amounts to approximately 3 months, taking into queuing time for frequent re-submissions, this amounted to the calculation taking, in practice, around 7 months. The number of iterations/hour could, in theory, be sped up by, for example, increasing the number of processors or executing the calculations on entire nodes (as opposed to splitting across multiple nodes which slows the simulation due to extra communication time between processors). However both of these options increase the amount of queue waiting time by such an amount that they are no longer beneficial. Note that calculations on other systems in this work were later able to make use of a more efficient, Tier 2 service. These will be discussed in later chapters.

The computational cost per iteration is dominated by the long range electrostatic interactions. The method used to calculate the electrostatic forces is Smooth Particle Mesh Ewald, which scales with the number of beads b_{N} in the simulation as $\propto b_{\mathrm{N}} \log b_{\mathrm{N}}$ (note that the number of beads grows as $b_{\mathrm{N}} \propto L^3$). This approximate scaling, for a simulation case with $n = 1$ and concentration of 7%, is shown in Fig. 6.11. It was decided that $L = 50$ was the largest feasible box size that could be run in the time frame with this scaling. Based on the scaling $\propto b_{\mathrm{N}} \log b_{\mathrm{N}}$, larger box size of $L = 60$ would take approximately 1.8 times longer to run than a $L = 50$, for the same number of iterations.

While monitoring the mean aggregation number N_{agg} is one of the most common methods of determining equilibration [17, 281, 282, 284], other authors have taken different approaches. A variety of parameters can be monitored as a function of simulation time in order to determine that adequate equilibration has occurred. Some have determined that equilibrium has been achieved by the more simple approach of simply monitoring the number of micelles [285], as opposed to their average size. Other, even more simple, approaches include requiring a minimum simulation time before data sampling begins [75] (although this is more common in simulations with an element of pre-assembly), while others have taken more com-
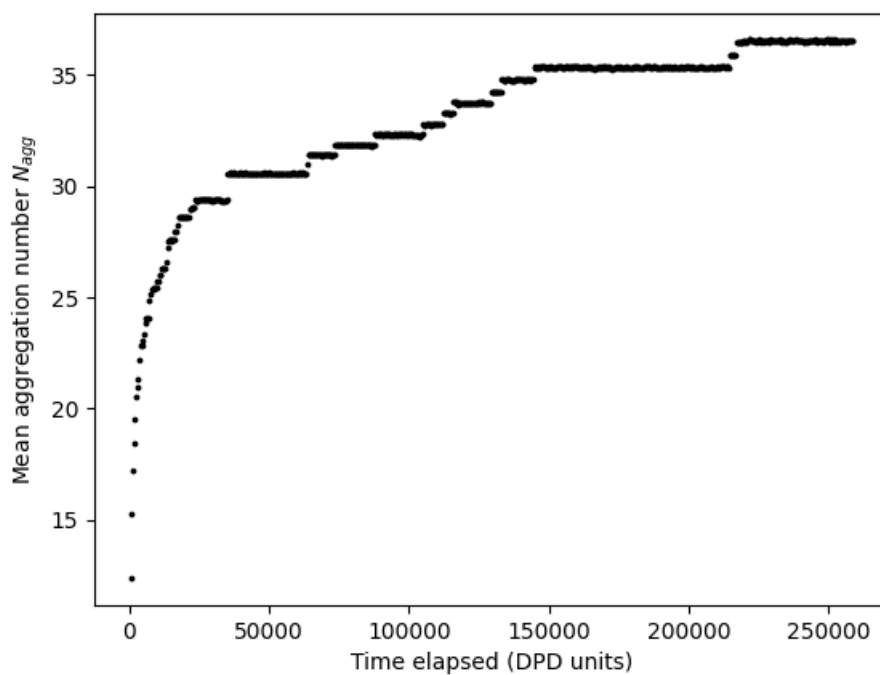
Figure 6.9: Equilibration of N_{agg} for a 7% solution containing molecules with $n = 3$. Simulation performed on a cubic box with size $L = 50$, containing 2265 surfactant molecules and 350085 water beads.
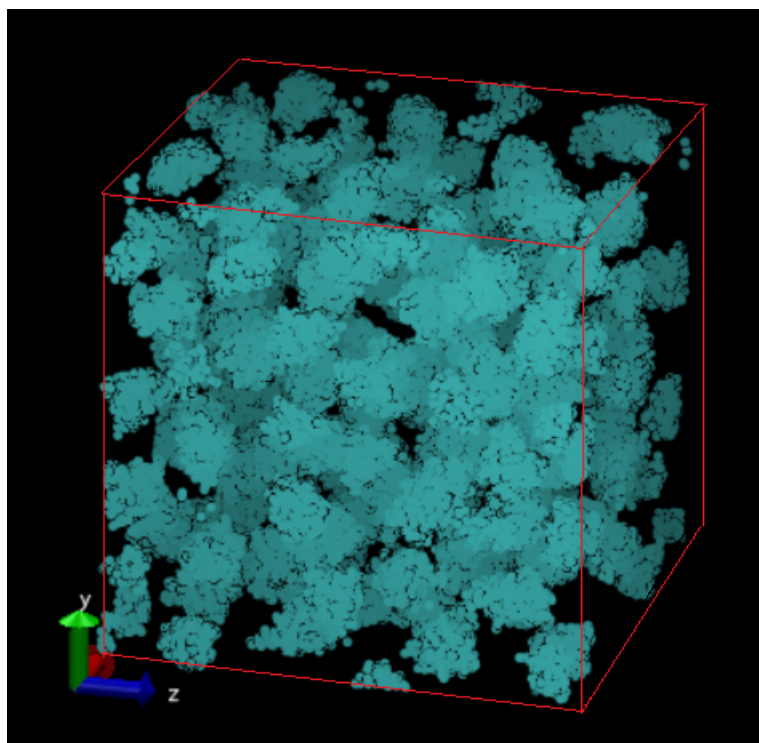
Figure 6.10: Equilibrated DPD simulation box containing a 20% solution of SDS ($n = 0$).

189
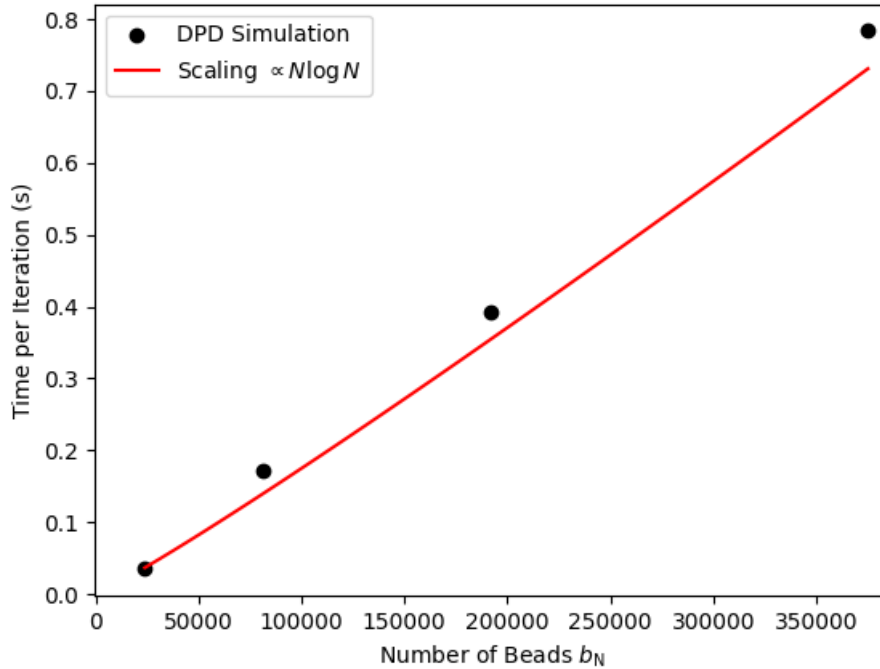
Figure 6.11: The scaling of DPD simulations with electrostatic interactions in DL_MESO. The electrostatic interactions dominate the computational cost per iteration, scaling as approximately $b_N \log b_N$ where b_N is the number of beads in the system. Scaling was calculated by performing simulations on 8 processors.

plex approaches. For example Faramarzi $et\ al.$ [74] observe that there is a sharp change in the micellar radius of gyration once equilibration has been achieved, potentially making this a variable of interest. It is interesting to note that even in simulations of pre-assembled micelles, it has been reported that a significant amount of simulation time is required to achieve equilibration in parameters such as the radius of gyration [73]. Johnston $et\ al.$ [284] also trial calculating various observables in order to monitor the approach to equilibrium. One metric that the authors determine to be satisfactory, is the monitoring of the number of surfactant molecules in sub-micellar clusters ($i.e.$ molecules that are either free monomers or are in clusters not large enough to yet be considered micelles). However, the authors also make the observation that no protocol can be expected to work for all molecules and force fields that might be studied, and therefore a better equilibration method might be through monitoring a combination of observables. In this work we deemed that monitoring the mean aggregation number was sufficient for our purposes, since it is predicted from previous authors work [17] that the
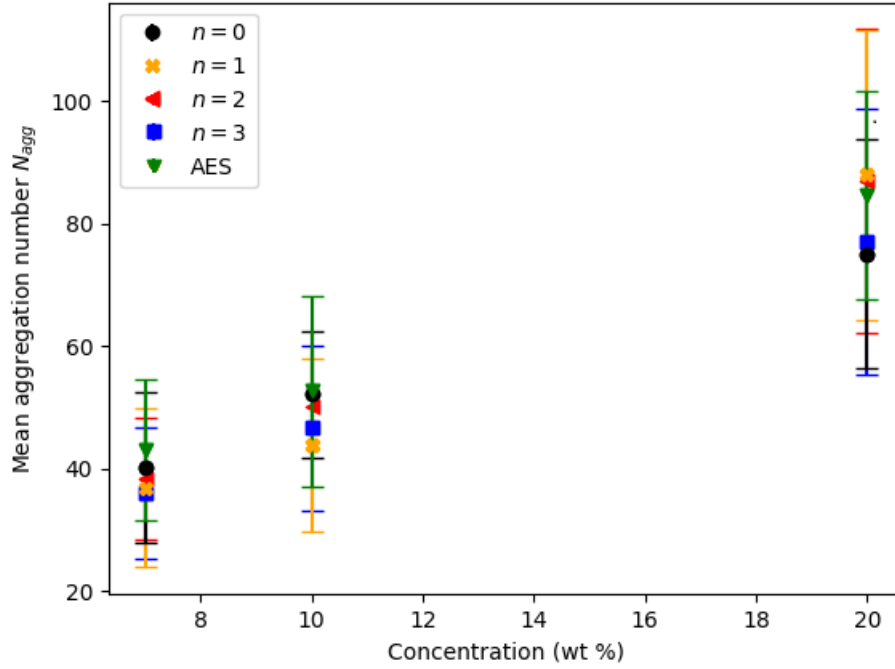
Figure 6.12: Mean aggregation number N_{agg} against solution concentration. Plot shows the results for varying degrees of ethoxylation value n, as well as the results for a case with a distribution of n, which represents AES. Error bars represent the standard deviation over the sampling period.

micelles will most likely not achieve experimental aggregation numbers for any of the simulation cases.

6.3.1.3 Aggregation Number

The mean aggregation number N_{agg} for each simulation case is calculated using the method discussed in Section 6.2.2.2. The effect of varying the concentration and ethoxylation n on the value found is shown in Fig. 6.12, and the increase in aggregation number N_{agg} is approximately linear with increasing concentration. The strongest dependence on the final calculated value is found to be with concentration, as opposed to variation in n. The variation in the values of N_{agg} for different values of n, but similar concentrations, are likely to be due to varying levels of equilibration or random fluctuations, as opposed to having physical meaning.

The weighted aggregation number N_{W} is also calculated for each case, the definition of which is also described in Section 6.2.2.2, and reported in Table 6.6. This quantity is commonly used to report the final aggregation number of micellar

	$c = 7\%$	$c = 10\%$	$c = 20\%$
$n = 0$	$N_{\text{agg}} = 40 \pm 12$ $N_{\text{W}} = 44 \pm 15$ $N_{\text{agg}}/N_{\text{W}} = 1.09$	$N_{\text{agg}} = 52 \pm 10$ $N_{\text{W}} = 54 \pm 11$ $N_{\text{agg}}/N_{\text{W}} = 1.04$	$N_{\text{agg}} = 75 \pm 19$ $N_{\text{W}} = 80 \pm 28$ $N_{\text{agg}}/N_{\text{W}} = 1.06$
$n = 1$	$N_{\text{agg}} = 37 \pm 13$ $N_{\text{W}} = 41 \pm 21$ $N_{\text{agg}}/N_{\text{W}} = 1.12$	$N_{\text{agg}} = 44 \pm 14$ $N_{\text{W}} = 48 \pm 18$ $N_{\text{agg}}/N_{\text{W}} = 1.10$	$N_{\text{agg}} = 88 \pm 24$ $N_{\text{W}} = 94 \pm 33$ $N_{\text{agg}}/N_{\text{W}} = 1.07$
$n = 2$	$N_{\text{agg}} = 38 \pm 10$ $N_{\text{W}} = 41 \pm 12$ $N_{\text{agg}}/N_{\text{W}}=1.07$	$N_{\text{agg}} = 50 \pm 10$ $N_{\text{W}} = 52 \pm 12$ $N_{\text{agg}}/N_{\text{W}} = 1.07$	$N_{\text{agg}} = 87 \pm 25$ $N_{\text{W}} = 94 \pm 28$ $N_{\text{agg}}/N_{\text{W}}=1.08$
$n = 3$	$N_{\text{agg}} = 36 \pm 11$ $N_{\text{W}} = 39 \pm 13$ $N_{\text{agg}}/N_{\text{W}} = 1.09$	$N_{\text{agg}} = 47 \pm 13$ $N_{\text{W}} = 51 \pm 16$ $N_{\text{agg}}/N_{\text{W}} = 1.08$	$N_{\text{agg}} = 77 \pm 22$ $N_{\text{W}} = 83 \pm 28$ $N_{\text{agg}}/N_{\text{W}} = 1.08$
AES	$N_{\text{agg}} = 43 \pm 12$ $N_{\text{W}} = 46 \pm 12$ $N_{\text{agg}}/N_{\text{W}} = 1.07$	$N_{\text{agg}} = 53 \pm 15$ $N_{\text{W}} = 57 \pm 19$ $N_{\text{agg}}/N_{\text{W}} = 1.09$	$N_{\text{agg}} = 85 \pm 17$ $N_{\text{W}} = 88 \pm 20$ $N_{\text{agg}}/N_{\text{W}} = 1.04$

Table 6.6: Values for the mean aggregation number N_{agg} and weighted aggregation number N_{W} for varying micellar solutions.

systems in literature [17], since it is more commonly reported than the number average from experiments. The weighted aggregation number is in all cases larger than the standard mean aggregation number N_{agg}, as a result of the polydispersity of the micelle sizes.

The value of $N_{\text{W}} = 44$, obtained for the weighted aggregation number for SDS ($n = 0$) solutions at 7% concentration, is in agreement with that obtained by Anderson *et al.* (2018) [17], although not in agreement with what is reported experimentally [21, 22]. Therefore there is a significant under-prediction of the aggregation number, where it is approximately half of that found experimentally. However, the aggregation number of the micelles grows rapidly with increasing concentration in the DPD simulations, at a rate which is not seen experimentally. This means that at a concentration of 20% the under prediction in DPD when compared with experiment is much less severe. Experimentally, the mean aggregation number at this concentration is reported as $N_{\text{agg}} = 104$ [20, 22]. In this work a 20% SDS solution is predicted to have a mean aggregation number of $N_{\text{agg}} = 80$. Resulting in an an aggregation number that is 77% of that determined experimentally. Contrastingly, in the work of Anderson *et al.* (2018) [17], the aggregation

number for an equivalent system is $N = 134$, which is a significant over-prediction. However, in this work the system is made up of, on average, 128 micelles, while in Anderson *et al.* (2018) [17] the system is made up of just 3–4 micelles.

The over-prediction in their work could be a result of the small number of micelles in the system. The narrowing of the gap between the DPD results in this work and those found experimentally, once we reach higher concentrations, could suggests that the simulation factor causing the under-prediction becomes less important at higher concentration, or that if the under-prediction is a result of poor equilibration, this becomes less relevant at high concentrations. It could be the case that at low concentrations the micelles are further apart, and due to the strong inter-micellar repulsions, they struggle to reach close enough to coalesce into larger micelles.

The average separation of the micelles can be calculated for each simulation case. The system is characterised by the radial distribution function $g(r)$ which describes how the density varies as a function of distance from an individual micelle. This function is calculated by calculating a distance from the centre of mass of a micelle to other micelles in the simulation box. This function is normalised to the mean density of the system. The first peak in $g(r)$ represents the nearest neighbour distance. As the distance from the reference particle increases, the oscillations in $g(r)$ dampen, and it approaches a value of 1 (*i.e.* approaches average density). A figure showing this is presented in Fig. 6.13. The location if the first peak for varying concentration and n is shown in Table 6.7. The average separation generally decreases with increasing concentration and increases with increasing n. Interestingly, the average distance between micelles correlates much more closely with varying n, than the mean aggregation number does. As n increases, there are fewer surfactant molecules in a solution with equivalent weight concentration. This means that as the aggregation number stays approximately constant with n, fewer micelles are formed, and therefore their average spacing increases. Experimentally, for SDS micelles at 20% concentration at room temperature, this separation is de-
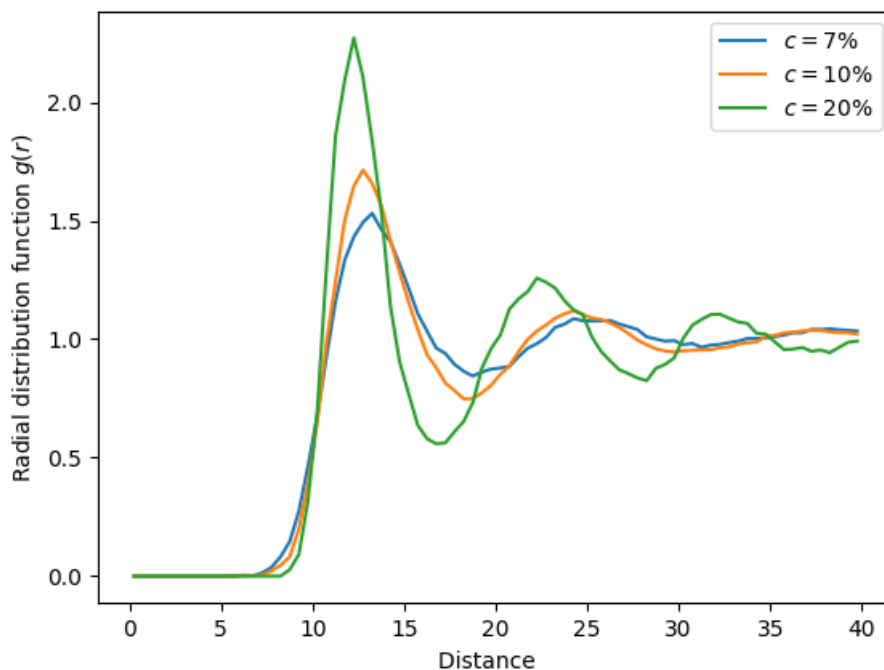
Figure 6.13: Radial distribution function for increasing concentration. Distance in DPD units. Results shown for case in which $n = 3$.

		Concentration c (%)		
		$c = 7$	$c = 10$	$c = 20$
	$n = 0$	11.75	11.25	10.25
	$n = 1$	11.75	11.25	11.25
Ethoxylation n	$n = 2$	12.75	12.25	12.25
	$n = 3$	13.25	12.75	12.25
	AES	12.25	11.75	11.25

Table 6.7: Average micelle separation for different values of n, with values given in DPD units. Note that all values have an uncertainty of ± 0.25, which is calculated as the width of the bins in Fig. 6.13.

termined to be 5.7nm [266]. In DPD the value found, converted into real units (see section 3.3.3 for this conversion), is 5.8 ± 0.1nm, which is in good agreement, despite the smaller aggregation number. However, for the 20% concentration case the mean aggregation number is less severely under-predicted than in the lower concentration cases. In these cases the inter-micellar spacing might have greater divergence from the experimentally measured value, however the experimental results for lower concentrations are more difficult to interpret [266].

For the AES case with a distribution of n, an investigation is performed into the how different length molecules are distributed across the micelles. It might be expected that molecules which are similar in length prefer to form micelles together, resulting in a larger spread of micelle sizes compared to polydisperse cases. However, this is not found. The micelles generally contain a fraction of each molecule type, which is consistent with their overall abundance in the solution.

6.3.1.4 Radius of Gyration of Micelles

In order to investigate the relationship between the aggregation number N of an individual micelle and size of that micelle, Fig. 6.14 shows the radius of gyration R_{G} plotted against N for a variety of simulation cases. There is a clear increase in the value of R_{G} with increasing N for all cases of n. There is also very little dependence of R_{G} on concentration, for a given aggregation number N. The largest observable difference in the results from different concentration solutions, is that the maximum aggregation number achieved shifts to higher values, at increasing concentration.

Since there is very little difference in the relationship between R_{G} and N for different concentrations c, the results for each case of c can be combined in order to compare the effect of varying n. Therefore a comparison of the different values of R_{G} obtained from varying the number of ethoxy groups n in the molecule, is shown in Fig. 6.15. Larger values of R_{G} are found for increasing n, owing to the increase in the molecular length and therefore increasing micelle size. As the aggregation

(a) $n = 0$

(b) $n = 1$

(c) $n = 2$

(d) $n = 3$

(e) $n = AES$
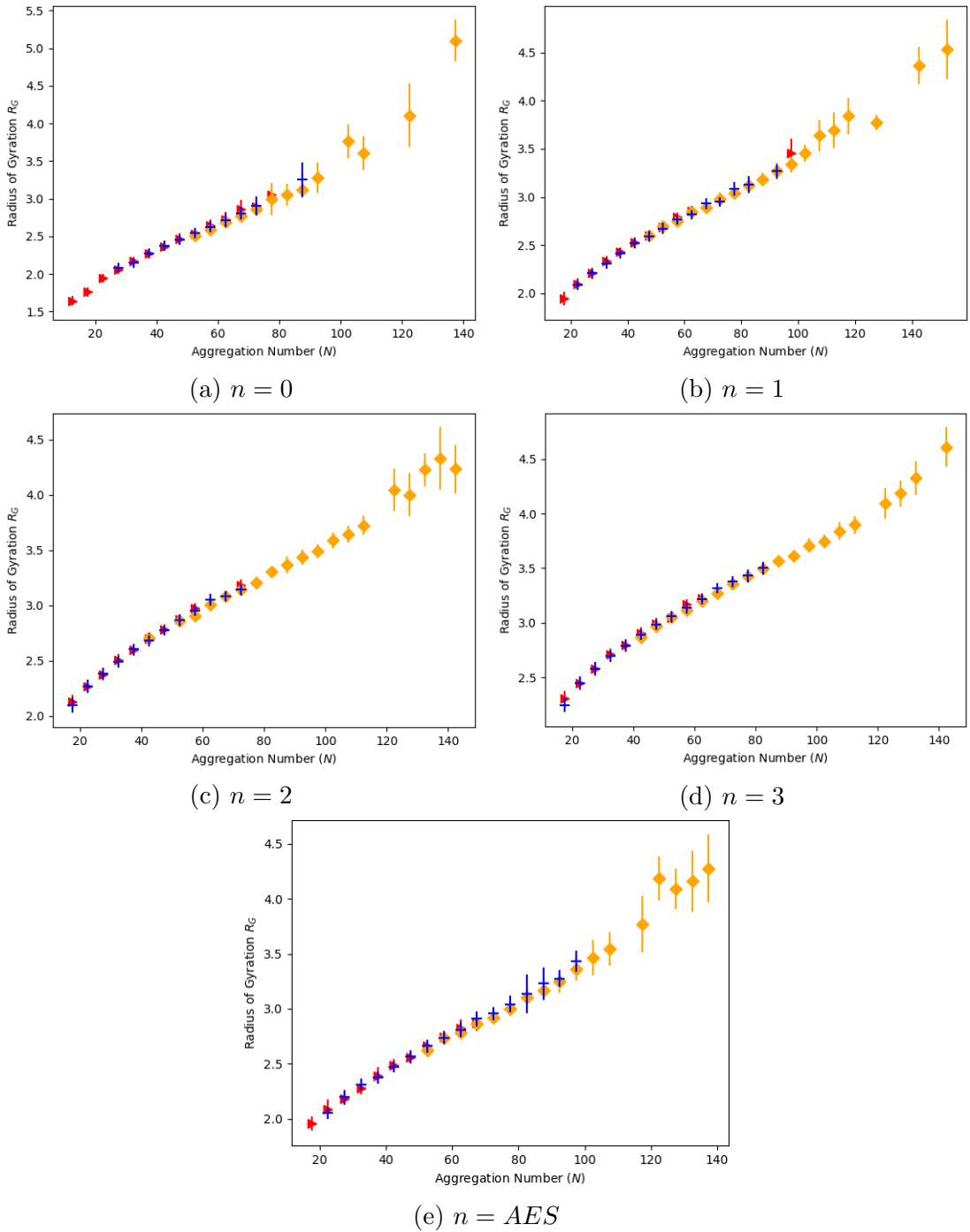
Figure 6.14: R_G plotted against N for a variety of choices of ethoxylation values n. For each case of n the results from 3 different simulations of varying concentration are plotted: 7% (red), 10% (blue), and 20% (orange). The simulations reach higher aggregation numbers as the concentration of the simulation increases. The aggregation number N is binned into bins of size 5 and error bars represent the standard deviation.
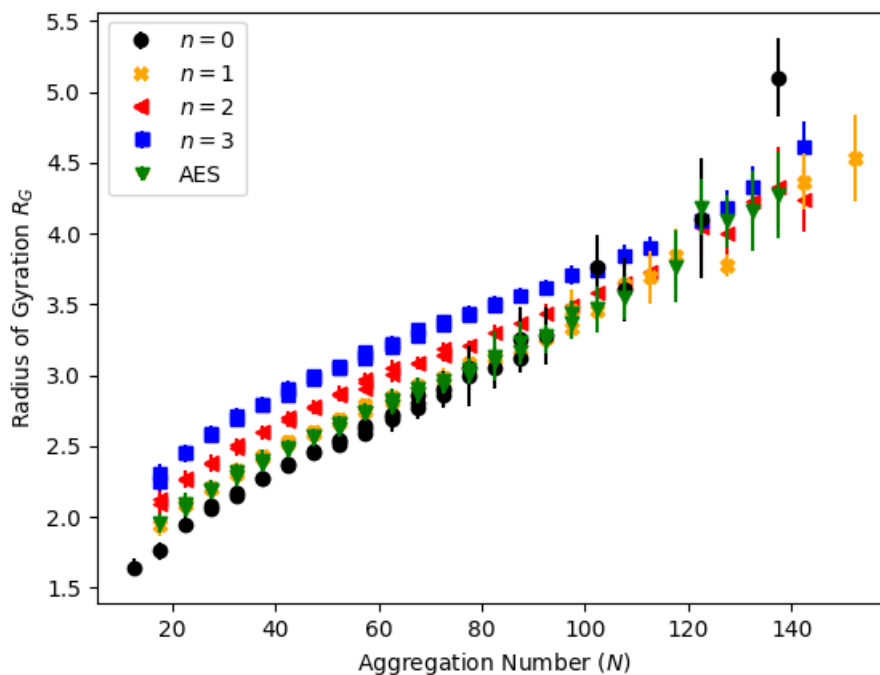
Figure 6.15: R_{G} against aggregation number N for a variety of solutions with varying ethoxylation n values. In this figure the results from all three concentrations simulated (7, 10 and 20%) are combined. The aggregation number N is binned into bins of size 5 and error bars represent the standard deviation.

number increases, the radius of gyration grows at a faster rate for molecules with smaller values of n, as opposed to longer molecules with larger n. This could be suggesting that micelles formed from molecules with lower n become asymmetric more rapidly, with increasing aggregation number.

In order to investigate the effect of varying N on the shape of a micelle, Fig. 6.16 shows the relationship between R_{G}^3/N and N for all simulation cases. For spherical micelles the value of R_{G}^3/N should be independent of N, however it is illustrated in Fig. 6.8 that for non-spherical micelles this relationship can deviate. In all simulation cases Fig. 6.16 shows that there is a range in N for which $R_{\mathrm{G}}^3 \propto N$ holds, and the plot of R_{G}^3/N against N produces an horizontal line with zero gradient. However, at very low and high values of N the relationship deviates, suggesting a non spherical nature. For most cases, the actual size of the range where the relationship holds is quite narrow, and the transition from oblate to prolate occurs quite rapidly.

Once again, note that there is only a very slight difference between the different

concentration solutions. If it is assumed that the micelles take a spheriod shape, then Fig. 6.8 shows that the deviations in R_{G}^3/N that can result from the micelle taking an oblate or prolate shape. It is likely that the deviations at low aggregation numbers N are as a result of prolate shape, while deviations at high aggregation numbers are observed to be from increasingly oblate shape. In this analysis we assume that transition to rod-like structures has not yet taken place, however at higher concentration solutions above 20%, this assumption no longer becomes applicable. The phase behaviour of concentrations above 20% will be discussed in more detail in the following chapter.

Once again, the results from varying concentrations can be pooled for the ratio R_{G}^3/N, as there is not much deviation with changing concentration. Fig. 6.17 compares the relationship between R_{G}^3/N and N, for varying n values. It is clear that the range of aggregation numbers over which the micelles take a spherical shape varies with n. A value for the the middle of this range can be found, by averaging over the values of N where the plot of R_{G}^3/N *vs.* N has zero gradient. Similarly, the value of R_{G} at this value of N is also calculated. This means we can plot the increase in the size of spherical micelles, as a result of varying n. This is shown in Fig. 6.18. The plot shows the relationship with both parameters increases linearly with n. The linear relationship between R_{G} and n means that the micelles are growing proportionally to the increase in the surfactant molecule's length. Also plotted are the values for micelles containing a distribution of n (representing AES), which take the values $N_{\mathrm{agg}} = 53.4$ and $R_{\mathrm{G}} = 0.365$. The values of R_{G} and aggregation number calculated for AES solutions (with an average value of $n = 0.76$) fit in reasonably well with the trends calculated from the monodisperse cases. There is a slight indication that the properties of mixtures of surfactants of varying n, cannot simply be calculated from interpolation of pure component cases, since the values at 0.76 are slightly lower than expected. However this looks to be a relatively subtle effect.

In the region of low aggregation number (*i.e.* at values of N below the plateau),

(a) $n = 0$

(b) $n = 1$

(c) $n = 2$

(d) $n = 3$

(e) $n = AES$
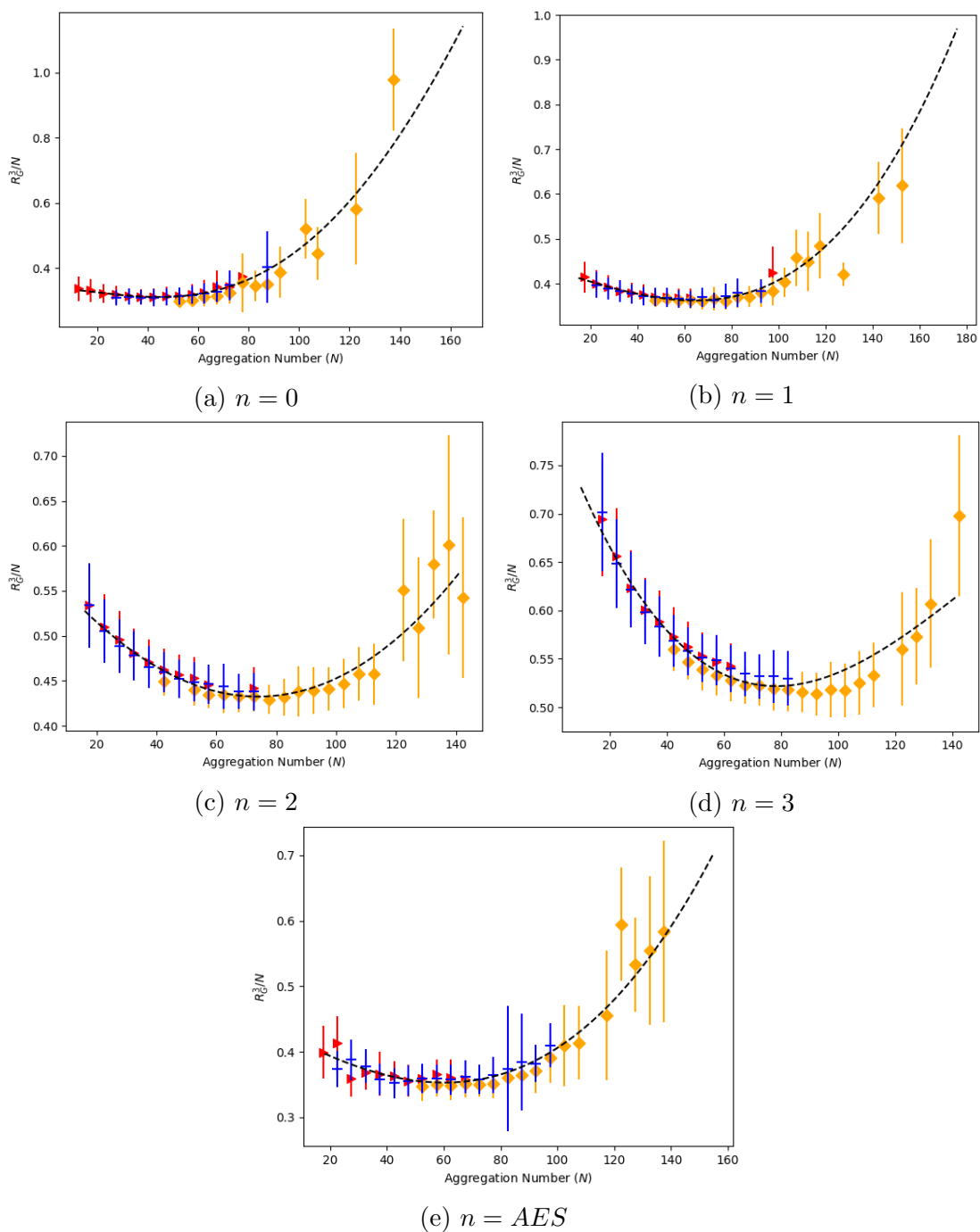
Figure 6.16: R_{G}^3/N plotted against N for a variety of choices of ethoxylation values n. For each case of n the results from 3 different simulations of varying concentration are plotted: 7% (red), 10% (blue), and 20% (orange). The simulations reach higher aggregation numbers as the concentration of the simulation increases. The aggregation number N is binned into bins of size 5 and error bars represent the standard deviation. Fits are intended to be a guide to the eye, and are performed using a fit to a polynomial function of degree 3, using a least squares method in Python.
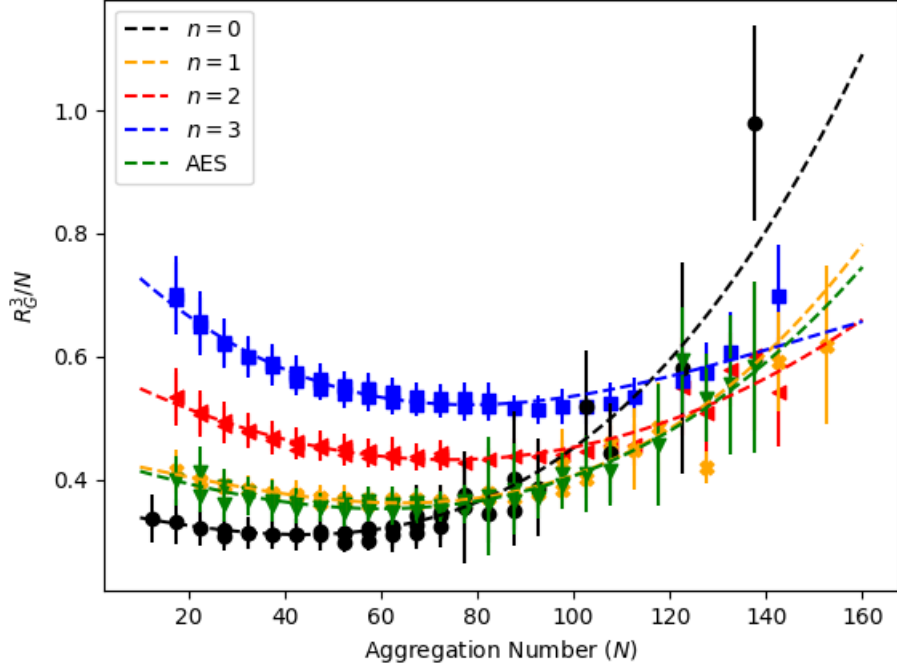
Figure 6.17: R_{G}^3/N against aggregation number N for a variety of solutions with varying ethoxylation n values. In this figure the results from all three concentrations simulated (7, 10 and 20%) are combined. The aggregation number N is binned into bins of size 5 and error bars represent the standard deviation.

the deviation from spherical shape is more pronounced with increasing n. For example, for systems described by $n = 3$, the value of R_{G}^3/N at $N = 17$ is $\approx 36\%$ larger than the value of R_{G}^3/N in the middle of the plateau (*i.e.* the region that describes spherical micelles at $N \approx 95$). Whereas for systems in which $n = 0$, the increase in R_{G}^3/N for spherical micelles (identified at $N \approx 40$), to micelles at aggregation number $N = 17$, is only $\approx 7\%$. If the higher aggregation region of Fig. 6.17 is considered, the opposite behaviour is true. The tendency of the micelles formed with smaller values of n to become non-spherical more easily is consistent with other computational studies [281, 282].

Although the DPD simulations under-predict the value for the mean aggregation number, the shape of the micelles for a given aggregation number are reasonably consistent with experiment. For example, at an aggregation number of $N = 83$, the value of R_{G}^3/N for SDS is estimated to be $R_{\mathrm{G}}^3/N \approx 0.364$, while when the micelles are spherical, the ratio is found as $R_{\mathrm{G}}^3/N = 0.312$ resulting in a ratio of the two values $0.364/0.312 \approx 1.17$. Experimentally at $N_{\mathrm{agg}} = 83$, the ratio of the
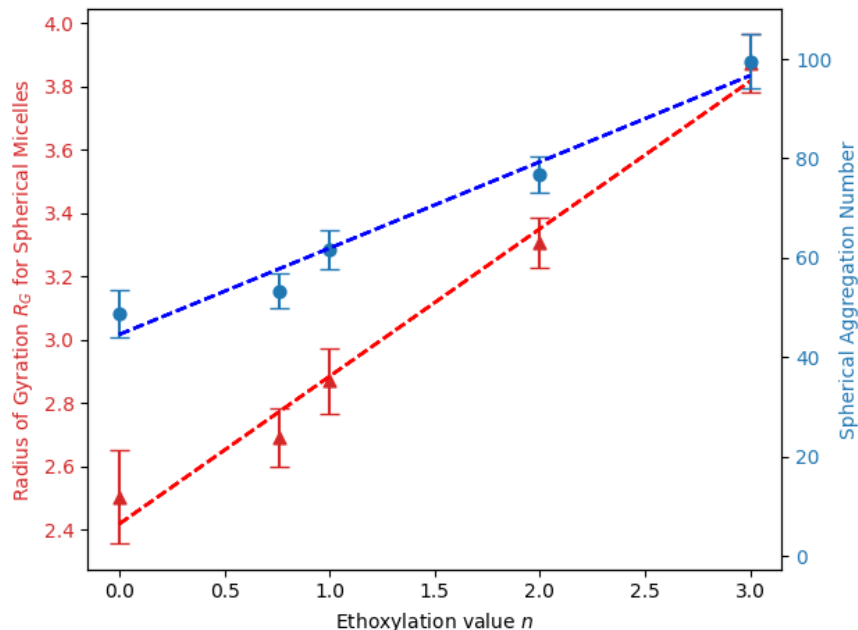
Figure 6.18: The radius of gyration R_G (DPD units) and mean aggregation number is calculated for micelles which are deemed to be approximately spherical, based on the value of R_G^3/N. Plotted is the variation of these two quantities with varying chain length n. Error bars shown represent the standard deviation. Also plotted is the value calculated for AES, which has an average value of $n = 0.76$.

axis in the prolate shape are reported to be $b_1/b_2 = 1.49$ [21]. Based off the figure shown in Fig. 6.8, this should result in a ratio of R_G^3/N to be 1.13, comparing well with what is found in DPD. The fit to the relationship between R_G^3/N *vs.* N for SDS micelles gets more uncertain as the aggregation number increases, due to fewer micelles forming at high values of N.

6.3.1.5 Radius of Gyration of Molecules

In this section we turn our attention to the size and shape of the individual molecules that form the micelles. As well as calculating the radius of gyration R_G for a micelle, made up of many molecules, the radius of gyration can be calculated for each constituent molecule R_g in that micelle, using Eq. 6.12. This means that the variation of R_g with aggregation number N can be found, in order to investigate the effect that increasing micelle size has on the size of the molecules forming that micelle.

The value of R_g will increase with increasing ethoxylation n, just from the fact
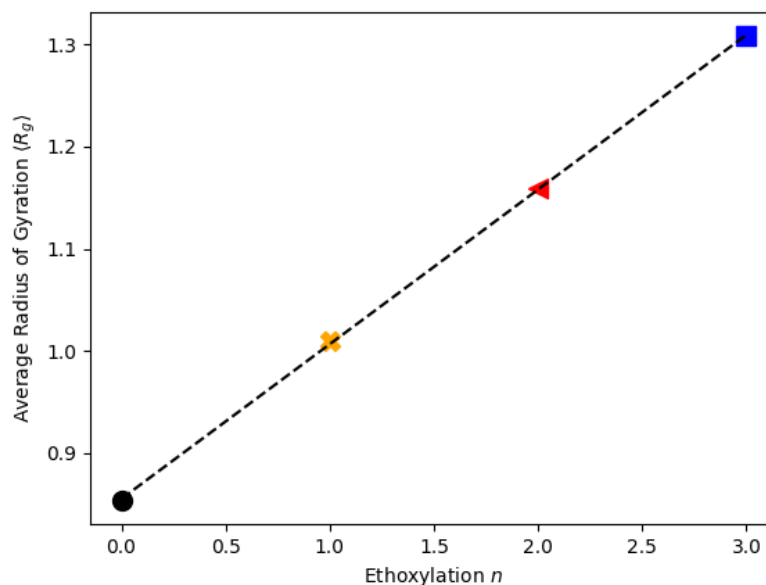
Figure 6.19: Average radius of gyration of molecules R_g of different length n. The value of R_g for a given n is obtained by averaging across simulations conducted at concentrations $c = 7, 10, 20\%$. The error bars, calculated at the standard deviation, are smaller than the symbol sizes.

that the addition of the ethoxylation bead (OCH_2CH_2) increases the length of the molecule. The average value of R_g, for a given value of n (averaged across different concentrations), is shown in Fig. 6.19. The average value of R_g increases linearly, as expected due to the additional ethoxylation bead.

Plots of the radius of gyration R_g against aggregation number, for a variety of simulation cases, is shown in Fig. 6.20. It is shown that the radius of gyration R_g increases with increasing aggregation number N, before plateauing at a maximum value. However the radius of gyration only changes by a very small fraction, such that the error bars would obscure the plot. Therefore, it is difficult to definitively confirm that there is a trend.

6.3.1.6 Conclusion

In this section the equilibrium behaviour of micellar solutions of varying concentration c and varying ethoxylation n have been investigated. The mean aggregation numbers are generally an under-prediction of those found experimentally, although there is an increase in N_{agg} with increasing concentration, as expected. No sta-
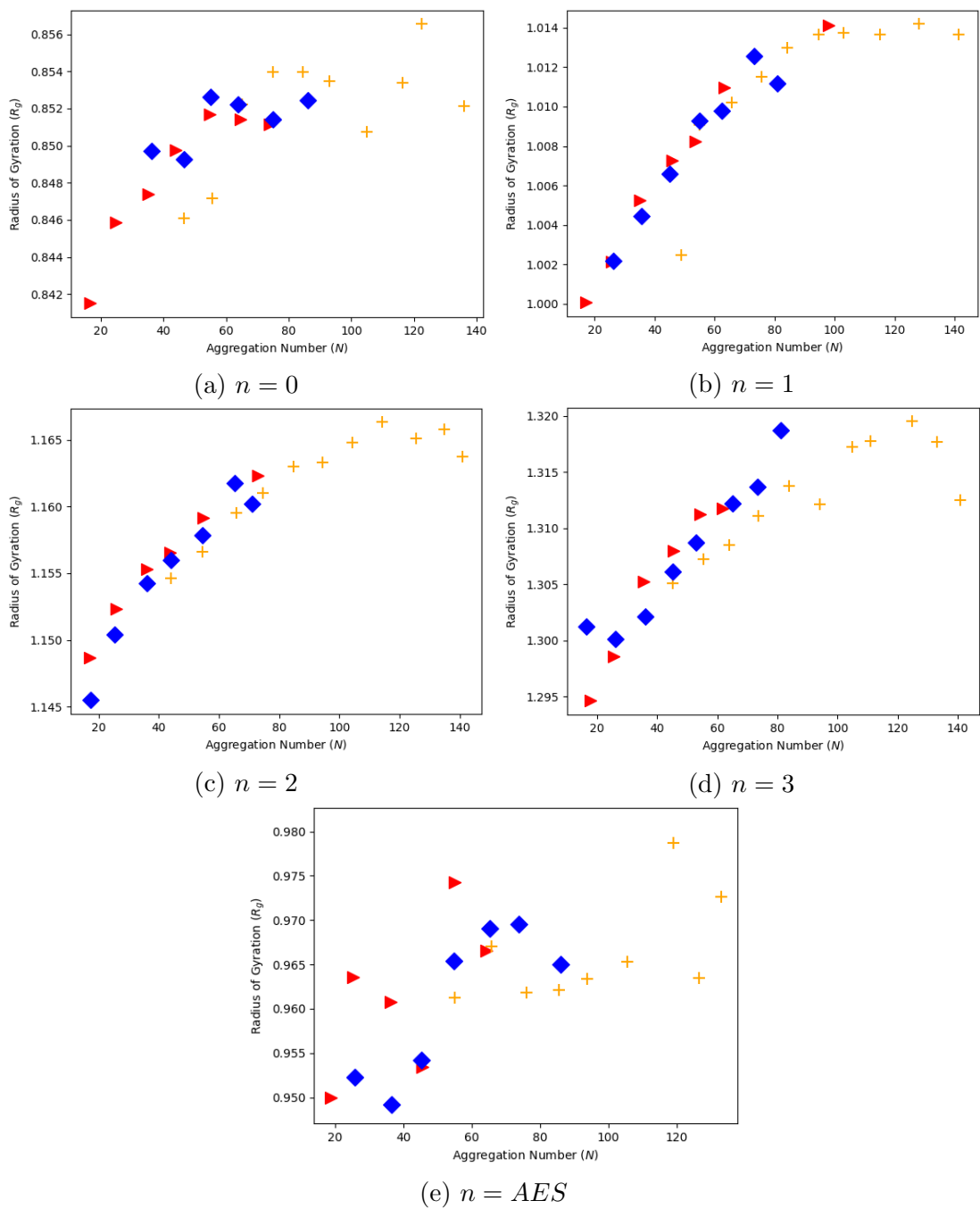
Figure 6.20: R_g plotted against N for a variety of choices of ethoxylation values n. For each case of n the results from 3 different simulations of varying concentration are plotted: 7% (red), 10% (blue), and 20% (orange). The aggregation number N is binned into bins of size 10. Note that the error bars are not plotted, as the standard deviation of each bin is so large that it obscures the plot when included.

tistical difference is found in the mean aggregation numbers for different n at any value of the concentration, although some dependence on n was expected from experimental observations [286].

The under-prediction of the aggregation number is likely to be due to the treatment of the electrostatic interaction, which was also discussed by Anderson *et al.* [17]. These authors suggest that one potential problem with the electrostatic treatment is the assumption of a uniform dielectric permittivity in the simulations. We notice that the disparity between experimental results and simulated results decreases with increasing concentration. It is thought that the long range effect of the electrostatic interaction becomes outweighed by the importance of the short range interactions as the concentration increases. In the following section chapter we will investigate the effect of increasing concentration into the lyotropic regimes, so will see if mistreatment of the electrostatic interaction becomes unimportant as the concentration increases. Of course fully understanding the reason behind the under prediction of the aggregation number requires further research. In particular, the effect that 'smearing' the charge, as opposed to treating the beads as point charges, should be fully investigated. Further to this, a later chapter in this thesis (Chapter 8) uses molecular dynamics to investigate SDS micelles. It will be shown in this chapter that quantum mechanical calculations determine that the charge distribution on an SDS molecule is more complex than how it has been approximated in the DPD simulations. In this DPD work, the charge has all been confined to the first bead in the chain ($CH_2OSO_3^{-1}$), whereas in reality there is a distribution of charge across the entire molecule. It would be a worthwhile area of research to assess how much of an effect this simplification has on the final results.

The size of the micelles as a function of their aggregation number N was quantified using the radius of gyration R_G, and the shape could then be quantified by the ratio R_G^3/N. It was concluded that the aggregation number N at which spherical micelles form, varied with n. The aggregation number at which the transition from spherical micelles to prolate micelles shifts to higher values as the number of

ethoxy groups in the surfactant chain increases. The ability to accurately quantify the shape of the micelles in a DPD simulation is incredibly useful, given the difficulty obtaining similar results from experiments. The ambiguity across different experimental methods and results from different researchers was highlighted in Section 6.2.

The remainder of this chapter will now study the different methods which can be used to calculate the viscosity of the systems described. Also covered will be how the systems behave when subject to a shear force, and the effect this has on the micelles.

6.4 DPD Simulations for Micellar Solutions Under Shear and Viscosity

In the equilibrium simulations discussed thus far, the traditional thermostat has been used. However, Section 3.3.6 discussed how the traditional thermostat for DPD does not generate a very realistic viscosity (or diffusion coefficient) for fluids. This can be rectified by applying an additional thermostat. At the beginning of this chapter, it was stated that for the viscosity calculations, it is chosen to switch to using the Stoyanov-Groot thermostat. In first applying the traditional DPD and then switching to thermostated DPD later on, we get the benefit of the rapid equilibration from traditional DPD, but also generate more realistic Schmidt numbers for studying the rheological behaviour. The effect of different Schmidt numbers can be investigated for micellar solutions subject to shear. Therefore, the first part of this section will be dedicated to investigating how the Stoyanov-Groot thermostat behaves, when applied to a simple simulation case consisting of purely water beads. Following this we will move onto using DPD methods in order to apply shear to the micellar systems, and also calculate the viscosity.

6.4.1 Thermostating and Parameter Choices

A variety of initial simulations were performed on simulation boxes containing only water beads, in order to investigate the effect of varying certain parameters including: collision frequency Γ (as described in Section 3.3.6), time step Δt, box size L and shear rate $\dot{\gamma}$. The primary aim of this section is to investigate the effect of varying these parameters on the viscosity and diffusion coefficient of the simulation (and therefore the effect on the Schmidt number). As water is expected to be Newtonian, the calculated viscosity should be independent of the applied shear rate. The viscosity can be calculated using two different methods. The first is by using auto-correlation functions, as is described by Eq. 3.39. This is an equilibrium method in which no shear is applied, and is only applicable because we already assume that the fluid will have Newtonian behaviour. The second method relies on the application of shear, and the viscosity is calculated using the off-diagonal stress tensors described by Eq. 3.40. Using this second method we can apply varying shear rate to confirm Newtonian behaviour, and compare with the viscosity calculated via the auto-correlation method. The diffusion coefficient can be calculated by two different methods, however they both only require an equilibrium simulation. The diffusion coefficient can be calculated using correlation functions described in Eq. 3.45, alternatively it can also be calculated using the mean squared displacement, as shown in Eq. 3.44. We will calculate the diffusion coefficient D via both methods in order to compare and verify that both methods are consistent. In summary, this section aims to answer the following questions:

- Does calculating the diffusion coefficient via the mean squared displacement and autocorrelation methods produce the same result?

- Does calculating the viscosity via the autocorrelation and the shearing methods produce the same result?

- Is the viscosity calculated via the shearing method independent of the shear rate used?
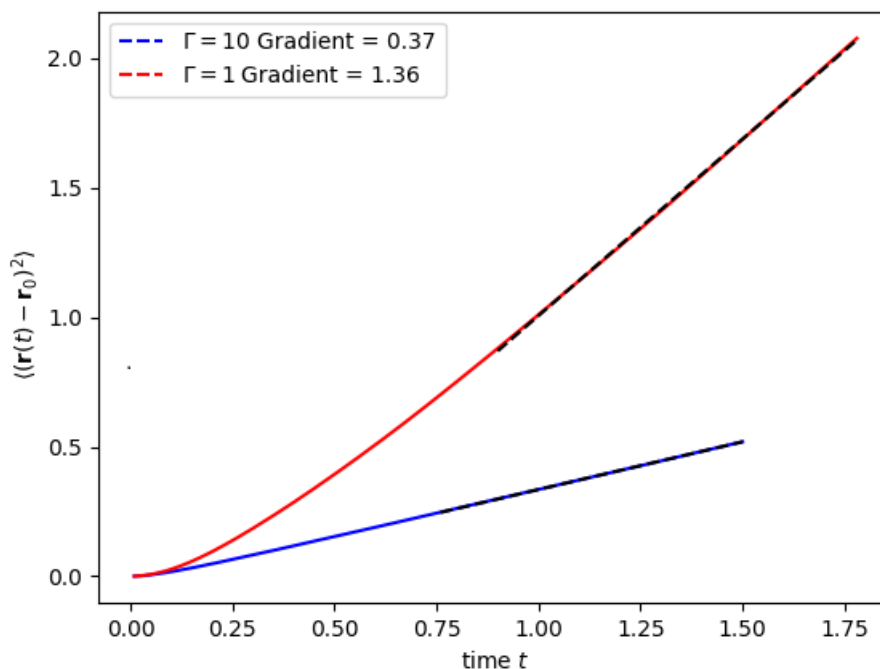
Figure 6.21: Plot of $\langle (\mathbf{r}(t) - \mathbf{r}_0)^2 \rangle$ (MSD) against time for a different values of collision parameter Γ. A fit to the linear portion of the plot can be used to find the diffusion coefficient. Time step used $\Delta t = 0.01$ and box size $L = 20$.

- Does box size alter the calculation of the viscosity or diffusion coefficient?

- How do choices for Γ and Δt affect the viscosity and diffusion coefficients?

6.4.1.1 Calculating Diffusion Coefficient

The diffusion coefficient is calculated by two different, equilibrium methods. The first is the mean squared displacement (MSD) method. The MSD is plotted against run time t for two different Γ values in Fig. 6.21. From these fitted gradients the diffusion coefficient D can be found using Eq. 3.44. Plots showing the time step independence and Γ dependence for the diffusion coefficient D, as calculated using the MSD method, are shown in Fig. 6.22.

The diffusion coefficient can also be calculated using Green–Kubo formulas, which relate D to the integral of the velocity autocorrelation function (see Eq. 3.45). An example of the velocity autocorrelation is shown in Fig. 6.23. The function decays to zero at long time scales, so the area under the curve is integrated
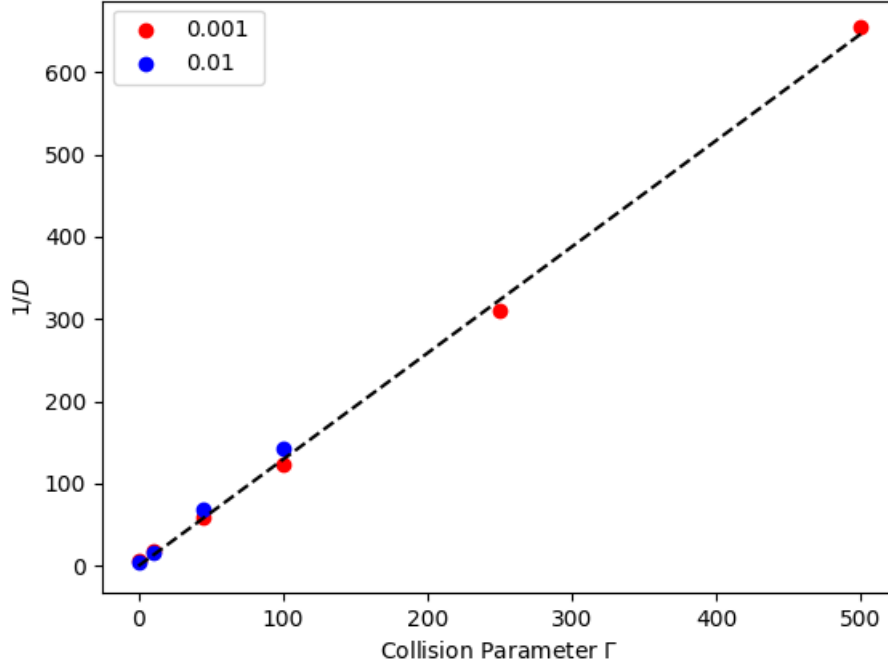
Figure 6.22: Plot of the inverse of the diffusion coefficient $(1/D)$ against collision parameter Γ for different time steps $\Delta t = 0.01$ and $\Delta t = 0.001$. Diffusion coefficient is calculated using the MSD method for box size $L = 20$. Line of best fit is to data points for $\Delta t = 0.001$.

	$\Gamma = 1$	$\Gamma = 10$	$\Gamma = 250$	$\Gamma = 500$
MSD Method	0.152	0.0541	0.00323	0.00151
Autocorrelation Method	0.156	0.0550	0.00324	0.00152

Table 6.8: Diffusion coefficients calculated for a variety of collision parameters Γ, for both methods of calculating the diffusion coefficient D. Time step used is $\Delta t = 0.001$ and box size is $L = 20$ for all calculations.

up to a suitable cutoff, after which the remaining contribution to the integral is assumed to be zero. The values found for calculating D from both methods are found to be equivalent, as illustrated by a selection of data in Table 6.8.

6.4.1.2 Calculating Viscosity

The viscosity is calculated using two different methods. One being the equilibrium method that uses autocorrelation functions, the other is a non-equilibrium method which relies on the application of shear and averaging the off-diagonal stress tensor components. The results obtained from the shearing method will be discussed first,
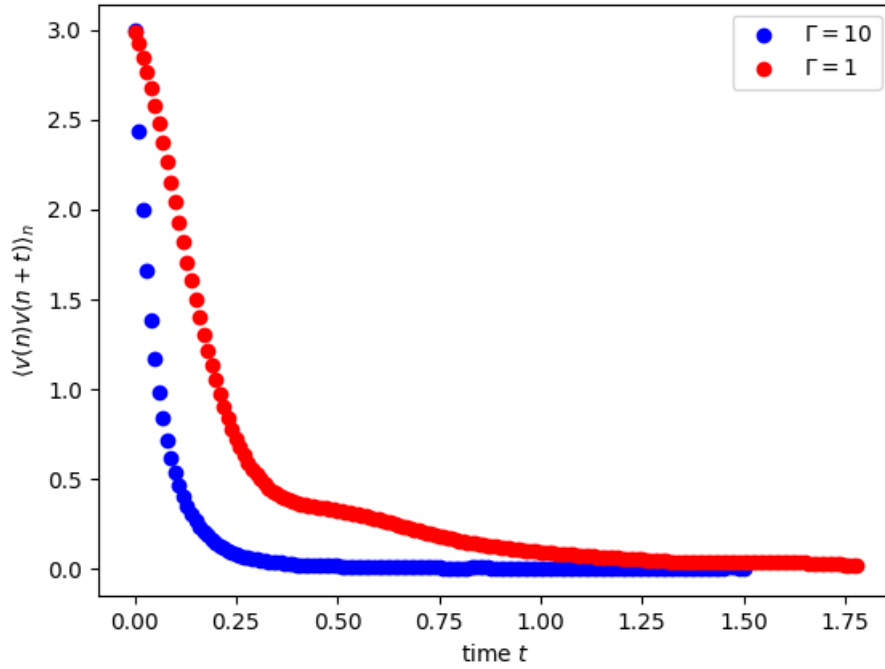
Figure 6.23: Plot of $\langle v(n)v(n+t)\rangle_n$ against time for a different values of collision parameter Γ. The area under the curve can be integrated to find a value for the diffusion coefficient. Time step used $\Delta t = 0.01$ and box size $L = 20$.

before comparing with those obtained from autocorrelation function methods.

Upon initial application of shear, the value of the off-diagonal stress tensor σ_{xy} of the solution (calculated using Eq. 3.41) exhibits an initial response, and this is shown in Fig. 6.24. Over this initial response time, the average value of the stress tensor is changing, before plateauing to an equilibrium which can be used for calculating the viscosity. Table 6.9 shows the effect of varying shear rate $\dot{\gamma}$, for varying cases of time step Δt and collision parameter Γ. Table 6.9 allows us to draw a number of different conclusions. The first is that the viscosity that can be obtained via a simulation is capped by the value of $\Gamma\Delta t$ which, as it represents a probability in the application of the theromostat, must be $\Gamma\Delta t \leq 1$. The second conclusion is that, provided this constraint is satisfied, the viscosity calculated is independent of the time step used, but the values start to deviate when both Δt and Γ are large (even if $\Gamma\Delta t \leq 1$ is satisfied). Finally, the results also show that the obtained value of viscosity is effectively independent of the shear rate, in all cases of Γ and Δt, confirming Newtonian behaviour.

Obtaining a final viscosity value is easier for some sets of parameters illustrated

		$\Gamma = 1$	$\Gamma = 100$	$\Gamma = 250$
$\dot{\gamma} = 0.06$	$\Delta t = 0.01$	1.01	45.3	46.4
	$\Delta t = 0.001$	1.02	35.1	90.7
	$\Delta t = 0.0001$	1.03	33.8	84.1
$\dot{\gamma} = 0.0006$	$\Delta t = 0.01$	1.05	45.6	46.7
	$\Delta t = 0.001$	1.03	35.8	86.8
	$\Delta t = 0.0001$	1.01	35.1	85.2

Table 6.9: Viscosity calculated for a box containing pure water, and varying the collision parameter Γ, shear rate $\dot{\gamma}$ and time step Δt. All simulations are performed using box size $L = 20$.

	$\Gamma = 1$	$\Gamma = 10$	$\Gamma = 100$	$\Gamma = 250$	$\Gamma = 500$
$\dot{\gamma} = 0.06$	0.19	0.22	0.66	1.1	1.6
$\dot{\gamma} = 0.006$	0.020	0.023	0.066	0.11	0.16

Table 6.10: Signal-to-noise ratio (SNR) of the off-diagonal stress tensor σ_{xy} for varying shear rate $\dot{\gamma}$ and varying collision parameter Γ. Values obtained from simulations using time step $\Delta t = 0.001$ and $L = 20$.

in Table 6.9 than others. Finding the viscosity can involve needing to average over a vary large number of stress tensor outputs in order to find an equilibrated value (*i.e.* a value that is no longer considered to be changing with further iterations). The cases in which it is easier to obtain the viscosity are when there is a greater signal-to-noise (SNR) ratio of the outputted off-diagonal stress tensors. The definition of the SNR as used in this work is defined as the ratio of the mean value of the off-diagonal stress tensor outputs, to the standard deviation of the outputted data. Table 6.10 shows the value of SNR for varying shear rate $\dot{\gamma}$ and varying collision parameter Γ. It is shown that the signal-to-noise ratio is much stronger for higher shear rates and larger values of Γ. In fact, the value of SNR decreases in proportion to decreases in $\dot{\gamma}$. This implies that obtaining viscosity values increases with difficulty with decreasing shear rate. The larger value of SNR implies that it might be beneficial to use larger values of Γ, in order to investigate the relationship between the applied shear rate and the viscosity. However, the simulations with larger values of Γ take longer to run, outweighing the benefit of a larger SNR. For example, simulations using $\Gamma = 45$ take approximately 4 times longer per iteration, than simulations conducted using $\Gamma = 0$.
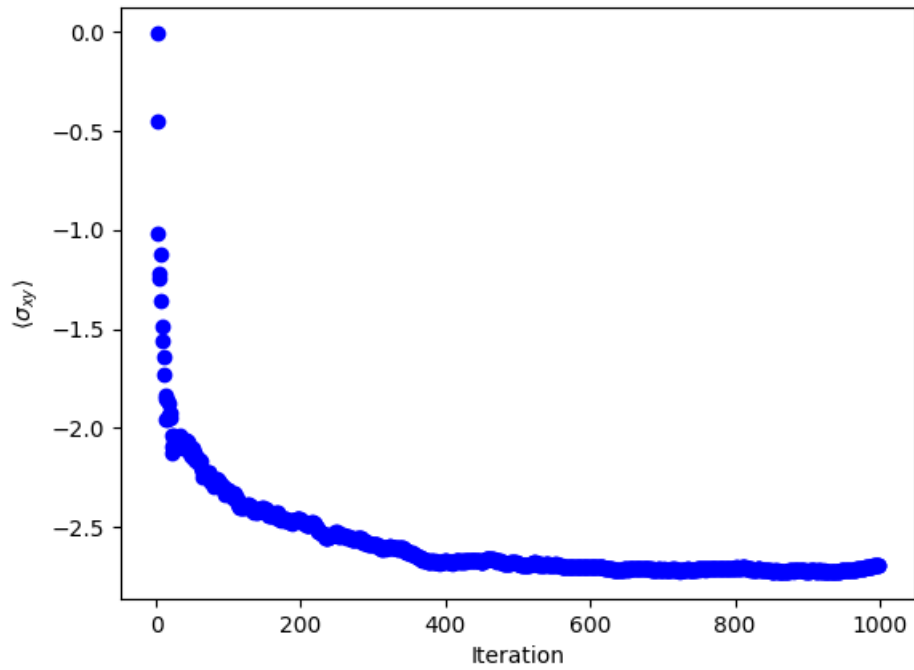
Figure 6.24: Response of a solution consisting of water beads, in a simulation of box size $L = 20$, to an initial application of shear with shear rate $\dot{\gamma} = 0.06$. In the example given, parameters used are $\Delta t = 0.01$ and $\Gamma = 100$, which results in a final value of $\langle \sigma_{xy} \rangle = -2.73$ and $\eta = 45.4$. Plotted is the average value of the off-diagonal stress tensor σ_{xy} against the iteration. Following the reach of a plateau, data can be collected in order to calculate the value of σ_{xy} for calculating the viscosity.
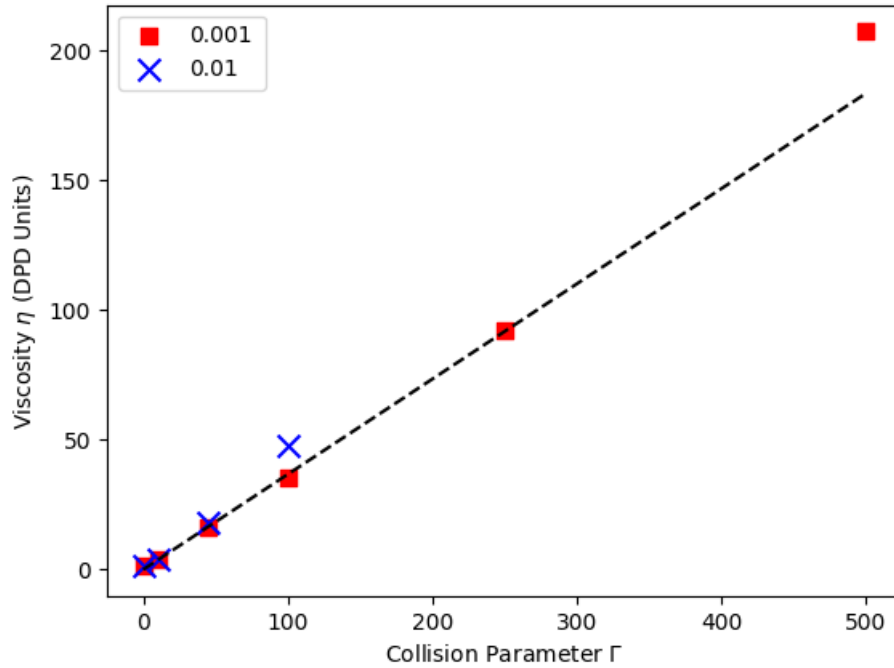
Figure 6.25: The relationship between collision parameter Γ and the resulting viscosity of a solution containing only water beads. The viscosity is obtained using the shearing method, a shear rate of $\dot{\gamma} = 0.006$, and box size $L = 20$. Two different time steps are trialled $\Delta t = 0.01$ and $\Delta t = 0.001$. Fit is applied to the points from the $\Delta t = 0.001$ for $\Gamma \leq 250$.

Fig. 6.25 confirms that the relationship between viscosity η and Γ is linear, as is expected for this thermostat. Also shown are the results from different time steps, showing that the results are equivalent. The relationship deviates from nonlinearity when the value of $\Gamma \Delta t$ begins to get large.

The viscosity η can also be calculated via Green–Kubo formulas, which relates η to the integral of the autocorrelation function of the off diagonal stress tensor. In order to investigate whether this method produces equivalent results to the above method, the viscosity is calculated using a variety of different Γ choices, and the autocorrelation function is shown in Fig. 6.26. The curves shown in 6.26 are then integrated up to a sufficiently large value of t, in order to obtain a value for η. It is shown that as the value of Γ increases (*i.e.* the friction increases), the autocorrelation function decays more rapidly, which is consistent with that found by other researchers [287]. This poses a problem for using this method at high Γ values. A comparison of the viscosity values obtained via the autocorrelation
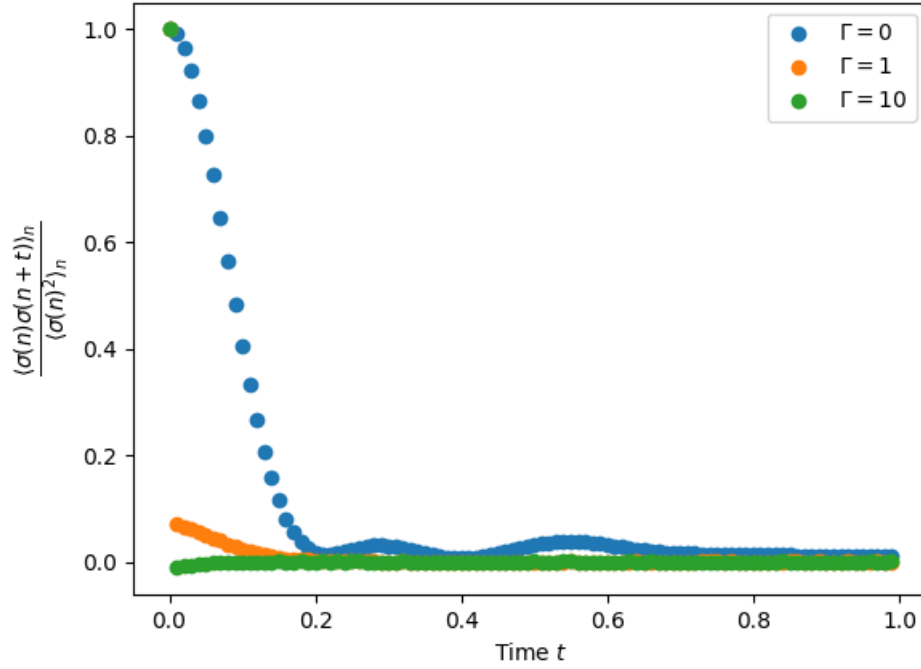
Figure 6.26: Examples of the autocorrelation functions obtained for different values of the collision parameter Γ. The auto-correlation function is integrated over time, in order to provide values for the viscosity. Values of viscosity obtained from integrating curves: $\eta = 0.703$ ($\Gamma = 0$), $\eta = 0.961$ ($\Gamma = 1$), and $\eta = 3.95$ ($\Gamma = 10$).

method and the shearing method are shown in Table 6.11. Also included are the results from varying box size L. It is clear that the results obtained via the two different methods are equivalent within a reasonable margin. The results from the two different box sizes are also equivalent.

6.4.1.3 Relationship Between Γ and Schmidt Number

Fig. 6.22 confirms that the relationship between Γ and $1/D$ is linear, and Fig. 6.25 confirms that the relationship between Γ and η is linear. The relationships only began to display slightly non-linearity at very high values of $\Gamma \Delta t$. Therefore Fig. 6.27 shows the relationship between Γ and the Schmidt number, confirming a Sc $\propto \Gamma^2$ relationship.
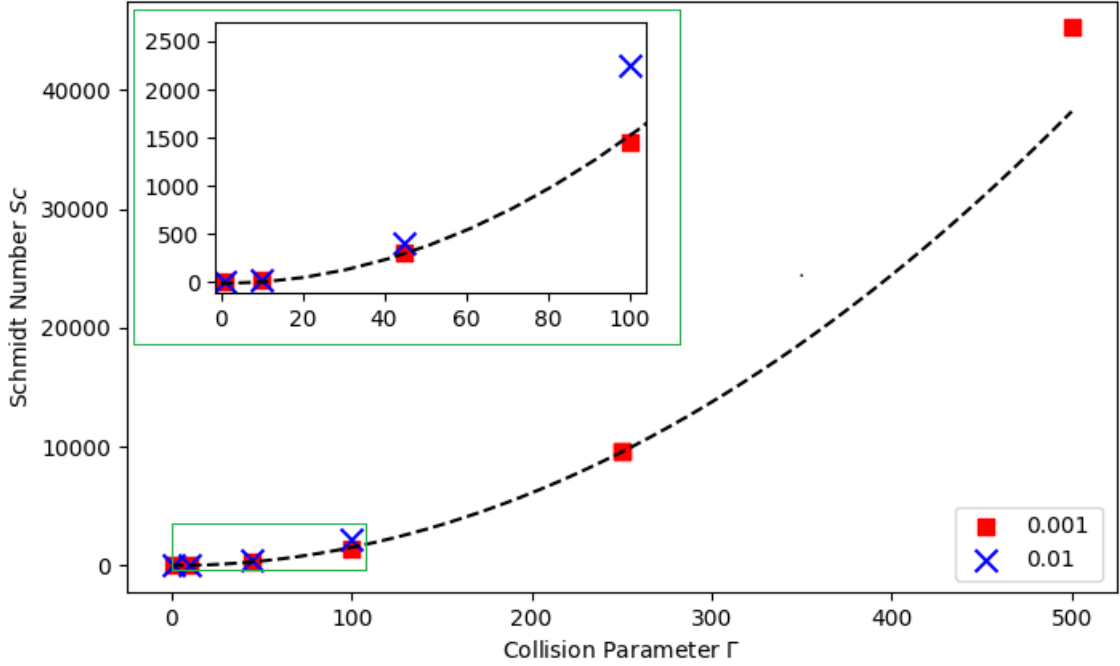
Figure 6.27: The relationship between collision parameter Γ and the resulting Schmidt number of a solution containing only water beads. Two different time steps are trialled $\Delta t = 0.01$ and $\Delta t = 0.001$. The fit of the form $\text{Sc} = A\Gamma^2 + B$ where A and B are constants are applied to the points from the $\Delta t = 0.001$ for $\Gamma \leq 250$.

		$\Gamma = 1$	$\Gamma = 45$
Shearing Method	$L = 20$	1.01	17.9
	$L = 40$	1.02	18.1
Autocorrelation Method	$L = 20$	0.961	18.0
	$L = 40$	0.978	18.1

Table 6.11: Viscosity calculated using both the shearing and auto-correlation methods, for box sizes $L = 20$ and $L = 40$. Time step used is $\Delta t = 0.01$ for all calculations with shear rate $\dot{\gamma} = 0.06$ for the calculations involving the application of shear.

6.4.1.4 Conclusion

For the purpose of calculating the viscosity, the autocorrelation function method is superior in some ways. The shearing method requires the simulation box to be run for longer in order to obtain the same result. However, the autocorrelation function method can only be used to find the viscosity for Newtonian fluids, which may be applicable for micellar cases, but not the liquid crystal phases. The autocorrelation function for the viscosity calculation also decays much more rapidly for larger

values of the collision parameter Γ, meaning that only low values of Γ can be used in this method. It has been shown that the viscosity is independent of the box size, irrespective of the calculation method used, or the choice of Γ. Of course, for the micellar phase, additional considerations need to be made related to the number of micelles formed in the box, as the box size will need to be sufficiently large in order to have a large enough number of micelles.

The range of Schmidt numbers that can be obtained via the Stoyanov-Groot thermostat is very large. For pure water at 25°C, experimentally determined values for the self-diffusion coefficient and the viscosity find a Schmidt number of approximately Sc ≈ 400. This means that an equivalent Schmidt number in DPD would be generated with a collision parameter of $\Gamma \approx 45$.

In the following section both viscosity calculation methods will be used in order to investigate the rheological behaviour of micellar solutions.

6.4.2   Viscosity via the Autocorrelation Method

In order to investigate the viscosity of the simulation cases described in Section 6.3, the autocorrelation method is first applied. The method is applied to the equilibrated micellar simulation boxes. The thermostat is switched to the Stoyanov-Groot thermostat, and a selection of collision parameter values are trialled. This begins with $\Gamma = 0$ (*i.e.* a pairwise variation of the Nosé-Hoover thermostat). $\Gamma = 0$ is selected due it being shown in the previous section that the autocorrelation function decays (as a function of time) more slowly when Γ is small. Therefore for low Γ values it will be easier to find a value for the viscosity via this method. The time step remains at $\Delta t = 0.01$.

The difference in the autocorrelation functions obtained for different concentrations, is shown in Fig. 6.28. The same cutoff $t_\mathrm{C} = 1.8$ for integration over time t is applied to all simulation cases for consistency, at a value at which all functions have decayed to approximately zero.

The obtained viscosity for all simulation cases is shown in Fig. 6.29. Simi-
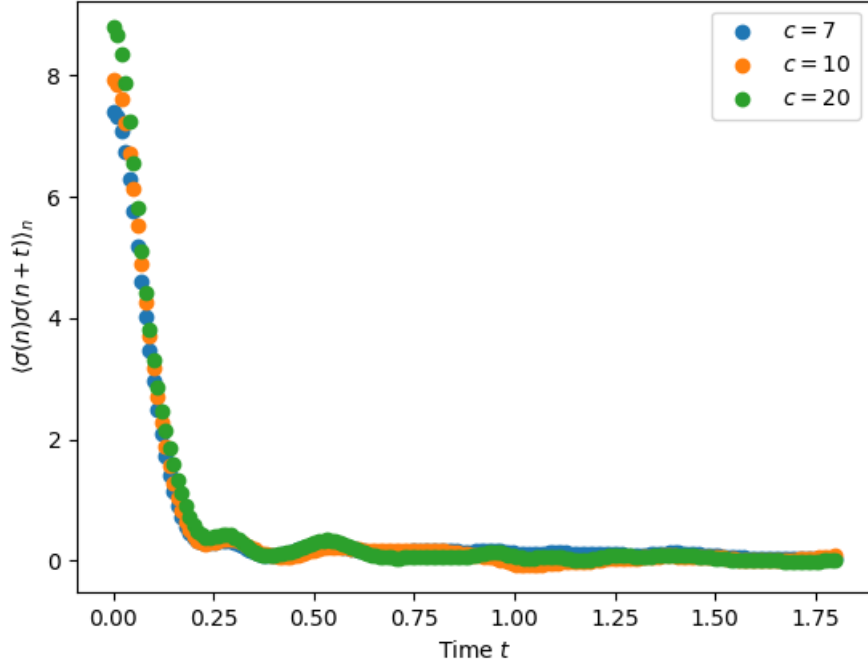
Figure 6.28: The autocorrelation function against time obtained for the case of mixed n (representing AES) for different concentration cases c (wt%).

larly to the aggregation number plot shown in Fig. 6.12, the viscosities obtained for varying n at each concentration are relatively indistinguishable, with overlapping error bars. However, there is a clear growth in the viscosity with increasing concentration. The growth of the viscosity with increasing concentration is at a smaller rate than predicted experimentally. For example, the ratio of the viscosity calculated η to the viscosity of water η_W, as found via DPD, takes the values $\eta/\eta_W = 1.1$ (7%), $\eta/\eta_W = 1.3$ (10%) and $\eta/\eta_W = 1.6$ (20%). In contrast the values obtained experimentally are for SDS $\eta/\eta_W = 1.5$ (7%), $\eta/\eta_W = 1.9$ (10%) and $\eta/\eta_W = 4.1$ (20%). For AES the ratios obtained are larger at higher concentration: $\eta/\eta_W = 1.5$ (7%), $\eta/\eta_W = 2.0$ (10%) and $\eta/\eta_W = 8.3$ (20%). However, the under-prediction is expected, due to the under-prediction of the aggregation number of the micelles in DPD.

Ideally, we would now investigate if the choice of Γ effects the relative viscosity changes (*i.e.* value of η/η_W). However, it was reported in the previous section that for increasing values of Γ the autocorrelation decays more quickly. It was found that at larger values of Γ, the autocorrelation function decayed too quickly
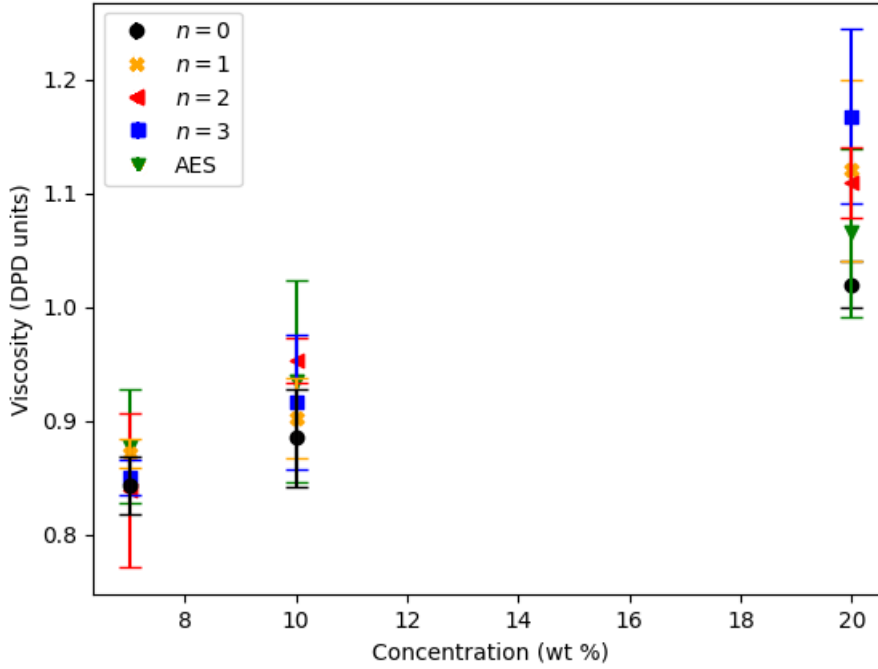
Figure 6.29: Viscosity calculated for the micellar solutions with $\Gamma = 0$ using the autocorrelation method. The error bars represent the standard deviation of the values obtained from different off-diagonal stress tensor values. For reference the viscosity of water obtained using this value of Γ is $\eta = 0.70$ and time step $\Delta t = 0.01$

to calculate accurate values of the viscosity, in a way that meant a meaningful comparison of the different cases could be made. However, we vary the value of Γ anyway, in order to see if it results in any change in the radius of gyration of the molecules R_{g}, in a similar way to other research [145]. For these simulations, the final configuration obtained in Section 6.3 was taken as the initial configuration for the simulations varying Γ. The value of the radius of gyration was found to be independent of the collision parameter Γ for all simulation cases of ethoxylation n and concentration c. An example of this for the case in which $n = 0$ and the concentration $c = 20\%$ is shown in Table 6.12. This is in agreement with Symeonidis $et\ al.$ [145], who find that for DPD simulations modelling polymer chains, and applying the Lowe-Andersen thermostat with varying choices of Γ, when no shear is applied, the effect of varying Sc is minimal on the value for the radius of gyration $\langle R_{\mathrm{g}}^2 \rangle$. However, they also report than when when shear is applied there is a large difference in the value of $\langle R_{\mathrm{g}}^2 \rangle$ at different Γ values. This will be investigated in the next section.

Thermostat parameters	Radius of gyration R_g
No thermostat	0.8541 ± 0.0007
$\Gamma = 10$	0.8548 ± 0.0006
$\Gamma = 45$	0.8546 ± 0.0005
$\Gamma = 250$	0.8543 ± 0.0005

Table 6.12: The average value of R_g obtained for simulations with varying collision parameter Γ. Also shown are the original results obtained from the previous section, when applying no additional thermostat is applied. In these simulations $n = 0$ and the concentration $c = 20\%$. The uncertainties are calculated as the standard deviation.

6.4.3 Shearing Micelles

This section will look at applying shear to the micellar solutions. This will allow for investigation into if the application of shear has any effect on the size and shape of the micelles. Since the micellar solutions exhibited Newtonian rheology in Chapter 4, this would not be expected at moderate values of shear rate, as any size change would be thought to affect the rheology. However, for extremely high values of the shear rate, other authors have reported stretching of micelles, leading to a non-Newtonian rheology [62]. This section will also calculate the viscosity from these solutions, using the off diagonal stress tensor components that are non-zero due to the application of the shear force.

6.4.3.1 Simulation Set-Up

The process of using applied shear in order to calculate viscosity is explained in Section 3.4. Lees-Edwards boundary conditions are used, which is an adaptation of the standard periodic boundary conditions, for inducing shear flow. The application of these boundary conditions generates a linear velocity profile. The simulations are initialised from the previously equilibrated results in the earlier part of this chapter. The simulations are then switched to being performed in the Stoyanov-Groot thermostat, in order to change the value of the Schmidt number.

In order to investigate the effect of the collision parameter on the shearing calculations, two values of Γ are trialled. Of particular interest is the impact Γ has on the calculated viscosity profile, and the the radius of gyration of the

molecules, since in published work these have been parameters of interest (with varying Schmidt number) [145,146]. The first collision parameter trialled is $\Gamma = 45$. This value was chosen as it represents a realistic Schmidt number for the fluid. The second was a value of $\Gamma = 250$, in order to generate a significantly larger Schmidt number for comparison. This value is chosen since it will be used in the viscosity calculations in the following chapter for the liquid crystals (to be discussed further in Section 7.3). In the simulations using $\Gamma = 45$, a time step of $\Delta t = 0.01$ can be used, however, when $\Gamma = 250$ the time step must be reduced and a time step of $\Delta t = 0.001$ is used.

In this chapter the aim was to reproduce the experimental simulations as much as possible, which means that low shear rates should be used. Shear rate has units of $[\text{time}]^{-1}$, so using the conversion between DPD units and real time described in Section 3.3.3, this means that for the shear rate $\dot{\gamma} = 1 \text{DPD unit} = 4.61 \times 10^{11} \text{s}^{-1}$. Given that the rheometer measurements for the micellar solutions go up to a value of shear rate around $\dot{\gamma} = 60 \text{s}^{-1}$, the typical range of shear rates in other DPD works are very large. However, one of the main barriers to achieving low shear rates is the amount of noise in the simulation, and the SNR ratio was shown to increase at a rate equivalent to the rate of decrease in the shear rate in Table 6.10. Theoretical values at low shear rates can still be obtained, using very long simulation times. A range of shear rates are trialled in this study, varying from $\dot{\gamma} = 1.2 \times 10^{-6}$ to $\dot{\gamma} = 1.2 \times 10^{-1}$ (in DPD units), with increments of 10. The simulation cases investigated include: $n = 0$ (10% and 20%), mixed n (10% and 20%) and $n = 1$ (10% and 20%).

6.4.3.2 Micellar Shape

This section will begin with looking at the simulations performed using collision parameter $\Gamma = 45$. At the low values of shear rate trialled, there was no observable difference in the shape of the micelles, when compared with the equilibrium simulations. However, at very extreme shear rates, changes in the micellar shape

start to become observable. This is shown for the $n = 1$ case at 20% concentration in Fig. 6.30. At shear rates $\leq 1.2 \times 10^{-4}$, the micelles retain the same shape and configuration as in the equilibrium simulations. However at a shear rate of $\dot{\gamma} = 1.2 \times 10^{-3}$, some of the longer, more worm-like micelles become aligned in direction of the shear flow. With subsequent increase in the shear rate, the micelles noticeably elongated in the direction of shear flow. Finally, an increase to $\dot{\gamma} = 1.2 \times 10^{-1}$ breaks down the micelles into something closer to a nematic phase. This abrupt change occurs at around the same shear rate for all of the simulation cases trialled.

The micellar shape change has a significant effect on the radius of gyration of the micelles R_{G}. It might be assumed that it would be difficult to calculate a value for R_{G}, or the mean aggregation number N_{agg}, at high shear rates, due to the distances between any aggregates becoming very small. However, when the same processing codes are applied to the resulting final configurations (as the ones used in the previous section), the aggregation number and radius of gyration of the micelles found are shown in Fig. 6.31. At very high shear rate ($\dot{\gamma} = 1.2 \times 10^{-1}$) the codes still pick up on the drop in the aggregation number, but there is an increased likely hood of adjacent micelles being miss-classified as connected, therefore the absolute value of the aggregation number may be not entirely reliable at this shear rate. Moderate amounts of shear have the effect of slightly enhancing the aggregation number, by encouraging free micelles to join aggregates. Once the micelles start to significantly stretch, at increased shear rate, they break into smaller micelles, decreasing the mean aggregation number. The radius of gyration grows significantly under shear, mostly due to the stretch of the micelles in the direction of shear. Once the micelles break down in to smaller micelles at higher shear rate this radius of gyration drops accordingly. Both the 10% and 20% concentrations show similar trends with increasing shear rate.

The impact of the shear rate on the radius of gyration of the individual molecules R_g, is shown in Fig. 6.32, with the effect being most pronounced when
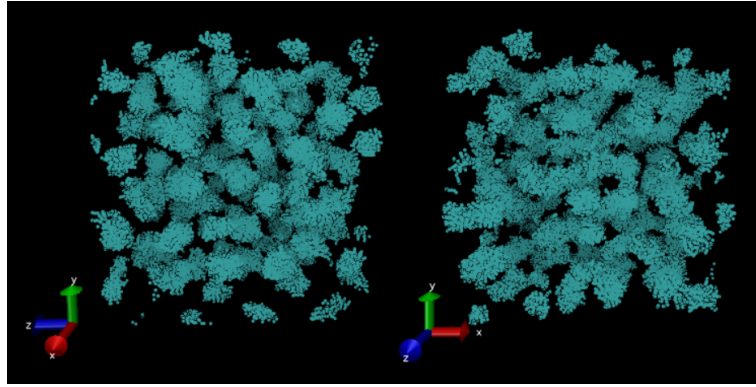
(a) $\dot{\gamma} = 1.2 \times 10^{-4}$
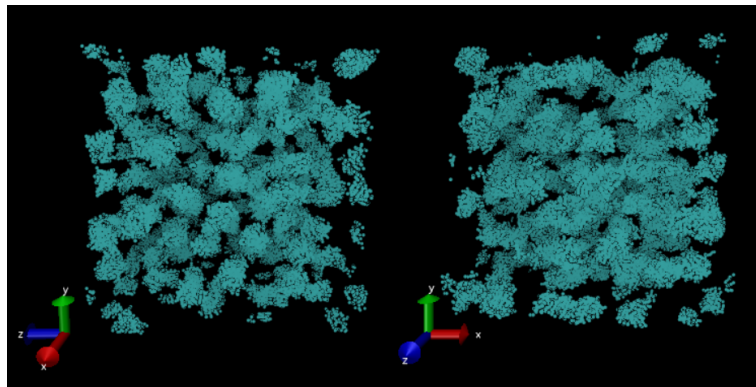
(b) $\dot{\gamma} = 1.2 \times 10^{-3}$
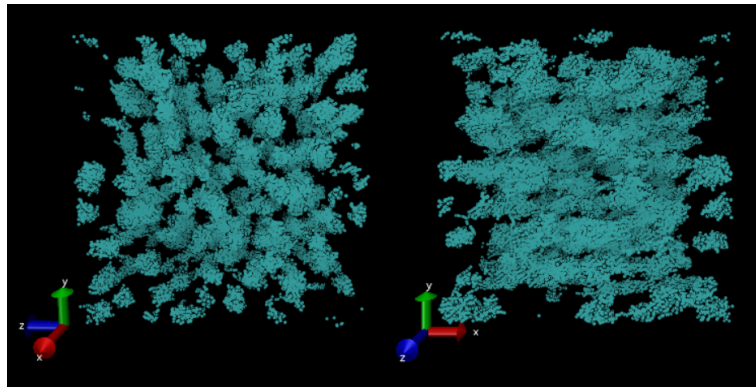
(c) $\dot{\gamma} = 1.2 \times 10^{-2}$
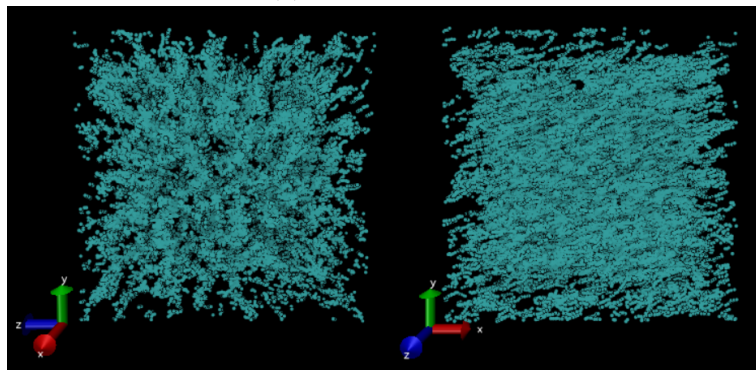
(d) $\dot{\gamma} = 1.2 \times 10^{-1}$

Figure 6.30: A micellar solution with 20% concentration, and molecules described by $n = 1$, at increasing rates of shear in a DPD simulation. Note that only the surfactant molecules are shown for clarity. Calculation performed using collision parameter $\Gamma = 45$.

(a) $c = 10\%$ (b) $c = 10\%$

(c) $c = 20\%$ (d) $c = 20\%$
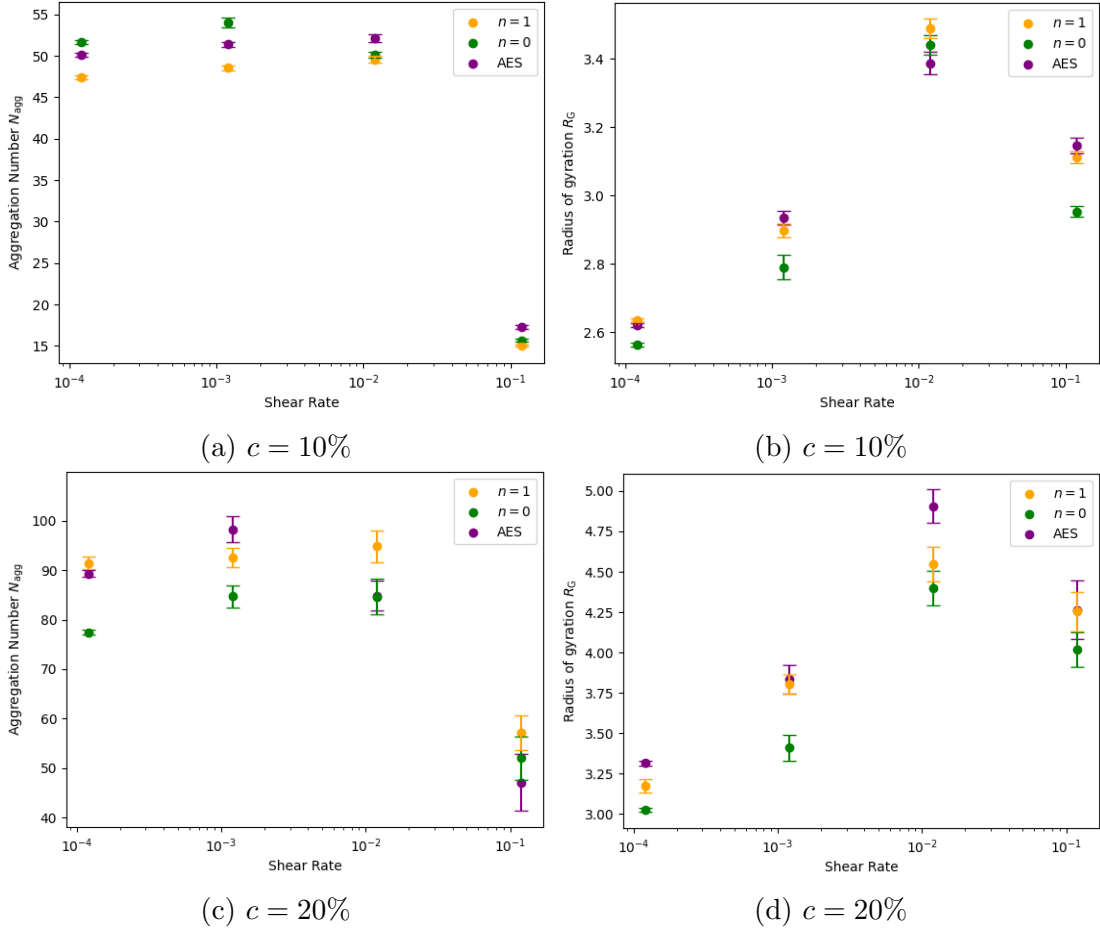
Figure 6.31: Effect of shear rate on the mean aggregation number N_{agg} and micellar radius of gyration R_{G}, for solutions with $n = 0$, $n = 1$, AES and concentrations $c = 10\%$ and $c = 20\%$.

the micelles have completely broken down. Interestingly, the molecules show a decrease in their radius of gyration with increasing shear rate, not an increase as might be expected, which would be due to a stretch. The decrease in the radius of gyration is likely to be because of a straightening of the molecule.

So far all of the presented results are obtained for collision parameter $\Gamma = 45$. Also trialled, was increasing the collision parameter to $\Gamma = 250$. This significantly raises the Schmidt number of the solution, in order to answer the question of whether the Schmidt number alters the results of the calculation. The resulting configurations for the $n = 1$ and 20% case is shown in Fig. 6.33 (which is equivalent to the case shown in Fig. 6.30 when $\Gamma = 45$). It is observed that increasing the value of Γ lowers the value of the shear rate at which the transition from spherical micelles to stretched micelles, and finally dissaggregated micelles occur.

(a) $n = 0$ (b) AES
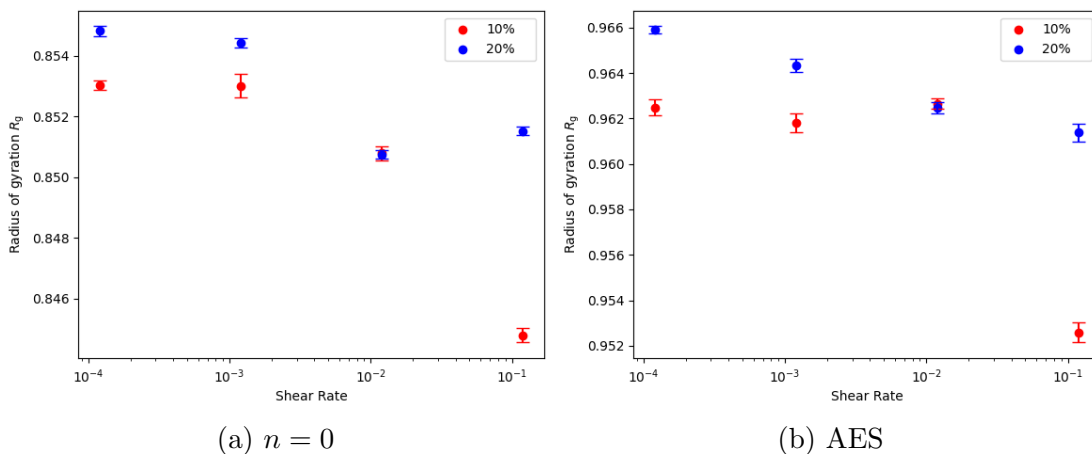
Figure 6.32: Effect of shear rate on the radius of gyration R_g for solutions with $n = 0$ and AES and concentrations $c = 10\%$ and $c = 20\%$.

The effect of varying Γ on the mean aggregation number and radius of gyration of the micelles is shown in Fig. 6.34. There is relatively little difference between the two choices of Γ. Some slight differences begin to appear at higher shear rates, although this is likely to be related to the transition from non-spherical micelles occurring at a lower shear rate for the higher Γ case. It was shown in the previous section, that varying the collision parameter Γ had minimal effect on the radius of gyration of molecules R_g, when no shear is applied. The variation of R_g with shear rate, for both values of Γ trialled, is shown in Fig. 6.35. The effect of varying Γ has more of an effect on the individual molecules than it did on the micelles as a whole. The radius of gyration displays very different behaviour at extremely high shear rates, when the micelles have largely broken down. Symeonidis *et al.* [145] find that the radius of gyration of molecules grows with increasing shear rate, irrespective of Γ, although grows significantly less for systems with larger Γ. However this was for a purely polymer system with no micelle formation. In our case the radius of gyration drops once the molecules are no longer in a micelle at $\Gamma = 45$ and increases when $\Gamma = 250$. Micelle formation has been shown earlier in the chapter to lead to increases in the radius of gyration, explaining the drop. Once the micelles break down in this system, the molecules behave much more like a standard polymer system would.
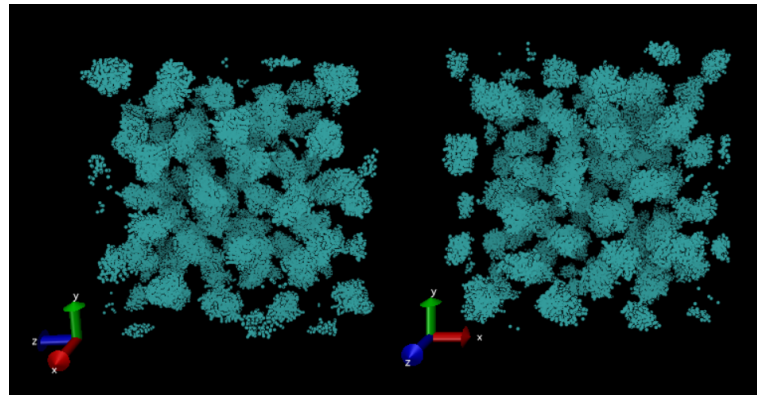
(a) $\dot{\gamma} = 1.2 \times 10^{-4}$
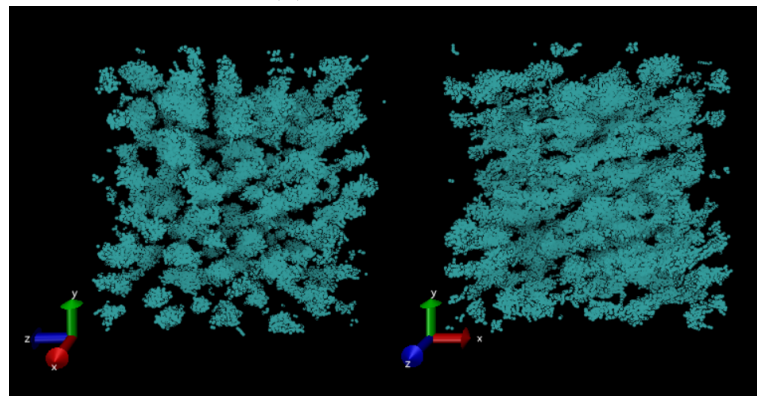
(b) $\dot{\gamma} = 1.2 \times 10^{-3}$
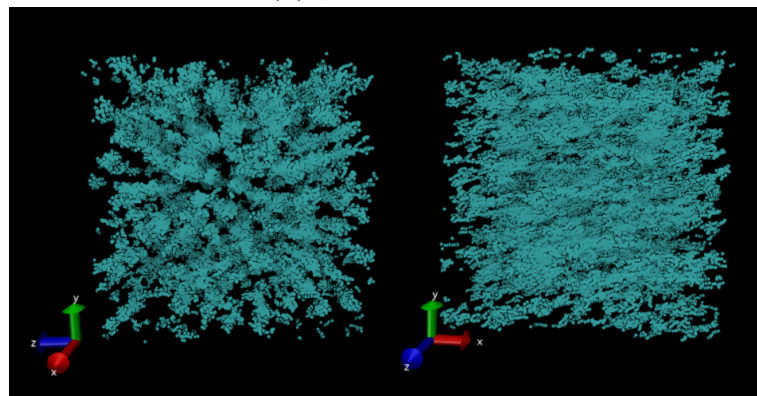
(c) $\dot{\gamma} = 1.2 \times 10^{-2}$
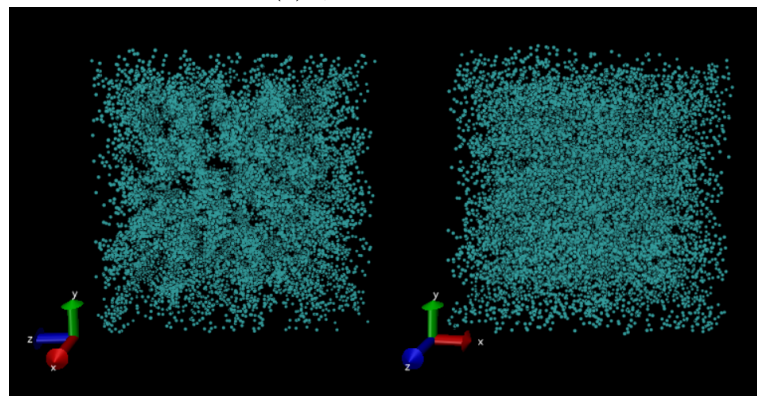
(d) $\dot{\gamma} = 1.2 \times 10^{-1}$

Figure 6.33: A micellar solution with 20% concentration, and molecules described by $n = 1$, at increasing rates of shear in a DPD simulation. Note that only the surfactant molecules are shown for clarity. Calculation performed using collision parameter $\Gamma = 250$.
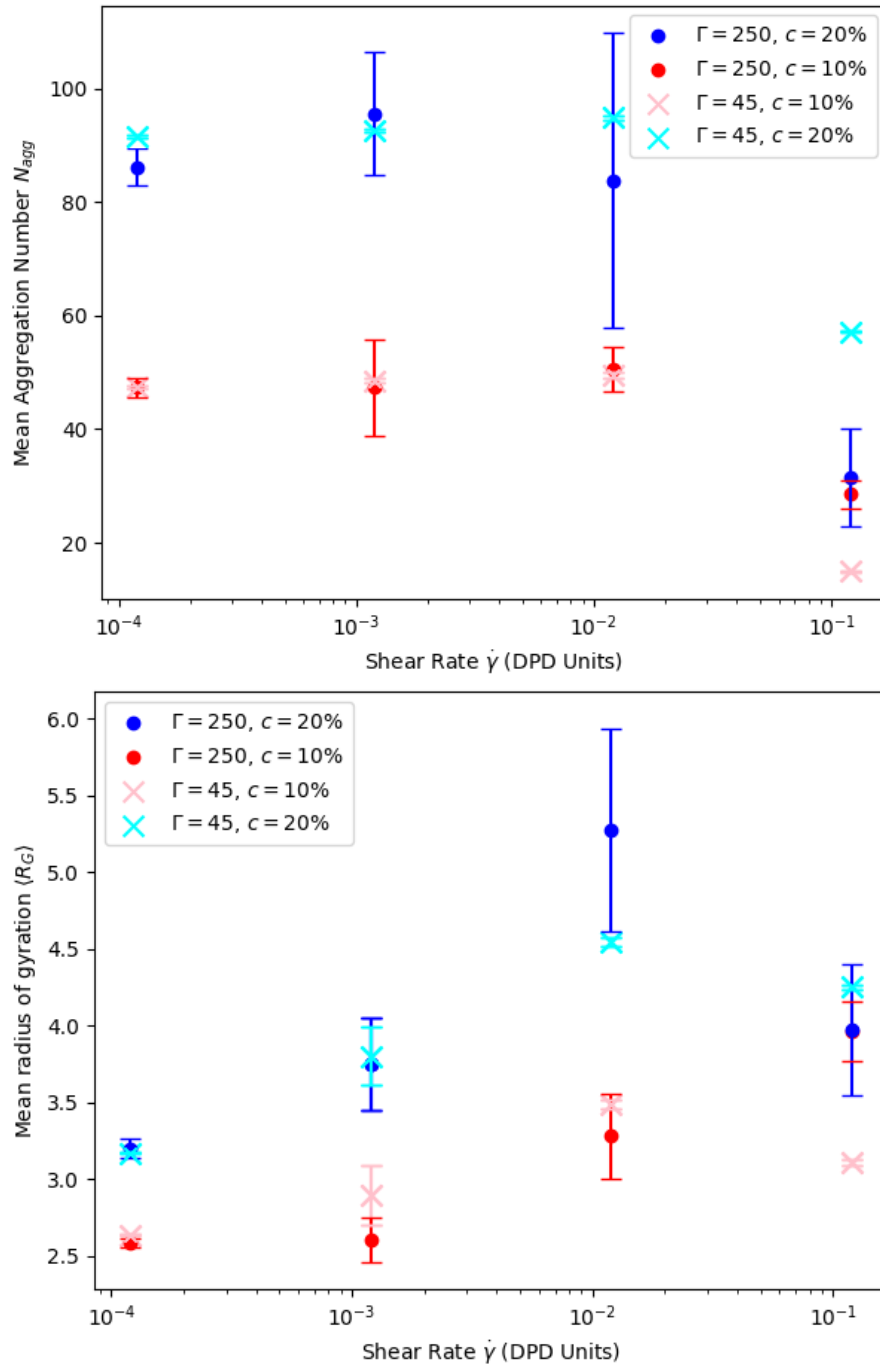
Figure 6.34: Comparison of the values of N_{agg} and R_{G} obtained using different values of Γ. Results shown for two different concentrations c.
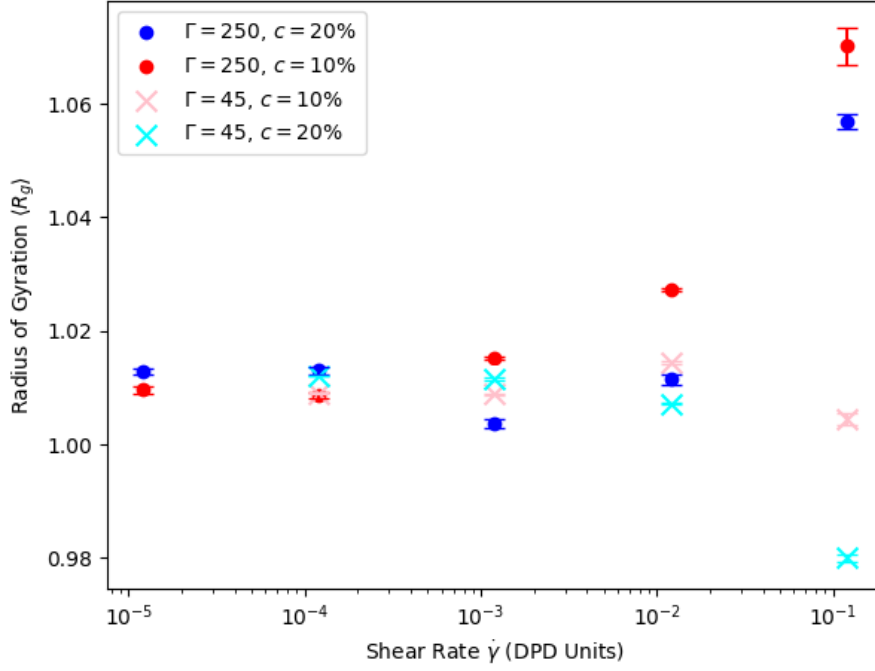
Figure 6.35: Comparison of the values of R_g obtained using different values of Γ. Results shown for two different concentrations c.

6.4.3.3 Viscosity Calculation

Although simulations are run using shear rates in the range from $\dot{\gamma} = 1.2 \times 10^{-6}$ to $\dot{\gamma} = 1.2 \times 10^{-1}$, it is found that, there is too much noise in simulations with $\dot{\gamma} < 1.2 \times 10^{-4}$ to obtain a converged value for the viscosity. For the simulations conducted using $\Gamma = 45$, a comparison of the different values calculated for the viscosity for concentration and n is shown in Fig. 6.36. The same results are also plotted in Fig. 6.37, comparing the effect of varying n. The results show largely shear thinning behaviour, which is likely related to the change in the micellar shape and their break down. Due to the difficulty in accessing lower shear rates, it can't be observed if this viscosity eventually plateaus to a Newtonian relationship with the shear rate at lower shear rate values (*i.e.* in the region in which the micelles are not thought to be changing shape). However, comparing the values of the viscosity at the lower shear rates, it is observable that the viscosity calculated for the AES and $n = 1$ values are significantly larger than for the $n = 0$ case, particularly for the case in which the concentration is larger. This is, at least qualitatively, consistent with what is expected from experiment.

(a) $n = 0$

(b) $n = 1$

(c) AES
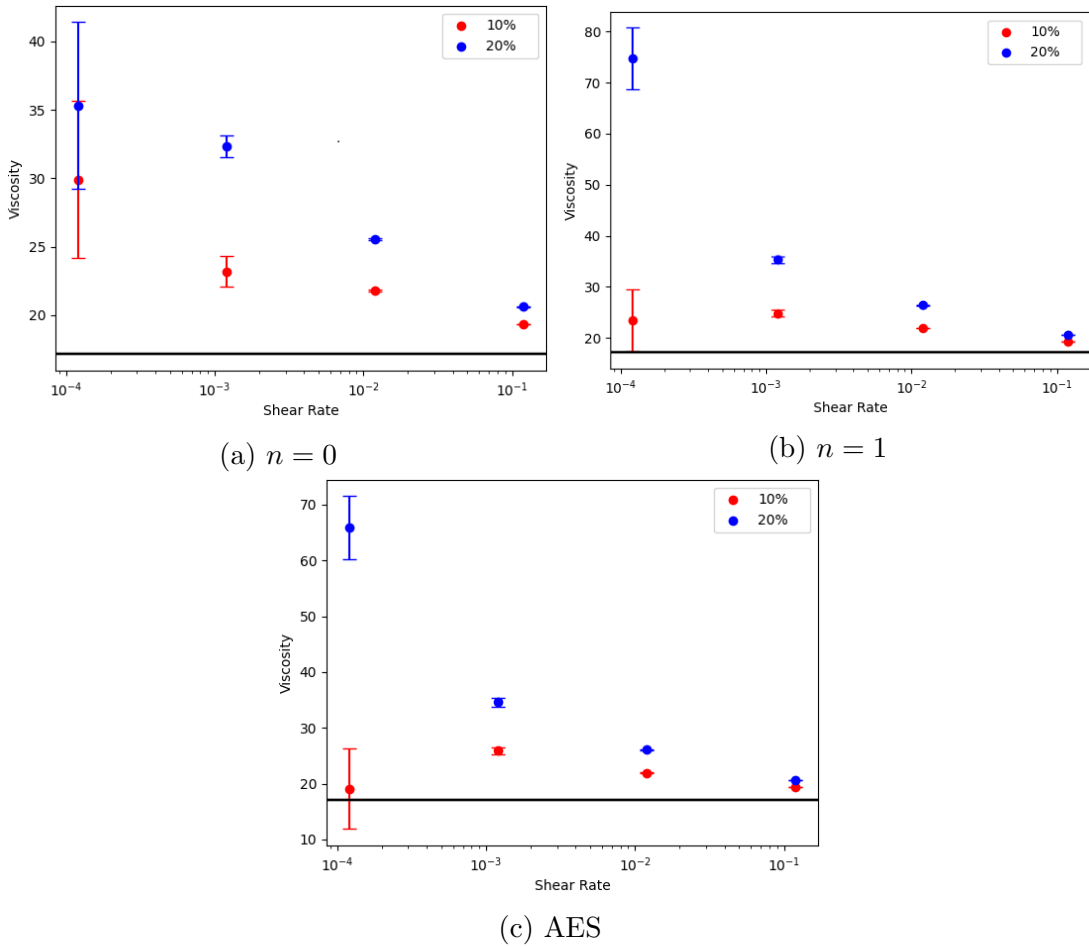
Figure 6.36: Viscosity calculated at varying shear rates from applying shear in DPD calculations. Individual plots correspond to the ethoxylation n, while in each plot two different concentrations are shown. Error bars correspond to the standard error. The horizontal black line indicates the viscosity of water at a value of $\Gamma = 45$.

(a) $c = 10\%$

(b) $c = 20\%$
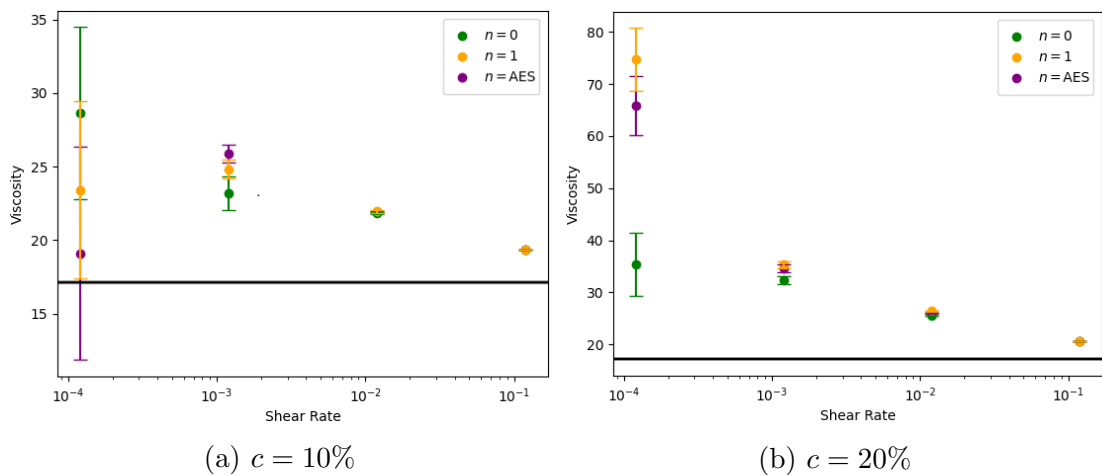
Figure 6.37: Viscosity calculated at varying shear rates from applying shear in DPD calculations. Individual plots correspond to different concentrations c, while in each plot three different values of n are shown. Error bars correspond to the standard error.
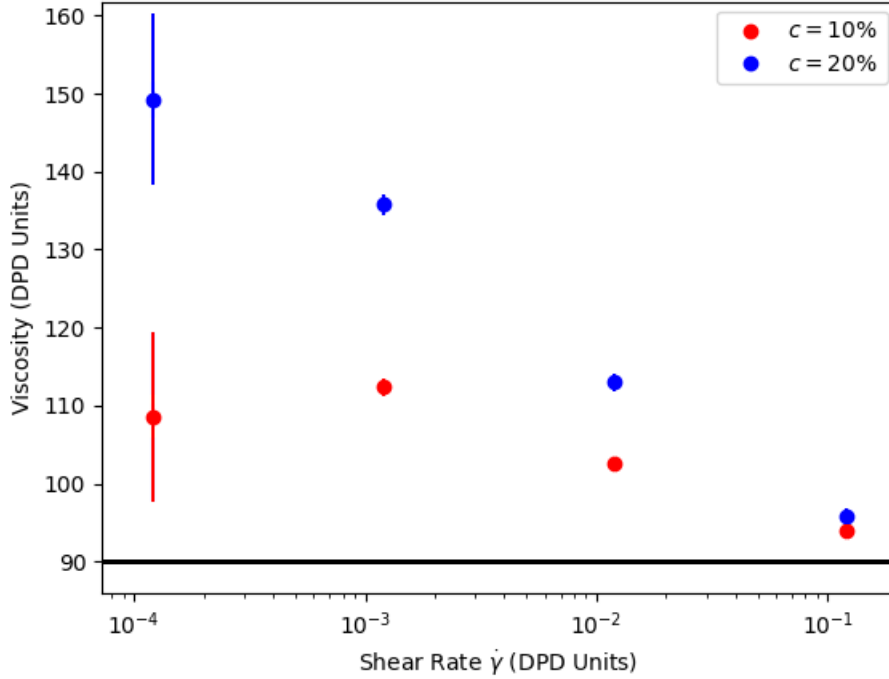
Figure 6.38: Viscosity calculated for molecules with $n = 0$ in micellar solutions using $\Gamma = 250$. Error bars correspond to the standard error.

The relationship between the viscosity and the shear rate, calculated using $\Gamma = 250$, is qualitatively fairly similar to that found in the $\Gamma = 45$ case. However, the viscosity overall is of a larger magnitude. An example shown for the $n = 0$ case is shown in Fig. 6.38. The data points with shear rates $\dot{\gamma} = 1.2 \times 10^{-3}$–$1.2 \times 10^{-1}$ are well converged, and there is good confidence in the viscosity calculated in this shear rate range. Some points with $\dot{\gamma} = 1.2 \times 10^{-4}$ are not shown because there was too much noise in the final data in order to ascertain whether the simulations had fully converged. They also are of note for having relatively large error bars. The general trend is similar to the results obtained using $\Gamma = 45$. The relative viscosity changes (η/η_{W}) for $\Gamma = 45$ and $\Gamma = 250$ are compared in Fig. 6.39 for the viscosity calculated in the shear rate range $\dot{\gamma} = 1.2 \times 10^{-3}$–$1.2 \times 10^{-1}$. Only the results obtained from the higher shear rate are used in this calculation, since there is a larger amount of confidence in these calculated values compared to the values obtained at $\dot{\gamma} = 1.2 \times 10^{-4}$. The ratio of η/η_{W} is significantly larger for the simulations using $\Gamma = 45$ *vs.* those from $\Gamma = 250$, indicating that Γ is relevant when calculating viscosity ratios, and a simulation cannot simply be scaled by one

(a) $n = 0$ (b) AES
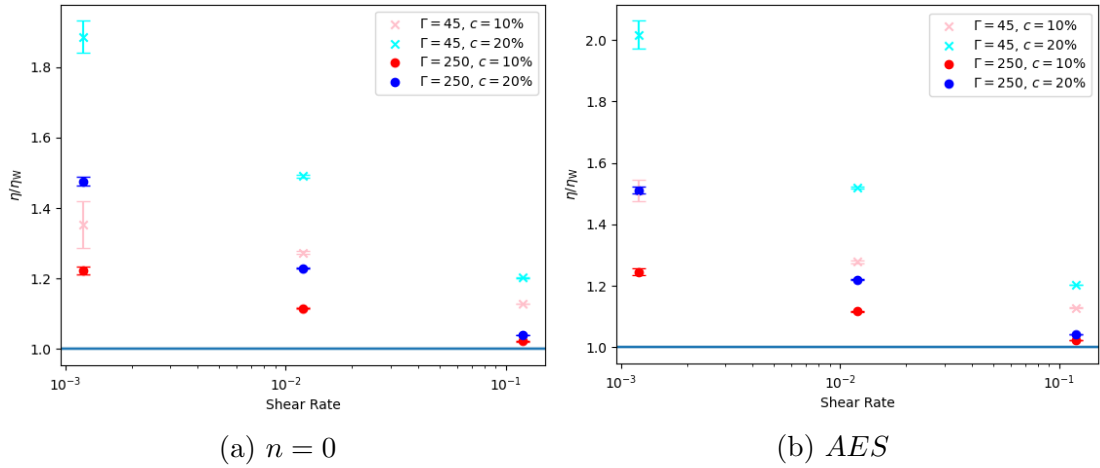
Figure 6.39: Comparison of the ratio of the shear viscosity η calculated in a micellar solution under shear, to the viscosity of water η_{W}. Results shown for varying Γ, concentration c and ethoxylation n.

reference viscosity value.

Ideally the simulations would be conducted at increasingly lower shear rates in order to find a point at which they plateau to a constant η/η_{W} value. While the value for η/η_{W} is lower than what is found experimentally, the results indicate that this may be a result of a high shear rate being used, and that perhaps if the shear rate were lowered for the value of η/η_{W} would reach something that closer matches the experimental results.

6.4.3.4 Summary

In this section we study the impact that shear flow has on micelles in solution. The shear force can have a large impact on the micelles, which at increasing shear rate can lead to micellar break down. A small amount of shear is indicated to slightly enhance aggregation of the micelles, while increasing the size of the micelles and aligning and stretching them in the direction of shear flow. This may be an approach for investigating whether the equilibration of micellar systems can be encouraged by applying a small amount of shear during the micelle formation period, in order to increase the mean aggregation number towards values found experimentally.

Whether the Schmidt number of the solution has any effect on the results

obtained via DPD, has been open to debate in literature. It was found that varying the value of Γ in simulations not subject to shear had no impact on the values of the radius of gyration. The influence of Γ on R_g was found to have even less of an impact than Symeonidis *et al.* [145] found for polymer systems, likely because the micellar structure has a greater effect on the radius of gyration (when compared to a free monomer) than altering the value of Γ would. In this section we determine that the effect of increasing the Schmidt number can alter the values of the radius of gyration at high shear rates. This effect is most pronounced when the molecules are no longer in structured micelles, which is consistent with the behaviour found by Symeonidis *et al.* [145].

The ratio of η/η_W is very different depending on the choice of Γ. However, this analysis was performed at very high shear rates only, when the micellar shape has begun to change, so is not necessarily applicable when the shear rate is lowered.

Chapter 7

Lyotropic Liquid Crystal Phases

The previous chapter studies the effect of varying the concentration and chain length on the micelles formed. For the lamellar and hexagonal phases, these factors are also expected to affect the structure formed. The structures formed can be parameterised by the periodicity of the liquid crystals that form. For the lamellar phase this is primarily the d-spacing, while for the hexagonal phase it is the inter-rod spacing. Experimentally these values are often obtained by small angle X-ray scattering (SAXS) [15, 48, 49]. This experimental method is based on the long-range order in the liquid crystalline states, which give rise to Bragg reflections.

The focus of this chapter will be to investigate if DPD can reproduce the liquid crystalline phases of AES-like molecules, by comparing the liquid crystal structure parameters found using DPD with those found experimentally. Following this we can fully investigate the effect that varying the concentration and ethoxylation has on the phase diagram, and structure of the liquid crystals. This chapter will begin with a short summary of some existing experimental data for AES-like molecules in Section 7.1, before moving on to compare with that found via DPD simulations in Section 7.2.

The final section, Section 7.3 in this chapter considers the impact of shear force on the liquid crystal phases. The shear rate can be varied in order to quantify this impact in terms of the shear rate, and to also investigate the effect that the shear rate has on the viscosity calculated.

7.1 Lyotropic Structure Experiments

This section will briefly highlight existing literature reporting the structure parameters for the lamellar and hexagonal phases, as determined by SAXS. Experiments involve the deflection of X-ray radiation through interaction with electrons in the medium. These experiments result in intensity data as a function of momentum transfer. The positions of peaks in this data are characteristic of the different liquid crystalline phases [48], and the peak locations can be used to calculate the d-spacing and inter-rod spacing values.

SDS is commonly accepted to form the hexagonal phase in the intermediate concentration range, as discussed in Section 2.3.1.2. Table 7.1 lists experimentally obtained inter-rod spacing values for varying concentration and temperature. This work considers the phase formation at temperatures of $\approx 25°$ (or 298K), however values at higher temperatures are also presented in Table 7.1, as the inter-rod spacing for SDS is not found to vary significantly with temperature. It is shown that the value of the spacing decreases with increasing concentration.

For other solutions with values of ethoxylation different to SDS, solutions are more often found to exist in both the hexagonal and lamellar phases at room temperature. The values for d-spacing and inter-rod spacing are most often reported for surfactants as part of a mixture of surfactant types [288] (*i.e.* a solution containing two or more different types of surfactant), as opposed to for a binary system, so experimental data is limited. Values reported for the lamellar spacing for AES at a concentration of 70% are 4.05nm at 30° [289]. For monodisperse solutions of surfactant SLE$_3$S, the reported d-spacing value at a concentration of 72% at room temperature is 4.39nm [4]. As AES has an average ethoxylation value of $n = 1.03$, this may indicate an increase in the d-spacing with increasing ethoxylation at similar concentrations.

The experimental data for the d-spacing and inter-rod spacing at room temperature for these systems was found to be limited, with the SDS solutions being an exception.

	$c = 40$	$c = 50$	$c = 60$
303K [23]	5.44	-	-
313K [24]	4.95 ± 0.5	4.73 ± 0.05	4.60 ± 0.02
343K [25]	4.96 ± 0.1	4.61 ± 0.1	4.36 ± 0.1

Table 7.1: Experimental values of the inter-rod spacing for SDS solutions, as reported by various authors [23–25] at different temperatures. Results presented in units (nm). Note that the concentration c in references [23] and [25] are weight concentrations while in reference [24] c is a volume concentration, however we can assume that the density is close to $\approx 1 \text{g/cm}^3$.

7.2 DPD Simulations for Equilibrium Phases

The previous chapter looked at the phases formed in the concentration range 0–20%, which was confirmed to be entirely micellar. This section will cover the phases formed above this concentration range, which is expected to be in the range of the lyotropic liquid crystal phases.

DPD has been shown to reproduce the phase behaviour of lyotropic liquid crystal systems, including hexagonal [63, 98], cubic [98], and lamellar [63, 97, 98, 275, 290, 291] phases. A variety of experimentally observed phenomena are able to be reproduced using DPD simulations. For example, for lamellar systems, the orientation of lamellar layers relative to the direction of shear, as found experimentally, has been reported [275, 290]. DPD simulations that study the lamellar layer formation under shear can provide insights into why parallel orientations are less stable, for some surfactant types, at higher shear rates [275, 290]. The shear viscosity for the parallel and perpendicular lamellar orientations, with respect to the flow direction, can also be investigated more easily in DPD which can be difficult to measure experimentally [291].

This section will begin with an investigation into the equilibrium phases formed by AES-like molecules in solution. It will begin with an overview of how the simulations were set-up, in Section 7.2.1, including how the simulation box sizes were chosen. The generation of the lyotropic liquid crystal phases is affected by the choice of box size, which will also be discussed in Section 7.2.1. Finally, the determined phase boundaries for solutions containing varying ethoxylation values n

and varying concentration are determined via DPD, and reported in Section 7.2.2. As well as this, values for the d-spacing and inter-rod spacing are calculated, in order for comparison with experimental results reported in Section 7.1.

7.2.1 Simulation Set-Up and Box Size

The set-up for these simulation boxes is nearly identical to the set-up for the micellar solutions described in the previous chapter, with the set-up and parameter choices discussed in Section 6.3.1.1. It was shown in the previous chapter, that as the concentration of the micellar solution increases, the agreement between the DPD results and experimental results increases. Therefore it is hoped that as the concentration increases further, the same parameters can accurately reproduce the structure factors for the lyotropic crystals. The main difference between the set-up of the simulations in this chapter and the micellar case (other than the concentration) is the box sizes that will be used. The choice of box size is more complicated than in the micellar case, and is discussed theoretically in Section 3.5. The effect of varying the box size for the lamellar and hexagonal phases in practice is discussed in the remainder of this sub-section.

7.2.1.1 Box Size: Lamellar Phase

The lamellar layers can form at any orientation within the box, in order to find a d-spacing value that minimises the potential energy of the phase formed. However, there is a relationship between the box size used and the available d-spacing values that the lamellar phase can form, because the structure is restricted by the application of periodic boundary conditions. These restrictions are described in Section 3.5.1, and the resulting constraint described in Eq. 3.46.

In order to confirm this theoretical relationship, a variety of box sizes L are trialled for a test case in which the concentration of the box is set at $c = 70\%$, and the surfactant molecules in the box are defined by hydrocarbon chain length $x = 5$ and ethoxylation $n = 0$. Suppose we define a vector that is normal to

the surface of the lamellar bi-layers, which can be easily calculated by finding the director of the box, from the orientation of the individual molecules within the bilayers, as described in Section 2.2.1. Next define angle θ as the polar angle to this normal vector. Note that this angle θ will always be between 0 and 45° (or $\pi/4$ rad). A plot of how θ varies with increasing box size is shown in Fig. 7.1, and shows the rotation of the lamellar layers in order to adapt to the changing box size. The value of θ gradually increases for a given number κ of bi-layers formed, where it reaches a maximum angle before forming an additional layer and rotating back to $\theta = 0$. An example of lamellar layers formed for two different box sizes is shown in Fig. 7.2. The increasing value of θ can be understood by considering Fig. 3.8, which is a 2-dimensional representation of the problem. The bi-layers must form in order to satisfy relationship $L \cos \theta = \kappa d$, where d is the d-spacing. In order to maintain a constant value of κd, as L increases, $\cos \theta$ must compensate by decreasing, leading to an increase in θ. This then leads to an efficient method of calculating the d-spacing for a lamellar layer system, as simply

$$d = \frac{L \cos \theta}{\kappa}. \tag{7.1}$$

The angle θ is found to be able to be calculated with a high degree of precision, due to the large number of molecules in the simulation box, making this a very accurate method for determining a value for d.

As was previously discussed, although the system can rotate by θ to obtain its ideal d-spacing value to minimise the box energy, the values of θ are constrained to being values that satisfy the periodic boundary conditions. The 'available' values as predicted by Eq. 3.46 for different box sizes is shown in Fig. 7.3. It can be seen that there are more accessible values of d as the box size increases, leading to the conclusion that ideally one would simulate the largest box size possible, in order to investigate d-spacing values for different systems. However, since the number of beads b_N grows as $b_N \propto L^3$, a balance must be made between large enough box sizes and computational work. It is decided that for simulations investigating
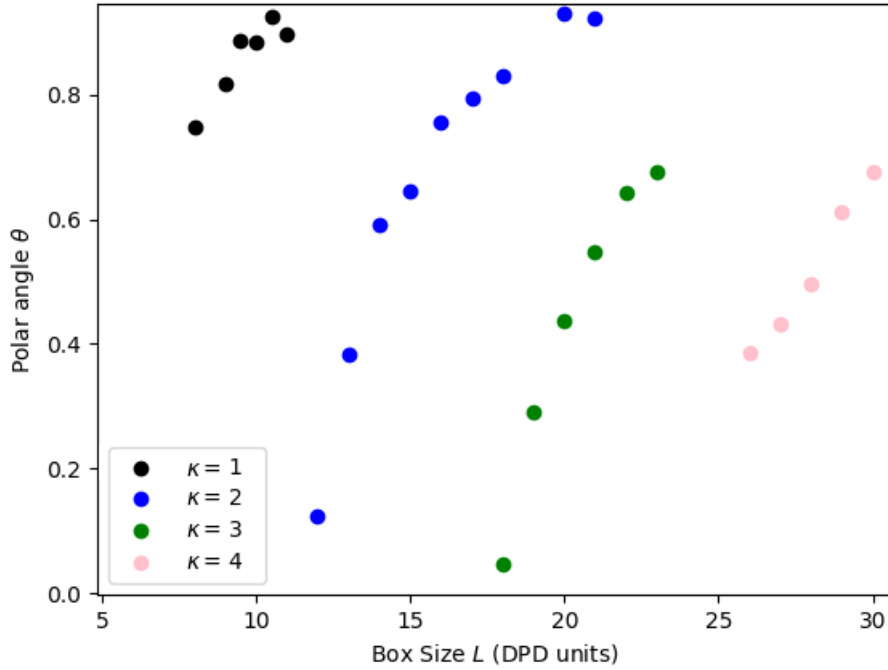
Figure 7.1: The effect of varying box size L on the orientation formed by a simulation of the lamellar phase. The θ is the polar angle, to a vector normal to the lamellar bi-layers, and is presented in units of radians. κ is the number of layers formed in the box. The concentration of the box is $c = 70\%$, and the surfactant molecules in the box are defined by hydrocarbon chain length $x = 5$ and ethoxylation $n = 0$.

how the d-spacing value changes with varying concentration and molecular chain length, that $L = 40$ gives a good balance between computational effort and a large enough box size to give meaningful results.

7.2.1.2 Box Size: Hexagonal Phase

For the hexagonal phases, the impact of varying the box size is more complicated, due to the additional dimension in the problem. Initial simulations trialling concentrations expected to be in the hexagonal range did not yield any stable configurations, which was suspected to be as a result of a long equilibration time. In order to get around this problem, shear was applied to the box, which had the effect of encouraging the phase to form more rapidly. This process and the results will be discussed in the following section. The choice of the box size was therefore made on an estimate of what the unit cell dimensions would be, based on the experimental data listed in Table 7.1. Assuming that the inter-rod spacing
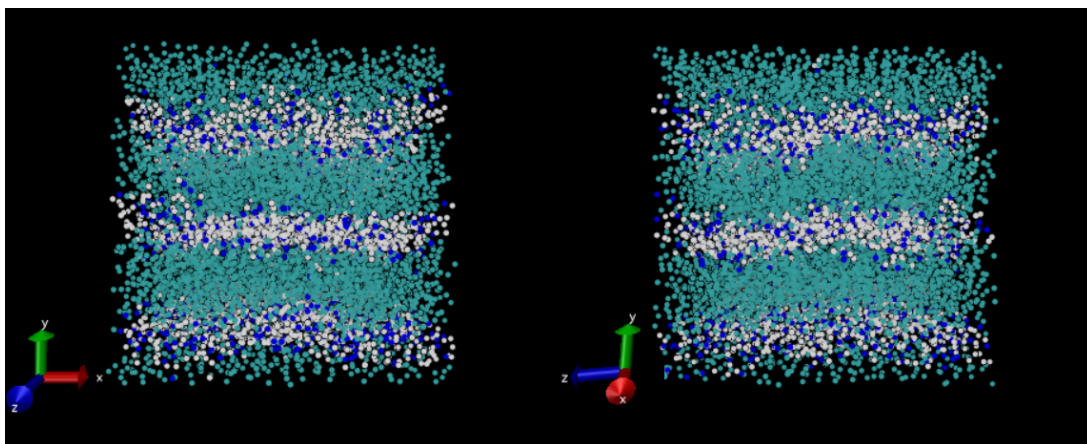
(a) $L = 18$
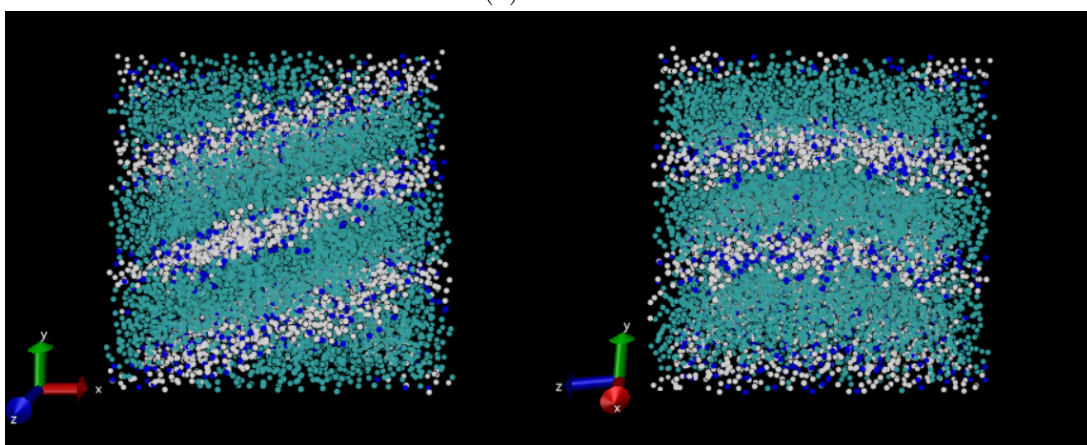
(b) $L = 19$

Figure 7.2: Different orientation of the lamellar layers in to simulations of differing box size. Different colours represent different type of beads: water (white), surfactant molecule (light blue), Na counterion (dark blue). Images created using VMD [13]. The left and right images show the simulation box from two different perspectives.
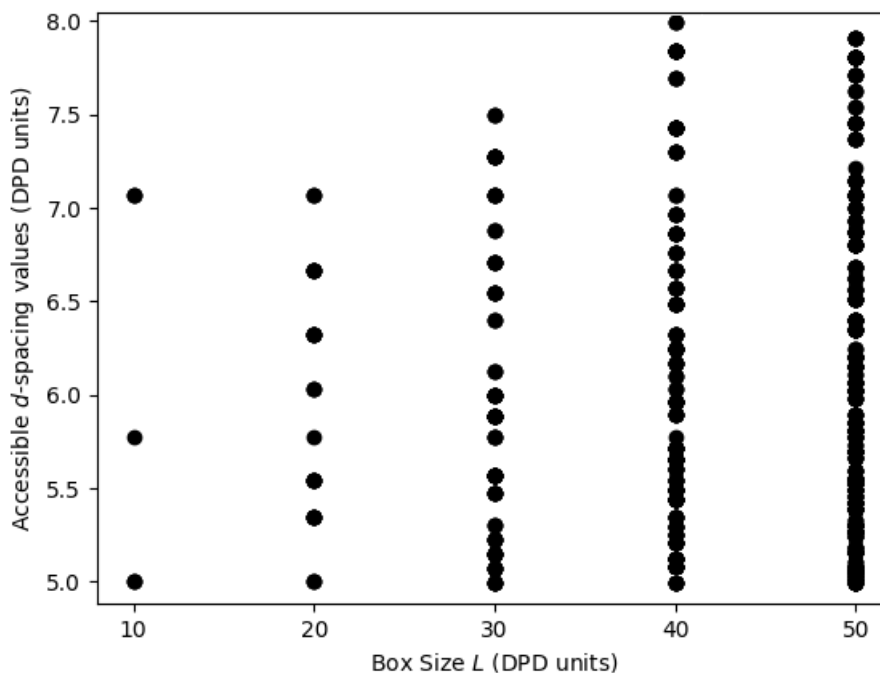
Figure 7.3: The effect of varying box size L on the possible d-spacing values that the bi-layers can take. Points plotted for d-spacing values between 5 and 8.

will take a value of around $r = 5$nm, which (using $r_C = 5.65 \times 10^{-10}$m) is around 9 DPD units, it was determined that a box of size $L = 40$ would provide space for at least 4–5 unit cells within the box.

7.2.2 Equilibrium Phase Diagram and Structure

A variety of concentrations are trialled in the range from 30% to 80%, which is expected to be the region consisting of the liquid crystal phases. For each concentration trialled, a number of simulations investigating the effect of varying the ethoxylation n are also trialled. For each concentration, four monodisperse simulations are performed (for $n = 0, 1, 2, 3$), as well as a case which has varying n, corresponding to the distribution in AES. This is identical to the different cases that were trialled in the previous chapter for the micellar phase. Full details on the number of surfactant molecules for each simulation can be found in Appendix D.

For all of the cases trialled, it is concluded that the phases either form a lamellar or hexagonal phase. No cubic phases are found at any concentration or value

of n. At the lower end of the concentration range ($\approx 30\%$) there appears to be a transition region between the hexagonal and micellar phases, which will be discussed in Section 7.2.2.1.3.

This section will begin with a discussion on the equilibration period for each of the phases, including how the hexagonal phase is induced with the application of shear. Following the determination of the phase behaviour for varying n and concentration, the phase structure can be analysed more closely.

7.2.2.1 Equilibration Period

7.2.2.1.1 Lamellar Phase

The equilibrium simulations in this section were mostly performed on a Tier 2 HPC service (CSD3 [292]), which was more efficient than the simulations performed on the Tier 3 Leeds service (see Section 6.3.1.2 in the previous chapter for discussion on the iteration time). Each node on CSD3 has 32 CPUs (cores), and so the domain is split into non-cubic sub-domains ($4 \times 2 \times 4$). Jobs run on whole nodes by default so the calculation is more efficient increasing the number of iterations per unit time.

It is primarily visual inspection that is used in order to confirm that the lamellar phases have reached their equilibrium structure *e.g.* when there are clear, well defined layers of alternating water and surfactant molecules. An example of the equilibration of a lamellar phase is shown in Fig. 7.4. It is found that the lamellar phases form over a relatively smaller number of iterations, when compared to the time scales involved in equilibrating the micellar solutions, and systems that form hexagonal phases. The lamellar systems of higher concentration generally take fewer iterations to reach an equilibrium state than those with lower concentrations. For example, for the system containing surfactant molecules with $n = 1$, the case in which $c = 80\%$ takes 7.2×10^6 iterations (or 7.2×10^4 time units) to fully equilibrate into separated lamellar layers. This is equivalent to approximately 6,000 CPU hours. While for the same surfactant molecule, a system consisting of
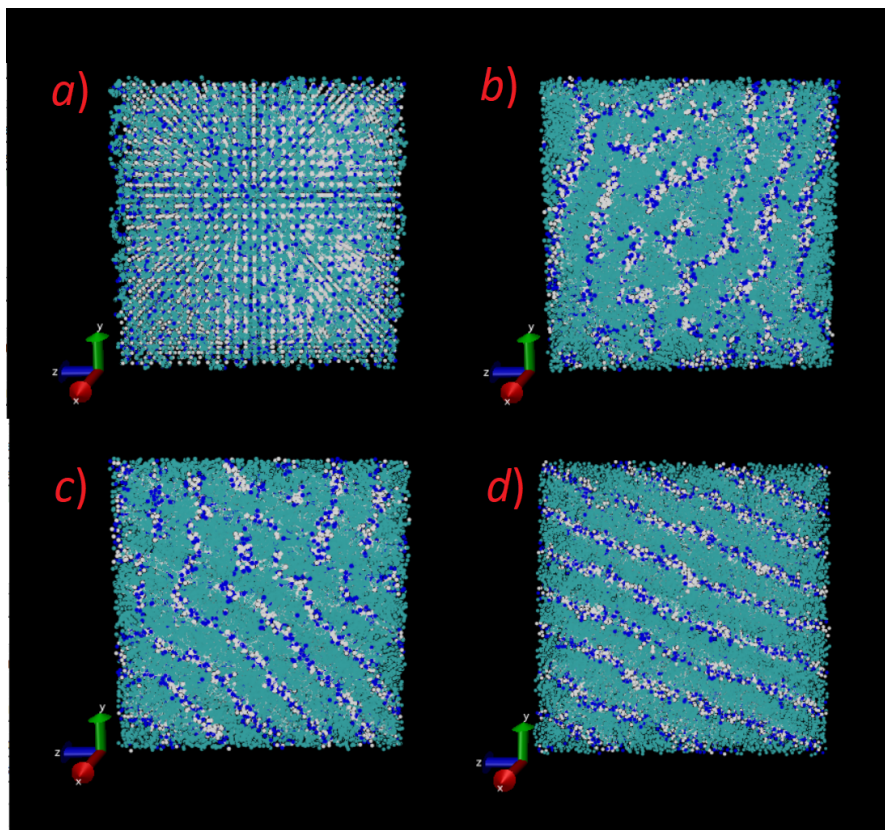
Figure 7.4: The equilibration of a case in which the number of ethoxylation beads $n = 0$ and concentration $c = 80\%$, which results in lamellar layers is shown at different iterations I. a) $I = 0$; b) $I = 2 \times 10^5$; c) $I = 1.4 \times 10^6$; d) $I = 2.2 \times 10^6$. Beads are coloured according to their type: light blue (surfactant chain), dark blue (sodium ions), white (water). Figure created using VMD [13].

$c = 60\%$ takes 1.3×10^7 iterations (or 1.3×10^5 time units). This is equivalent to approximately 10,000 CPU hours. The phases also take fewer iterations to form when there are fewer ethoxy units n in the surfactant molecule, $e.g.$ when $n = 0$, the $c = 80\%$ case takes only 2.2×10^6 iterations (or 2.2×10^4 time units) to form, which is just 1,800 CPU hours.

The lamellar phases are categorised into two different cases, which will simply be referred to as 'perfect' and 'imperfect'. In higher concentration cases, the phase typically forms into well defined, discrete layers of alternating water and surfactant layers. The parallel layers of water do not connect once the phase has formed, as do not the equivalent layers of surfactant molecules. However, for cases that have a concentration which is on the edge of the lamellar region (before transformation into a hexagonal phase), the lamellar phase can form with
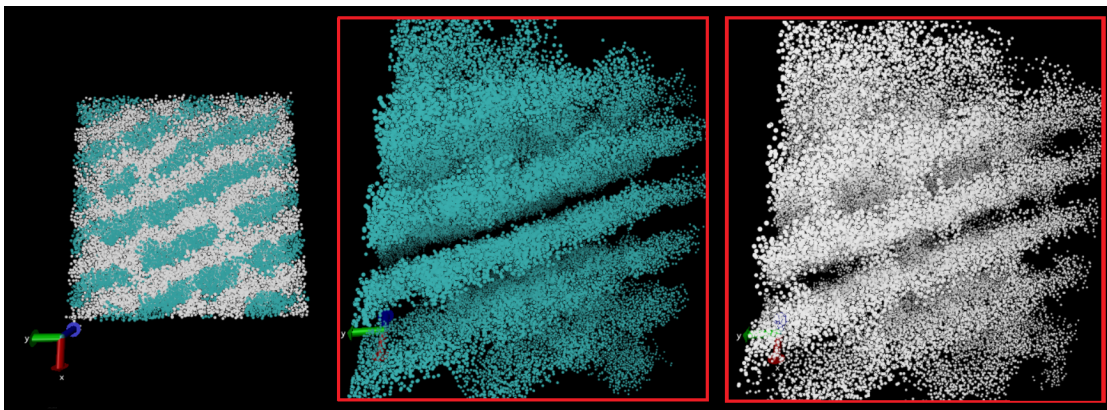
Figure 7.5: Simulation case in which the number of ethoxy groups $n = 1$ and the concentration $c = 60\%$. The phase forms lamellar layers, although while the surfactant layers are well separated (blue), the water layers form dynamic bridges (white). Figure created using VMD [13].

bridges that spontaneously form and disconnect between the alternating water layers. This behaviour is shown in Fig. 7.5. These bridges are shown to persist in the simulation, although still in dynamic motion, even with further iterations.

7.2.2.1.2 Hexagonal Phase

The equilibration period for the hexagonal phase is significantly longer than for lamellar structures. Boxes of size $L = 40$, with concentrations which are expected to form the hexagonal phase, do not reach a steady, structured formation when run over significantly larger numbers of iterations than the lamellar cases. A selection of simulations are performed at a smaller box size of $L = 20$, in order to investigate if equilibriation can be encouraged when the box size isn't as demanding. Cases trialled at this box size are $c = 40\%$ with $(n = 0, 1, 2)$ and $c = 50\%$ with $(n = 0, 1, 2)$. This would, of course, greatly decrease the accessible rod spacings that can form *vs.* an $L = 40$ sized box. Over the course of 9×10^7 iterations, only two of these cases form an hexagonal phase, which are the two concentration cases with $n = 2$, both at values of average inter-rod spacing $r \approx 10$. Therefore, an different approach is required in order to investigate the hexagonal phases.

It is found that when shear is applied to the simulation box (with size $L = 40$), the hexagonal phase forms much more quickly. It can be confirmed that the hexagonal phase structure formed by this method is stable, by the preservation

241

of structure once the shear is removed. The application of shear does however have the effect of orientating the phases such that the hexagonal rods lie in the in-shear-plane orientation, as described by Fig. 4.10. This then confines the formation of the hexagonal phase to being able to orientate itself in only 2-dimensions (as opposed to 3-dimensions without shear), in order to find the optimal inter-rod separation r. This leads to the restrictions on r imposed by the periodic boundary conditions, as described in Section 3.5.2. An example of how shear can be used to encourage the formation of the hexagonal phase is shown in Fig. 7.6. For the case in which shear is applied to the simulation box, the molecules take on a structured hexagonal configuration. Without shear the molecules do not, even over a much larger number of iterations, and it is assumed the box is still undergoing equilibration. Therefore, in the interest of time constraints, the study of the structure of hexagonal phases at different concentrations and values of n will focus on the final configuration as obtained by inducing the phase with shear.

7.2.2.1.3   Worm-like Micellar

For concentrations just above the micellar region ($\approx 30\%$) there appears to be a phase that forms that is neither entirely micellar or hexagonal. On first observation, the simulation box appears to consist of inter-woven micellar rods, which could be assumed to be a poorly equilibrated hexagonal phase. Once subjected to shear, these micelles align in the direction of shear, just has the hexagonal phase does. To a degree, these micellar rods also form hexagonal like separations, between the stretched micelles, but do not necessarily form infinitely long rods. Gaps can be observed in the rods that lie in the direction of shear. This phase cannot be classed as a true hexagonal phase, due to the gaps in the rods, but also because once the shear force to the box is removed, any structure which does resemble hexagonal like separation between rods, quickly breaks down. An example of a the phase structure before and after shearing is shown in Fig. 7.7.
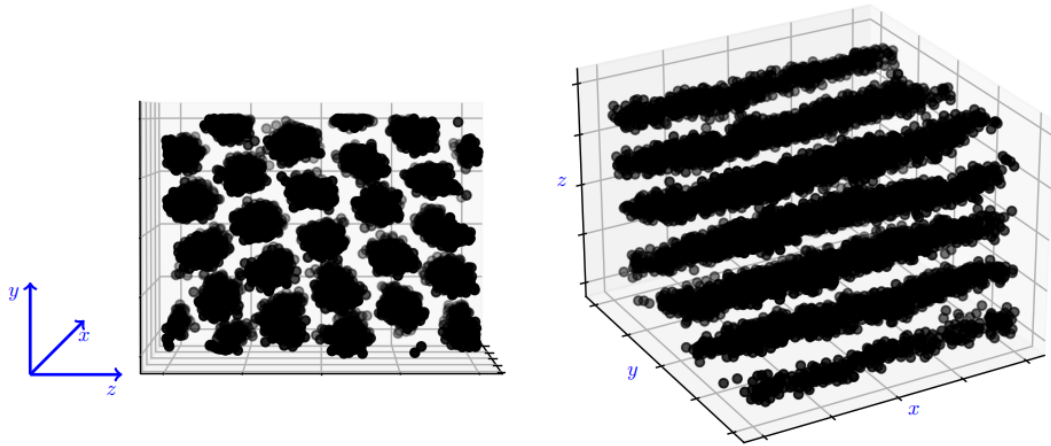
(a) With shear. Couette flow in the simulation box is induced by moving the x-z plane in the x direction, so that the hexagonal rods are aligned along the x-axis, and a velocity gradient is induced in the y direction.
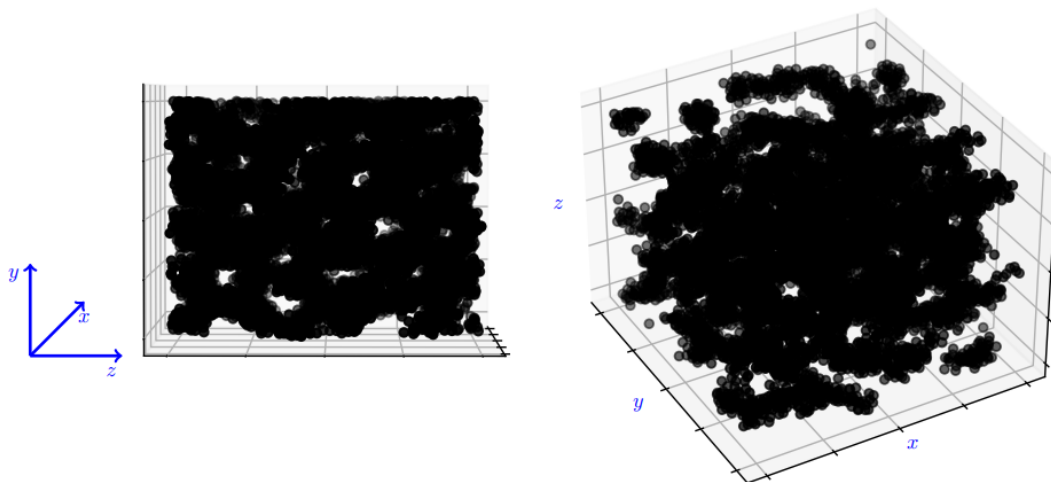
(b) Without Shear. An equilibrium phase does not form in the run period for this case.

Figure 7.6: Formation of the hexagonal phase in a cubic box with periodic boundary conditions of size $L = 40$. The surfactant molecules in the example shown take a distribution of ethoxylation n, in order to model AES, at a concentration of 40%. Only the surfactant molecules are plotted for clarity, the space in between the rods is filled with water beads (not shown). Fig (a) shows the resulting bead configuration after 3×10^6 iterations, while Fig (b) shows the lack of phase formation after 5×10^7 iterations.
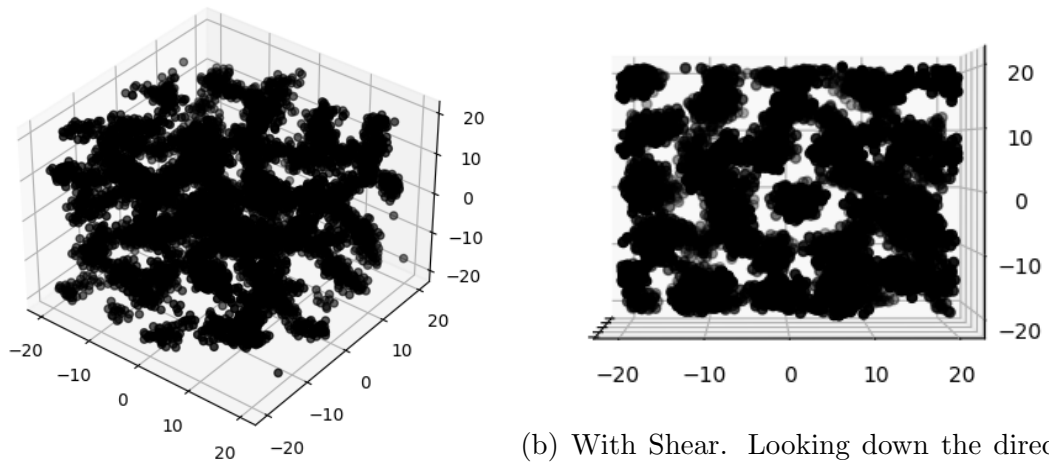
(a) Without Shear

(b) With Shear. Looking down the direction of partially formed rods.
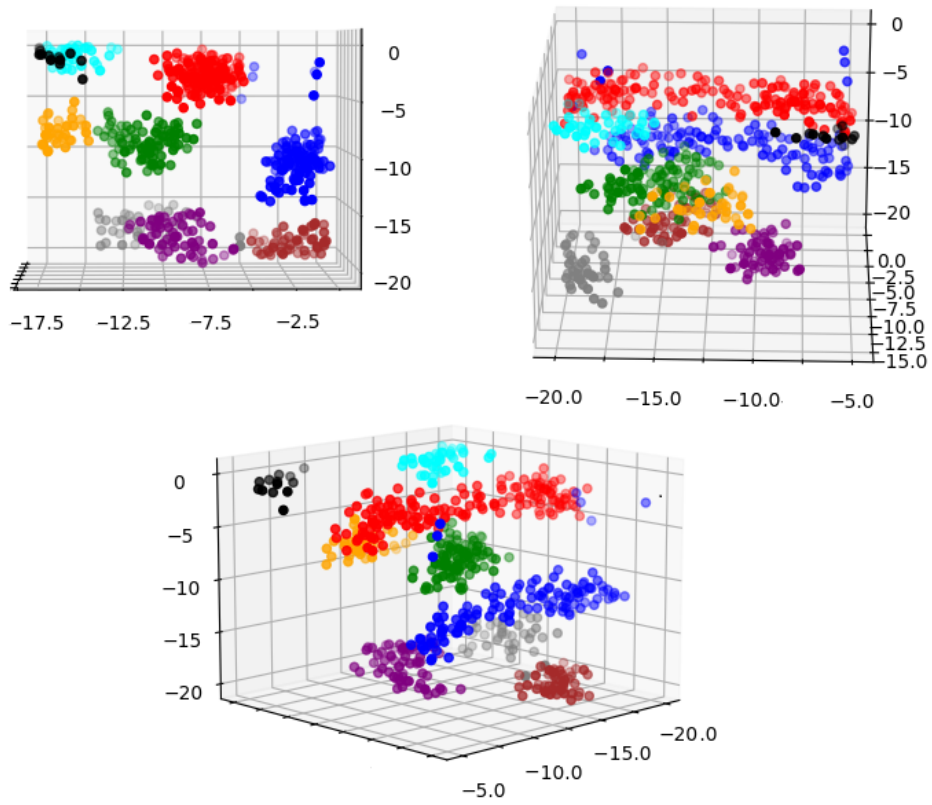
Figure 7.7: DPD simulation with concentration $c = 30\%$, for with (a) and without (b) shear. Figure (c) shows a sub-region of the domain when shear is applied. The sub-region is selected to show that there are some infinitely long rods which lie in the direction of shear flow, but there are also broken rods and smaller micelles in the domain. Simulation box has size $L = 40$.
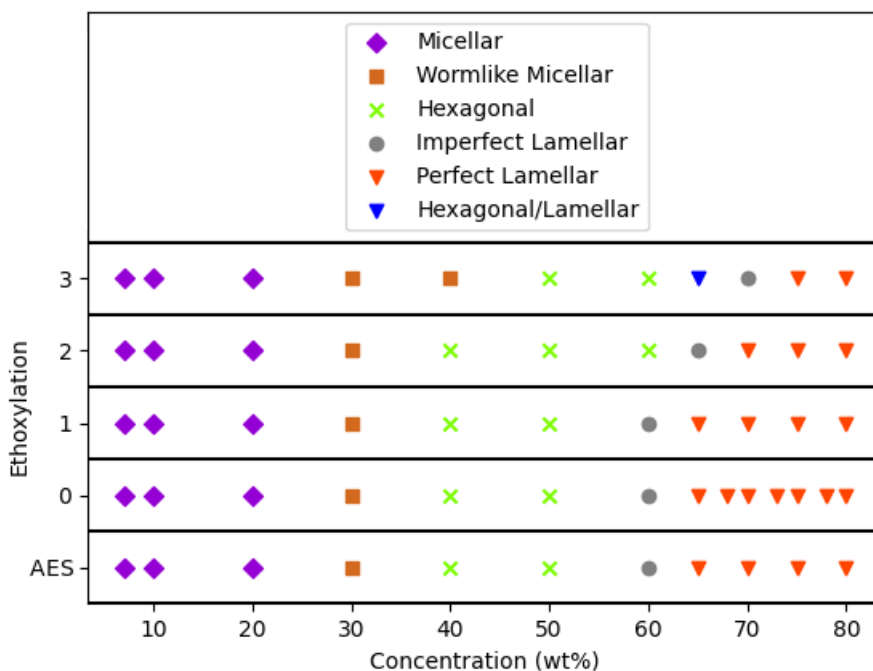
Figure 7.8: The phase diagram, as determined via DPD, for a varying values of ethoxylation n.

7.2.2.2 Phase Diagram

The resulting phase behaviour determined for varying n and concentration is shown in Fig. 7.8. Five main phases are plotted, including the micellar region (discussed in detail in the previous chapter); the worm-like micellar phase that is explained in Section 7.2.2.1.3, the hexagonal phase, and two lamellar phases (perfect and imperfect). There is also a sixth case labelled as 'Hexagonal/Lamellar' for the case in which $n = 3$. In this case the phase formed a hybrid of the hexagonal and lamellar phases, in which parallel layers formed, but these layers did then not completely break down into individual rods, although some non-uniformity is seen across the layer. This case is illustrated in Fig. 7.9. The phase is pictured from the same view point as that shown for a perfect hexagonal phase in Fig. 7.6 (*i.e.* down the length of the rods). If the phase in Fig. 7.9 was hexagonal, we would expect to see individual rods forming, while if it was lamellar the layers would have constant thickness from the top to the bottom of the box.

The phase boundary between the hexagonal and lamellar phases shifts to higher concentration, at larger values of n. As well as this, the boundary between the
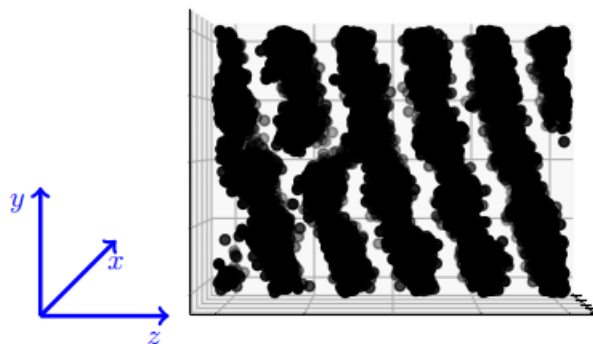
Figure 7.9: Phase formed in the case where $n = 3$ at 65%, black molecules are the hydrocarbon portion of the surfactant chain and the other beads are not shown for clarity. The phase almost takes the form of parallel layers, but the layers form interconnecting rods. This phase is concluded to be a hexagonal/lamellar hybrid.

micellar phase and hexagonal phase shifts slightly at $n = 3$. The location of the hexagonal-lamellar phase boundary is fairly consistent with that determined experimentally for AES in Chapter 4. In Chapter 4, there was some uncertainty as to what kind of phase was formed by a concentration of 28%. POM imaging suggested that the phase took the form of an hexagonal phase, but rheologically it behaved very different from the other hexagonal phases at higher concentrations. For example, solution handles very differently to what one might expect from an hexagonal solution (*i.e.* it flows relatively easily, compared to the gel like behaviour of a hexagonal phase). In the Raman spectroscopy measurements, presented in Chapter 5, the ratio of the *trans* to *gauche* conformations fits more closely with the trend in the micellar region. It is possible that at a concentration of 28%, the phase is subject to shear induced phase transition. The Raman measurements can be performed with no application of shear to the sample before measurement, however the act of preparing the sample for POM imaging applies some shear, in order to prepare the thin layer. DPD results support this claim, as they show that the phase forms something hexagonal like while subject to shear, but that this quickly breaks down once the shear is removed.

Focus will now turn to investigating the different d-spacing and inter-rod spacing values, for the phases illustrated in Fig. 7.8.

7.2.2.3 Values For d-spacing and Inter-rod Spacing

7.2.2.3.1 Lamellar Phase

A plot showing the d-spacing formed for lamellar cases of varying concentration c and ethoxylation n is shown in Fig. 7.10. Note that results are not shown for cases where ($n = 3$ and $c < 70$) and ($n = 2$ and $c < 65$) as these cases form a hexagonal phase to be discussed in the following section. Also shown are the available values of the d-spacing that are accessible in a box of size $L = 40$. It is worth consideration that the spacing between the available d-spacings increases at higher d-spacings values. Therefore if we were to consider running simulations containing molecules that were longer in length than those trialled, it would be likely to be necessary to increase the size of the box to increase the number of available orientations, and therefore spacings, the layers could take. The layer separation is shown to increase with increasing n, and decrease with increasing concentration. This trend with concentration is consistent with what is found experimentally for most types of surfactant [49, 50, 53, 54].

There is only a small amount of difference between the spacing formed by the $n = 1$ and AES simulation cases. The AES distribution case has an average value of $n = 0.76$ in the simulations, which explains why the values for AES are slightly below the ones for when $n = 1$. The fact that the simulation is a distribution of chain lengths seems to have relatively little impact on the d-spacing formed, beyond being impacted by the average value of n. An interesting consideration is whether the d-spacing for the AES case can be calculated using the d-spacing from the monodisperse simulations (with $n = 0$ and $n = 1$). Therefore, we calculate values

$$d_{\text{Interp}}^{\text{Spacing}} = \frac{d_{\text{AES}}^{\text{Spacing}} - d_0^{\text{Spacing}}}{d_1^{\text{Spacing}} - d_0^{\text{Spacing}}} \tag{7.2}$$

for each value of concentration. In this equation d_0^{Spacing}, d_1^{Spacing} and $d_{\text{AES}}^{\text{Spacing}}$ are the d-spacings for the $n = 0$, $n = 1$ and AES cases respectively. For concentrations 65–80%, we find this takes an average value of $d_{\text{Interp}}^{\text{Spacing}} = 0.81 \pm 0.03$ (where $c = 60\%$ is excluded as it is assumed to be an anomalous value). Comparing this with

the average ethoxylation of AES as $n = 0.76$, implies that the d-spacing for the polydisperse lamellar phase can be reasonably interpolated from the monodisperse lamellar calculations.

The values in Fig. 7.10 can be converted into real units using $r_C = 5.65 \times 10^{-10}$m as the conversion factor. Experimentally obtained values via SAXS include: $d = 4.39$nm at 72% for $n = 3$; and $d = 4.05$nm at 70% for AES (see Section 7.1 for details on experimental data). Equivalent values from Fig. 7.10 produce values in real units of $d = 4.35$nm for $n = 3$ and $d = 3.57$nm for AES (note that although a calculation wasn't performed for $n = 3$ at 72%, the values for 70% and 75% simulations are identical, so this value is interpolated to be identical in a 72% case). While there is excellent agreement for the solution case $n = 3$, there is more of a difference between the experimental value and the DPD value for AES. Since, in order to model AES using a finite number of molecules, the distribution for AES was simplified. Most of the long molecular chains were removed from the distribution and this could be the reason behind the smaller value for the d-spacing.

In practice, the lamellar phase is not found experimentally for SDS at room temperature. Although the generation of the lamellar phase in DPD at this temperature has also been reported by other authors modelling SDS [63]. Experimentally, the phase at room temperature may be a non-uniform solution consisting of regions where the SDS still exists in crystallised form. The existence of the phase in DPD may be due to the fact that this behaviour would be hard to reproduce in DPD, due to the relatively small box size (relative to the length scales in the non uniform scenario).

7.2.2.3.2 Hexagonal Phase

When using box sizes $L = 40$, for simulations which are not found to form lamellar layers under equilibrium conditions, these can then be inferred to be belonging to slowly forming hexagonal phases, which is then confirmed upon the application of shear. The simulated hexagonal phases can be described by a unit cell, as shown
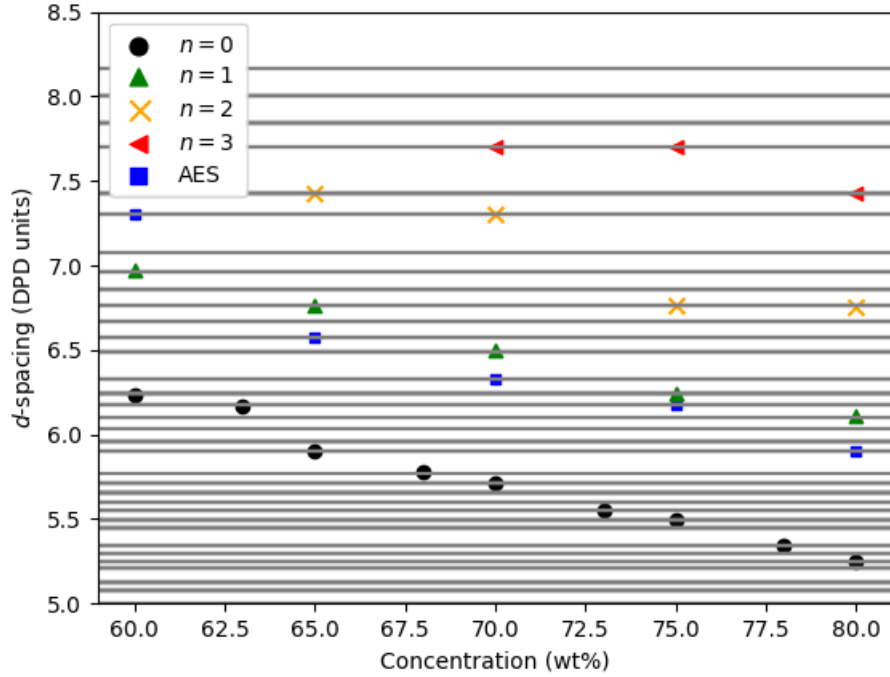
Figure 7.10: The d-spacing values for the lamellar phase, for varying concentration and ethoxylation n, in a box of size $L = 40$. The horizontal lines in grey represent the available d-spacings for a box of size $L = 40$, as calculated using Eq. 3.46.

in Fig. 2.10. Due to the restrictions of the periodic boundary conditions, $|\vec{a}| \neq |\vec{b}|$.
Therefore for each simulated hexagonal phase, three different length values can be calculated ($|\vec{a}|$, $|\vec{b}|$ and $|\vec{a} + \vec{b}|$), as well as an average of these three lengths for a value of the average inter-rod spacing r. For the identified hexagonal phases, the variation of the inter-rod spacing r with n and concentration, is shown in Fig. 7.11.

For the hexagonal phase it is more difficult to create a finite list of the accessible spacing values for a given box size L, as was done for the lamellar phase. This is because while in theory there exists a large number of varying integers that can satisfy Eq 3.47, in practice the rods form in such a way that appears to keep the magnitude of lattice vectors $|\vec{a}|$ and $|\vec{b}|$ as similar as possible. This makes sense from a logical point of view, as the case in which $|\vec{a}| = |\vec{b}|$ is thought to minimise the potential energy. Based on the restrictions given by Eq. 3.47 alone, there are a huge number of possible inter-rod spacings that the unit cell can take. If the restriction is imposed that the difference in length of the vectors defining the unit
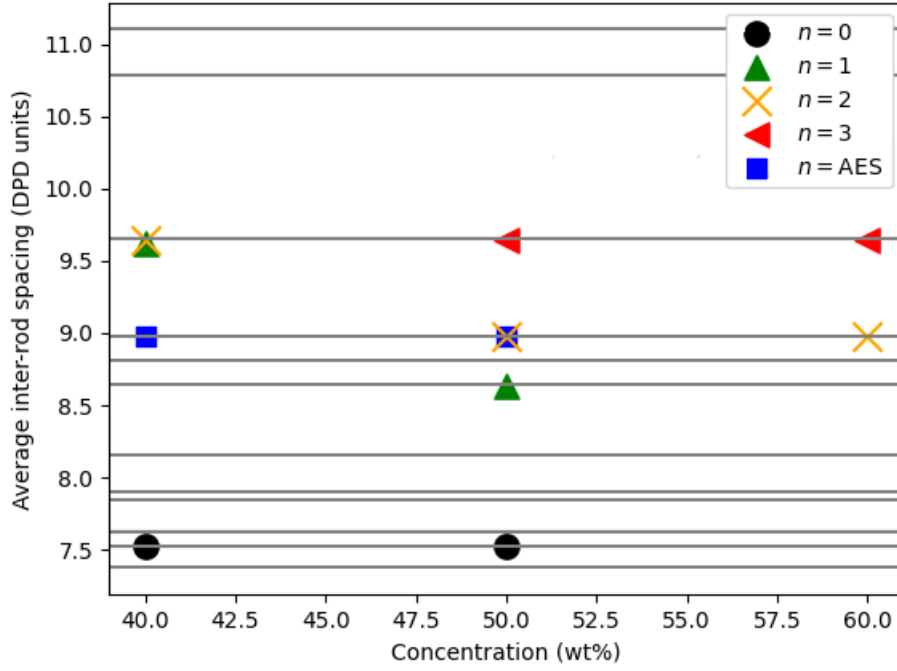
Figure 7.11: The average inter-rod spacing value formed in hexagonal phases at different concentrations and values of ethoxylation n in the surfactant chain. The horizontal lines are the available spacings, as obtained by the method described in the text.

cell, should not be more than a particular cut off d_{co}, a reduced number of available inter-rod spacings r can be obtained. Mathematically this can be written as

$$|(|\vec{a}| - |\vec{b}|)| < d_{\text{co}},$$

$$|(|\vec{a}| - |(\vec{a} + \vec{b})|)| < d_{\text{co}}, \qquad (7.3)$$

$$|(|\vec{b}| - |(\vec{a} + \vec{b})|)| < d_{\text{co}}.$$

It is observed that in the DPD simulations, the unit cell never forms for cases in which $1.5 < d_{\text{co}}$. Therefore an estimate for the available inter-rod spacings r can be obtained applying the cut off to be $d_{\text{co}} = 1.5$. Combining the above constraint and the restrictions given by Eq. 3.47, the unit cell can form average inter-rod spacing values illustrated in Fig. 7.11 by horizontal lines. The values of the lattice vectors that define the unit cell that results in these average inter-rod spacings are listed in Table 7.2 (which are included so that the reader can observe the variation in the three defining spaces of the unit cell). It is clear from these horizontal lines

that the number of available inter-rod spacings that can be obtained in a box size of $L = 40$ is relatively low. This is particularly true for the higher values of inter-rod spacing r, as the jump between $r = 9.65$ to the next available value $r = 10.8$ is relatively large. In the range $7.5 < r < 11$ the number of available values for a box of size $L = 40$ is just 10, while an increase to box size $L = 50$ is found to generate 45 different available values of r, when applying the same conditions as those used to plot the horizontal lines in Fig. 7.11. However, based on the scaling discussed in the previous chapter (see Section 6.3.1.2), an increase in box size from $L = 40$ to $L = 50$ would take over twice as long to complete the same number of iterations. Additionally, the choice of a cubic box usually means that the hexagonal phase forms in a way in which the lattice vectors are not the same (*i.e.* $|\vec{a}| \neq |\vec{b}|$), and therefore is strictly speaking not a hexagonal phase. It might be more ideal to simulate the phase in non cubic box, in order to generate phases in which $|\vec{a}| = |\vec{b}|$.

$|\vec{a}|$	$|\vec{b}|$	$|(\vec{a} + \vec{b})|$	Average r
10.995	10.995	11.314	11.101
11.180	11.180	10.000	10.787
10.000	10.000	8.944	9.648
8.868	9.366	8.696	8.977
8.498	8.498	9.428	8.808
9.330	8.616	8.000	8.649
7.693	8.690	8.081	8.155
8.000	8.538	7.180	7.906
8.000	7.775	7.775	7.850
7.906	7.071	7.906	7.628
7.373	7.068	8.131	7.524

Table 7.2: The lengths of the lattice vectors that define the unit cell that forms for an hexagonal phase under shearing, in a box of size $L = 40$. The values of $|\vec{a}|$, $|\vec{b}|$ and $|\vec{a} + \vec{b}|$ can be averaged to find the average inter-rod spacing r for a given unit cell. The values listed are those that satisfy the conditions given by Eq. 3.47 and 7.3, in which $d_{co} = 1.5$.

From the results shown in Fig. 7.11, conclusions can still be made about the effect of varying ethoxylation n and concentration, despite the small number of available inter-rod spacings. There is an increase in the spacing r with increasing

n, as well as a decrease in spacing r with increasing concentration. This behaviour is similar to the lamellar case.

The decrease in r with increasing concentration is what is expected experimentally, from the results presented in Table 7.1. The inter-rod spacing for SDS at room temperature ($n = 0$) is found, via DPD, to take a value in real units of $r = 4.25$nm. This is lower than the expected values of 5.0nm (40%) and 4.7nm (50%) which are found experimentally. This is similar to the lamellar phase, in which the d-spacing is also under predicted.

It is discussed in Section 4.3.3 that experimentally the hexagonal rods tend to form in the parallel orientation described in Figure 4.11, when subject to an applied shear. The alignment of the rods in the direction of shear in DPD is consistent with experiment. The unit cell also forms in a way that is consistent with a parallel or near parallel orientation. For most cases, the phase cannot form the perfect arrangements shown in Figure 4.11, because they rotate in order to form the desired inter-rod spacing. However, the average inter-rod spacing $r = 9.648$ is formed by a unit cell where the length of one of the lattice vectors is exactly 10 (*i.e.* the box size divided by the length of the lattice vector is an integer $40/10 = 4$). Therefore, the phase forms in a way that is a perfect parallel or perfect perpendicular orientation, as described by Figure 4.11. There are four cases in Fig. 7.11 which form a hexagonal lattice using this set of lattice vectors. There is likely to be preference of the hexagonal phases to form the parallel arrangement, because all four of these cases form parallel arrangement (*i.e.* the lattice vector $\vec{a}$ is perpendicular to the x-axis).

7.2.2.4 Molecular Changes due to Phase Change

In the previous chapter, it was discussed how the radius of gyration R_{g} of individual molecules can be influenced by the aggregation number of the micelle that they belong to. This section will present the average radius of gyration values for concentrations across the entire phase diagram, including the liquid crystal phases

discussed in this chapter, as well as a summary of the results for the micellar phases discussed in the previous chapter.

Experimentally, it was also determined in Chapter 5, using Raman Spectroscopy, that the conformation of molecules can be influenced by the concentration and phase behaviour of a solution. The second half of this section will look at whether DPD can capture the same conformational behaviour that is found experimentally for AES solutions of varying concentration.

7.2.2.4.1   Radius of Gyration R_{g}

Fig. 7.12 shows the calculated radius of gyration for molecules in solutions of different concentrations. For the polydisperse solution representing an AES solution, the average radius of gyration can be broken down into the different components that contribute to the AES distribution, which is shown in Fig. 7.13. The overall value of R_{g} for the AES simulations, presented in Fig. 7.12, is the number average of the different values of n in Fig. 7.13.

Generally, the figures show that the radius of gyration increases with increasing concentration. The average radius of gyration increases in the micellar phase, due to the increase in aggregation number. Once the solution enters the worm-like micellar phase described in Section 7.2.2.1.3, the relationship between R_{g} and the concentration becomes less obvious across differing n values. Certainly for the SDS case ($n = 0$) the value of R_{g} increases in the micellar region, largely plateaus in the worm-like/hexagonal region, and then increases linearly in the lamellar region. The value for the radius of gyration can be affected by both the shape of the molecule (how coiled it is) and how long it is (how stretched), which may be contributing to the confusing relationship. For example, the molecule in the lamellar phase is often assumed to be in a fairly *trans* configuration, which is likely to be why it has a larger radius of gyration than a molecule in a micellar phase. However, with increasing concentration, and changing thickness of the lamellar layer, the molecule could become more stretched or squashed, affecting its radius of gyration. In particular there is a definite decrease in the radius of gyration,

(a) $n = 0$

(b) $n = 1$

(c) $n = 2$

(d) $n = 3$

(e) $n = AES$
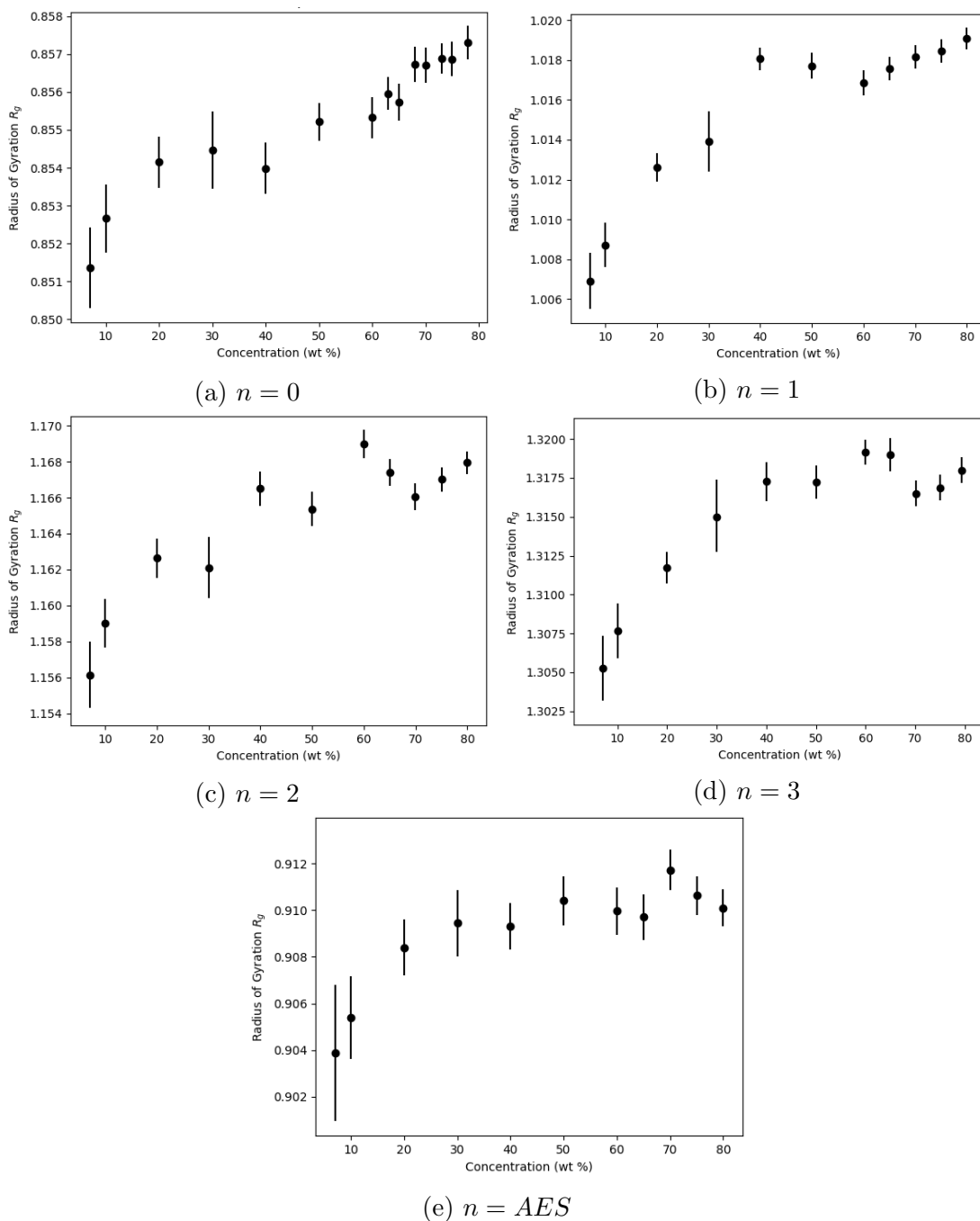
Figure 7.12: R_g plotted against concentration for a variety of choices of ethoxylation values n. The error bars represent the standard deviation.

(a) $n = 0$

(b) $n = 1$

(c) $n = 2$

(d) $n = 3$
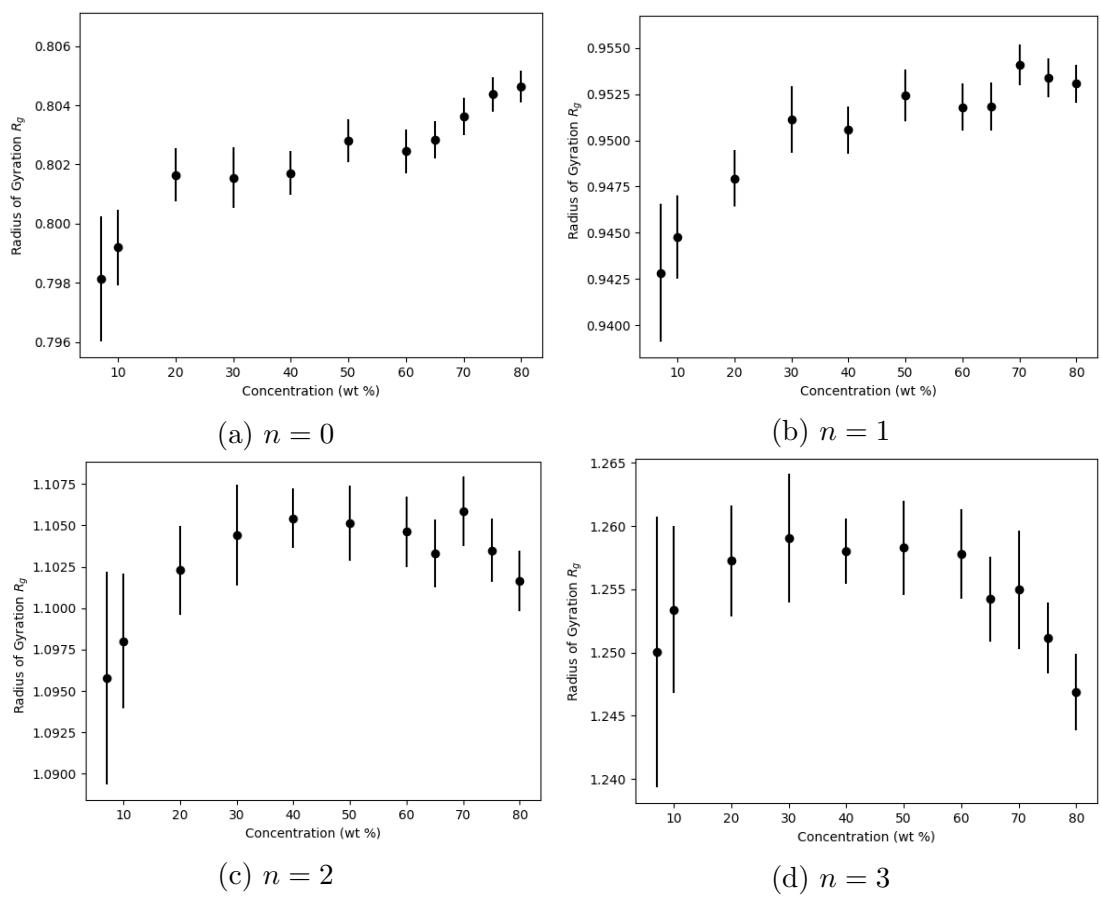
Figure 7.13: R_g plotted against concentration for the molecules of varying n making up an AES solution. The error bars represent the standard deviation.

over the lamellar phase period, for the $n = 3$ component molecules of the AES distribution (see Fig. 7.13). In the Raman spectroscopy measurements, it was the conformation, as opposed to molecular length, that was being measured. Therefore in the following subsection, the *trans/gauche* ratio across the phase diagram will be studied.

7.2.2.4.2   Ratio of *trans/gauche* Conformations

In order to compare with the experimental results for the conformational changes due to phase change, obtained via Raman Spectroscopy in Chapter 5, a value for the *trans/gauche* ratio is calculated from the DPD simulations. The meaning of *trans* and *gauche* conformations of a molecule is defined in Section 5.1.

For the purpose of analysis in numerical simulations, a range is usually defined for which an angle can be classified as *trans* or *gauche*. In this work the following definition is used: *trans* $(150° < \theta < 180°)$ and *gauche* $(30° < \theta < 90°)$. The angle θ is defined in Fig. 5.1 as the dihedral angle. Experiments obviously cannot calculate these dihedral angles exactly. Instead experiments allow us to find estimates for the number of molecules in the *trans* or *gauche* state, by the different vibrational spectra produced by these two molecular states, when using an experimental technique such as Raman Spectroscopy.

In the experimental work, the reported *trans/gauche* ratio relates to the dihedral angle between bonded atoms. The ratio of *trans* to *gauche* bonds as calculated via DPD simulation is, strictly speaking, not directly equivalent. This is due to the coarse graining of the molecule, since the angle which is calculated, is between connected beads (which contain a number of atoms). However, since the surfactant hydrocarbon chain is relatively long, it is still expected that calculation of the *trans* and *gauche* angles between beads will yield valuable information about the conformation of the molecule. In particular, the effect that mesophase has on molecular conformation.

The value of the ratio *trans/gauche* is plotted in Fig. 7.14. Three distinct regions are identified based on the value of the ratio for each case of n, and fitted

independently with linear relationships. The relationship between the phase that a solution belongs to and the shape of a molecule, is more more clear in this case than it was for the radius of gyration. The cases corresponding to higher values of n are found to correspond to lower values of the ratio, indicating that the molecule is more prone to increased curvature when the length of the molecule is increased. This is true for all three of the distinct regions in concentration.

Recall that the worm-like micellar regions (cases around 30% concentration) showed different structures before and after shear. Once subjected to shear they form hexagonal like separations between the stretched micelles, but do not form infinitely long rods. For these cases, calculations were performed for simulation boxes before and after shear has been applied. Interestingly, very little difference was found between the two cases. This is illustrated with the results from one of the shearing cases also being plotted in Fig. 7.14, which shows very little difference with the non-shear case.

It is difficult to compare quantitatively with the results obtained experimentally, as Raman spectroscopy only provides an estimate of the ratio of *trans/gauche* conformations. The Figs. 5.11 and 5.15 given in Chapter 5 provide the best estimates for the conformational variation with concentration. The Raman spectroscopy results show that the ratio of *trans/gauche* increases with increasing concentration across the phase diagram, however the ratio increases in each phase region at a different rate. The ratio is most dependant on concentration in the lamellar region, followed by the micellar region, with a weak dependence on concentration in the hexagonal region. This same behaviour is broadly found from the DPD calculations, however the boundary location is slightly different. In the DPD calculations, the shift from the first unique region to the (relatively concentration invariant) middle range of the phase diagram occurs at a lower concentration than identified by Raman spectroscopy. The transition from this middle region, into the third unique region in Fig. 7.14, closely aligns with the location of the phase change into the lamellar phase, as illustrated in the DPD phase diagram in Fig.
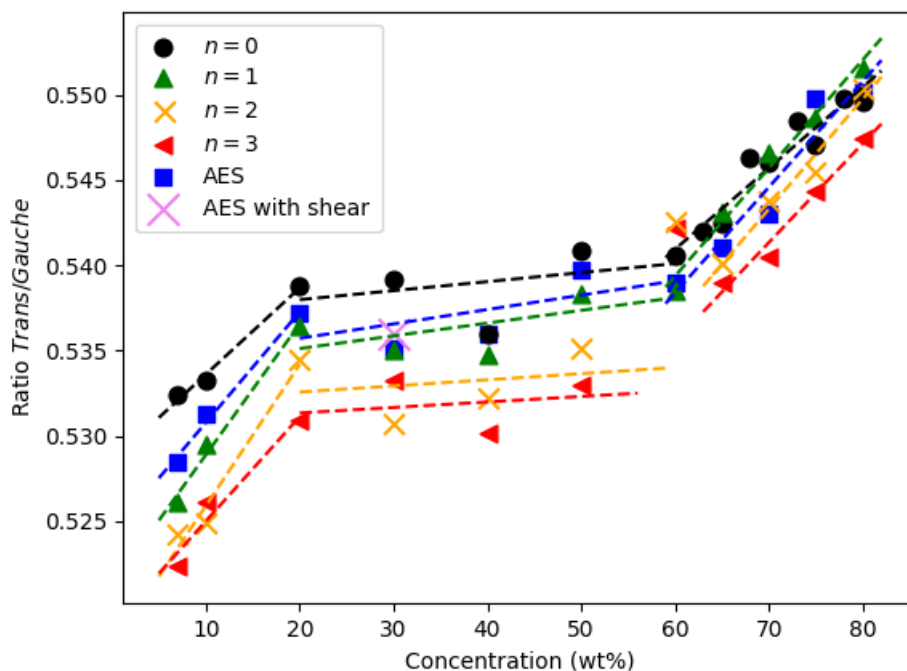
Figure 7.14: The ratio of *trans* to *gauche* conformations as obtained via DPD simulations. Note that the error bars are not included as they obscure the scale of the plot, and therefore they are omitted for clarity. Fits are performed in regions where a trend with concentration is observed for a particular value of n. Also included is one case where the result was obtained from a simulation subject to shear, for comparison.

7.8.

There are two somewhat anomalous data points in Fig. 7.14, belonging to $n = 2$ and $n = 3$, at a concentration of 60%. At this concentration and value of n we are at the upper edge of the hexagonal phase window. This anomalous point could be because the hexagonal phase that forms is the unnatural equilibrium phase for this simulation case. This could be because there is no natural inter-rod spacing available in the simulation box size, or the more likely scenario is that naturally the phase would form an isotropic cubic phase. Experimentally, the cubic phase for SLE$_3$S forms in the range 62—67% [4]. In this work the hexagonal phase is encouraged to form via the application of shear, which may have the side effect of transforming a cubic phase into the hexagonal phase.

7.2.2.5 Conclusion

In this section the equilibrium behaviour of SLES surfactants in the concentration range 30–100% has been investigated. At the low end of this concentration range the phase is in transition from a micellar to a hexagonal phase, forming worm-like micelles. With further increase in concentration, by 40% (except for $n = 3$), transition into a well-formed hexagonal phase occurs. The hexagonal phase was identified as taking a long time to form under equilibrium conditions so shear was applied in order to induce its formation. This may have had the unintended effect of eliminating the identification of any cubic phases, which transformed into hexagonal phases upon shearing. With further increase in concentration, around 60-65%, the phase transitions into a lamellar phase. Other researchers have also observed significantly longer equilibration times for the hexagonal phase *vs.* the lamellar structures [293, 294]. In fact in Ref [293] Groot reports that the hexagonal phase is observed to take 8 times longer to form than the lamellar phase. However, this typically less of a problem for other researchers, who are not concerned with calculating the inter-rod spacing or the d-spacing values, and therefore they usually use significantly smaller simulation boxes [63, 98, 294].

Despite the abundance of research for SDS surfactant systems, there are very few existing studies of the phase behaviour and properties of binary SLE_nS surfactant solutions available in literature. This is despite the fact that SLE_nS surfactants are common components of commercial products, and that varying n greatly affects a variety of properties of the solution. Only two studies could be found, Peroukidis *etl al.* [282] who use MD simulations, and Panoukidou *et al.* [281] who perform DPD simulations. However both focused exclusively on the micellar region of the phase diagram.

The d-spacing and inter-rod spacing could be calculated for each simulation case. While it is common to find simulations studying hexagonal and lamellar phases in existing literature, it is less common for researchers to use their results to calculate values for the inter-rod and lamellar spacings. The values that these

variables could take were dependant on the box size, due to the application of periodic boundary conditions. For the lamellar phase a box size of $L = 40$ provided a suitable number of accessible d-spacing values for the systems. However, for the hexagonal phase further simulations would benefit from larger box sizes being trialled, in order to increase the number of accessible inter-rod spacings. The cubic nature of the box also meant that a perfect hexagonal unit cell could not be formed, therefore future work studying hexagonal phases may benefit from more tailored choices of box dimensions.

Typically, experimental phase diagrams will often include two phase regions [15, 295], for example, for a mixture of a micellar/hexagonal. In these regions the solution is thought to consist of coexisting micellar and hexagonal phases. This means that the solution has variable composition across a sample. This inhomogeneity would be very hard to capture in a small simulation box with periodic boundary conditions. Therefore our assessment of the concentrations on the boundary between the micellar and hexagonal phase may not be accurate. From the research in this work it appears the contrasting experimental behaviour is due to a shear induced phase change, but it is equally likely to be a solution consisting of two co-existing phases.

The radius of gyration of the molecules and the ratio of *trans* to *gauche* conformations in a molecule are compared across the whole phase diagram, including the micellar phase. While the radius of gyration does have an observable relationship with increasing concentration, the ratio of *trans/gauche* has a more clear one. The relationship also agrees reasonably well with the experimental results in Chapter 5, although with slightly different transitions between the micellar/hexagonal and hexagonal/lamellar phases.

7.3 DPD Simulations for Lyotropic Liquid Crystals Under Shear

It has been reported by various authors [7, 153, 189–194] that the lamellar and hexagonal phases orientate under the application of shear, when measured experimentally. The orientation of the hexagonal phase in DPD simulations was confirmed in the previous section, and this was deemed to be largely consistent with experiments on hexagonal phases for general surfactant systems [153, 189–191]. One of the aims of this section, is to investigate the orientation that the lamellar layers prefer to take in a DPD simulation of AES-like systems, upon the application of shear. Lamellar layers in other surfactant systems have been shown to prefer to exist in the parallel orientation at most shear rates, with some evidence in some systems that there is a transition to the perpendicular orientation at high values of the shear rate [7, 192, 193, 195]. This section will also consider if application of a shear force causes any structural change to the surfactant phases, including changes to the shape of the molecules, compared with the equilibrium configurations discussed in the previous chapter.

From the application of shear, a value for the viscosity can also be calculated, using the method discussed in Section 3.4. In the previous chapter, the viscosity for the micellar phases was calculated via two different methods: an equilibrium method using auto-correlation functions; and a non-equilibrium method that relies on the simulation box's response to an applied shear force. This was only possible because the micellar solutions were expected to behave with Newtonian rheology. However, Chapter 4 details how the rheology of the lyotropic liquid crystals are expected to behave with shear thinning properties, therefore only the non-equilibrium shearing method will be used to calculate the viscosity in this chapter.

7.3.1 Simulation Set-Up

In the previous chapter, the decision was made that a choice of $\Gamma = 45$ would generate micellar solutions with realistic Schmidt numbers. However, lyotropic liquid crystals typically have very high viscosity values (see Chapter 4) and very low values of diffusion. Pure water has an experimental self-diffusion coefficient of $2.3 \times 10^{-9} \mathrm{m^2 s^{-1}}$ at 25°C [296], whereas for liquid crystals the diffusion coefficient is typically measured at least one order of magnitude smaller [297–299]. The effect of higher viscosity and lower diffusion coefficient generates an even larger value of the Schmidt number, although due to the non-Newtonian nature of the liquid crystals it is not possible to obtain an exact value. Due to the computational effort required in generating the shear profile, just one collision parameter is trialled in this section, with a value of $\Gamma = 250$, requiring a time step of $\Delta t = 0.001$. This choice of Γ generates a Schmidt number for water beads of $\approx 10,000$ (*i.e.* 25 times larger than in the micellar solutions using $\Gamma = 45$). This value is selected due to it being one of the largest Schmidt numbers obtainable, without having to further lower the time step.

For an investigation into the orientation that lamellar layers form at in DPD systems, the simulations are conducted from an initially random configuration. This will be studied in the following section. Following this the viscosity of the lamellar and hexagonal systems will be studied from pre-formed lamellar and hexagonal structures, which will be explained in more detail in Section 7.3.3.

7.3.2 Orientation of the Lamellar Phase

In order to form a perfect parallel or perpendicular arrangement of lamellar layers under the application of shear (*i.e.* an arrangement such that the lamellar layers are parallel with one of the cubic box surfaces), the box size should be chosen to be an integer multiple of the equilibrium d-spacing. If a non-integer box size is chosen, then the layers still choose to form at diagonal orientations, even under the application of shear. This is likely to be because the potential energy benefit

of forming at the correct d-spacing value is greater than the impact of shear. The practice of setting the box sized based on a known equilibrium d-spacing, is a procedure taken by other researchers studying similar systems [290]. This method does, however, assume that there is no change in the d-spacing value with varying shear rate. For each case trialled, this equilibrium d-spacing is taken from the results in Fig. 7.10.

It is convenient that for the case in which $n = 0$ at 70%, an integer number of lamellar layers are formed by a box of size $L = 40$. Additional simulations are conducted for the $n = 1$ and AES distribution of n cases at 70%. For these cases we chose to use a box size of $L = 39$ for $n = 1$ and $L = 25$ for the AES case. Shear in this work is applied by using Lees-Edwards boundary conditions, shown in Fig. 3.4, so that the flow velocity is directed along the x axis and a linear velocity profile is generated along the y-axis.

In the work of others, using DPD to study lamellar phases, there has been a reported transition from the parallel orientation at low shear rates, to the perpendicular phase at higher shear rates [290, 300, 301]. For example, You et $al.$ [300] report a transition at around $\dot{\gamma} = 0.2$, while Martin and Brennan [290] report a transition at a similar shear rate of around $\dot{\gamma} = 0.4$. In this work we investigate the lamellar layer formation at high shear ranges, in order to investigate the orientation the layers form at. The cases trialled in this work are all at a concentration of 70%, with values of ethoxylation $n = 0$ and $n = 1$ and an AES distribution. A shear rate of $\dot{\gamma} = 6 \times 10^{-2}$ produces the parallel orientation of lamellar layers for all values of n. A subsequent increase to $\dot{\gamma} = 6 \times 10^{-1}$ leads to a breakdown of the parallel layers, and the system is no longer a lamellar phase. The phase most closely resembles a nematic liquid crystal phase at these high shear rates. These two cases, along with the orientation of the director, are shown in Fig. 7.15. For the lamellar phase, the director of the box is approximately defined as being in the direction parallel to the normal of the layers (along the y-axis). Upon transition into the nematic phase the director aligns approximately along the direction of the
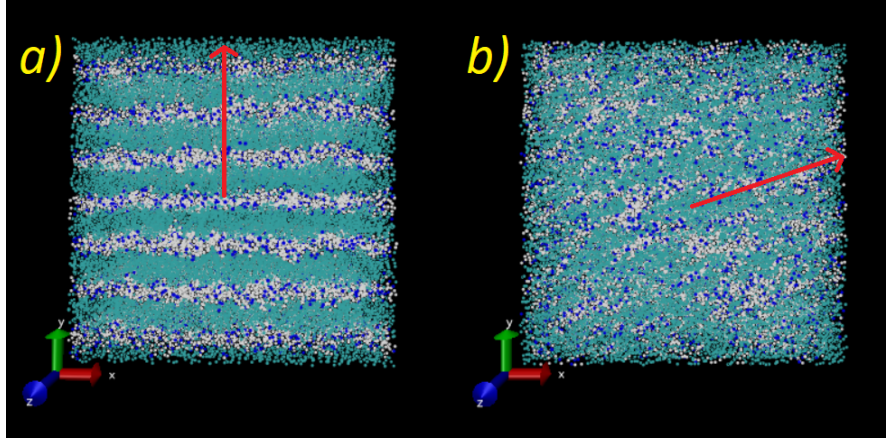
Figure 7.15: Shear is applied to a DPD simulation box consisting of molecules described by $n = 0$ at a concentration of 70%. The flow velocity is in the x-axis and the velocity gradient is along the y-axis. Figure (a) shows the molecules form a lamellar phase with a parallel orientation under a shear rate of $\dot{\gamma} = 6 \times 10^{-2}$. Figure (b) shows the breakdown of the lamellar layers at a shear rate of $\dot{\gamma} = 6 \times 10^{-1}$. Also shown (red arrow) is the orientation of the director of the molecules for the two cases. The box size is $L = 40$. Beads are coloured by their type: surfactant molecule (light blue), sodium ion (dark blue), water (white).

shear flow (along the x-axis). For the case shown in Fig. 7.15, the director for the nematic phase is calculated as (0.96, 0.29, 0), in other words it is at an angle of 17° to the x-axis. A selection of intermediate shear rates between $\dot{\gamma} = 6 \times 10^{-2}$ and $\dot{\gamma} = 6 \times 10^{-1}$ are trialled in order to investigate the possibility of an intermediate perpendicular orientation (at shear rates $\dot{\gamma} = 9 \times 10^{-2}$ and $\dot{\gamma} = 3 \times 10^{-3}$) and no evidence is found for the formation of a perpendicular phase.

7.3.3 Initial Configurations for Varying Shear Rate

The viscosity calculations in this chapter are conducted so that they are as close to the experimental set-up as possible. The viscosity is calculated experimentally, in Chapter 4, by measuring the way the solutions respond to an applied shear force. At shear rates that are typically measured in a rheometer, the lamellar layers are most likely to be orientated in the parallel orientation, as opposed to the nematic transition that occurs at very high shear rates. The viscosity relationship with applied shear rate is experimentally found to change following subsequent up-down shear cycles, due to high levels of orientation being induced at high values

of the shear rate. Therefore, the simulations performed at varying shear rates will all be initialised with an arrangement of molecules that are already in pre-formed, perfectly aligned lamellar layers. This replicates the experimental situation, in which a shear profile is found following the parallel shear alignment induced by a high shear rate.

When the simulations are initialised with an initially random configuration and a low shear rate is applied, the lamellar phases are found to still be capable of forming diagonally. In order to induce the perfect alignment a high shear rate is applied. It was found in the previous section that the preferred alignment is the parallel orientation for all cases trialled. Following this alignment, the applied shear can be removed, and the phases allowed to settle, before the reintroduction of the shear force at other shear rates, in order to investigate the viscosity *vs.* shear rate profile. A shear rate of $\dot{\gamma} = 6 \times 10^{-2}$ is used in order to induce the alignment of the lamellar phase, for the viscosity calculations.

Similarly to above, the hexagonal simulations should be conducted so that the hexagonal rods lay in the direction of shear. Since the hexagonal phase structures were already induced by the application of shear, the same configuration that was already generated in the previous section can be used for calculating the viscosity profile. Prior to this calculation, the shear that was applied to induce the hexagonal phase formation is removed for a period of time, in order to allow the phase to settle, before using the box to investigate the viscosity profile for the simulation box.

7.3.4 Equilibration Period

The initial focus for the viscosity calculations, was to investigate if DPD could reproduce the correct shear thinning viscosity *vs.* shear profile, since there is little existing literature performing this calculation for these systems. A variety of independent simulations are conducted for different shear rates. Due to length of time required to perform these simulations, because of the large amount of noise

in the stress tensor, this becomes a huge amount of computational effort when the shear rate is lowered. Only a small selection of the cases described in the previous section will be investigated for their viscosity *vs.* shear rate profiles. Initially, two cases were selected at different concentrations c, both using ethoxylation value $n = 0$, $c = 70\%$ (lamellar) and $c = 40\%$ (hexagonal), in order to see if they could reproduce the shear thinning relationship found in liquid crystals in Chapter 4. In theory it may be easier to access lower shear rates compared to for the micellar phases, due to the viscosity for liquid crystals being larger, and therefore generating a larger signal-to-noise ratio.

As a result of the large amount of noise in the off-diagonal stress tensor σ_{xy}, in order to assess the equilibration of the systems, a moving average is calculated. This is illustrated for the hexagonal shearing case of 40% concentration with $\dot{\gamma} = 6 \times 10^{-3}$ in Fig. 7.16, including the moving average for different window sizes A_{w}. Similarly to previous calculations, the simulation box initially exhibits a response to the application of shear, before the average value of σ_{xy} plateaus. After the initial response time, data for σ_{xy} can start being collected and averaged in order to obtain a value for the viscosity.

The level of noise in σ_{xy} is found to be largely similar for the lamellar and hexagonal cases. When the shear rate is decreased, the window of the moving average has to get increasingly larger, in order to cope with the increasing SNR. This is shown for the lamellar case with 70% and $\dot{\gamma} = 6 \times 10^{-6}$ in Fig. 7.17. The large amount of fluctuation of the value of σ_{xy} for decreasing shear rates is why the simulation time increases rapidly at low shear rates. Therefore, further decreases in the shear rate start to become inaccessible.

7.3.5 Viscosity *vs.* Shear Profile

The viscosity *vs.* shear rate profile, for the simulation case $n = 0$ with $c = 40\%$ and $c = 70\%$, is shown in Fig. 7.18. Both cases show shear thinning behaviour, consistent with the rheology measured in Chapter 4. At high shear rates the
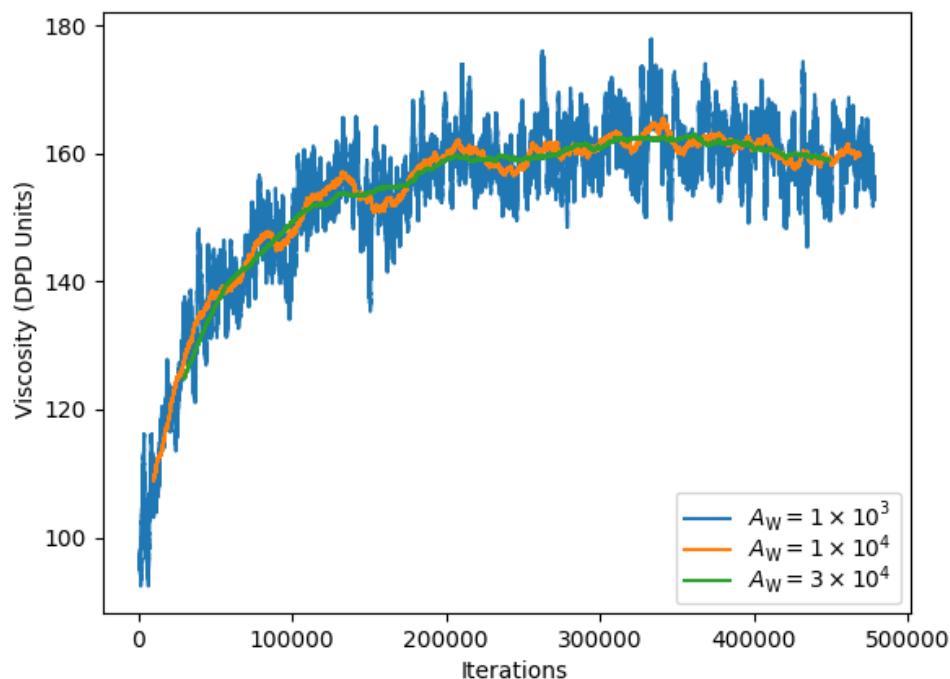
Figure 7.16: Instantaneous viscosity (calculated using Eq. 3.40) as a function of iteration, from a simulation consisting of $c = 40\%$ for molecules with $n = 0$. The output is analysed using moving averages. The effect of increasing window size, A_W, on the moving average is shown.
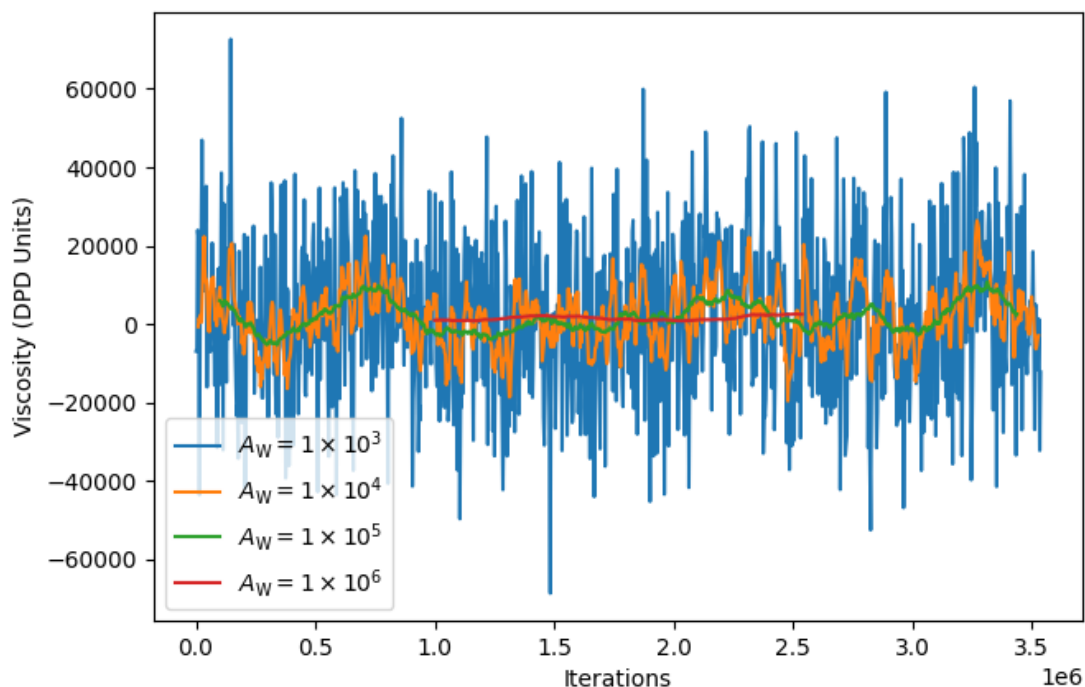
Figure 7.17: Instantaneous viscosity (calculated using Eq. 3.40) as a function of iteration, from a simulation consisting of $c = 70\%$ for molecules with $n = 0$. The output is analysed using moving averages. The effect of increasing window size A_W on the moving average average is shown.
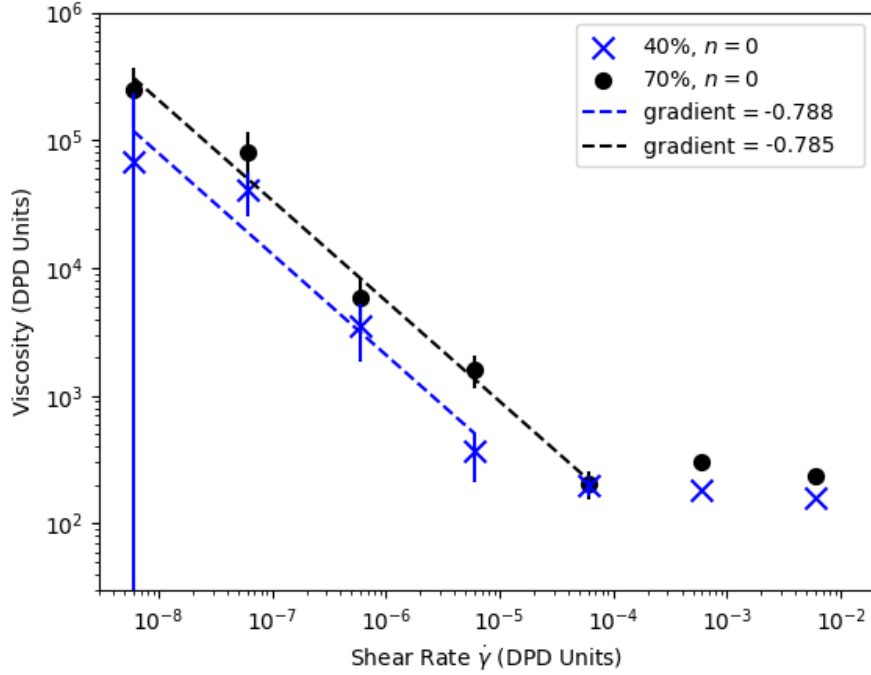
Figure 7.18: Viscosity *vs.* shear rate profile generated using DPD simulations for a system consisting of molecules with $n = 0$. Results are shown for two different concentrations which correspond to two different phases: 40% (hexagonal) and 70% (lamellar). The error bars are calculated as the standard error $\sigma/\sqrt{N}$ where σ is the standard deviation and N is the number of outputs of the stress tensor.

calculated viscosity plateaus to an approximately constant value. It was found that for shear rates lower than those presented, it was too difficult to obtain a consistent value for the viscosity, due to the huge amount of noise in the signal. The large error bar for the case with $\dot{\gamma} = 6 \times 10^{-9}$ is an illustration of this. The simulations at lower shear rates require significantly longer run times. For example, in order to obtain the result for the lamellar (70%) data point at $\dot{\gamma} = 6 \times 10^{-3}$, only 2.5×10^5 iterations are performed before a reasonable average is obtained. For the data point corresponding to $\dot{\gamma} = 6 \times 10^{-9}$, 4×10^6 iterations are performed, corresponding to around 26,000 CPU hours.

The plateau at high shear rates occurs at almost the same shear rate value in both phase cases, which isn't what is found for similar systems experimentally (see Fig. 4.17). The shear thinning regions for both the hexagonal (40%) and lamellar (70%) phases are fit using the power law relationship in Eq. 4.10. The gradient of this relationship is slightly lower than what is found for similar systems

experimentally, although since the fit is to data points that immediately preceded the plateau, the gradient is expected to be slightly reduced compared with the gradient at lower shear rates. Note that the viscosity calculated at a shear rate of $\dot{\gamma} = 0.6$ isn't included in the plot as this is when the transition to the nematic phase occurs. However, the value of the viscosity calculated at this shear rate has a value of $\eta = 68.0 \pm 0.1$, which is significantly lower than any of the values obtained when the molecules are still in the lamellar phase structure, indicating a significant drop in the viscosity once the lamellar phase disintegrates.

7.3.6 Molecular Changes

This section will now discuss the impact that shear has on the molecules within the simulation box. While the structure of the phases is visually unchanged with varying shear rate (*i.e.* the shape and structure of the lamellar layers and hexagonal rods remains, visually, unchanged), the molecules may undergo stretching or shape changes within the layers as a result of the shear force.

Consider angle Ψ, which is defined as the angle between a normal to the lamellar layers $\hat{n}$, and the director of the surfactant molecules. In previous sections, we have considered these two vectors to be equivalent to each other, and have been able to use this fact in order to calculate the lamellar layer separation. However, when subject to shear, there can be a difference between these two vectors. This is illustrated in Fig. 7.19. Under shearing the lamellar layers remain parallel to the $x - z$ plane, and therefore the normal to these layers remains as $\hat{n} = (0, 1, 0)$. The angle between the director and the normal of the layers is shown in Fig. 7.20. The molecules shift to being at an angle within the lamellar layers.

This movement has an effect on the radius of gyration R_g of the molecules, which is shown for the same case described above, in Fig. 7.21. While a significant amount of reorientation of the molecules is found for shear rates at $\dot{\gamma} = 6 \times 10^{-4}$, only a small amount of growth in the radius of gyration is found at this shear rate. When the shear rate increases to $\dot{\gamma} = 6 \times 10^{-3}$, the molecules significantly
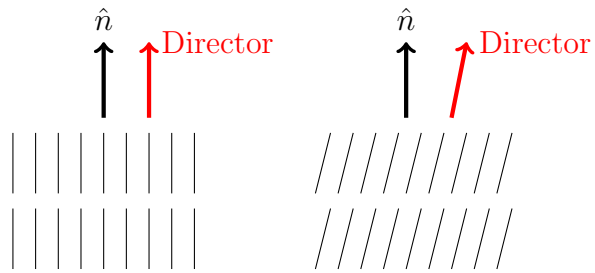
Figure 7.19: Illustration of the orientation of the molecules under shear. The molecules retain their parallel layers, but are no longer parallel with the normal to the layer.
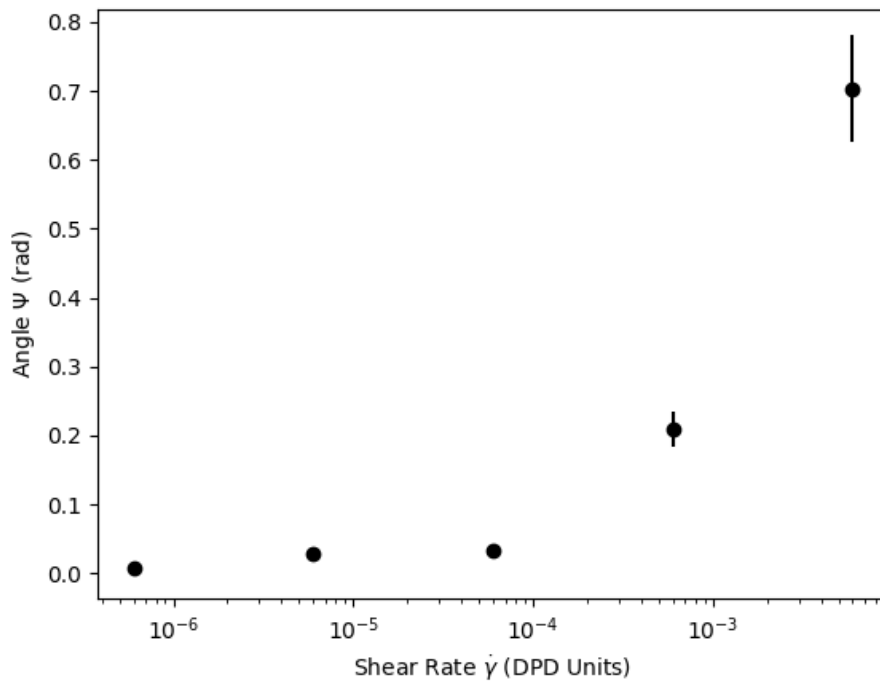
Figure 7.20: Angle Ψ between the normal to the lamellar layers and the director of the surfactant molecules, as a function of the shear rate.

orientate themselves, and the molecules' stretch is represented by the growth in the radius of gyration. At a shear rate of $\dot{\gamma} = 6 \times 10^{-2}$ (not shown in Fig. 7.20), the lamellar phase breaks down and the molecules no longer exist in parallel layers. Based on the rate of growth of angle Ψ in Fig. 7.20, the molecules at $\dot{\gamma} = 6 \times 10^{-2}$ would have angle $\Psi \approx 1.5$rad. This is likely to be a reason that the lamellar phase breaks down in the simulation box at this shear rate. This change in the director has been observed in the work of others. For example, Guo [7] report the change in the orientation of the director, around a period of time when undulation begins in the lamellar layers, signifying an instability. This is then followed by the reorientation into the perpendicular orientation. However, in this work no reorientation into a perpendicular phase is found following the inset of instability from high shear rate. Instead the phase immediately transforms into the nematic phase.

It is possible that experimentally the lamellar layers would not disintegrate at extremely high shear rate, as they do in the simulations. In the simulations, the disintegration is suspected to be due to the orientation of the molecules with in the layers. However, due to the box size being chosen based on the equilibrium d-spacing, the spacing and thickness of the lamellar layers is unable to vary as a function of shear rate. This may mean that the thickness of the layers is forced to maintain an undesirable d-spacing value under the application of shear.

The radius of gyration is also calculated for the hexagonal phase, as a function of the shear rate. This is shown in Fig. 7.22. Similarly to the lamellar phase, there is little change in the radius of gyration except for very extreme values of the shear rate. Unlike the lamellar phase, the structure of the hexagonal phase is allowed more freedom to adjust its periodicity (inter-rod spacing r), since it can rotate in the y-z plane. Of course it is still limited by the restrictions discussed in the previous section. It is found that at almost all values of increasing shear rate, there is no change in the value of r, until reaching a shear rate of $\dot{\gamma} = 6 \times 10^{-2}$. At this point its average inter-rod spacing r increases from $r = 7.52$ to $r = 7.85$.
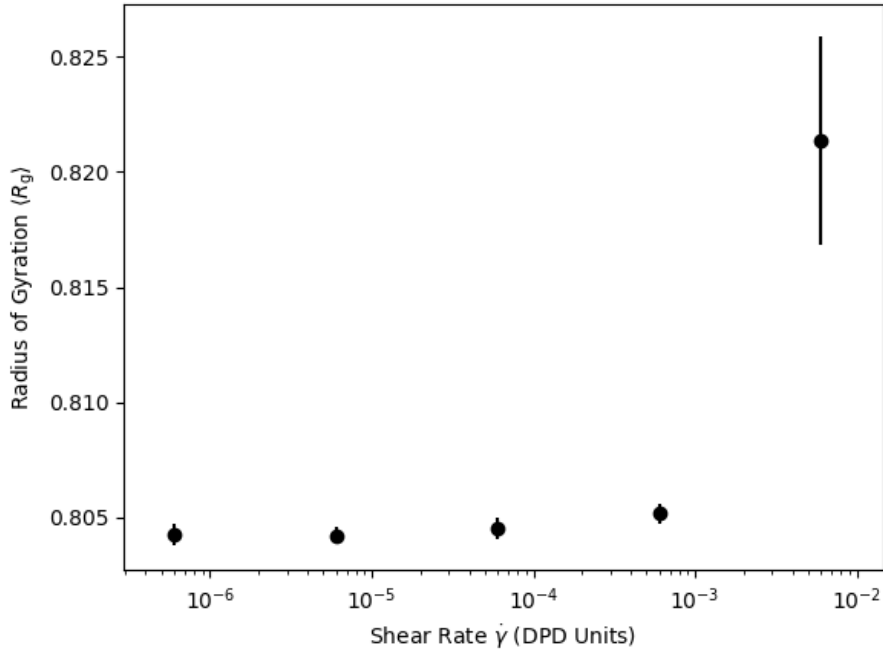
Figure 7.21: The radius of gyration as function of shear rate for molecules in the lamellar phase with concentration $c = 70\%$ and $n = 0$.

Note that in the previous section all of the hexagonal phases were aligned using a shear rate $\dot{\gamma} = 6 \times 10^{-3}$.

7.3.7 Other Orientations

In this work the lamellar phases used for the viscosity calculations were induced from an initially random configuration, into the parallel orientation using a shear rate of $\dot{\gamma} = 0.06$. Subsequent trials at higher shear rates did not yield any evidence of the preference of the phase to form at a perpendicular orientation, at any shear rate. In fact at a value of $\dot{\gamma} = 0.6$ the lamellar phase disintegrates. This means that in all of the viscosity calculations so far, we calculate Miesowicz viscosity component η_2, as described by Fig. 3.5. Although we see no evidence of a natural transition to the perpendicular orientation of the lamellar layers, simulations can still be performed in order to investigate the viscosity component η_3 (the perpendicular phase). Since the perpendicular phase is not induced at any shear rate from an initially random configuration, this can be performed by taking a lamellar phase that is already in a parallel orientation, and rotating to the perpendicular.
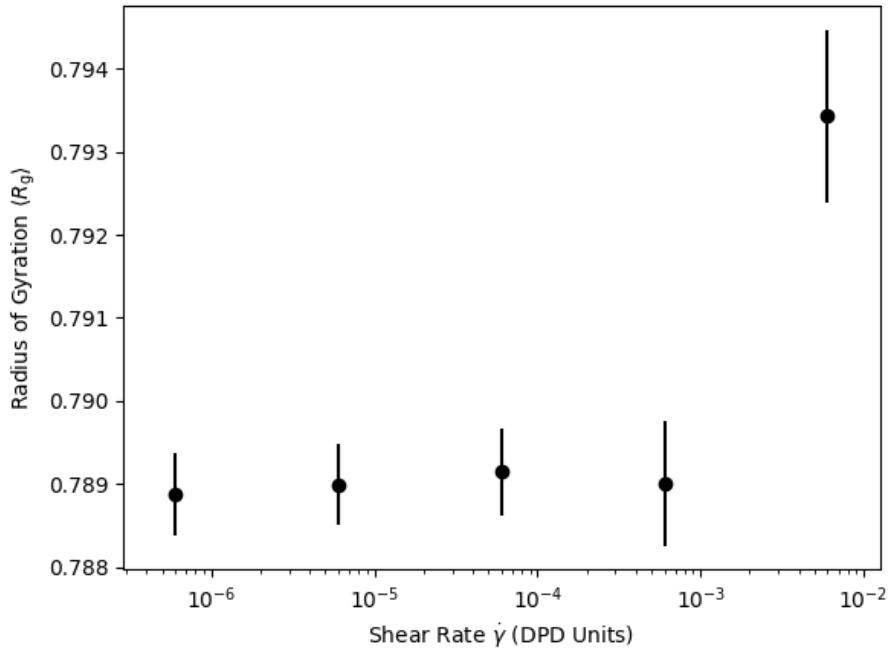
Figure 7.22: The radius of gyration as function of shear rate for molecules in the hexagonal phase with concentration $c = 40\%$ and $n = 0$.

Some authors [7, 195, 300] have argued that the transition to this perpendicular phase occurs naturally, due to the perpendicular orientation having a lower viscosity than the parallel. A comparison of the calculated viscosity components η_2 and η_3, at high shear rates, is shown in Fig. 7.23. It can be observed that the viscosity calculated for the perpendicular cases (η_3) is indeed lower than the values calculated for the parallel cases (η_2), even though the transition to the perpendicular cases was not naturally observed at higher shear rates. This suggests that the transition from the parallel orientation to the perpendicular case is not entirely determined by the viscosity, and there are other factors influencing the preferred orientation of the lamellar phase.

7.3.8   Other Simulation Cases

Additional simulations are performed for the lamellar phase on systems consisting of $n = 1$ and a distribution of n representing AES. However, due to time constraints, values were not obtained for shear rate values less than $\dot{\gamma} = 6 \times 10^{-6}$. The results for these are shown in Fig. 7.24, showing that all of he results obtained
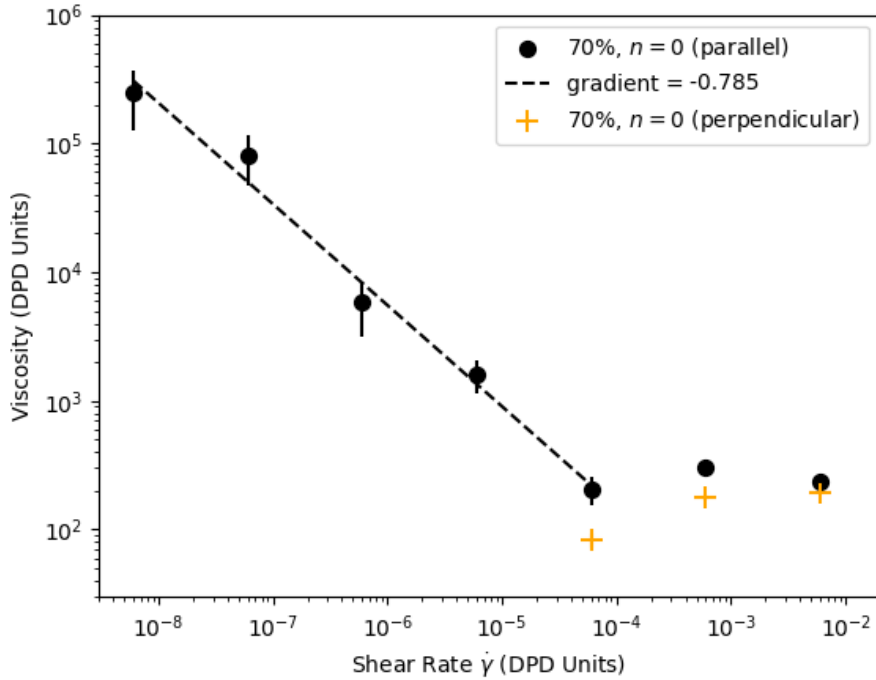
Figure 7.23: Viscosity *vs.* shear rate profile generated using DPD simulations for a lamellar system with concentration $c = 70\%$ and $n = 0$. Results are shown for two different orientations which correspond to different Miesowicz viscosity components η_2 (parallel) and η_3 (perpendicular).

are mostly in the plateauing region of the plot. However, it can still be observed that the values obtained for the viscosity for the AES, $n = 0$ and $n = 1$ cases are relatively similar. In the case for AES and $n = 0$, the increase in viscosity at lower shear rates occurs at roughly the same shear rate, however, there is an indication that the increase in viscosity will occur at a lower value of the shear rate with increasing n, based off the case in which $n = 1$.

7.3.9 Matching Shear Rate to Real Shear Rate

If the gradient of the viscosity *vs.* shear rate relationship was independent of the shear rate, then the gradient between the DPD results and the experimental results should be equivalent. A comparison of interest in this section would obviously be if the transition to plateauing shear rate is the same as what is observed experimentally. This requires a conversion of the shear rate in DPD units to real units. In Section 3.3.3 the time scale for DPD simulations was matched to those in physical units by matching the units of $k_{\mathrm{B}}T$ in DPD and real units at room temperature.
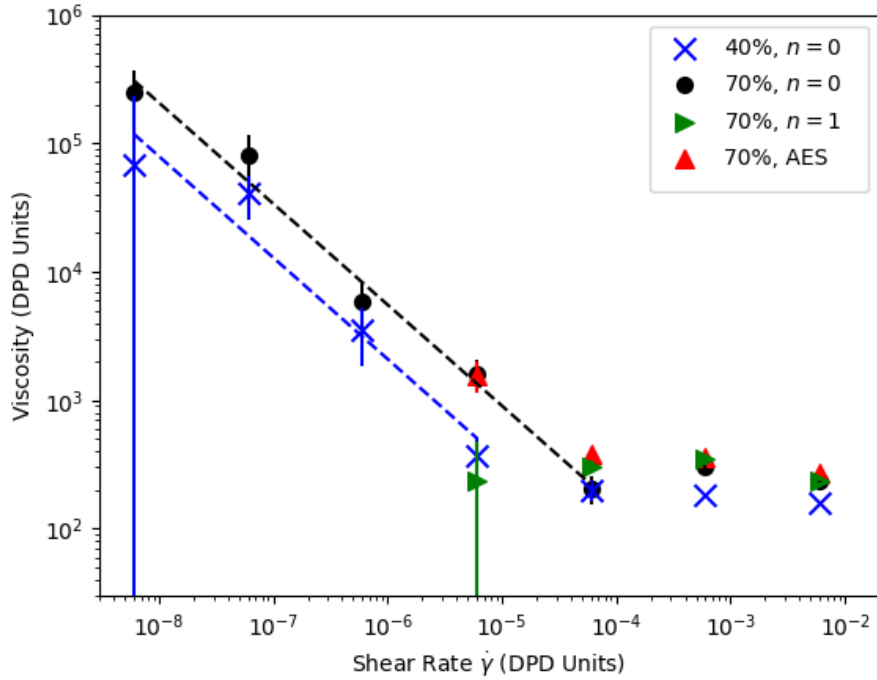
Figure 7.24: Viscosity *vs.* shear rate profile generated using DPD simulations for a variety of systems with varying n. Results are shown for two different concentrations which correspond to two different phases: 40% (hexagonal) and 70% (lamellar).

This isn't necessarily the best unit conversion to use for matching the shear rates used. It has been noted that the link between the DPD and physical units is still not clear and further studies are needed [302]. The mapping between length scales that has been used so far in this work, has obtained reasonably comparable results with experimental results. However, it is usually the time unit conversion that is more controversial, and is performed in a large variety of ways. Another very common method, besides that described in Section 3.3.3, is to convert DPD time into physical time by matching the experimental self-diffusion coefficients of liquid water D_{exp} to those in DPD, D_{DPD} [303, 304], using the expression

$$\tau_C = \frac{N_m D_{DPD} r_C^2}{D_{exp}} \quad (7.4)$$

where N_m is the bead mapping number defined in Eq. 3.33. For this system this generates fairly similar time matching values (compared to the value of τ_C derived in Section 3.3.3) of $\tau_C = 4.2 \times 10^{-11}$s using $\Gamma = 45$ and $\tau_C = 9.0 \times 10^{-13}$s using

$\Gamma = 250$.

In many cases, models are calibrated for a specific application. This means that the parameters of the model are modified to obtain physically relevant values for the quantities of interest that describe the target system with a possible disparity between other physical quantities [304]. For example, Townsend *et al.* [305] model solid particles suspended in a fluid. They relate DPD units to physical units by calculating the diffusion coefficient of the solid particles suspended in the static fluid. They then convert into physical units by comparing with the experimental diffusion coefficient of the solid particles. This results in a fairly large estimate for the time scale, compared to the previously discussed methods. They also performed experiments to compare the DPD simulations using Ultra-Small Angle X-ray Scattering, which complemented well with the findings using the DPD simulations and this conversion parameter for time. Fedosov [306] perform DPD simulations modelling polymer fluids. They observe that, experimentally, transition from the plateau to the power-law region occurs at shear rates $O(\lambda_0^{-1})$ where λ_0 is the relaxation time. Since this is also true for the DPD simulations, they determine that the matching of the relaxation time can be used to relate the real and DPD time scales. Clearly there is no well established link between DPD time units and physical time units, making a direct comparison in this work difficult.

7.3.10 Summary

In this section we investigated the effect of shear on the lamellar phase, and the orientation of the lamellar layers relative to the shear flow direction. It was found that the lamellar layers prefer to form at the parallel orientation at most shear rates, and there is a transition to a nematic phase, when the layers break down, at high shear rates. Contrary to what is observed for some lamellar systems under shear, we did not observe a perpendicular orientation of the layers at any shear rate. The break down in the layers is thought to be related to the change in the orientation of the molecules (the director) under the influence of shear. Typically

the reason given for a transition to a perpendicular phase is that it has a lower viscosity. Although the perpendicular phase is shown to have a lower viscosity at high shear rates, this transition is still not observed.

Following this, the viscosity *vs.* shear profile is investigated for a lamellar case and hexagonal case. Both are found to exhibit shear thinning behaviour, and then a plateau at high shear rates. The main difficulty in using DPD to calculate the viscosity *vs.* shear rate relationship is the inability to reach lower shear rates due to the amount of noise in the values for the stress tensor. Secondly, the conversion of the DPD shear rate to a shear rate in real units is tricky, because there is not a clear link between the two, and further studies are needed.

Ideally it would also be nice in future work to investigate the effect of varying Γ on the simulation results obtained. While the SNR ratio would be expected to be larger, a smaller value for Γ would increase the number of iterations of the system that could be achieved. This may make the lower shear rates more accessible.

Chapter 8

Molecular Dynamics

The method of DPD relies on making a number of simplifications to the structure of the molecules, as well as the forces by which they interact with each other. MD, by contrast, can be performed to simulate each individual atom within the molecule, therefore increasing the level of detail available in the simulation.

In order to investigate the extent to which the simplifications made in the DPD calculations have an effect on the parameters calculated in previous chapters, a selection of equivalent MD simulations are performed for SDS molecules, and are reported in this chapter. There are a variety of differing approaches within MD, that can be used to investigate the micellar phases formed from surfactant molecules. Primarily this includes whether the simulation is performed with an element of atomistic coarse graining, or via an all-atom method. This chapter will begin with an overview of the different approaches to study micellar phase formation, before moving onto discussing the simulations performed in this work.

8.1 Micellar Phases in Molecular Dynamics

While, in theory, all-atom MD simulations can be performed, until recent years MD simulations investigating the aggregation behaviour of surfactants was conducted purely using coarse-grained simulations [76–81, 282]. From a practical aspect this was because an all-atom simulation could not reach the time scales required for

micelle formation. In a coarse-grained simulation, a number of atoms are grouped together in order to reduce the number of calculations that need to be performed with each iteration (although to a lesser extent than in DPD). This increases the time scales that are accessible in the simulation, and allows the micellisation process to be studied. Of course it also reduces the level of detail in the simulation, but once again to a lesser extent than DPD simulations do.

All-atom simulations can sometimes be performed, but rarely are done so, from a random initial configuration. Instead these simulations usually begin with a pre-formed micelle, with an aggregation number which is close to what is expected from experimental data. Often these simulations are of a very small number, or individual, micelles [80,82–84]. In this technique researchers are not usually interested in the self assembly process which leads to micelles, but in aspects of the micelle structure. The method of performing simulations beginning with pre-assembled micelles is the only way that all-atom simulations can be performed on micelle sizes that have aggregation numbers close to what is found experimentally. Beginning an all-atom simulation with a random initial configuration usually leads to significantly under-predicted micelle sizes [85]. The major drawback to performing calculations on pre-assembled micelles is that it relies on the assumption that the size the micelle forms at is already known. While the simulation sizes are often small, this method has been employed for a number of years, and has reached conclusions about micelle structure that agree with experimental observation. For example, early research conducted by Watanabe *et al.* [82] was performed for micelles consisting of just 15 monomers, but reproduced the experimental observation that micellisation leads to an increased proportion of *trans* conformations in the alkyl chains. In more recent studies, such as the one by Chun *et al.* [307], an SDS micelle consisting of 60 SDS molecules is simulated, and a variety of information that agreed with experiment is obtained, including the geometrical radius and conformational information about the molecules inside the micelle.

In order to investigate the process of spontaneous aggregation into micelles,

coarse-grained simulations are more appropriate in order to achieve the required time scales. For example. Fujiwara *et al.* [78] show that for micelles that eventually form an oblate shape, the micelle formation process is as follows. The simulation begins at a random initial configuration, as time elapses small micelles are formed in several positions, and then at much time later several small micelles coalesce into a large, disk shaped micelle. Micellar size distributions can also be calculated in simulations which contain a number of micelles [78], which cannot be accurately calculated from all-atom simulations consisting of very few micelles.

Rarely have simulations been performed using all-atom modelling, beginning with random initial configurations. Such simulations are generally not preformed for systems containing long molecular chains, such as SDS, as they do not result in fully equilibrated simulation boxes. With modern computational resources, micelle aggregation can be observed, but at lower aggregation numbers than expected due to slow equilibration. This means that while properties such as the mean aggregation number can be calculated, they can not be compared in a meaningful way with experimental results. However, while more uncommon than coarse-grained simulations, there are examples where authors such as Sammalkorpi *et al.* [85] have reported results from partially equilibrated micelle solutions. In their system the micelles are still evolving, and the average micelle sizes observed are much lower than those found via experiment. However, the dependence of quantities as related to their aggregation size N can be reported in a similar way to what was presented in Chapter 6.

The work reported in this chapter will focus on performing equilibrium, all-atom simulation of SDS solutions, using MD. This chapter will focus entirely on equilibrium simulations (*i.e.* solutions not subject to a shear force) and will be performed for solutions exclusively in the micellar phase. There are several existing studies using coarse-grained MD for SDS, but relatively few using all-atom methods. It would be more beneficial to compare with a result from all-atom simulations, as opposed to another coarse graining method that may suffer from

similar simplification effects as DPD. As the DPD method involves simplifying the molecule through course graining, and by simplifying the forces in order to speed up the simulation, the DPD method may not capture the level of detail that can be obtained through more detailed modelling. For example, an interesting study was conducted by Peroukidis *et al.* [308], who modelled SDS molecules using coarse-grained MD simulations. They found that the aggregation number with concentration was greatly over predicted. They then mapped the resulting configuration from their coarse-grained study to an all-atom simulation, using the coarse grained results as an input to their all-atom study. From the all-atom study they found that the micelles dissolved and broke up, to achieve aggregation numbers that closely replicate experimental results. This clearly suggested that there were problems in attempting to reproduce correct micellar behaviour using coarse-grained simulations, that could only be captured in an all-atom study.

This chapter aims to compare some of the parameters that were calculated in Chapter 6, with equivalent parameters in a more detailed MD simulation. The exclusively micellar concentration range is selected due to the expectation that at no concentration of surfactant molecules, would all-atom MD simulations result in a fully-equilibrated phase. However, a partially equilibrated micellar phase can be more easily studied than unequilibrated lyotropic crystal phases. Even though the MD simulations will not reach a fully equilibrated result, due to the time scales that would be involved, a number of micelles form in the partially equilibrated simulation boxes, which can still be studied.

8.2 Computational Method

In this work LAMMPS (Large-scale Atomic/Molecular Massively Parallel Simulator) [27] is used in order to perform the MD calculations. LAMMPS is an open source, classical molecular dynamics code which is well developed for parallel computers. LAMMPS has a huge range of capabilities, and many different models and algorithms can be selected for different applications.

The main variable in setting up MD simulations is the choice of the force field. As described in Section 3.2, the meaning of 'force field' in the context of MD simulations refers to the parameter sets used in the equations controlling the forces between atoms. The parameters used for the SDS molecules are obtained from the Automated Topology Builder (ATB) and Repository [14]. The ATB uses quantum mechanical calculations in order to assign force field parameters. Further details of these parameters can be found in the Appendix E. For water molecules there exist a huge number of different models that have been specifically developed for modelling liquid water in MD calculations. The most common are three-site models, which have three interaction points corresponding to the three atoms of the water molecule. Generally, most modernly developed water models (*e.g.* OPC [309], SPC/E [310], TIP3P [311]) reproduce the correct density of water at room temperature [312]. The model selected for these calculations is the TIP3P model [311], which, since its original inception, has later been adapted for use with a long-range Coulomb solver [313] (*e.g.* Ewald or PPPM). The choice of the TIP3P model is consistent with other researchers for studying micellisation [282, 314], although it has been shown that the choice of water model does not affect the predictions for the mean aggregation number of micelles [282]. In this work the PPPM solver is used for the electrostatic interactions.

The simulation is set-up in a cubic box with periodic boundary conditions, with molecules at randomly generated positions. Care is taken to ensure that positions are generated such that atoms do not overlap, which would lead to inter-atomic potentials computing large forces, causing the simulation to become numerically unstable. The molecules are generated with an initial density that is lower than the target mass density, in order to aid with the generation of sufficiently spaced apart molecules. Following this, an energy minimisation of the system is performed, by iteratively adjusting atom coordinates, in order to minimise the total potential energy of the system. This procedure creates the initial configuration for the system.

Simulations are then conducted using a isothermal-isobaric (NPT) ensemble. LAMMPS uses Nose-Hoover equations of motion, in order to calculate the forces between the atoms. Coupling parameters are required for both the thermostat T_{damp} and barostat P_{damp} elements, which are specified in time units, and determine how rapidly the temperature or pressure is relaxed. Choices of $T_{\text{damp}} = 100$ time steps and $P_{\text{damp}} = 1000$ time steps are made for the thermostat and barostats, respectively, as recommended by the LAMMPS documentation. If P_{damp} is too small, the pressure and volume can fluctuate wildly. Likewise, if T_{damp} is too small the temperature will fluctuate. If the parameters are too large then the pressure and temperature will take a long time to equilibrate. Therefore the pressure, volume, and temperature are observed during calculation, in order to confirm that these parameter choices are optimal for this simulation case. The simulation is run at a constant pressure of 1atm and a temperature of 300K. Over the course of the simulation, the box volume decreases until the density reaches an equilibrium, steady-state value. A time step of 1fs was used throughout the simulations. The Lennard-Jones interactions were cut off at 1.5nm, and the PPPM Ewald method was used for the long-ranged electrostatic interactions.

8.2.1 Simulated Systems

Three different SDS concentrations are trialled, corresponding to weight percentages of 5, 10, and 20%. A variety of different box sizes were trialled for concentrations corresponding to the 5 and 10% solutions, while only one box size is trialled for the 20% concentration. The different-sized simulations are defined by the total number of molecules inside the box, *e.g.* for the case of a 5% solution with 100,000 molecules, the simulation is made up of 328 SDS molecules and 99,672 water molecules, resulting in a total of 312,792 atoms in the simulation box. One box size is chosen for the 20% case as it is expected to take the longest to equilibrate, so the smallest box size that is appropriate is chosen. A simulation box containing 20,000 molecules is used, and this size is selected as it contains 334 sur-

factant molecules, which is a sufficient number to produce a number of micelles, based on the known experimental aggregation number. This will also allow for an inter-micellar distance calculation.

These box sizes are larger than are typically used for all-atom MD calculations, and therefore are expected to take a significant amount of time to equilibrate.

8.2.2 Data Analysis

The micelle clusters are identified in a similar way to the DPD simulations (discussed in Section 6.2.2.1). Molecules are assigned to a particular cluster if their hydrocarbon tail falls within a cutoff radius of another molecule belonging to that cluster. For the purpose of direct comparison with the DPD results, the cut off is assigned to be 5.65×10^{-10}m, which is the same as used in the DPD analysis, converted into real units.

For comparison with Chapter 6, values are calculated for: the aggregation number and the radius of gyration of the micelles R_G, as a function of their aggregation number N. In order to analyse the size and shape of the molecules, values are also calculated for the radius of gyration of the molecule R_g and the ratio of *trans* to *gauche* conformations.

8.3 Equilibration Period

Over the course of the simulation, the simulations reach a constant average mass density and constant average temperature. The fluctuation over the final measurement period is shown in Fig. 8.1. The quantities fluctuate more for boxes consisting of fewer molecules, however the magnitude of fluctuation is within reasonable limits for all box sizes.

The aggregation number, as a function of iteration, for an MD simulation consisting of a 20% concentration is shown in Fig. 8.2. The approach of beginning the simulation at a low density compared to the target density causes the box size
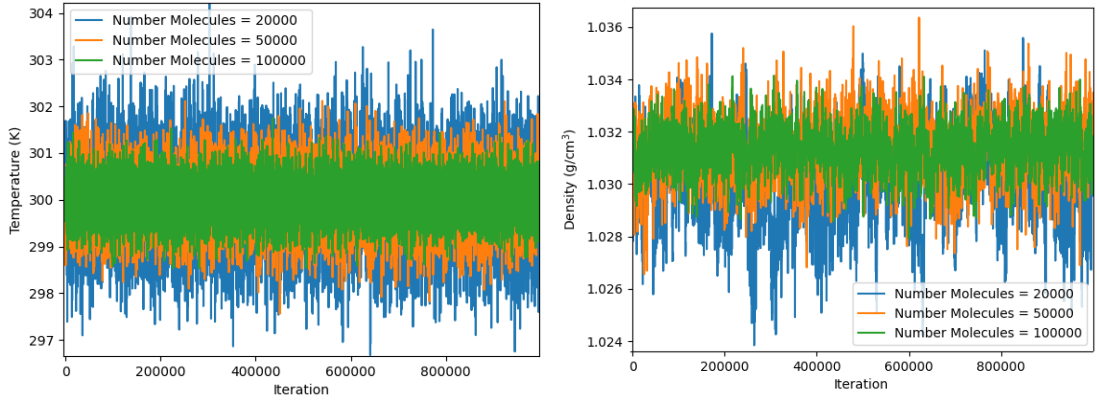
Figure 8.1: Variation of the temperature and density of the simulation boxes over the period of data collection. Data shown for different box sizes consisting of a 10% concentration.

to rapidly collapse, bringing the molecules together in a non-ideal configuration. This also briefly creates an artificially large aggregation number. This non-ideal configuration causes the box to re-expand for re-orientation of the molecules, before the box decreases in size as the molecules gradually organise into a configuration that minimises the forces between them. The aggregation number then gradually comes to a constant value.

Each simulation case is performed over similar time frame, with the domain divided across the same numbers of processes (64 cores *i.e.* $4 \times 4 \times 4$ division). This means that the simulations containing fewer molecules are able to run for a larger number of iterations than the ones containing more. For example, for the 10% concentration case, the simulation consisting of 10,000 molecules achieves 3.1×10^8 iterations, while the simulation consisting of 100,000 achieves 4.2×10^7 iterations. Using that the simulations are performed using a time step of $\Delta t = 1 \times 10^{-15}$s, these simulations result in run times of 3.1×10^{-7}s and 4.2×10^{-8}s, respectively. In both of these examples, the simulations were allowed to run for similar lengths of time, amounting to approximately 165,000 CPU hours each. This means that in order to reach similar time scales as the DPD simulations, a greater amount of computational resources were used, even though even the largest MD simulation boxes are significantly smaller (in terms of their volume) than the DPD simulations.

285
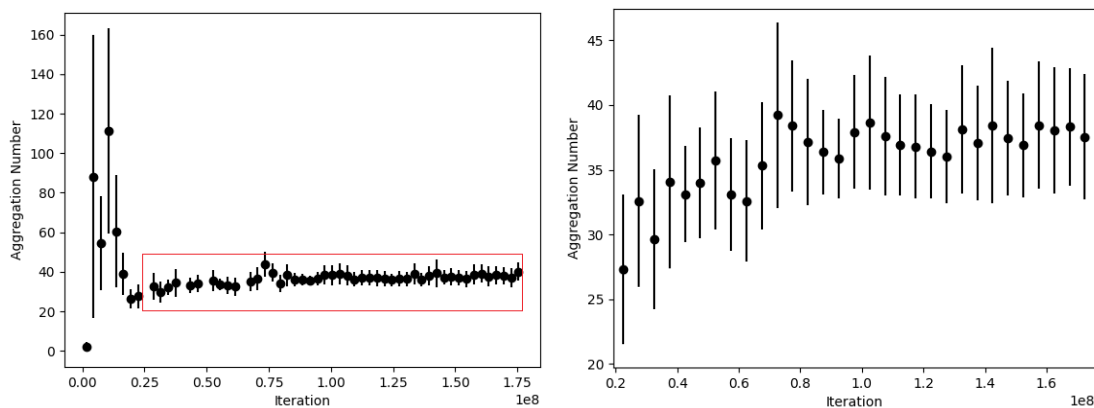
Figure 8.2: Equilibration of the aggregation number in an MD simulation. The bins are of size 3×10^6 in the iteration axis. The error bars represent the standard deviation of each bin.

8.4 Simulation Results

8.4.1 Aggregation Number

A plot of the mean aggregation number N_{agg} for all simulation cases is shown in Fig. 8.3. It is interesting to note that the mean aggregation numbers achieved from varying simulation sizes for concentrations 5% and 10% are not that different, and the smallest simulation box sizes are only marginally higher in their values of N_{agg}. This is unexpected, as one might assume that the simulation cases which have fewer molecules in are much further along in their equilibration than the larger boxes, which is assumed would lead to larger mean aggregation numbers. At all concentrations trialled, the mean aggregation numbers achieved are lower than those seen in experiments, and also significantly lower than those reported in DPD simulations in Fig. 6.12. This was to be expected, given one of the benefits of DPD is the increased diffusion that leads to quicker equilibration.

Fig. 8.4 shows the final formation of micelles in the case of 20% concentration. The micelles in their final configuration are located at approximately average distances from each other, as a result of their electrostatic repulsion. In Chapter 6 it was found that the radial distribution functions $g(r)$ for the 7% and 10% concentrations decay quickly with distance. The 20% concentration shows a higher degree of long-range order than the lower concentrations, but still dampens to
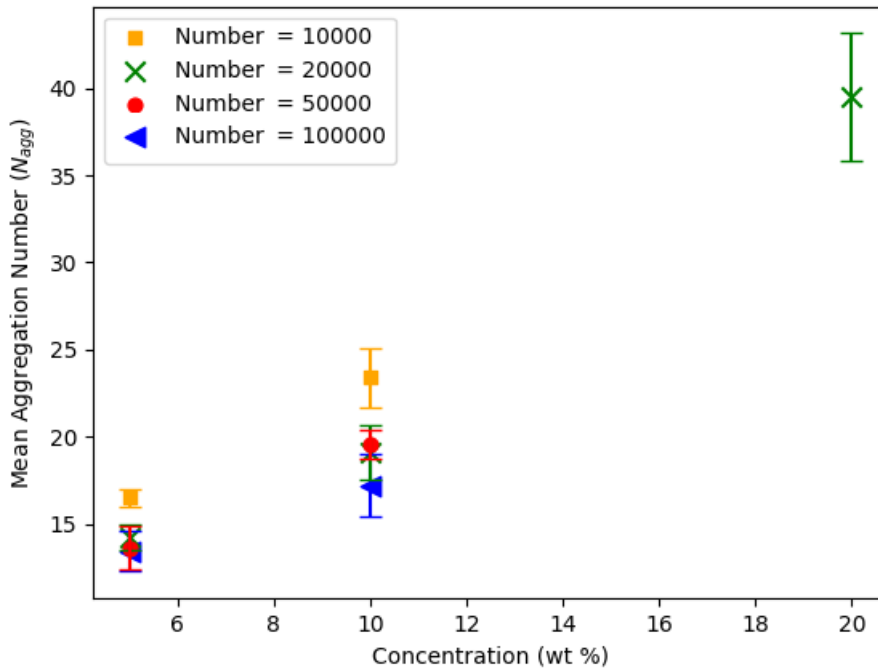
Figure 8.3: Mean aggregation number N_{agg} against solution concentration. Different scatter points show the results obtained for simulations in varying box sizes. Error bars represent the standard deviation over the sampling period.

$g(r) = 1$ reasonably quickly as the distance increases. From the first peak in $g(r)$, an inter-micellar distance was calculated. Generally the radial distribution function can only meaningfully be analysed at distances up to half of the simulation box edge length, for a system with periodic boundary conditions. Due to the small box sizes in the MD calculations, it is difficult to assess any long range order of the micelles. However, the average spacing can be calculated in a similar way from the MD results to DPD (see Section 6.3.1.3), and the location of the first peak in the radial distribution function is listed in Table 8.1. Two peaks are identified in the concentration of 20%, which suggests some underlying cubic structure (*i.e.* there are two nearest neighbour distances), however this is possibly due to the small box size used in the simulations, and the fact that relatively few micelles form in a simulation box of this size. Both of these peaks occurs at a much lower distance than was obtained in the DPD (58 ± 1Å) and found experimentally (57Å [266]), however an under-prediction of the aggregation number would explain why the nearest neighbour micelles are closer. However, analysis of the inter-micellar distances is complicated by the small box sizes.

287
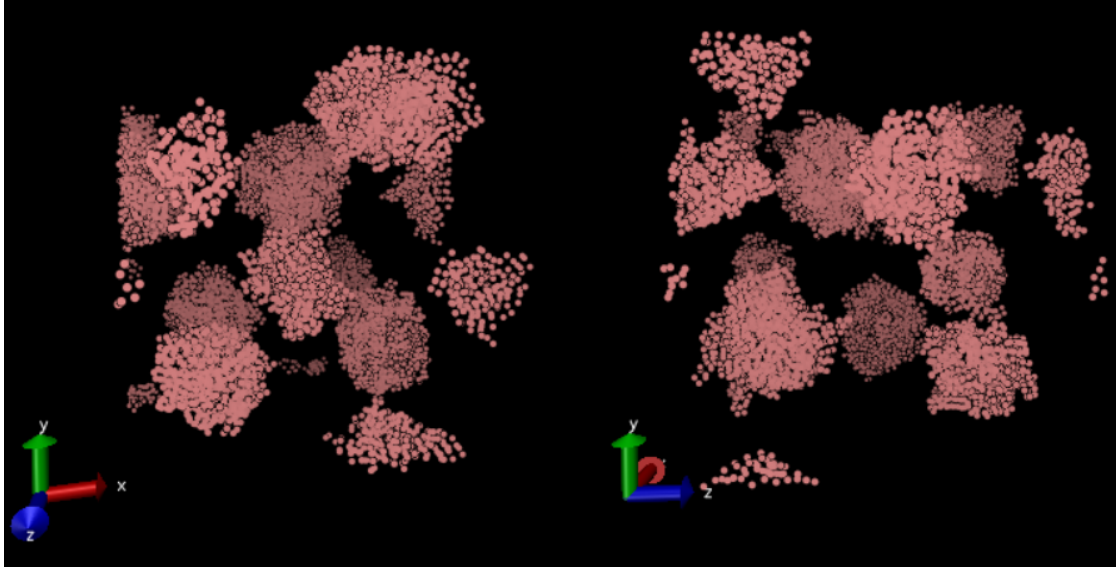
Figure 8.4: Formation of micelles in MD, in a simulation box consisting of 20,000 molecules with a concentration of 20%. The surfactant molecules are illustrated by the pink beads. Water molecules are not shown for clarity.

Concentration (wt.%)	Simulation Size (Molecules)	Simulation Edge Length	Peak Location (Å)
5	100000	143.9 ± 0.1	39.0 ± 0.5
10	100000	145.0 ± 0.1	42.7 ± 0.5
20	20000	88.4 ± 0.1	44.2 ± 0.5 & 51.2 ± 0.5

Table 8.1: Location of first peak in the radial distribution functions $g(r)$ for different simulation cases. The location of this first peak finds a value for the nearest neighbour in micellar solutions.

8.4.2 Radius of Gyration R_G

The radius of gyration R_G of the micelles against the aggregation number N is shown in Fig. 8.5. The value of R_G for a given aggregation number N is relatively independent of the simulation size used, as well as the overall concentration of the box, in agreement with the DPD results. Fig. 8.6 combines the results from all box sizes and concentrations, in order to plot the R_G of the micelles against their aggregation number N, as well as the relationship between R_G^3/N and N. As discussed in Chapter 6, this quantity helps us to assess the shape of micelles as a function of N, as for spherical micelles this value would be independent of N. The value of R_G^3/N decreases from aggregation numbers around $N \approx 10$ to $N \approx 60$, which is in partial agreement with the results obtained in DPD for $n = 0$. DPD finds that beyond about $N \approx 60$, R_G^3/N increases significantly, as the micelles start to take on a prolate shape. As none of the MD simulation results achieved aggregation numbers this high, this behaviour is not seen.

The minima in the plot of R_G^3/N in DPD occurs at around $N = 44$. Since in the MD results, we only have one data point beyond this value of N, it is difficult to suggest exactly where an equivalent plateau in the MD results will be with respect to N, and thus what the value of N that results in transition from a spherical to a prolate shape. Based on this single data point alone, the micelles will take their spherical shape at a larger value of aggregation number than $N \approx 44$, with plateau being more likely to be around $N \approx 60$. This would be in better agreement with some of the experimental data presented in section 6.2. For example, experimentally, it is often reported that the concentration at which SDS micelles start to become prolate is at around 1%, and solutions at this concentration are reported to have a mean aggregation number of $N_{\text{agg}} = 66$ [22] (see Table 6.5). Of course, there is still reasonable disagreement experimentally at the exact value that SDS micelles begin to become prolate. This could explain explain why in Fig. 7.14, which details the *trans/gauche* ratio as determined via DPD as a function of concentration, the boundary at approximately 20% is at

(a) $c = 5\%$

(b) $c = 10\%$

(c) $c = 20\%$

(d) All concentrations.
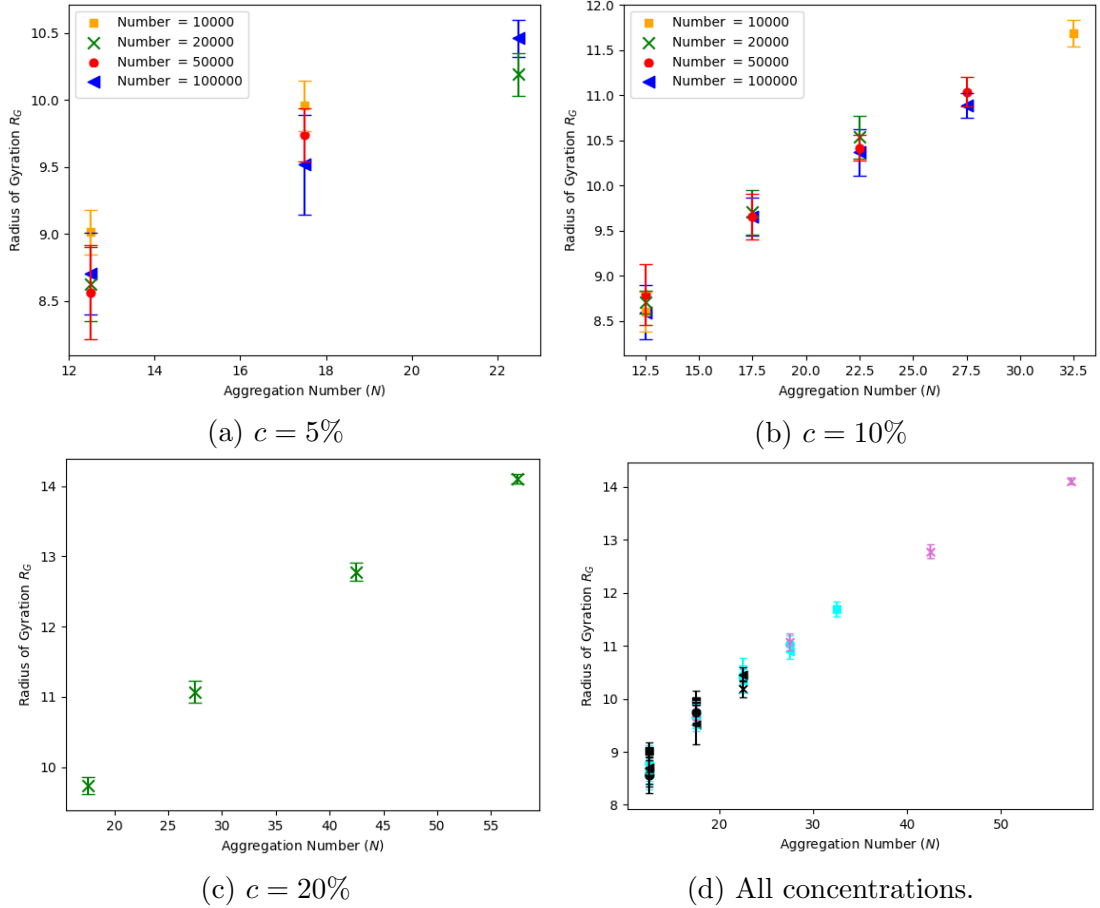
Figure 8.5: R_G plotted against N for a variety of concentrations c. For each concentration various different box sizes containing 10000, 20000, 50000 and 100000 molecules are shown. However, for the 20% concentration case only one box size containing 50000 molecules is trialled. The aggregation number N is binned into bins of size 5 and error bars represent the standard deviation. In Figs (a)-(c) scatter symbols are coloured by the size of the simulation box, whereas for Fig. (d) symbols are coloured by their concentration: 5% (black), 10% (blue), 20% (pink). R_G is plotted in units of Angstroms (Å).

a slightly different concentration, when compared with the experimental Raman results. DPD could be over predicting the rate at which the micelles become non-spherical.

Wang *et al.* [79] model the aggregation of a single micelle composed of 60 SDS molecules, using coarse-grained MD simulations. They obtain micelle radius of 19.9Å for this case. Similarly Chun *et al.* [307] performed all-atom simulations with aggregation number of 60 and found a micelle radius of 21Å. Wang *et al.* [79] calculate their value as the distance between hydrophilic head group to the micelle center of mass, while Chun *et al.* [307] calculate their value by calculating the

(a) R_G plotted against N (b) R_G^3/N against N
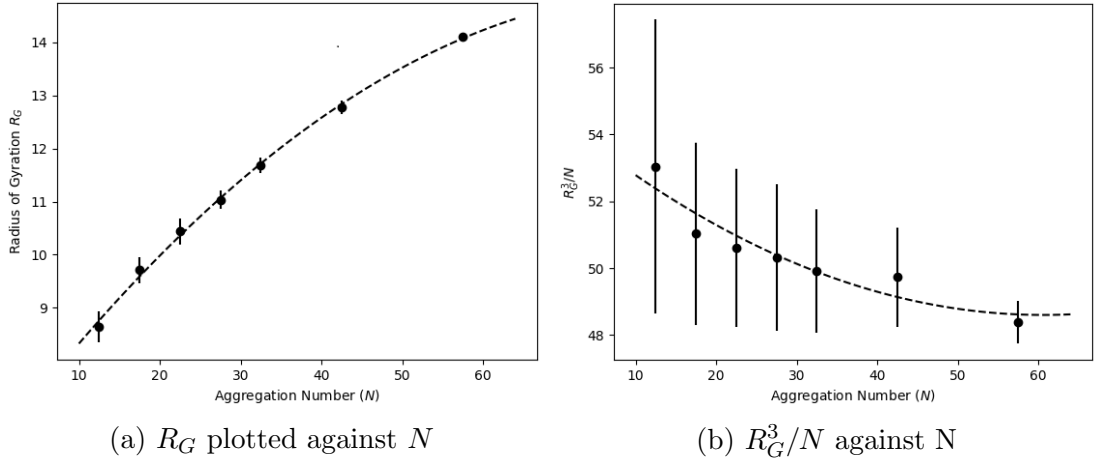
Figure 8.6: Combination of results from all concentrations and box sizes trialled. The aggregation number N is binned into bins of size 5 and error bars represent the standard deviation. R_G is plotted in units of Angstroms (Å).

radius of gyration of the micelle R_{G} and making use of Eq. 6.11. In this work, a micelle of size $N = 60$ is determined to have a radius of gyration of $R_{\mathrm{G}} = 14.3$Å, taken from the fit in Fig. 8.6. Using the relationship given in Eq. 6.11, between the radius of a gyration of a micelle and its geometrical radius (assuming spherical shape and constant density), this is converted into an effective micelle radius of 18.4Å, which is in reasonable agreement with the findings from other MD studies.

The value found for the radius of gyration in DPD and MD are directly compared in Fig. 8.7. The estimate for the micelle sizes for a given aggregation number are in relatively good agreement with each other, although the MD simulations don't reach anywhere near as high aggregation numbers, even for the 20% concentration case.

8.4.3   Conformation of Molecules

One of the main purposes of this study was to see if the DPD simulations were reproducing the conformational behaviour of the molecules as well as an all-atom MD simulation would. Combining the results from all simulations (*i.e.* all concentrations and box sizes) a relationship can be found between the radius of gyration of an individual molecule, and the aggregation number of the micelle (to which that molecule belongs). The results of this, compared with the results obtained
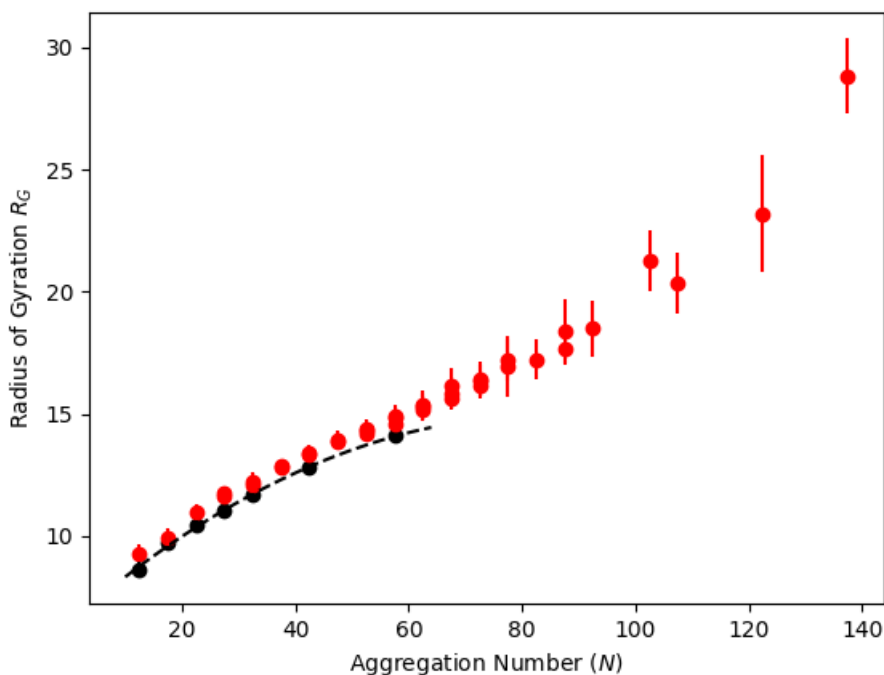
Figure 8.7: Comparison of the relationship between the micelle radius of gyration R_G and aggregation number N, as obtained via DPD (red) and MD (black) simulations. R_G is plotted in units of Angstroms (Å). The conversion between DPD units and real units uses 1 DPD length unit = 5.65Å.

using DPD, are shown in Fig. 8.8. There is a sharp increase in the value for R_g for molecules in well-defined micelles $7 < N$, and then a plateau. While the DPD results showed a more clear increase in R_g with increasing aggregation number, the relationship between R_g and N in MD is less clear, although the absolute values are in reasonable agreement with each other. The less well-defined relationship between R_g and the aggregation number N in MD could be a result of less well-equilibrated micelles. There are relatively few micelles of the larger kind available for analysis in the MD study, which may contribute to the noise in the analysis of the results for larger micelles (as evidenced by the fact that the mean aggregation numbers for the simulation cases are generally < 20). However, there exists a very strong relationship between the radius of gyration of a molecule, and the ratio of *trans* to *gauche* bonds in the molecule. This is illustrated in Fig. 8.9.
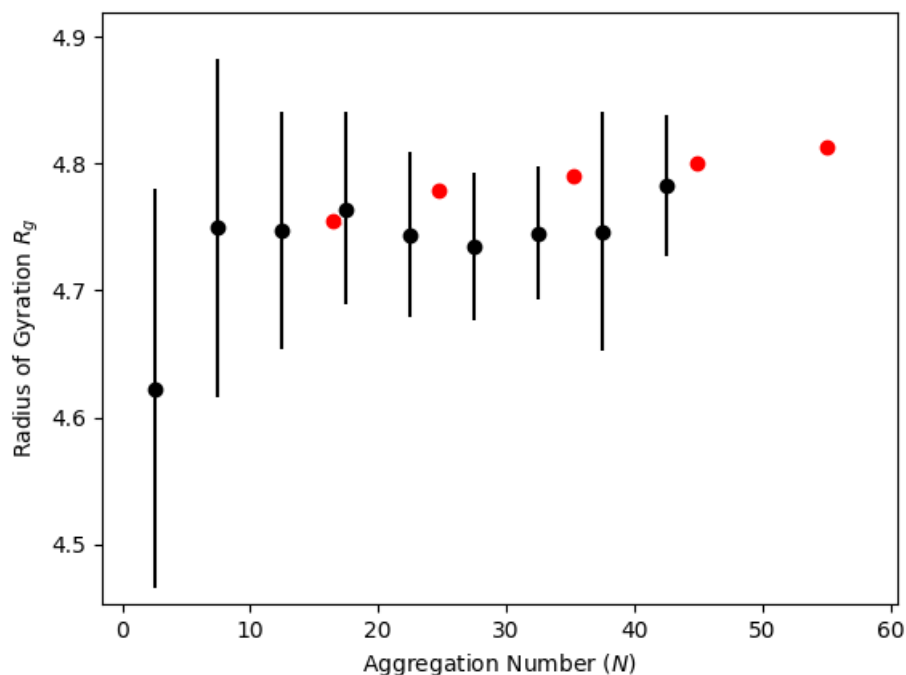
Figure 8.8: Radius of gyration of molecules R_g against the aggregation number N of the micelle they belong to. The black points are the results obtained using MD calculations, while the red points are the DPD results converted into real units. The error bars represent the standard deviation of the bins, while the error bars for the DPD results are not shown as to not obscure the results due to large error bars. R_g is plotted in units of Angstroms (Å).
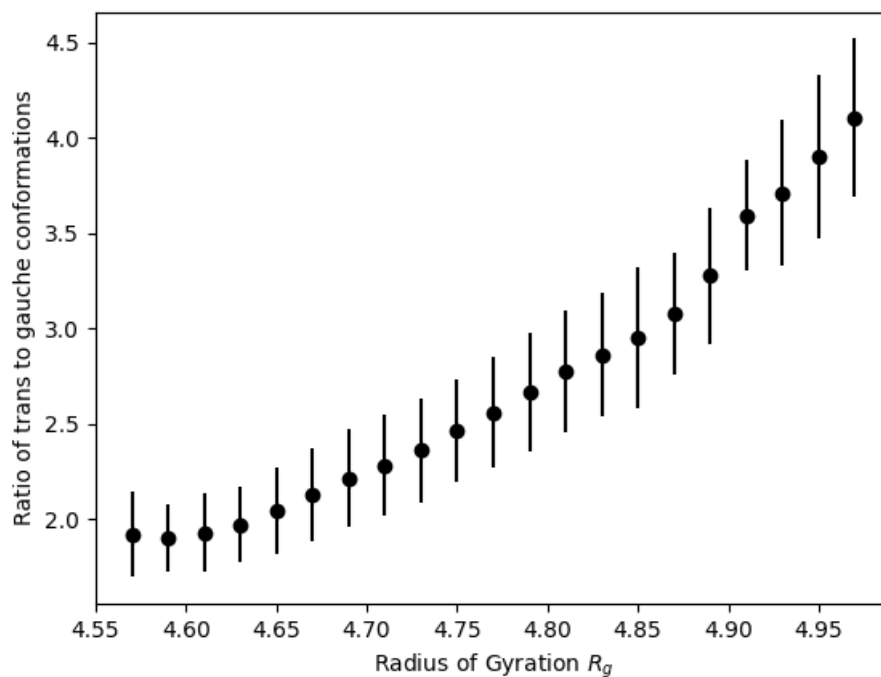
Figure 8.9: Relationship between the ratio of *trans/gauche* conformations in molecule against its radius of gyration R_g.

8.4.4 Conclusion

In this chapter we aimed to conduct a small selection of all-atom MD simulations, in order to investigate if the results from the coarse-grained DPD simulations in Chapter 6, were consistent with a more detailed simulation. As expected, the aggregation numbers achieved in these simulations were much lower than what is found experimentally, however, results could still be obtained as a function of the aggregation number N for comparison. It is common to cite the reason behind under-predicted aggregation numbers as poor equilibration. It can be observed in Fig. 8.2 that the aggregation number appear to reach a plateau after long iterations, once almost all of the surfactant molecules in solution have joined up into micelles. The time scales involved for subsequent micelle coalescence is expected to be long. The reason given by Sammalkorpi [85] for the low aggregation number in all-atom simulations of SDS micelles, is related to this reasoning. They conclude that the micelles are in a local energy minimum, and if the minimum is deep enough, it is unlikely that we would be able to see any further size evolution within the time window we are able to examine using all-atom MD simulations.

Since no micelles were formed at an aggregation number where the micelle was expected to take a prolate shape, as determined via DPD, a comparison of these types of micelles could not be made. In order to reach larger aggregation numbers, in a similar way to Peroukidis *et al.* [308], an interesting study would be to map the results of the DPD simulation results onto an all-atom MD simulation. After a relatively short equilibration time, a comparison of the radius of gyration and *trans/gauche* parameters, could be conducted for more similar aggregation numbers.

However, in the region of aggregation numbers for which the MD results could be compared to the DPD results, see Fig. 8.7, the calculation of the radius of gyration of the micelles R_G is remarkably similar between the two simulation methods. Therefore there is good evidence that DPD can be used in place of the more detailed MD simulations for this kind of work, despite the simplifications

made in DPD. In particular, since a larger amount of computational effort was required to produce the MD results *vs.* the DPD results in previous chapters, this confirms that DPD is an attractive simulation method of choice.

Chapter 9

Conclusion and Future Work

In this work a variety of experimental and numerical methods have been used to study anionic surfactant solutions of the form $CH_3(CH_2)_x(OCH_2CH_2)_nOSO_3Na$ (AES). These surfactants are common anionic surfactants used in a variety of personal care products, and in commercial AES used in these products there is usually a distribution of x and n. The experimental investigations provide data with which the simulations could be compared. Despite the prevalence of AES in commercial personal care products, little existing published research on the phase diagram could be found. In Chapter 4, experimental methods such as polarised optical microscopy imaging and rheological measurements aided in the identification of the mesophases formed, as well as helping to identify the concentration phase boundaries between the different mesophases. This was confirmed in Chapter 5 using Raman spectroscopy measurements, which identified conformational changes as a result of mesophase changes. The identification of the boundary between the micellar and hexagonal phases proved to be the most difficult to determine, since different experimental techniques indicated different behaviour. This suggested a coexistence of the micellar and hexagonal phases, at concentrations on the boundary.

The main computational tool used in the work in this thesis is dissipative particle dynamics (DPD). Overall the phase diagrams identified using DPD techniques are in reasonable agreement with those found experimentally, including the

location of the phase boundaries identified. The unusual behaviour at the phase boundary between the micellar phase and the hexagonal phase was indicated using DPD, to be likely due to shear induced alignment of worm-like micelles. Although further work studying this region in particular is necessary to explain the behaviour fully. If the solution behaviour is due to a co-existence of the micellar and hexagonal phases, this homogeneity would not be able to be captured in a small simulation box.

In order to investigate the micellar phase in more detail, experimental measurements using dynamic light scattering (DLS) were performed in Chapter 6. The aim of these measurements was to quantify changes in the micellar shape and size, due to increasing concentration. Measurements were made on both AES and SDS solutions, in order to investigate the effect of varying ethoxylation n. These measurements proved difficult to interpret, which was likely due to strong inter-micellar electrostatic interactions. By extrapolating the results to infinitely dilute concentration, an estimate of the micelle size for SDS and AES could be obtained for spherical micelles. These results were in agreement with the theory that the micelle radius increased proportionally to an increase in the average chain length of the surfactant molecule. However, for investigating the changes in size at higher concentrations, a different experimental method is required. For example small angle X-ray scattering or small angle neutron scatting. However, as discussed in Section 6.2, these methods are more complicated than dynamic light scattering and can still sometimes lead to conflicting results.

There is still a reasonably large gap in the literature for the experimental investigation of lyotropic liquid crystal structures formed by pure, monodisperse surfactants. This was highlighted by the lack of available data for comparison in Chapter 7, for the lamellar d-spacing and the inter-rod spacing of the hexagonal phase. This could be measured by means of small angle X-ray or neutron scattering. There is also significant lack of experimental data available describing the size and shape of micelles in micellar solutions, for varying ethoxylation n (with

the exception of SDS molecules). The micellar size, even the aggregation number, is difficult to measure experimentally, with different experimental methods producing inconsistent results.

There were some aspects of experimental surfactant behaviour that could not be studied using the DPD method used in this thesis. For example, in Chapter 4 POM imaging highlighted what appeared to be enhanced alignment of the lamellar phases at the solution-air interface. However, fluid/gas interfaces cannot be studied using DPD, since standard DPD requires that the simulation beads be at an approximately constant density throughout the domain. This is due to the fact that the conservative interaction between beads is entirely repulsive. An attractive component would be required in order to form phases of different densities *e.g.* to have coexisting liquid and gas phases in order to study the boundary. This has led to the development a simulation method which is an extension to the DPD method, called many-body dissipative particle dynamics (MDPD) to describe these systems. Therefore, it would be interesting to expand this research to the MDPD method, in order to investigate interfacial phenomena, such as that highlighted by the experimental work.

The simulation method chosen for the bulk of this work was dissipative particle dynamics (DPD). This simulation method has commonly been applied to nonionic surfactant solutions, and has benefits over typical molecular dynamics (MD) techniques. While modelling of this nature (*i.e.* on the atomic scale) may be more commonly performed using MD, this method is not suitable for the long time and length scales involved in surfactant solutions. Despite the fact that in commercial AES there is usually a distribution of x and n, polydisperse distributions such as these are rarely investigated using numerical techniques. In fact, even for monodisperse distributions studied, very little existing literature investigating the effect of varying n could be found. However, DPD has only recently been extended to ionic systems, and research in this area is still scarce. The electrostatic force must be treated differently in DPD *vs.* MD, and is still an area that requires further

research. The treatment of this force is suspected to be one of the causes behind the under-prediction of the mean aggregation number in Chapter 6.

The inclusion of the electrostatic force also becomes the dominating factor in the computational efficiency. Without electrostatic interactions the computational cost scales linearly with the number of DPD beads b_N (*i.e.* $O(b_N)$) [315], while with electrostatics the scaling becomes $O(b_N \log b_N)$, significantly reducing the number of iterations that can be performed with increasing simulation size. Therefore, in this work, the large box sizes used required relatively long run times. For the micellar phase it is more difficult to determine if equilibration has been reached (compared to the liquid crystal phases) based on the final resulting configuration alone. This led to the approach to run the simulations for as long as reasonably possible. However, large box sizes were necessary in order to obtain a large number of micelles in the simulation box. This lead us to be able to find a distribution of micelle sizes for every simulation case, as well as to find values for the nearest neighbour from the radial distribution function.

Despite the aggregation number under-prediction, we could investigate the micellar shape, as a function of aggregation number N, by plotting R_G^3/N *vs.* N, where R_G is the radius of gyration of the micelles. For spherical micelles this relationship would be linear if the density of the micelles remains constant. However, it was found that for each choice of n, there was only a narrow window of aggregation numbers for which this was true. By identifying the region in which this condition was satisfied, we could locate the aggregation number at which the molecules were most spherical, for a given value of n. The aggregation number required for spherical micelles was found to increase with increasing n. The radius for the spherical micelles was also found to increase in proportion to the increase in length of the molecule, which is consistent with what was found using DLS.

One of the challenges associated with studying micellar solutions via DPD, is the under-prediction of the aggregation number. There are a number of ways that this could potentially be tackled. The primary problem is that bringing two,

smaller micelles together, in order to form one large micelle, must over-come an energy barrier. It is likely that the micellar solutions struggle to reach larger aggregation numbers due to the emergence of a local equilibrium at a lower aggregation number, meaning the time scales to see any increase in micelle size would be extremely long. However, it is observed by Peroukidis *et al.* [308] that micelles which are initialised with a larger aggregation number than is optimal, can break down into smaller micelles relatively easily. Therefore, initialising a DPD simulation with an aggregation number that is too large may be a way of reaching aggregation numbers that more closely replicate experimental results, since micellar breakdown happens on a much shorter time-scale than micelle coalescence.

Alternatively, one could take an approach which still initialises surfactant molecules randomly throughout the domain. It was observed in Fig. 6.12 that the aggregation number at larger concentrations is much closer to the experimental value. This is likely due to closer proximity of micelles at higher concentrations, leading to it being more likely that they have opportunity to combine into large micelles. Therefore, for example, in order to study a box with a 7% concentration, one could start with an equilibrated box at 20% concentration. Then we could remove a number of the micelles in order to achieve a desired, lower, concentration.

In this work we chose to analyse the shape of micelles exclusively using the radius of gyration. Attempts were made to find alternative ways to quantify the shape of micelles, in particular using fits to their surface, however most of these methods failed due to difficulty identifying the surface of a dynamic micelle. Random protrusions and oscillations make finding size information from simulation difficult. However, it would be beneficial to continue exploring alternative methods for analysing micelle shape, since a variety of different authors have approached this task differently, and there is no general consensus on the best way to study micelle shape. In particular, when a study was performed to investigate the viability of fitting to the micelle surface, it was found that large, spherical micelles can be fit to more easily than smaller or asymmetrical micelles. However, even

in this case there remains an ambiguity as to the size of the micelle. The density of the micelle did not have an abrupt end, therefore the point of cut off for the micelle is difficult to define. This makes comparisons with experimental size data more difficult. Others have quantified micellar sphericity by variables such as the eccentricity (which is defined using moments of inertia [75]), although this was not investigated in this work.

One aspect of the micellar solutions that was not analysed in this thesis is the distribution of ions in the solution. For example, Fig. 2.7 illustrates how in micellar solutions ions can arrange themselves in a way to electrostatically screen micelles. An understanding of the distribution of ions in solution may aid in explaining the interactions between micelles, and potentially help us to understand the DLS results. Similarly, it would also be potentially interesting to study the density distribution of the different bead types, as a function of their distance from the micelle centre. This would provide quantitative information on how the micelles are structured. This may be particularly interesting for micelles in the AES simulations, which are constructed from a distribution of molecular lengths.

The box sizes used for investigating the liquid crystal systems ($L = 40$) was slightly smaller than the micellar systems ($L = 50$), based on an estimate of the effect the periodic boundary conditions would have on the structures. Each box size L correlated to an available number of d-spacings and inter-rod spacings r, with an increasing number of available spacings with increasing box size. While the lamellar phases formed under equilibrium conditions given sufficient run time, the hexagonal phases could only be encouraged to form with the addition of an applied shear. This had the side effect of causing shear induced alignment in the simulation box, reducing the number of available inter-rod spacings for the hexagonal phase. Ideally the hexagonal calculations should be repeated for a slightly larger simulation box, in order to increase the number of available inter-rod spacings available to each concentration case, for investigating the effect of varying n and c. The use of a cubic box also meant that a true hexagonal structure could

not be generated, as the phase was usually skewed or stretched in order to fulfil the periodic boundary conditions. This makes determining the true value of the inter-rod spacing difficult. However, the values obtained for the d-spacing and hexagonal inter-rod spacing compare reasonably well with the limited data that is found experimentally. This is despite the same DPD parameters resulting in an under-prediction of the mean aggregation number in the micellar phase. This is consistent with the thought that the treatment of electrostatic interactions is playing a part in the under-prediction of the aggregation number. The long-range interactions will play a larger role in the behaviour of solutions with lower concentrations, whereas at higher concentrations the short-range interactions will have greater impact. This is also consistent with the observation that the gap between the experimental aggregation number and DPD aggregation number decreases with increasing concentration.

The extent to which monodisperse simulations can be used to reproduce the behaviour of polydisperse surfactants has been investigated in this work. This is of note, since the majority of computational work focuses on monodisperse cal-culations, while the majority of experimental work focuses on the polydisperse. For example, Fig. 6.18 shows that for micelles produced by a polydisperse sur-factant, the radius of gyration R_{G} and the aggregation number N of micelles can largely be predicted from interpolation from monodisperse simulations. In other words the parameters R_{G} and N, for a surfactant with an average ethoxylation value of $n = 0.76$, can be reasonably predicted from the values calculated from monodisperse simulations with $n = 0$ and $n = 1$. Furthermore, calculations in Sec-tion 7.2.2.3 indicated that the d-spacing for polydisperse cases could be calculated using interpolation from the monodisperse cases of $n = 0$ and $n = 1$. A similar in-vestigation could not be made for the inter-rod spacing of the hexagonal phase, due to the limited number of spacings available resulting from the box size. However, since once one polydisperse case was trialled, an investigation could be performed for a range of different average n values, in order confirm this observation.

One of the most interesting comparisons between the DPD and experimental results were the conformational changes as a result of the phase change. One might expect that this behaviour would struggle to be captured in DPD, due to the simplification of the molecules through coarse graining. However, the increase in the ratio of *trans* to *gauche* conformations in the hydrocarbon chain, which was identified using Raman spectroscopy, was also found using DPD. Considering the difficulty in interpreting spectroscopy data, such as that presented in Chapter 5, the confirmation that DPD can reproduce the correct behaviour makes studying other aspects of molecular conformations easier. This may also help interpret some of the peaks that appear in Raman spectroscopy data, that historically are hard to categorise.

We were also able to investigate the impact of shear force on each of the phases. Experimentally, the hexagonal and lamellar phases exhibit alignment under the application of shear, which was also shown in the DPD simulations. A shear thinning profile could be calculated for the lamellar and hexagonal phases, which plateaued at higher shear rates. This is broadly consistent with the behaviour expected from experimental measurements. At high values of shear rate, the phases break down and transform to a nematic phase, which has a director in alignment with the direction of shear flow. For the micellar phase, increasing shear rate leads to stretch and aligns micelles in the direction of shear flow. This leads to shear thinning behaviour. In all simulation cases, reaching lower shear rates is increasingly difficult, due to the noise in the off diagonal stress tensor. This effectively places a lower limit on the value of shear rate that can be applied. DPD is perhaps most useful for investigating the shear behaviour at high shear rates, which is not easily performed in a rotational rheometer.

In this work we touched upon the effect of varying collision parameter Γ in the thermostat. The results indicated that the choice of Γ does have an effect on the behaviour of the solutions, and therefore has an effect on the parameters calculated in this work. However, more work is required to fully establish the effect Γ has on

surfactant solutions, since only a couple of different values were trialled.

Mapping the length scale in the DPD simulations to real units was performed by matching the density of pure water to that measured experimentally at room temperature. This proved to be a reasonable mapping, based on the comparison of quantities with length units (*e.g.* radius of gyration of molecules R_{g} and micelles R_{G}) with those calculated experimentally and in the MD simulations. However mapping the time scale in DPD to real units is more difficult and needs further investigation. This makes mapping the shear rate from DPD simulations to real units difficult. Much existing literature performs a mapping based on matching the specific system being studied, which is not easily generalised to other systems.

Finally, we also performed a small selection of MD simulations in the micellar region, in order to compare with the results obtained via DPD. It is worth comparing the DPD simulations with another simulation method, as well as experimental results, as some of the experimental results can be difficult to interpret. Experimentally it is difficult to calculate information such as the micellar size as a function of aggregation number. MD simulations involve a greater amount of detail than the DPD simulations do, therefore MD simulations require much more computational effort than DPD simulations, but were shown to yield similar results for the parameters of interest in this work. For example, there is remarkably good matching between the two simulation methods for the relationship between the radius of gyration of the micelles against their aggregation number. However, the DPD simulations are able to achieve higher aggregation numbers than those in MD, meaning that DPD simulations are a desirable alternative to MD simulations when studying these systems.

There is much further scope for additional study of AES-like molecules using DPD simulation. In particular, most commercial products contain a mixture of surfactant types. Simulations containing both AES molecules and other surfactants can be investigated, now that the validity of DPD for pure systems has been confirmed. A common area of research is the effect of adding salts, since this has

been greatly shown to influence the shape and size of micelles. Also, in this work we focused on the effect of varying the number of (OCH_2CH_2) groups on the phase diagram and the mesophase structure. However, commercial AES also possesses polydispersity in the hydrocarbon chain length. It was assumed in this work that the effect of varying the number of (OCH_2CH_2) groups was more significant than varying the length of the alkyl chain, but this may be worth investigation. In particular, it would be useful to investigate if a polydisperse alkyl chain would increase the d-spacing values and inter-rod spacings to something which more closely matches experimental data.

Bibliography

[1] I. Dierking and S. Al-Zangana, "Lyotropic liquid crystal phases from anisotropic nanomaterials," *Nanomaterials*, vol. 7, no. 10, p. 305, 2017. 12, 46

[2] D. Lombardo, M. A. Kiselev, S. Magazù, and P. Calandra, "Amphiphiles self-assembly: Basic concepts and future perspectives of supramolecular approaches," *Advances in condensed matter physics*, 2015. 12, 48, 49

[3] P. Kékicheff, C. Grabielle-Madelmont, and M. Ollivon, "Phase diagram of sodium dodecyl sulfate-water system: 1. a calorimetric study," *Journal of colloid and interface science*, vol. 131, no. 1, pp. 112–132, 1989. 13, 56, 57, 58

[4] A. S. Poulos, C. S. Jones, and J. T. Cabral, "Dissolution of anionic surfactant mesophases," *Soft matter*, vol. 13, no. 31, p. 5332, 2017. 13, 58, 59, 90, 101, 102, 114, 232, 258

[5] S. D. Stoyanov and R. D. Groot, "From molecular dynamics to hydrodynamics: a novel galilean invariant thermostat," *The Journal of Chemical Physics*, vol. 122, no. 11, p. 114112, 2005. 13, 70, 71, 84, 85, 86

[6] A. W. Lees and S. F. Edwards, "The computer study of transport processes under extreme conditions," *Journal of physics. C, Solid state physics*, vol. 5, no. 15, pp. 1921–1928, 1972. 14, 87, 88

[7] H. Guo, "Shear-induced parallel-to-perpendicular orientation transition in the amphiphilic lamellar phase: A nonequilibrium molecular-dynamics simulation study," *The Journal of Chemical Physics*, vol. 124, no. 5, p. 054902, 2006. 14, 91, 113, 114, 261, 271, 273

[8] J. Glusker, M. Lewis, and M. Rossi, *Crystal Structure Analysis for Chemists and Biologists.* Methods in Stereochemical Analysis, Wiley, 1994. 17, 130

[9] M. S. M. Alger, *Polymer science dictionary.* London: Chapman & Hall, second edition. ed., 1997. 17, 129, 130, 134

[10] "What is raman spectroscopy?." https://www.nanophoton.net/raman/raman-spectroscopy.html. Accessed: 14-01-2019. 17, 132

[11] M. Zaharescu and O. C. Mocioiu, *Infrared Spectroscopy*, pp. 213–230. Vienna: Springer Vienna, 2013. 17, 133

[12] E. Sutherland, S. M. Mercer, M. Everist, and D. G. Leaist, "Diffusion in solutions of micelles. what does dynamic light scattering measure?," *Journal of chemical and engineering data*, vol. 54, no. 2, pp. 272–278, 2009. 20, 163, 164, 165, 167

[13] W. Humphrey, A. Dalke, and K. Schulten, "VMD – Visual Molecular Dynamics," *Journal of Molecular Graphics*, vol. 14, pp. 33–38, 1996. 26, 27, 237, 240, 241

[14] A. K. Malde, L. Zuo, M. Breeze, M. Stroet, D. Poger, P. C. Nair, C. Oostenbrink, and A. E. Mark, "An automated force field topology builder (ATB) and repository: Version 1.0," *Journal of Chemical Theory and Computation*, vol. 7, no. 12, pp. 4026–4037, 2011. 32, 61, 67, 282, 355, 357

[15] H. Li, L. Dang, S. Yang, J. Li, and H. Wei, "The study of phase behavior and rheological properties of lyotropic liquid crystals in the LAS/AES/H_2O system," *Colloids and surfaces. A, Physicochemical and engineering aspects*,

vol. 495, pp. 221–228, 2016. 33, 51, 54, 55, 56, 95, 96, 101, 113, 116, 231, 260

[16] R. L. Anderson, D. J. Bray, A. S. Ferrante, M. G. Noro, I. P. Stott, and P. B. Warren, "Dissipative particle dynamics: Systematic parametrization using water-octanol partition coefficients," *The Journal of Chemical Physics*, vol. 147, no. 9, p. 094503, 2017. 33, 79, 80, 81, 82, 182

[17] R. L. Anderson, D. J. Bray, A. Del Regno, M. A. Seaton, A. S. Ferrante, and P. B. Warren, "Micelle formation in alkyl sulfate surfactants using dissipative particle dynamics," *Journal of chemical theory and computation*, vol. 14, no. 5, pp. 2633–2643, 2018. 33, 71, 75, 76, 79, 80, 81, 82, 83, 180, 182, 183, 185, 186, 187, 188, 190, 192, 193, 204

[18] M. Gudelj, P. Šurina, L. Jurko, A. Prkić, and P. Bošković, "The additive influence of propane-1,2-diol on SDS micellar structure and properties," *Molecules (Basel, Switzerland)*, vol. 26, no. 12, p. 3773, 2021. 33, 161, 162

[19] M. Bergstrom and J. S. Pedersen, "Structure of pure SDS and DTAB micelles in brine determined by small-angle neutron scattering (SANS)," *Physical chemistry chemical physics*, vol. 1, no. 18, pp. 4437–4446, 1999. 34, 173, 174

[20] S. Khodaparast, W. N. Sharratt, G. Tyagi, R. M. Dalgliesh, E. S. Robles, and J. T. Cabral, "Pure and mixed aqueous micellar solutions of sodium dodecyl sulfate (SDS) and dimethyldodecyl amine oxide (DDAO): Role of temperature and composition," *Journal of colloid and interface science*, vol. 582, pp. 1116–1127, 2021. 34, 175, 192

[21] M. Ludwig, R. Geisler, S. Prévost, and R. von Klitzing, "Shape and structure formation of mixed nonionic-anionic surfactant micelles," *Molecules (Basel, Switzerland)*, vol. 26, no. 14, pp. 4136–, 2021. 34, 173, 175, 192, 201

308

[22] B. Hammouda, "Temperature effect on the nanostructure of SDS micelles in water," *Journal of research of the National Institute of Standards and Technology*, vol. 118, no. 2, pp. 151–167, 2013. 34, 173, 176, 186, 192, 289

[23] S. Mitra, R. Karri, P. K. Mylapalli, A. B. Dey, G. Bhattacharya, G. Roy, S. M. Kamil, S. Dhara, S. K. Sinha, and S. K. Ghosh, "Re-entrant direct hexagonal phases in a lyotropic system of surfactant induced by an ionic liquid," *Liquid crystals*, vol. 46, no. 9, pp. 1327–1339, 2019. 35, 233

[24] I. D. Leigh, M. P. McDonald, R. M. Wood, G. J. T. Tiddy, and M. A. Trevethan, "Structure of liquid-crystalline phases formed by sodium dodecyl sulphate and water as determined by optical microscopy, x-ray diffraction and nuclear magnetic resonance spectroscopy," *Journal of the Chemical Society, Faraday Transactions 1: Physical Chemistry in Condensed Phases*, vol. 77, no. 12, pp. 2867–, 1981. 35, 52, 57, 117, 233

[25] R. Itri, L. Amaral, and P. Mariani, "Structure of the hexagonal phase of the sodium dodecyl sulfate and water system," *Physical review. E, Statistical physics, plasmas, fluids, and related interdisciplinary topics*, vol. 54, no. 5, pp. 5211–5216, 1996. 35, 52, 117, 233

[26] M. Seaton, R. Anderson, S. Metz, and W. Smith, "DL_MESO: Highly scalable mesoscale simulations," *Molecular Simulation*, vol. 39, 2013. 42, 182, 185

[27] A. P. Thompson, H. M. Aktulga, R. Berger, D. S. Bolintineanu, W. M. Brown, P. S. Crozier, P. J. in 't Veld, A. Kohlmeyer, S. G. Moore, T. D. Nguyen, R. Shan, M. J. Stevens, J. Tranchida, C. Trott, and S. J. Plimpton, "LAMMPS - a flexible simulation tool for particle-based materials modeling at the atomic, meso, and continuum scales," *Computer Physics Communications*, vol. 271, p. 108171, 2022. 42, 281

[28] *Disinfection, sterilization, and preservation.* Philadelphia, Pa., London: Lippincott Williams & Wilkins, fifth edition. ed., 2001. 43

[29] W. Poon and D. Andelman, *Soft Condensed Matter Physics in Molecular and Cell Biology.* Scottish Graduate Series, CRC Press, 2006. 43

[30] E. Kissa, *Fluorinated Surfactants and Repellents, Second Edition,.* Surfactant Science, Taylor & Francis, 2001. 43

[31] D. Attwood and A. Florence, *FASTtrack Physical Pharmacy.* Fast Track Pharmacy Series, Pharmaceutical Press, 2012. 44, 48

[32] G. Tiddy, "Surfactant-water liquid crystal phases," *Physics reports*, vol. 57, no. 1, pp. 1–46, 1980. 45

[33] P. Kumar and K. Mittal, *Handbook of Microemulsion Science and Technology.* Taylor & Francis, 1999. 45

[34] S. Kumar, *Chemistry of Discotic Liquid Crystals: From Monomers to Polymers.* Liquid Crystals Book Series, CRC Press, 2016. 45, 46

[35] J. M. Seddon, "Structure of the inverted hexagonal (H_{II}) phase, and non-lamellar phase transitions of lipids," *Biochimica et biophysica acta. Reviews on biomembranes*, vol. 1031, no. 1, pp. 1–69, 1990. 46, 53

[36] S. G. Oh and D. O. Shah, "The effect of micellar lifetime on the rate of solubilization and detergency in sodium dodecyl sulfate solutions," *Journal of the American Oil Chemists' Society*, vol. 70, no. 7, pp. 673–678, 1993. 47

[37] B. Jönsson, *Surfactants and polymers in aqueous solution.* John Wiley, 1998. 47

[38] H. Helmholtz, "Ueber einige gesetze der vertheilung elektrischer ströme in körperlichen leitern mit anwendung auf die thierisch-elektrischen versuche," *Annalen der Physik*, vol. 165, no. 6, pp. 211–233, 1853. 48

[39] M. Gouy, "Sur la constitution de la charge électrique à la surface d'un électrolyte," *J. Phys. Theor. Appl.*, vol. 9, no. 1, pp. 457–468, 1910. 48

[40] D. L. Chapman, "Li. a contribution to the theory of electrocapillarity," *The London, Edinburgh, and Dublin Philosophical Magazine and Journal of Science*, vol. 25, no. 148, pp. 475–481, 1913. 48

[41] O. Stern, "Zur theorie der elektrolytischen doppelschicht," *Zeitschrift für Elektrochemie und angewandte physikalische Chemie*, vol. 30, no. 21-22, pp. 508–516, 1924. 48

[42] B. L. Bales, "A definition of the degree of ionization of a micelle based on its aggregation number," *The journal of physical chemistry. B*, vol. 105, no. 29, pp. 6798–6804, 2001. 48

[43] O. Usyarov, "The electrical double layer of micelles in ionic surfactant solutions in the presence of a background electrolyte: 1. diluted micellar solutions of sodium dodecyl sulfate," *Colloid journal of the Russian Academy of Sciences*, vol. 69, no. 1, pp. 95–102, 2007. 49

[44] A. Neto and P. Toledano, *Phase Transitions In Complex Fluids*. World Scientific Publishing Company, 1998. 49, 50

[45] C. Solans, J. Esquena, N. Azemar, C. Rodriguez, and H. Kunieda, "Chapter 13 - highly concentrated (gel) emulsions: formation and properties," in *Emulsions: Structure Stability and Interactions* (D. Petsev, ed.), vol. 4 of *Interface Science and Technology*, pp. 511–555, Elsevier, 2004. 49, 50

[46] K. Fontell, K. K. Fox, and E. Hansson, "On the structure of the cubic phase i1 in some lipid-water systems," *Molecular Crystals and Liquid Crystals Letters*, vol. 1, no. 1-2, pp. 9–17, 1985. 49

[47] P. Sakya, J. M. Seddon, R. H. Templer, R. J. Mirkin, and G. J. T. Tiddy, "Micellar cubic phases and their structural relationships: the nonionic surfactant system C12EO12/water," *Langmuir*, vol. 13, no. 14, pp. 3706–3714, 1997. 49

[48] M. A. Siddig, S. Radiman, L. Jan, and S. Muniandy, "Rheological behaviours of the hexagonal and lamellar phases of glucopone (APG) surfactant," *Colloids and Surfaces A: Physicochemical and Engineering Aspects*, vol. 276, no. 1, pp. 15–21, 2006. 51, 231, 232

[49] P. Alexandridis, U. Olsson, and B. Lindman, "A record nine different phases (four cubic, two hexagonal, and one lamellar lyotropic liquid crystalline and two micellar solutions) in a ternary isothermal system of an amphiphilic block copolymer and selective solvents (water and oil)," *Langmuir*, vol. 14, no. 10, pp. 2627–2638, 1998. 51, 52, 231, 247

[50] V. Luzzati and F. Husson, "The structure of the liquid-crystalline phases of lipid-water systems," *The Journal of cell biology*, vol. 12, no. 2, pp. 207–219, 1962. 51, 52, 117, 247

[51] P. E. Harper, D. A. Mannock, R. N. Lewis, R. N. McElhaney, and S. M. Gruner, "X-ray diffraction structures of some phosphatidylethanolamine lamellar and inverted hexagonal phases," *Biophysical Journal*, vol. 81, no. 5, pp. 2693–2706, 2001. 51, 52

[52] T. Zhu and M. Caffrey, "Thermodynamic, thermomechanical, and structural properties of a hydrated asymmetric phosphatidylcholine," *Biophysical Journal*, vol. 65, no. 2, pp. 939–954, 1993. 51

[53] E. Hirsch, J. Wittmann, and F. Candau, "Structure amd viscdmetric behavior of gel phases in quaternary systems containing anionic surfactants," *Journal of Dispersion Science and Technology*, vol. 3, no. 4, pp. 351–372, 1982. 51, 117, 247

[54] J. C. Flood, *Solution and Liquid Crystalline Properties of Sodium Lauroyl Methyl Isethionate/Water Mixtures.* PhD thesis, 2015. 51, 247

[55] S. Zourab, I. Al-Kashef, and I. Kayali, "Phase behavior of dodecyl dimethyl amino oxide/sodium dodecyl sulfate in the presence of perfluorooctanol,"

Journal of dispersion science and technology, vol. 22, no. 1, pp. 111–117, 2001. 51, 117

[56] G. Lindblom and L. Rilfors, "Cubic phases and isotropic structures formed by membrane lipids — possible biological relevance," *Biochimica et biophysica acta. Reviews on biomembranes*, vol. 988, no. 2, pp. 221–256, 1989. 53

[57] J. M. Seddon and R. H. Templer, "Cubic phases of self-assembled amphiphilic aggregates," *Philosophical transactions of the Royal Society of London. Series A: Physical sciences and engineering*, vol. 344, no. 1672, pp. 377–401, 1993. 53

[58] V. Luzzati, H. Delacroix, A. Gulik, T. Gulik-Krzywicki, P. Mariani, and R. Vargas, "The cubic phases of lipids," *Studies in surface science and catalysis*, vol. 148, pp. 17–40, 12 2004. 53

[59] Y. Liu, L. Dang, H. Tan, and H. Wei, "Phase behavior of commercial AES/ethanol/H₂O ternary system," *Journal of dispersion science and technology*, vol. 37, no. 5, pp. 633–639, 2016. 54

[60] M. Hato and K. Shinoda, "Krafft points of calcium and sodium dodecylpoly(oxyethylene) sulfates and their mixtures," *Journal of Physical Chemistry*, vol. 77, no. 3, pp. 378–381, 1973. 54

[61] C. Minero, E. Pramauro, E. Pelizzetti, V. Degiorgio, and M. Corti, "Micellar properties of sodium dodecylpoly(oxyethylene) sulfates," *Journal of Physical Chemistry*, vol. 90, no. 8, pp. 1620–1625, 1986. 55

[62] L. Zhang, W. Kang, D. Xu, H. Feng, P. Zhang, Z. Li, Y. Lu, and H. Wu, "The rheological characteristics for the mixtures of cationic surfactant and anionic–nonionic surfactants: the role of ethylene oxide moieties," *RSC advances*, vol. 7, no. 22, pp. 13032–13040, 2017. 55, 218

[63] M. Choudhary and S. M. Kamil, "Phase diagram study of sodium dode-cyl sulfate using dissipative particle dynamics," *ACS omega*, vol. 5, no. 36, pp. 22891–22900, 2020. 56, 182, 233, 248, 259

[64] R. M. Miller, J. T. Cabral, E. S. J. Robles, N. J. Brooks, and O. Ces, "Crys-tallisation of sodium dodecyl sulfate–water micellar solutions with struc-turally similar additives: counterion variation," *CrystEngComm*, vol. 20, no. 42, pp. 6834–6843, 2018. 56

[65] R. Guo, L. Tianqing, and Y. Weili, "Phase behavior and structure of the sodium dodecyl sulfate/benzyl alcohol/water system," *Langmuir*, vol. 15, no. 2, pp. 624–630, 1999. 56

[66] M. P. McDonald and W. E. Peel, "Solid and liquid crystalline phases in the sodium dodecyl sulphate + hexadecanoic acid + water system," *Journal of the Chemical Society, Faraday Transactions 1: Physical Chemistry in Condensed Phases*, vol. 72, p. 2274, 1976. 56, 57

[67] J. Bahadur, A. Das, and D. Sen, "Evaporation-induced structural evolu-tion of the lamellar mesophase: a time-resolved small-angle X-ray scattering study," *Journal of applied crystallography*, vol. 52, no. 5, pp. 1169–1175, 2019. 57

[68] Y. Aray, J. G. Parra, R. Paredes, L. J. Álvarez, and A. Diaz-Barrios, "Ex-ploring the nature of the interactions between the molecules of the sodium dodecyl sulfate and water in crystal phases and in the water/vacuum inter-face," *Heliyon*, vol. 6, no. 6, p. 04199, 2020. 58

[69] V. M. Coiro, F. Mazza, and G. Pochetti, "Crystal phases obtained from aqueous solutions of sodium dodecyl sulfate. the structure of a monoclinic phase of sodium dodecyl sulfate hemihydrate," *Acta crystallographica. Sec-tion C, Crystal structure communications*, vol. 42, no. 8, pp. 991–995, 1986. 58

[70] R. G. Laughlin, "Status of aqueous surfactant phase science," *Journal of the American Oil Chemists' Society*, vol. 67, pp. 705–710, 1990. 58

[71] A. Capaccio, S. Caserta, S. Guido, G. Rusciano, and A. Sasso, "Dissolution of a surfactant-water lamellar phase investigated by combining time-lapse polarized light microscopy and confocal raman spectroscopy," *Journal of Colloid and Interface Science*, vol. 561, pp. 136–146, 2020. 58, 99

[72] S. Sami, M. F. Menger, S. Faraji, R. Broer, and R. W. A. Havenith, "Q-force: Quantum mechanically augmented molecular force fields," *Journal of Chemical Theory and Computation*, vol. 17, no. 8, pp. 4946–4960, 2021. 60, 61, 67

[73] T. T. Chong, R. Hashim, and R. A. Bryce, "Molecular dynamics simulation of monoalkyl glycoside micelles in aqueous solution: Influence of carbohydrate headgroup stereochemistry," *The journal of physical chemistry. B*, vol. 110, no. 10, pp. 4978–4984, 2006. 60, 190

[74] S. Faramarzi, B. Bonnett, C. A. Scaggs, A. Hoffmaster, D. Grodi, E. Harvey, and B. Mertz, "Molecular dynamics simulations as a tool for accurate determination of surfactant micelle properties," *Langmuir*, vol. 33, no. 38, pp. 9934–9943, 2017. 60, 190

[75] S. Lebecque, J. Crowet, M. Nasir, M. Deleu, and L. Lins, "Molecular dynamics study of micelles properties according to their size," *Journal of molecular graphics & modelling*, vol. 72, pp. 6–15, 2017. 60, 188, 301

[76] B. L. Bhargava, R. Devane, M. L. Klein, and S. Balasubramanian, "Nanoscale organization in room temperature ionic liquids: a coarse grained molecular dynamics simulation study," *Soft matter*, vol. 3, no. 11, pp. 1395–1400, 2007. 60, 61, 278

[77] S. Fujiwara, T. Itoh, M. Hashimoto, and Y. Tamura, "Molecular dynamics simulation of micelle formation in amphiphilic solution," *Molecular simulation*, vol. 33, no. 1-2, pp. 115–119, 2007. 60, 61, 278

[78] S. Fujiwara, T. Itoh, M. Hashimoto, and R. Horiuchi, "Molecular dynamics simulation of amphiphilic molecules in solution: Micelle formation and dynamic coexistence," *The Journal of Chemical Physics*, vol. 130, no. 14, p. 144901, 2009. 60, 61, 278, 280

[79] H. Wang, H. Zhang, C. Liu, and S. Yuan, "Coarse-grained molecular dynamics simulation of self-assembly of polyacrylamide and sodium dodecylsulfate in aqueous solution," *Journal of Colloid and Interface Science*, vol. 386, no. 1, pp. 205–211, 2012. 60, 61, 278, 290

[80] S. Jalili and M. Akhavan, "A coarse-grained molecular dynamics simulation of a sodium dodecyl sulfate micelle in aqueous solution," *Colloids and Surfaces A: Physicochemical and Engineering Aspects*, vol. 352, no. 1, pp. 99–102, 2009. 60, 61, 278, 279

[81] W. Shinoda, R. DeVane, and M. L. Klein, "Multi-property fitting and parameterization of a coarse grained model for aqueous surfactants," *Molecular Simulation*, vol. 33, no. 1-2, pp. 27–36, 2007. 60, 61, 278

[82] K. Watanabe, M. Ferrario, and M. L. Klein, "Molecular dynamics study of a sodium octanoate micelle in aqueous solution," *The Journal of Physical Chemistry*, vol. 92, no. 3, pp. 819–821, 1988. 60, 61, 279

[83] N. Yoshii and S. Okazaki, "A molecular dynamics study of structure and dynamics of surfactant molecules in sds spherical micelle," *Condensed Matter Physics*, vol. 10, p. 573, 2007. 60, 61, 279

[84] F. Palazzesi, M. Calvaresi, and F. Zerbetto, "A molecular dynamics investigation of structure and dynamics of *sds* and *sdbs* micelles," *Soft matter*, vol. 7, no. 19, p. 9148, 2011. 60, 61, 279

[85] M. Sammalkorpi, M. Karttunen, and M. Haataja, "Structural properties of ionic detergent aggregates: A large-scale molecular dynamics study of sodium dodecyl sulfate," *The journal of physical chemistry. B*, vol. 111, no. 40, pp. 11722–11733, 2007. 60, 61, 279, 280, 294

[86] L. D. Schuler, X. Daura, and W. F. van Gunsteren, "An improved GRO-MOS96 force field for aliphatic hydrocarbons in the condensed phase," *Journal of Computational Chemistry*, vol. 22, no. 11, pp. 1205–1218, 2001. 61, 67, 68

[87] J.-C. Desplat and C. Care, "A Monte Carlo simulation of the micellar phase of an amphiphile and solvent mixture," *Molecular physics*, vol. 87, no. 2, pp. 441–453, 1996. 61, 62

[88] R. G. Larson, L. E. Scriven, and H. T. Davis, "Monte Carlo simulation of model amphiphile-oil-water systems," *The Journal of Chemical Physics*, vol. 83, no. 5, pp. 2411–2420, 1985. 61, 62

[89] N. Poorgholami-Bejarpasi, M. Hashemianzadeh, S. M. Mousavi-Khoshdel, and B. Sohrabi, "Investigation of the mixing behavior of surfactants by lattice Monte Carlo simulation," *Journal of molecular modeling*, vol. 16, no. 9, pp. 1499–1508, 2010. 61, 62

[90] S. Hashemianzadeh, H. Gharibi, S. Mousavi-Khoshdel, B. Sohrabi, and M. Safarpoor, "Lattice Monte Carlo simulation of dilute ionic surfactants," *Journal of molecular liquids*, vol. 138, no. 1, pp. 147–154, 2008. 61, 62

[91] A. Bhattacharya, S. D. Mahanti, and A. Chakrabarti, "Self-assembly of neutral and ionic surfactants: An off-lattice Monte Carlo approach," *The Journal of Chemical Physics*, vol. 108, no. 24, pp. 10281–10293, 1998. 61, 62

[92] G. K. Bourov and A. Bhattacharya, "Effect of packing parameter on phase diagram of amphiphiles: An off-lattice gibbs ensemble approach," *The Journal of Chemical Physics*, vol. 127, no. 24, p. 244905, 2007. 61, 62

[93] T. Zehl, M. Wahab, R. Schmidt, P. Schiller, and H.-J. Mögel, "Monte Carlo studies on self-assembly of surfactants in aqueous solutions," *Journal of molecular liquids*, vol. 147, no. 3, pp. 178–181, 2009. 61, 62

[94] N. González-Segredo, M. Nekovee, and P. V. Coveney, "Three-dimensional lattice-boltzmann simulations of critical spinodal decomposition in binary immiscible fluids," *Phys. Rev. E*, vol. 67, p. 046304, Apr 2003. 62

[95] P. Love, M. Nekovee, P. Coveney, J. Chin, N. González-Segredo, and J. Martin, "Simulations of amphiphilic fluids using mesoscale lattice-Boltzmann and lattice-gas methods," *Computer Physics Communications*, vol. 153, no. 3, pp. 340–358, 2003. 62

[96] A. J. C. Ladd, M. E. Colvin, and D. Frenkel, "Application of lattice-gas cellular automata to the brownian motion of solids in suspension," *Phys. Rev. Lett.*, vol. 60, pp. 975–978, Mar 1988. 62

[97] J. C. Shillcock and R. Lipowsky, "Equilibrium structure and lateral stress distribution of amphiphilic bilayers from dissipative particle dynamics simulations," *The Journal of Chemical Physics*, vol. 117, no. 10, pp. 5048–5061, 2002. 62, 75, 182, 233

[98] T. L. Rodgers, O. Mihailova, and F. R. Siperstein, "Dissolution of lamellar phases," *The journal of physical chemistry. B*, vol. 115, no. 34, pp. 10218–10227, 2011. 62, 82, 182, 233, 259

[99] P. Prinsen, P. Warren, and M. Michels, "Mesoscale simulations of surfactant dissolution and mesophase formation," *Physical review letters*, vol. 89, no. 14, p. 148302, 2002. 62

[100] R. D. Groot and P. B. Warren, "Dissipative particle dynamics: Bridging the gap between atomistic and mesoscopic simulation," *The Journal of Chemical Physics*, vol. 107, no. 11, pp. 4423–4435, 1997. 62

[101] R. D. Groot, "Electrostatic interactions in dissipative particle dynamics—simulation of polyelectrolytes and anionic surfactants," *The Journal of Chemical Physics*, vol. 118, no. 24, pp. 11265–11277, 2003. 62, 71, 76

[102] V. Alopaeus, "Modeling surfactant and drop size dynamics in polydisperse liquid-liquid systems with population balances," *Chemical Engineering Science*, vol. 248, p. 117269, 2022. 63

[103] D. Li, A. Buffo, W. Podgórska, D. L. Marchisio, and Z. Gao, "Investigation of droplet breakup in liquid–liquid dispersions by cfd–pbm simulationsthe influence of the surfactant type," *Chinese journal of chemical engineering*, vol. 25, no. 10, pp. 1369–1380, 2017. 63

[104] H. Alla, S. Freifer, and T. Roques-Carmes, "A computational fluid dynamics model using the volume of fluid method for describing the dynamics of spreading of newtonian fluids," *Colloids and surfaces. A, Physicochemical and engineering aspects*, vol. 386, no. 1, pp. 107–115, 2011. 63

[105] M. M. Cross, "Rheology of non-newtonian fluids: A new flow equation for pseudoplastic systems," *Journal of colloid science*, vol. 20, no. 5, pp. 417–437, 1965. 63, 116

[106] A. W. Sisko, "The flow of lubricating greases," *Industrial & Engineering Chemistry*, vol. 50, no. 12, pp. 1789–1792, 1958. 63, 116

[107] W. H. Herschel and R. Bulkley, "Konsistenzmessungen von gummibenzollösungen," *Colloid and polymer science*, vol. 39, no. 4, pp. 291–300, 1926. 63

[108] J. E. Jones, "On the determination of molecular fields - from the variation of the viscosity of a gas with temperature," *Proceedings of the Royal Society of London. Series A, Containing papers of a mathematical and physical character*, vol. 106, no. 738, pp. 441–462, 1924. 64

[109] J. E. Lennard-Jones, "Cohesion," *Proceedings of the Physical Society*, vol. 43, pp. 461–482, sep 1931. 64

[110] R. A. Buckingham and J. E. Lennard-Jones, "The classical equation of state of gaseous helium, neon and argon," *Proceedings of the Royal Society of London. Series A. Mathematical and Physical Sciences*, vol. 168, no. 933, pp. 264–283, 1938. 64

[111] P. P. Ewald, "The calculation of optical and electrostatic grid potential," *Ann. Phys.*, vol. 3, no. 369, p. 253–287, 1921. 65

[112] B. A. Luty, M. E. Davis, I. G. Tironi, and W. F. V. Gunsteren, "A comparison of particle-particle, particle-mesh and ewald methods for calculating electrostatic interactions in periodic molecular systems," *Molecular Simulation*, vol. 14, no. 1, pp. 11–20, 1994. 65

[113] Z. A. Rycerz and P. W. M. Jacobs, "Ewald summation in the molecular dynamics simulation of large ionic systems," *Molecular Simulation*, vol. 8, no. 3-5, pp. 197–213, 1992. 65

[114] B. W. McCann and O. Acevedo, "Pairwise alternatives to ewald summation for calculating long-range electrostatics in ionic liquids," *Journal of chemical theory and computation*, vol. 9, no. 2, pp. 944–950, 2013. 65

[115] J. Eastwood, R. Hockney, and D. Lawrence, "P3m3dp—the three-dimensional periodic particle-particle/ particle-mesh program," *Computer Physics Communications*, vol. 19, no. 2, pp. 215–261, 1980. 65

[116] "LAMMPS documentation." https://docs.lammps.org/kspace_style.html, January 2022. 65

[117] E. Pollock and J. Glosli, "Comments on P3M, FMM, and the Ewald method for large periodic coulombic systems," *Computer Physics Communications*, vol. 95, no. 2, pp. 93–110, 1996. 65

[118] M. Griebel, S. Knapek, and G. Zumbusch, *Numerical Simulation in Molecular Dynamics: Numerics, Algorithms, Parallelization, Applications.* Texts in Computational Science and Engineering, Springer Berlin Heidelberg, 2007. 66

[119] P. M. Morse, "Diatomic molecules according to the wave mechanics. ii. vibrational levels," *Phys. Rev.*, vol. 34, pp. 57–64, Jul 1929. 66

[120] W. C. Swope, H. C. Andersen, P. H. Berens, and K. R. Wilson, "A computer simulation method for the calculation of equilibrium constants for the formation of physical clusters of molecules: Application to small water clusters," *The Journal of Chemical Physics*, vol. 76, no. 1, pp. 637–649, 1982. 67

[121] L. Verlet, "Computer 'experiments' on classical fluids. I. thermodynamical properties of Lennard-Jones molecules," *Physical review*, vol. 159, no. 1, pp. 98–103, 1967. 67

[122] S. J. Marrink, H. J. Risselada, S. Yefimov, D. P. Tieleman, and A. H. de Vries, "The MARTINI force field: coarse grained model for biomolecular simulations," *The Journal of Physical Chemistry B*, vol. 111, no. 27, pp. 7812–7824, 2007. 67

[123] S. L. Mayo, B. D. Olafson, and W. A. Goddard, "Dreiding: a generic force field for molecular simulations," *The Journal of Physical Chemistry*, vol. 94, no. 26, pp. 8897–8909, 1990. 68

[124] H. Berendsen, J. Postma, W. van Gunsteren, and J. Hermans, *Interaction Models for Water in Relation to Protein Hydration*, vol. 11, pp. 331–342. 1981. 68

[125] J.-I. Choe and B. Kim, "Determination of proper time step for molecular dynamics simulation," *Bulletin of the Korean Chemical Society*, vol. 21, 2000. 68

[126] M. Morra, *Water in Biomaterials Surface Science.* Wiley, 2001. 69

[127] J. Olafsen, *Experimental and Computational Techniques in Soft Condensed Matter Physics.* Cambridge University Press, 2010. 69

[128] B. Knapp, S. Frantal, M. Cibena, W. Schreiner, and P. Bauer, "Is an intuitive convergence definition of molecular dynamics simulations solely based on the root mean square deviation possible?," *Journal of computational biology*, vol. 18, no. 8, pp. 997–1005, 2011. 69

[129] H. J. C. Berendsen, J. P. M. Postma, W. F. van Gunsteren, A. DiNola, and J. R. Haak, "Molecular dynamics with coupling to an external bath," *The Journal of Chemical Physics*, vol. 81, no. 8, pp. 3684–3690, 1984. 70

[130] H. C. Andersen, "Molecular dynamics simulations at constant pressure and/or temperature," *The Journal of Chemical Physics*, vol. 72, no. 4, pp. 2384–2393, 1980. 70

[131] C. P. Lowe, "An alternative approach to dissipative particle dynamics," *Europhysics letters*, vol. 47, no. 2, pp. 145–151, 1999. 70, 84

[132] D. J. Evans and B. L. Holian, "The Nose–Hoover thermostat," *The Journal of Chemical Physics*, vol. 83, no. 8, pp. 4069–4074, 1985. 70, 71

[133] P. J. Hoogerbrugge and J. M. V. A. Koelman, "Simulating microscopic hydrodynamic phenomena with dissipative particle dynamics," *Europhysics letters*, vol. 19, no. 3, pp. 155–160, 1992. 71

[134] R. D. Groot and P. B. Warren, "Dissipative particle dynamics: Bridging the gap between atomistic and mesoscopic simulation," *The Journal of Chemical Physics*, vol. 107, no. 11, pp. 4423–4435, 1997. 71, 72, 74, 77, 78, 82, 85, 185

[135] P. Español and P. Warren, "Statistical mechanics of dissipative particle dynamics," *Europhysics letters*, vol. 30, no. 4, pp. 191–196, 1995. 71, 73

[136] C. Marsh, G. Backx, and M. Ernst, "Static and dynamic properties of dissipative particle dynamics," *Physical review. E*, vol. 56, no. 2, pp. 1676–1691, 1997. 71, 83

[137] A. Satō, *Introduction to practice of molecular simulation : molecular dynamics, Monte Carlo, Brownian dynamics, lattice Boltzmann, dissipative particle dynamics.* Elsevier insights, London: Elsevier, 2011. 72

[138] M. González-Melchor, E. Mayoral, M. E. Velázquez, and J. Alejandre, "Electrostatic interactions in dissipative particle dynamics using the Ewald sums," *The Journal of Chemical Physics*, vol. 125, no. 22, pp. 224107–224107, 2006. 76

[139] P. B. Warren and A. Vlasov, "Screening properties of four mesoscale smoothed charge models, with application to dissipative particle dynamics," *The Journal of Chemical Physics*, vol. 140, no. 8, p. 084904, 2014. 76

[140] D. H. Tsai, "The virial theorem and stress calculation in molecular dynamics," *The Journal of Chemical Physics*, vol. 70, no. 3, pp. 1375–1382, 1979. 78

[141] R. Groot and K. Rabone, "Mesoscopic simulation of cell membrane damage, morphology change and rupture by nonionic surfactants," *Biophysical journal*, vol. 81, no. 2, pp. 725–736, 2001. 79

[142] A. Khedr and A. Striolo, "DPD parameters estimation for simultaneously simulating water–oil interfaces and aqueous nonionic surfactants," *Journal of chemical theory and computation*, vol. 14, no. 12, pp. 6460–6471, 2018. 82

[143] H. Droghetti, I. Pagonabarraga, P. Carbone, P. Asinari, and D. Marchisio, "Dissipative particle dynamics simulations of tri-block co-polymer and water: Phase diagram validation and microstructure identification," *The Journal of Chemical Physics*, vol. 149, no. 18, p. 184903, 2018. 82

[144] X. Fan, N. Phan-Thien, S. Chen, X. Wu, and T. Yong Ng, "Simulating flow of dna suspension using dissipative particle dynamics," *Physics of fluids*, vol. 18, no. 6, p. 063102, 2006. 83

[145] V. Symeonidis, G. E. Karniadakis, and B. Caswell, "Schmidt number effects in dissipative particle dynamics simulation of polymers," *The Journal of Chemical Physics*, vol. 125, no. 18, p. 184902, 2006. 85, 217, 219, 223, 230

[146] T. F. Clarke, *Rheological characterization of polymers via dissipative particle dynamics.* PhD thesis, 2008. 86, 219

[147] E. Helfand, "Transport coefficients from dissipation in a canonical ensemble," *Phys. Rev.*, vol. 119, pp. 1–9, Jul 1960. 86

[148] B. Hess, "Determining the shear viscosity of model liquids from molecular dynamics simulations," *The Journal of Chemical Physics*, vol. 116, no. 1, pp. 209–217, 2002. 86

[149] J. H. Irving and K. J. G, "The statistical mechanical theory of transport processes. IV. the equations of hydrodynamics," *The Journal of Chemical Physics*, vol. 18, no. 817, 1950. 88

[150] M. Miezowicz, "Influence of a magnetic field on the viscosity of para-azoxyanisol," *Nature (London)*, vol. 136, no. 3433, p. 261, 1935. 89

[151] M. Miezowicz, "The three coefficients of viscosity of anisotropic liquids," *Nature (London)*, vol. 158, no. 4001, p. 27, 1946. 89

[152] I. Stewart, *The Static and Dynamic Continuum Theory of Liquid Crystals: A Mathematical Introduction.* Liquid Crystals Book Series, CRC Press, 2019. 89, 90

[153] W. Richtering, J. Laeuger, and R. Linemann, "Shear orientation of a micellar hexagonal liquid crystalline phase: A rheo and small angle light scattering study," *Langmuir*, vol. 10, no. 11, pp. 4374–4379, 1994. 90, 113, 114, 261

[154] P. Liu, E. Harder, and B. J. Berne, "On the calculation of diffusion coefficients in confined fluids and interfaces with an application to the liquid-vapor interface of water," *The journal of physical chemistry. B*, vol. 108, no. 21, pp. 6595–6602, 2004. 91

[155] D. J. Mitchell, G. J. T. Tiddy, L. Waring, T. Bostock, and M. P. McDonald, "Phase behaviour of polyoxyethylene surfactants with water. mesophase structures and partial miscibility (cloud points)," *Journal of the Chemical Society, Faraday Transactions 1: Physical Chemistry in Condensed Phases*, vol. 79, no. 4, p. 975, 1983. 95, 96

[156] A. Klaus, G. J. T. Tiddy, D. Touraud, A. Schramm, G. Stuhler, and W. Kunz, "Phase behavior of an extended surfactant in water and a detailed characterization of the concentrated phases," *Langmuir*, vol. 26, no. 22, pp. 16871–16883, 2010. 95, 96

[157] R. Strey, R. Schomäcker, D. Roux, F. Nallet, and U. Olsson, "Dilute lamellar and L$_3$ phases in the binary water-C$_{12}$E$_5$ system.," *Journal of the Chemical Society. Faraday transactions*, vol. 86, no. 12, pp. 2253–2261, 1990. 96

[158] L. M. Bergstrom, L. A. Bastardo, and V. M. Garamus, "A small-angle neutron and static light scattering study of micelles formed in aqueous mixtures of a nonionic alkylglucoside and an anionic surfactant," *The journal of physical chemistry. B*, vol. 109, no. 25, pp. 12387–12393, 2005. 96

[159] S. Kim, S. Y. Kwon, J. h. Moon, and M. W. Kim, "Length shortening and surfactant mixing behavior of nonionic/ionic mixed cylindrical micelle," *Chemical physics letters*, vol. 464, no. 1, pp. 82–86, 2008. 96

[160] H. Kunieda, H. Kabir, K. Aramaki, and K. Shigeta, "Phase behavior of mixed polyoxyethylene-type nonionic surfactants in water," *Journal of molecular liquids*, vol. 90, no. 1, pp. 157–166, 2001. 96

[161] O. Söderman, P. Stilbs, and W. Price, "NMR studies of surfactants," *The Journal of Physical Chemistry. B*, vol. 23A, no. 2, p. 121–135, 2004. 96

[162] V. S. Marinov, Z. S. Nickolov, and H. Matsuura, "Raman spectroscopic study of water structure in aqueous nonionic surfactant solutions," *The journal of Physical Chemistry. B*, vol. 105, no. 41, pp. 9953–9959, 2001. 96

[163] N. Eastaugh, V. Walsh, T. Chaplin, and R. Siddall, *Pigment Compendium: A Dictionary and Optical Microscopy of Historic Pigments.* 01 1974. 97

[164] R. Haynes, *Optical Microscopy of Materials.* Springer US, 2013. 98

[165] X. Liu, Z. Wang, L. Wei, and X. Wei, "Curcumin-encapsulated hexagonal liquid crystalline formed by Brij97/NaDC mixtures," *Journal of Dispersion Science and Technology*, vol. 35, no. 12, pp. 1699–1708, 2014. 99

[166] C. Blayo, E. A. Kelly, J. E. Houston, N. Khunti, N. P. Cowieson, and R. C. Evans, "Light-responsive self-assembly of a cationic azobenzene surfactant at high concentration," *Soft Matter*, vol. 16, pp. 9183–9187, 2020. 99

[167] R. Klein, G. J. T. Tiddy, E. Maurer, D. Touraud, J. Esquena, O. Tache, and W. Kunz, "Aqueous phase behaviour of choline carboxylate surfactants—exceptional variety and extent of cubic phases," *Soft matter*, vol. 7, no. 15, pp. 6973–, 2011. 102

[168] B.-H. Chen, C. A. Miller, J. M. Walsh, P. B. Warren, J. N. Ruddock, P. R. Garrett, F. Argoul, and C. Leger, "Dissolution rates of pure nonionic surfactants," *Langmuir*, vol. 16, no. 12, pp. 5276–5283, 2000. 102

[169] P. Warren and M. Buchanan, "Kinetics of surfactant dissolution," *Current opinion in colloid & interface science*, vol. 6, no. 3, pp. 287–293, 2001. 102

[170] X.-N. Bao, W.-D. Zhang, H.-Z. Gang, S.-Z. Yang, Y.-C. Li, and B.-Z. Mu, "Formation of viscoelastic micellar solutions by a novel cationic surfactant

and anionic salt system," *Colloids and Surfaces A: Physicochemical and Engineering Aspects*, vol. 611, p. 125795, 2021. 102

[171] K. Panthi, H. Sharma, U. P. Weerasooriya, and K. K. Mohanty, "Oil-tolerant nonionic worm-like micellar solution," *ACS Omega*, vol. 5, no. 48, pp. 30817–30825, 2020. 102

[172] J. Texter, *Reactions And Synthesis In Surfactant Systems.* Surfactant Science, Taylor & Francis, 2001. 102

[173] M. Instruments, "A basic introduction to rheology," 103, 105

[174] J. Eastoe, T. F. Towey, B. H. Robinson, J. Williams, and R. K. Heenan, "Structures of metal bis(2-ethylexyl) sulfosuccinate aggregates in cyclohexane," *Journal of Physical Chemistry*, vol. 97, no. 7, pp. 1459–1463, 1993. 106

[175] G. Montalvo and A. Khan, "Rheological properties of a surfactant-induced gel for the lysozyme–sodium dodecyl sulfate–water system," *Colloid and polymer science*, vol. 283, no. 4, pp. 402–412, 2005. 106, 107, 108, 109, 113, 116, 123, 124

[176] L. Kushner, B. Duncan, and J. Hoffman, "A viscometric study of the micelles of sodium dodecyl sulfate in dilute solutions," *Journal of research of the National Bureau of Standards*, vol. 49, no. 2, p. 85, 1952. 106

[177] K. ud Din, S. L. David, and S. Kumar, "Viscosities of sodium dodecyl sulfate solutions in aqueous ammonium salts," *Journal of Chemical & Engineering Data*, vol. 42, no. 6, pp. 1224–1226, 1997. 106

[178] A. Einstein, "Eine neue bestimmung der moleküldimensionen," *Annalen der Physik*, vol. 324, no. 2, pp. 289–306, 1906. 106

[179] M. Mooney, "The viscosity of a concentrated suspension of spherical particles," *Journal of colloid science*, vol. 6, no. 2, pp. 162–170, 1951. 107

[180] R. PAL, "Evaluation of the mooney viscosity/concentration equation for liquid-liquid emulsions," *Chemical engineering communications*, vol. 89, no. 1, pp. 209–214, 1990. 107

[181] M. Guettari, I. Ben Naceur, G. Kassab, and T. Tajouri, "Temperature effect on the inter-micellar collision and maximum packaging volume fraction in water/aot/isooctane micro-emulsions," *The Journal of chemical thermodynamics*, vol. 95, pp. 183–189, 2016. 107, 108, 111

[182] V. Vand, "Viscosity of solutions and suspensions. I. theory," *The Journal of Physical and Colloid Chemistry*, vol. 52, no. 2, pp. 277–299, 1948. 107

[183] M. Kodama and M. Miura, "The second CMC of the aqueous solution of sodium dodecyl sulfate. II. viscosity and density," *Bulletin of the Chemical Society of Japan*, vol. 45, no. 8, pp. 2265–2269, 1972. 108, 109

[184] D. Calvo, J. L. Ruiz, and M. Valiente, "Phase equilibria of mixtures of surfactants and viscoelastic properties of the liquid crystal phases," *Fluid phase equilibria*, vol. 425, pp. 358–364, 2016. 113, 118, 119, 123, 124

[185] C. Gallegos, J. M. Franco, and F. Cordobés, "Rheology of the lamellar liquid-crystalline phase in polyethoxylated alcohol/water/heptane systems," *Grasas y aceites (Sevilla)*, vol. 56, no. 2, pp. 96–105, 2005. 113, 114, 116, 118, 119, 123, 124

[186] M. R. Alcantara and L. C. F. Dias, "The cholesterization process on lyotropic liquid crystals studied by rheology," *Colloids and surfaces. A, Physicochemical and engineering aspects*, vol. 136, no. 1, pp. 155–158, 1998. 113, 116

[187] G. Chauhan, K. Ojha, and A. Baruah, "Effects of nanoparticles and surfactant charge groups on the properties of VES gel," *Brazilian Journal of Chemical Engineering*, vol. 34, no. 1, pp. 241–251, 2017. 113, 116

[188] J. Zhaoa, Z. Wanga, X. Weib, F. Liuc, W. Zhoua, X. Tanga, and T. Wua, "Phase behaviour and rheological properties of the lamellar liquid crystals

formed in dodecyl polyoxyethylene polyoxypropylene ether/water system," *Indian Journal of Chemistry - Section A Inorganic, Physical, Theoretical and Analytical Chemistry*, vol. 50, pp. 641–649, 05 2011. 113, 116, 118, 123, 124

[189] T. Tepe, M. Schulz, J. Zhao, M. Tirrell, F. Bates, K. Mortensen, and K. Almadal, "Variable shear-induced orientation of a diblock copolymer hexagonal phase," *Macromolecules*, vol. 28, no. 8, pp. 3008–3011, 1995. 113, 114, 115, 261

[190] C. E. Fairhurst, M. C. Holmes, and M. S. Leaver, "Shear alignment of a rhombohedral mesh phase in aqueous mixtures of a long chain nonionic surfactant," *Langmuir*, vol. 12, no. 26, pp. 6336–6340, 1996. 113, 114, 261

[191] G. Schmidt, S. Müller, P. Lindner, C. Schmidt, and W. Richtering, "Shear orientation of lyotropic hexagonal phases," *The journal of physical chemistry. B*, vol. 102, no. 3, pp. 507–513, 1998. 113, 114, 115, 261

[192] J. Berghausen, J. Zipfel, O. Diat, T. Narayanan, and W. Richtering, "Lamellar phases under shear: variation of the layer orientation across the couette gap," *Physical chemistry chemical physics : PCCP*, vol. 2, no. 16, pp. 3623–3626, 2000. 113, 114, 261

[193] J. Zipfel, J. Berghausen, G. Schmidt, P. Linder, P. Alexandridis, M. Tsianou, and W. Richtering, "Shear induced structures in lamellar phases of amphiphilic block copolymers," *PCCP. Physical chemistry chemical physics (Print)*, vol. 1, no. 17, pp. 3905–3910, 1999. 113, 114, 261

[194] F. N. Olivier Diat, Didier Roux, "Effect of shear on a lyotropic lamellar phase," *Journal de Physique II*, vol. 3, no. 9, pp. 1427–1452, 1993. 113, 114, 261

[195] K. Koppi, M. Tirrell, F. Bates, K. Almdal, and R. Colby, "Lamellae orientation in dynamically sheared diblock copolymer melts," *http://dx.doi.org/10.1051/jp2:1992245*, vol. 2, 11 1992. 114, 261, 273

[196] P. Versluis, J. C. van de Pas, and J. Mellema, "Microstructure and rheology of lamellar liquid crystalline phases," *Langmuir*, vol. 13, no. 21, pp. 5732–5738, 1997. 116, 118, 123, 124

[197] G. Montalvo, M. Valiente, and E. Rodenas, "Rheological properties of the l phase and the hexagonal, lamellar, and cubic liquid crystals of the CTAB/benzyl alcohol/water system," *Langmuir*, vol. 12, no. 21, pp. 5202–5208, 1996. 116, 117

[198] M. Kuzma, Y. W. Hui, and M. M. Labes, "Capillary viscometry of some lyotropic nematics," *Molecular Crystals and Liquid Crystals Incorporating Nonlinear Optics*, vol. 172, no. 1, pp. 211–215, 1989. 116

[199] M. Instruments, "Understanding yield stress measurements," 117

[200] J. Muñoz and M. C. Alfaro, "Rheological and phase behaviour of amphiphilic lipids," *Grasas y aceites (Sevilla)*, vol. 51, no. 1-2, pp. 6–25, 2000. 117, 119

[201] K. Ichihara, T. Sugahara, M. Akamatsu, K. Sakai, and H. Sakai, "Rheology of -gel formed by amino acid-based surfactant with long-chain alcohol: Effects of inorganic salt concentration," *Langmuir*, vol. 37, no. 23, pp. 7032–7038, 2021. 117, 119

[202] G. T. Dimitrova, T. F. Tadros, and P. F. Luckham, "Investigations of the phase changes of nonionic surfactants using microscopy, differential scanning calorimetry, and rheology. 1. synperonic A7, a C13/C15 alcohol with 7 mol of ethylene oxide," *Langmuir*, vol. 11, no. 4, pp. 1101–1111, 1995. 118

[203] H. Susi, D. Byler, and W. Damert, "Raman intensities of carbon-carbon stretching modes in a model membrane," *Chemistry and physics of lipids*, vol. 27, no. 4, pp. 337–344, 1980. 133, 135, 150, 151

[204] I. V. Plastinin, S. A. Burikov, and T. A. Dolenko, "Laser diagnostics of self-organization of amphiphiles in aqueous solutions on the example of sodium octanoate," *Journal of molecular liquids*, vol. 317, p. 113958, 2020. 133, 147, 148

[205] R. G. Snyder, J. R. Scherer, and B. P. Gaber, "Effects of chain packing and chain mobility on the raman spectra of biomembranes," *Biochimica et biophysica acta. Biomembranes*, vol. 601, pp. 47–53, 1980. 133

[206] M. Picquart, "Vibrational mode behavior of sds aqueous solutions studied by raman scattering," *Journal of Physical Chemistry*, vol. 90, no. 2, pp. 243–250, 1986. 134, 151, 152

[207] K. Larsson, "On the structure of isotropic phases in lipid-water systems," *Chemistry and physics of lipids*, vol. 9, no. 3, pp. 181–195, 1972. 134

[208] J. L. Bribes, R. Gaufres, S. Sportouch, and J. Maillols, "Phase transition in non-ionic surfactant—water systems as studied by raman spectrometry: Part I. water—α-octyl-ω-hydroxypentakis (oxyethylene)," *Journal of molecular structure*, vol. 146, pp. 267–272, 1986. 134

[209] Q. Shen, G.-Z. Li, Y.-Z. Huang, L.-X. Li, and J. Xu, "Studies on the phase diagram of the surfactant/1-pentanol/water ternary system II: The liquid crystalline phase," *Journal of dispersion science and technology*, vol. 20, no. 4, pp. 1235–1246, 1999. 134

[210] L. L. Thomas, T. J. Christakis, and W. L. Jorgensen, "Conformation of alkanes in the gas phase and pure liquids," *The journal of physical chemistry. B*, vol. 110, no. 42, pp. 21198–21204, 2006. 134

[211] H. Vogel and F. Jähnig, "Conformational order of the hydrocarbon chains in lipid bilayers. a raman spectroscopic study," *Chemistry and physics of lipids*, vol. 29, no. 1, pp. 83–101, 1981. 134, 135, 136, 151

[212] P. T. T. Wong and H. H. Mantsch, "Temperature-induced phase transition and structural changes in micellar solutions of sodium oleate observed by raman scattering," *Journal of Physical Chemistry*, vol. 87, no. 13, pp. 2436–2443, 1983. 134

[213] S. Burikov, S. Dolenko, T. Dolenko, S. Patsaeva, and V. Yuzhakov, "Decomposition of water raman stretching band with a combination of optimization methods," *Molecular physics*, vol. 108, no. 6, pp. 739–747, 2010. 135

[214] A. Tonegawa, A. Michiue, T. Masuda, K. Ohno, H. Matsuura, K. Yamada, and T. Okuda, "Deuterium NMR and Raman spectroscopic studies on conformational behavior of lipophilic chains in the C12E3/decane/water system," *Zeitschrift für Naturforschung A*, vol. 57, pp. 320–326, 06 2002. 135

[215] M. Bradley, "Curve fitting in raman and ir spectroscopy: Basic theory of line shapes and applications," 2007. 136

[216] S. Kint, P. H. Wermer, and J. R. Scherer, "Raman spectra of hydrated phospholipid bilayers. 2. water and head-group interactions," *Journal of Physical Chemistry*, vol. 96, no. 1, pp. 446–452, 1992. 136, 140, 142, 143, 144, 155

[217] U. S. N. B. of Standards, *Tables of Molecular Vibrational Frequencies. (Consolidated Volume 1).* National Bureau of Standards National Standard Reference Data series, 1972. 139, 154

[218] G. Socrates, *Infrared and Raman Characteristic Group Frequencies: Tables and Charts.* Wiley, 2004. 139, 140, 154

[219] G. Cazzolli, S. Caponi, A. Defant, C. M. C. Gambi, S. Marchetti, M. Mattarelli, M. Montagna, B. Rossi, F. Rossi, and G. Viliani, "Aggregation processes in micellar solutions: a raman study: Aggregation processes in micellar solutions," *Journal of Raman spectroscopy*, vol. 43, no. 12, pp. 1877–1883, 2012. 139, 154

[220] A. Tarazona, E. Koglin, B. B. Coussens, and R. J. Meier, "Conformational dependence of raman frequencies and intensities in alkanes and polyethylene," *Vibrational Spectroscopy*, vol. 14, no. 2, pp. 159–170, 1997. 139, 140

[221] J. Maxfield and I. Shepherd, "Conformation of poly(ethylene oxide) in the solid state, melt and solution measured by raman scattering," *Polymer (Guilford)*, vol. 16, no. 7, pp. 505–509, 1975. 139, 151, 154

[222] R. Iwamoto, "Infrared study on molecular conformations of dialkoxyethanes and related compounds," *Spectrochimica acta. Part A: Molecular spectroscopy*, vol. 27, no. 11, pp. 2385–2399, 1971. 139, 151, 154

[223] V. B. Kartha, L. C. Leitch, and H. H. Mantsch, "Infrared and raman spectra of alkali palmityl sulfates," *Canadian Journal of Chemistry*, vol. 62, no. 1, pp. 128–132, 1984. 140, 154

[224] G. Strobl and W. Hagedom, "Raman spectroscopic method for determining crystallinity of polyethylene," *J. Polym. Sci.*, vol. 16, p. 1181, 1978. 140

[225] Z. Nickolov, J. Earnshaw, F. Mallamace, N. Micali, and C. Vasi, "Light-scattering study of phase transitions in aqueous solutions of nonionic amphiphiles," *Physical review. E, Statistical physics, plasmas, fluids, and related interdisciplinary topics*, vol. 52, no. 5, pp. 5241–5249, 1995. 140

[226] N. Micali, C. Vasi, F. Mallamace, M. Corti, and V. Degiorgio, V, "Raman scattering and water structure in nonionic amphiphile solutions," *Physical review. E, Statistical physics, plasmas, fluids, and related interdisciplinary topics*, vol. 48, no. 5, pp. 3661–3666, 1993. 140

[227] Q. Sun and C. Qin, "Raman oh stretching band of water as an internal standard to determine carbonate concentrations," *Chemical geology*, vol. 283, no. 3, pp. 274–278, 2011. 141

[228] D. M. Carey and G. M. Korenowski, "Measurement of the raman spectrum of liquid water," *The Journal of Chemical Physics*, vol. 108, no. 7, pp. 2669–2675, 1998. 141

[229] J. B. Rosenholm, K. Larsson, and N. Dinh-Nguyen, "A raman spectroscopy study of micellar structures in ternary systems of water-sodium octanoate-pentanol/decanol," *Colloid and polymer science*, vol. 255, no. 11, pp. 1098–1109, 1977. 141, 151

[230] K. Kalyanasundaram and J. K. Thomas, "The conformational state of surfactants in the solid state and in micellar form. a laser-excited raman scattering study," *Journal of Physical Chemistry*, vol. 80, no. 13, pp. 1462–1473, 1976. 141

[231] R. Viana, A. Silva, and A. Pimentel, "Infrared spectroscopy of anionic, cationic, and zwitterionic surfactants," *Advances in Physical Chemistry*, vol. 2012, p. 903272, 2012. 141

[232] R. P. Sperline, "Infrared spectroscopic study of the crystalline phases of sodium dodecyl sulfate," *Langmuir*, vol. 13, no. 14, pp. 3715–3726, 1997. 141, 142

[233] R. Snyder, S. Hsu, and S. Krimm, "Vibrational spectra in the C-H stretching region and the structure of the polymethylene chain," *Spectrochimica acta. Part A: Molecular spectroscopy*, vol. 34, no. 4, pp. 395–406, 1978. 141

[234] Y. Shemouratov, K. Prokhorov, and G. Nikolaeva, "Raman study of ethylene-propylene copolymers and polyethylene-polypropylene reactor blends," *Laser Phys*, vol. 18, p. 554–567, 2008. 142, 143, 147, 149

[235] L. Chen, W. Zhu, K. Lin, N. Hu, Y. Yu, X. Zhou, L.-F. Yuan, S.-M. Hu, and Y. Luo, "Identification of alcohol conformers by raman spectra in the C-H stretching region," *The journal of physical chemistry. A, Molecules, spec-*

troscopy, kinetics, environment, & general theory, vol. 119, no. 13, pp. 3209–3217, 2015. 142

[236] M. El Hadri, A. Achahbar, J. El Khamkhami, B. Khelifa, V. Faivre, O. Abbas, and S. Bresson, "Lyotropic behavior of gelucire 50/13 by XRD, Raman and IR spectroscopies according to hydration," *Chemistry and physics of lipids*, vol. 200, pp. 11–23, 2016. 144, 155

[237] A. Joachimiak, T. Halamus, P. Wojciechowski, and J. Ulanski, "Structure of hydrogels based on lyotropic phases of cellulose derivative as studied by raman spectroscopy," *Macromolecular chemistry and physics*, vol. 206, no. 1, pp. 59–65, 2005. 149

[238] N. Yellin and I. W. Levin, "Hydrocarbon chain trans-gauche isomerization in phospholipid bilayer gel assemblies," *Biochemistry (Easton)*, vol. 16, no. 4, pp. 642–647, 1977. 151

[239] H. Matsuura and T. Miyazawa, "Vibrational analysis of molten poly(ethylene glycol)," *Journal of Polymer Science Part A-2: Polymer Physics*, vol. 7, no. 10, pp. 1735–1744, 1969. 151

[240] M. Instruments, "Dynamic light scattering : An introduction in 30 minutes," 2014. 159

[241] M. Instruments, "Calculating volume distributions from dynamic light scattering data," 2014. 159

[242] G. Mie, "Beiträge zur optik trüber medien, speziell kolloidaler metallösungen," *Annalen der Physik*, vol. 330, no. 3, pp. 377–445, 1908. 161

[243] J. Stetefeld, S. A. McKenna, and T. R. Patel, "Dynamic light scattering: a practical guide and applications in biomedical sciences," *Biophysical reviews*, vol. 8, no. 4, pp. 409–427, 2016. 161

[244] Y. Mirgorod, A. Chekadanov, and T. Dolenko, "Structure of micelles of sodium dodecyl sulphate in water: an X-ray and dynamic light scattering study," *Chemistry journal of Moldova*, vol. 14, no. 1, pp. 107–119, 2019. 162, 173

[245] K. Mehta, B. Bharatiya, A. Parekh, S. V. Bhatt, V. Shah, D. O. Shah, and T. Mukherjee, "Submicellar aggregates in aqueous sodium dodecyl sulphate solutions: Investigations by dynamic light scattering and water penetration through porous media," *Colloids and surfaces. A, Physicochemical and engineering aspects*, vol. 506, pp. 331–337, 2016. 162

[246] A. Ali, V. Bhushan, N. Malik, and K. Behera, "Study of mixed micellar aqueous solutions of sodium dodecyl sulfate and amino acids," *Colloid Journal*, vol. 75, 2013. 162

[247] R. F. Ali, A. Nazemi, and B. Gates, "Surfactant controlled growth of niobium oxide nanorods (supporting information)," *Crystal Growth and Design*, vol. 17, pp. 4637–4646, 09 2017. 162

[248] M. A. Bahri, M. Hoebeke, A. Grammenos, L. Delanaye, N. Vandewalle, and A. Seret, "Investigation of sds, dtab and ctab micelle microviscosities by electron spin resonance," *Colloids and surfaces. A, Physicochemical and engineering aspects*, vol. 290, no. 1, pp. 206–212, 2006. 162

[249] S. S. Berr and R. R. M. Jones, "Effect of added sodium and lithium chlorides on intermicellar interactions and micellar size of aqueous dodecyl sulfate aggregates as determined by small-angle neutron scattering," *Langmuir*, vol. 4, no. 6, pp. 1247–1251, 1988. 163, 173

[250] A. P. Doherty and K. Scott, "Interaction of cetyltrimethylammonium chloride micelles under static and hydrodynamic conditions," *Journal of the Chemical Society. Faraday transactions*, vol. 92, no. 22, p. 4541, 1996. 164

[251] M. Corti and V. Degiorgio, "Quasi-elastic light scattering study of intermicellar interactions in aqueous sodium dodecyl sulfate solutions," *Journal of Physical Chemistry*, vol. 85, no. 6, pp. 711–717, 1981. 164, 166

[252] G. D. J. Phillies, "Effects of intermacromolecular interactions on diffusion. i. two-component solutions," *The Journal of Chemical Physics*, vol. 60, no. 3, pp. 976–982, 1974. 166

[253] M. Aoudia, B. Al-Haddabi, Z. Al-Harthi, and A. Al-Rubkhi, "Sodium lauryl ether sulfate micellization and water solubility enhancement towards naphthalene and pyrene: Effect of the degree of ethoxylation," *Journal of surfactants and detergents*, vol. 13, no. 1, pp. 103–111, 2009. 169, 171

[254] J. Demaison and A. G. Császár, "Equilibrium CO bond lengths," *Journal of Molecular Structure*, vol. 1023, pp. 7–14, 2012. 171

[255] L. Pauling and L. O. Brockway, "Carbon—carbon bond distances. the electron diffraction investigation of ethane, propane, isobutane, neopentane, cyclopropane, cyclopentane, cyclohexane, allene, ethylene, isobutene, tetramethylethylene, mesitylene, and hexamethylbenzene. revised values of covalent radii," *Journal of the American Chemical Society*, vol. 59, no. 7, pp. 1223–1236, 1937. 171

[256] I. Akiba and K. Sakurai, "Characterizing block-copolymer micelles used in nanomedicines via solution static scattering techniques," *Polymer journal*, 2021. 173

[257] B. Cabane, R. Duplessix, and T. Zemb, "High resolution neutron scattering on ionic surfactant micelles: SDS in water," *J. Phys. France*, vol. 46, pp. 2161–2178, 01 1985. 173, 174

[258] L. J. Magid, Z. Li, and P. D. Butler, "Flexibility of elongated sodium dodecyl sulfate micelles in aqueous sodium chloride: A small-angle neutron scattering study," *Langmuir*, vol. 16, no. 26, pp. 10028–10036, 2000. 173

[259] M. Kakitani, T. Imae, and M. Furusaka, "Investigation of mixed micelles of dodecyldimethylamine oxide and sodium dodecyl sulfate by SANS: Shape, size, charge, and interaction," *Journal of Physical Chemistry*, vol. 99, no. 43, pp. 16018–16023, 1995. 173

[260] S. L. Gawali, M. Zhang, S. Kumar, D. Ray, M. Basu, V. K. Aswal, D. Danino, and P. A. Hassan, "Discerning the structure factor of charged micelles in water and supercooled solvent by contrast variation X-ray scattering," *Langmuir*, vol. 35, no. 30, pp. 9867–9877, 2019. 173, 175

[261] J. Lipfert, L. Columbus, V. B. Chu, S. A. Lesley, and S. Doniach, "Size and shape of detergent micelles determined by small-angle X-ray scattering," *The journal of physical chemistry. B*, vol. 111, no. 43, pp. 12427–12438, 2007. 173

[262] A. Bhadani, T. Okano, T. Ogura, T. Misono, K. Sakai, M. Abe, and H. Sakai, "Structural features and surfactant properties of core–shell type micellar aggregates formed by gemini piperidinium surfactants," *Colloids and Surfaces A: Physicochemical and Engineering Aspects*, vol. 494, pp. 147–155, 2016. 173

[263] S. Kumar, S. L. David, V. K. Aswal, P. S. Goyal, and K. ud Din, "Growth of sodium dodecyl sulfate micelles in aqueous ammonium salts," *Langmuir*, vol. 13, no. 24, pp. 6461–6464, 1997. 174

[264] E. Summerton, M. J. Hollamby, C. S. Le Duff, E. S. Thompson, T. Snow, A. J. Smith, C. Jones, J. Bettiol, S. Bakalis, and M. M. Britton, "Nuclear magnetic resonance and small-angle X-ray scattering studies of mixed sodium dodecyl sulfate and n,n-dimethyldodecylamine n-oxide aqueous systems performed at low temperatures," *Journal of Colloid and Interface Science*, vol. 535, pp. 1–7, 2019. 174

[265] S. Vass, J. S. Pedersen, J. Pleštil, P. Laggner, E. Rétfalvi, I. Varga, and T. Gilányi, "Ambiguity in determining the shape of alkali alkyl sulfate mi-

celles from small-angle scattering data," *Langmuir*, vol. 24, no. 2, pp. 408–417, 2008. 176

[266] S. L. Gawali, M. Zhang, S. Kumar, D. Ray, M. Basu, V. K. Aswal, D. Danino, and P. A. Hassan, "Discerning the structure factor of charged micelles in water and supercooled solvent by contrast variation X-ray scattering," *Langmuir*, vol. 35, no. 30, pp. 9867–9877, 2019. 177, 195, 287

[267] P. Hassan, G. Fritz, and E. W. Kaler, "Small angle neutron scattering study of sodium dodecyl sulfate micellar growth driven by addition of a hydrotropic salt," *Journal of colloid and interface science*, vol. 257, no. 1, pp. 154–162, 2003. 177

[268] R. Nagarajan, *Theory of Micelle Formation Quantitative Approach to Predicting Micellar Properties from Surfactant Molecular Structure*, pp. 1–110. 2007. 178

[269] K. S. Birdi, S. U. Dalsager, and S. Backlund, "Aggregation behaviour of sodium dodecyl sulphate micelles in aqueous solutions studied by membrane osmometry," *J. Chem. Soc., Faraday Trans. 1*, vol. 76, pp. 2035–2042, 1980. 179

[270] X. Li, K. Y. Mya, X. Ni, C. He, K. W. Leong, and J. Li, "Dynamic and static light scattering studies on self-aggregation behavior of biodegradable amphiphilic poly(ethylene oxide)poly[(r)-3-hydroxybutyrate]poly(ethylene oxide) triblock copolymers in aqueous solution," *The Journal of Physical Chemistry B*, vol. 110, no. 12, pp. 5920–5926, 2006. 179

[271] S. Bogusz, R. M. Venable, and R. W. Pastor, "Molecular dynamics simulations of octyl glucoside micelles: Structural properties," *The journal of physical chemistry. B*, vol. 104, no. 23, pp. 5462–5470, 2000. 179

[272] M. Almgren and S. Swarup, "Size of sodium dodecyl sulfate micelles in the presence of additives. 2. aromatic and saturated hydrocarbons," *Journal of Physical Chemistry*, vol. 86, no. 21, pp. 4212–4216, 1982. 180

[273] S. Meng, J. Zhang, Y. Wang, X. Li, C. Wu, T. Hou, L. Xiao, and G. Lu, "Simulating the rheology of surfactant solution using dissipative particle dynamics," *Molecular Simulation*, vol. 41, no. 9, pp. 772–778, 2015. 182, 183

[274] E. Boek, P. Coveney, H. Lekkerkerker, and P. v. d. Schoot, "Simulating the rheology of dense colloidal suspensions using dissipative particle dynamics," *Physical review. E, Statistical physics, plasmas, fluids, and related interdisciplinary topics*, vol. 55, no. 3, pp. 3124–3133, 1997. 182, 183

[275] B. L. Peters, A. Ramirez-Hernandez, D. Q. Pike, M. Muller, and J. J. de Pablo, "Nonequilibrium simulations of lamellae forming block copolymers under steady shear: A comparison of dissipative particle dynamics and brownian dynamics," *Macromolecules*, vol. 45, no. 19, pp. 8109–8116, 2012. 182, 183, 233

[276] H. Zhang, D. Li, L. Pei, L. Zhang, and F. Wang, "The stability of the micelle formed by chain branch surfactants and polymer under salt and shear force: Insight from dissipative particle dynamics simulation," *Journal of Dispersion Science and Technology*, vol. 37, no. 2, pp. 270–279, 2016. 182, 183

[277] P. Xu, J. Lin, L. Wang, and L. Zhang, "Shear flow behaviors of rod-coil diblock copolymers in solution: A nonequilibrium dissipative particle dynamics simulation," *The Journal of Chemical Physics*, vol. 146, no. 18, p. 184903, 2017. 182, 183

[278] M.-T. Lee, A. Vishnyakov, and A. V. Neimark, "Calculations of critical micelle concentration by dissipative particle dynamics simulations: The role of chain rigidity," *The Journal of Physical Chemistry B*, vol. 117, no. 35, pp. 10304–10310, 2013. 182

[279] C. M. Wijmans and B. Smit, "Simulating tethered polymer layers in shear flow with the dissipative particle dynamics technique," *Macromolecules*, vol. 35, no. 18, pp. 7138–7148, 2002. 183

[280] Y. Shan, X. Qiang, J. Ye, X. Wang, L. He, and S. Li, "Shear-induced microstructures and dynamics processes of phospholipid cylinders in solutions," *Scientific reports*, vol. 9, no. 1, pp. 15393–15, 2019. 183

[281] M. Panoukidou, C. R. Wand, A. Del Regno, R. L. Anderson, and P. Carbone, "Constructing the phase diagram of sodium laurylethoxysulfate using dissipative particle dynamics," *Journal of Colloid and Interface Science*, vol. 557, pp. 34–44, 2019. 183, 188, 200, 259

[282] S. D. Peroukidis, D. G. Mintis, I. Stott, and V. G. Mavrantzas, "Molecular simulation of the morphology and viscosity of aqueous micellar solutions of sodium lauryl ether sulfate (SLEnS)," *Journal of Physics: Materials*, vol. 4, no. 4, p. 044001, 2021. 183, 188, 200, 259, 278, 282

[283] "Arc (advanced research computing)." https://arc.leeds.ac.uk/, 2021. 187

[284] M. A. Johnston, W. C. Swope, K. E. Jordan, P. B. Warren, M. G. Noro, D. J. Bray, and R. L. Anderson, "Toward a standard protocol for micelle simulation," *The Journal of Physical Chemistry B*, vol. 120, no. 26, pp. 6337–6351, 2016. 188, 190

[285] P. Brocos, P. Mendoza-Espinosa, R. Castillo, J. Mas-Oliva, and A. Pineiro, "Multiscale molecular dynamics simulations of micelles: coarse-grain for self-assembly and atomic resolution for finer details," *Soft matter*, vol. 8, no. 34, pp. 95–914, 2012. 188

[286] S. E. Anachkov, K. D. Danov, E. S. Basheva, P. A. Kralchevsky, and K. P. Ananthapadmanabhan, "Determination of the aggregation number and charge of ionic surfactant micelles from the stepwise thinning of foam

films," *Advances in Colloid and Interface Science*, vol. 183-184, pp. 55–67, 2012. 204

[287] A. Chaudhri and J. R. Lukes, "Velocity and stress autocorrelation decay in isothermal dissipative particle dynamics," *Phys. Rev. E*, vol. 81, p. 026707, Feb 2010. 212

[288] O. Filho, R. Itri, and L. Amaral, "Decanol effect on the structure of the hexagonal phase in a lyotropic liquid crystal," *The Journal of Physical Chemistry B*, vol. 104, pp. 959–964, 02 2000. 232

[289] Q. Wang, *Formation and Structure of Acid Soap Crystals through in-situ Neutralisation in the Environments of Surfactant.* PhD thesis, School of Chemical and Process Engineering, University of Leeds, 2019. 232

[290] M. Lísal and J. K. Brennan, "Alignment of lamellar diblock copolymer phases under shear: insight from dissipative particle dynamics simulations," *Langmuir*, vol. 23, no. 9, pp. 4809–4818, 2007. 233, 263

[291] Y. Tomiyoshi, T. Kawakatsu, T. Aoyagi, and H. Morita, "Rheological properties of lamellae-forming diblock copolymers," *Advanced Theory and Simulations*, vol. 4, no. 7, p. 2100097, 2021. 233

[292] "CSD3 documentation." https://docs.hpc.cam.ac.uk/hpc/, 2021. 239

[293] R. D. Groot, *Applications of Dissipative Particle Dynamics in: Novel Methods in Soft Matter Simulations*, vol. 640. Springer. 259

[294] R. D. Groot and T. J. Madden, "Dynamic simulation of diblock copolymer microphase separation," *The Journal of chemical physics*, vol. 108, no. 20, pp. 8713–8724, 1998. 259

[295] K. K. Karukstis, W. C. Duim, G. R. Van Hecke, and N. Hara, "Biologically relevant lyotropic liquid crystalline phases in mixtures of n-octyl

-d-glucoside and water. determination of the phase diagram by fluorescence spectroscopy," *The journal of physical chemistry. B*, vol. 116, no. 12, pp. 3816–3822, 2012. 260

[296] M. Holz, S. R. Heil, and A. Sacco, "Temperature-dependent self-diffusion coefficients of water and six selected molecular liquids for calibration in accurate 1h nmr pfg measurements," *Phys. Chem. Chem. Phys.*, vol. 2, pp. 4740–4742, 2000. 262

[297] K. Roger, E. Sparr, and H. Wennerström, "Evaporation, diffusion and self-assembly at drying interfaces," *Phys. Chem. Chem. Phys.*, vol. 20, pp. 10430–10438, 2018. 262

[298] D. Constantin and P. Oswald, "Diffusion coefficients in a lamellar lyotropic phase: evidence for defects connecting the surfactant structure," *Physical review letters*, vol. 85, no. 20, pp. 4297–4300, 2000. 262

[299] A. S. Poulos, D. Constantin, P. Davidson, M. Impéror, P. Judeinstein, and B. Pansu, "A pgse-nmr study of molecular self-diffusion in lamellar phases doped with polyoxometalates," *The Journal of Physical Chemistry B*, vol. 114, no. 1, pp. 220–227, 2010. 262

[300] L.-Y. You, L.-J. Chen, H.-J. Qian, and Z.-Y. Lu, "Microphase transitions of perforated lamellae of cyclic diblock copolymers under steady shear," *Macromolecules*, vol. 40, no. 14, pp. 5222–5227, 2007. 263, 273

[301] A. Chremos, P. M. Chaikin, R. A. Register, and A. Z. Panagiotopoulos, "Shear-induced alignment of lamellae in thin films of diblock copolymers," *Soft Matter*, vol. 8, pp. 7803–7811, 2012. 263

[302] N. Mai-Duy, N. Phan-Thien, and T. Tran-Cong, "An improved dissipative particle dynamics scheme," *Applied mathematical modelling*, vol. 46, pp. 602–617, 2017. 275

[303] N. Lauriello, J. Kondracki, A. Buffo, G. Boccardo, M. Bouaifi, M. Lisal, and D. Marchisio, "Simulation of high schmidt number fluids with dissipative particle dynamics: Parameter identification and robust viscosity evaluation," *Physics of Fluids*, vol. 33, no. 7, p. 073106, 2021. 275

[304] P. M. Pieczywek, W. Płaziński, and A. Zdunek, "Dissipative particle dynamics model of homogalacturonan based on molecular dynamics simulations," *Scientific reports*, vol. 10, no. 1, pp. 14691–14691, 2020. 275, 276

[305] B. Townsend, F. Peyronel, N. Callaghan-Patrachar, B. Quinn, A. G. Marangoni, and D. A. Pink, "Shear-induced aggregation or disaggregation in edible oils: Models, computer simulation, and usaxs measurements," *Journal of Applied Physics*, vol. 122, no. 22, p. 224304, 2017. 276

[306] D. A. Fedosov, G. E. Karniadakis, and B. Caswell, "Steady shear rheometry of dissipative particle dynamics models of polymer fluids in reverse poiseuille flow," *The Journal of Chemical Physics*, vol. 132, no. 14, pp. 144103–144103, 2010. 276

[307] B. J. Chun, J. I. Choi, and S. S. Jang, "Molecular dynamics simulation study of sodium dodecyl sulfate micelle: Water penetration and sodium dodecyl sulfate dissociation," *Colloids and Surfaces A: Physicochemical and Engineering Aspects*, vol. 474, pp. 36–43, 2015. 279, 290

[308] S. D. Peroukidis, D. G. Tsalikis, M. G. Noro, I. P. Stott, and V. G. Mavrantzas, "Quantitative prediction of the structure and viscosity of aqueous micellar solutions of ionic surfactants: A combined approach based on coarse-grained MARTINI simulations followed by reverse-mapped all-atom molecular dynamics simulations," *Journal of Chemical Theory and Computation*, vol. 16, no. 5, pp. 3363–3372, 2020. 281, 294, 300

[309] S. Izadi, R. Anandakrishnan, and A. V. Onufriev, "Building water models: A different approach," *The Journal of Physical Chemistry Letters*, vol. 5, no. 21, pp. 3863–3871, 2014. 282

[310] H. J. C. Berendsen, J. R. Grigera, and T. P. Straatsma, "The missing term in effective pair potentials," *The Journal of Physical Chemistry*, vol. 91, no. 24, pp. 6269–6271, 1987. 282

[311] W. L. Jorgensen, J. Chandrasekhar, J. D. Madura, R. W. Impey, and M. L. Klein, "Comparison of simple potential functions for simulating liquid water," *The Journal of Chemical Physics*, vol. 79, no. 2, pp. 926–935, 1983. 282

[312] L. J. Kinnaman, R. M. Roller, and C. S. Miller, "Comparing classical water models using molecular dynamics to find bulk properties," *Journal of Chemical Education*, vol. 95, no. 5, pp. 888–894, 2018. 282

[313] D. J. Price and C. L. Brooks, 3rd, "A modified TIP3P water potential for simulation with Ewald summation," *The Journal of Chemical Physics*, vol. 121, no. 20, pp. 10096–10103, 2004. 282

[314] G. Liu, Y. Wei, F. Gao, S. Yuan, and C. Liu, "Origins of entropy change for the amphiphilic molecule in micellization: a molecular dynamics study," *Phys. Chem. Chem. Phys.*, vol. 18, pp. 11357–11361, 2016. 282

[315] N. Wagner and J. Mewis, *Theory and Applications of Colloidal Suspension Rheology.* Cambridge Series in Chemical Engineering, Cambridge University Press, 2021. 299

Appendix A

Derivation of Constraint on d-spacing for Lamellar Layers

This section will discuss derivation of Eq 3.46. Consider that for any value of y or z, a line that is parallel to the x-axis must pass though an integer number of layers formed (due to the period boundary conditions at $x = 0$ and $x = L$). Although, the spacing the layers project onto that line will be skewed. Therefore, the number of layers must satisfy $\kappa_x = L/\Delta x$ where Δx is the skewed separation of the layers along that line. Likewise for vectors in the x and y direction: $\kappa_y = L/\Delta y$ and $\kappa_z = L/\Delta z$. The values of Δx, Δy and Δz combine to find the d-spacing d as:

$$\left(\frac{d}{\Delta x}\right)^2 + \left(\frac{d}{\Delta y}\right)^2 + \left(\frac{d}{\Delta y}\right)^2 = 1. \tag{A.1}$$

Substituting in the above expressions for Δx, Δy and Δz finds expression in Eq 3.46. Illustration of how expression Eq A.1 is found is illustrated in Fig A.2. In two dimensions values Δx and Δy would combine to find spacing w as follows. From Fig A.2: $w = \Delta x \cos\varphi$ and $w = \Delta y \sin\varphi$, combining these two expressions leads to

$$\left(\frac{w}{\Delta x}\right)^2 + \left(\frac{w}{\Delta y}\right)^2 = 1. \tag{A.2}$$

Similar arguments can be made in 3 dimensions to extend this to an expression for d, as that given in A.1.
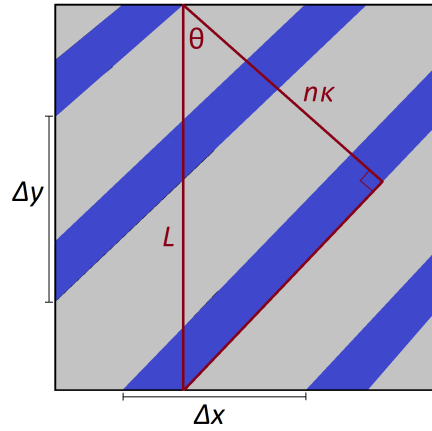
Figure A.1: Adapted version of Fig 3.8. Illustration of the formation of repeated lamellar layers in the simulation box. A triangle illustrates the constraints the periodic boundary conditions impose. The vertical line of this triangle has a length the same as box size L. A second line has length κd, where is an integer related to the number of layer repeats it passes though, and d is the spacing between the repeated layers. This line is normal to the periodic layers in the box and is in the same direction as the director for the molecules. These lines can form a right angled triangle such that $L \cos \theta = \kappa d$. Also illustrated is the meaning of Δx and Δy.
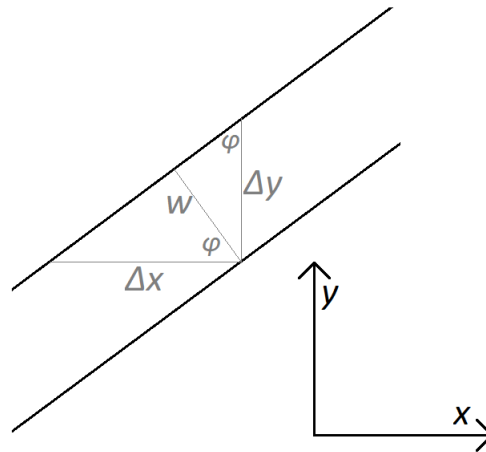
Figure A.2: Definition of symbols used in derivation of Eq. A.2. Note that $\varphi = (\pi/2) - \theta$.

Appendix B

Limit of Eq. 6.7 at low concentrations

Suppose that the concentrations can be represented as a function of surfactant concentration: $c_1 = A(1-x)$, $c_+ = Bx$ and $c_{\mathrm{mic}} = Cx$. Eq. 6.7 then becomes

$$
\begin{aligned}
D &= \frac{AB(1-x)xD_1D_+ + q^2AC(1-x)xD_1D_{\mathrm{mic}} + BCm^2x^2D_+D_{\mathrm{mic}}}{A(1-x)D_1 + BxD_+ + C(m-q)^2xD_{\mathrm{mic}}} \\
&\quad \times \frac{Bx + A(1-x) + C(m-q)^2x}{AB(1-x)x + q^2AB(1-x)x + BCm^2x^2} \\
&= \frac{x[AB(1-x)D_1D_+ + q^2AC(1-x)D_1D_{\mathrm{mic}} + BCm^2xD_+D_{\mathrm{mic}}]}{AD_1 + x[BD_+ - AD_1 + C(m-q)^2D_{\mathrm{mic}}]} \\
&\quad \times \frac{A + x[B - A + C(m-q^2)]}{x[AB(1-x) + q^2AB(1-x) + BCm^2x]} \\
&= \frac{ABD_1D_+ + q^2ACD_1D_{\mathrm{mic}} + x[BCm^2D_+D_{\mathrm{mic}} - ABD_1D_+ - q^2ACD_1D_{\mathrm{mic}}]}{AD_1 + x[BD_+ - AD_1 + C(m-q)^2D_{\mathrm{mic}}]} \\
&\quad \times \frac{A + x[B - A + (m-q)^2]}{AB + q^2AB + x[BCm^2 - ABq^2 - AB]}
\end{aligned}
$$

Taking $x \to 0$ gives

$$
\begin{aligned}
\lim_{x\to 0} D &= \frac{ABD_1D_+ + q^2ACD_1D_{\mathrm{mic}}}{AD_1} \times \frac{A}{AB(q^2+1)} \\
&= \frac{Cq^2D_{\mathrm{mic}} + BD_+}{B(q^2+1)}
\end{aligned} \tag{B.1}
$$

We can also use the fact that q will be relatively large to say that

$$\frac{Cq^2 D_{\mathrm{mic}} + BD_+}{B(q^2 + 1)} \times \frac{1/q^2}{1/q^2} = \frac{CD_{\mathrm{mic}} + BD_+/q^2}{B(1 + 1/q^2)} \approx (C/B)D_{\mathrm{mic}}. \qquad \text{(B.2)}$$

Appendix C

Number of beads in micellar DPD simulations

This section provides details for the simulations performed in Section 6.3. Tables C.1 and C.2 list the number of water beads and surfactant molecules for simulations of varying concentration, and varying ethoxylation n.

	$n = 0$		$n = 1$		$n = 2$		$n = 3$	
	N_W	N_Mol	N_W	N_Mol	N_W	N_Mol	N_W	N_Mol
7%	348,520	3,310	349,125	2,875	349,690	2,531	350,085	2,265
10%	337,000	4,750	337,875	4,125	338,590	3,641	339,074	3,266
20%	298,128	9,609	299,769	8,359	301,090	7,391	302,125	6,625

Table C.1: The number of water beads N_W and number of surfactant molecules N_Mol for each DPD micellar simulation case (for monodisperse solutions). Note that the number of beads in the surfactant molecule depends on n, ranging from 8 beads ($n = 0$) to 11 beads ($n = 3$). Box size defined by $L = 50$.

	N_W	N_Mol $n = 0$	N_Mol $n = 1$	N_Mol $n = 2$	N_Mol $n = 3$
7%	373,128	1,756	746	357	172
10%	338,075	2,469	1,047	500	500
20%	301,071	4,953	2,109	1,000	484

Table C.2: The number of water beads N_W and number of surfactant molecules N_Mol of each type, for each DPD micellar simulation case (for polydisperse solutions representing AES). Box size defined by $L = 50$.

Appendix D

Number of beads in liquid crystal DPD simulations

This section provides details for the simulations performed in Chapter 7. Tables D.1 and D.2 list the number of water beads and surfactant molecules for simulations of varying concentration, and varying ethoxylation n.

	$n = 0$		$n = 1$		$n = 2$		$n = 3$	
	N_W	N_{Mol}	N_W	N_{Mol}	N_W	N_{Mol}	N_W	N_{Mol}
30%	132,152	7,481	133,464	6,504	134,460	5,754	135,262	5,158
40%	111,168	10,104	112,854	8,794	114,160	7,784	115,176	6,984
50%	89,600	12,800	91,668	11,148	93,260	9,874	94,518	8,862
60%	67,456	15,568	69,861	13,571	71,720	12,028	73,200	10,800
65%	56,192	16,976	58,728	14,808	60,710	13,129	62,288	11,792
70%	44,712	18,411	47,424	16,064	49,530	14,247	51,200	12,800
75%	33,088	19,864	35,958	17,338	38,170	15,383	39,936	13,824
80%	21,312	21,336	24,312	18,632	26,640	16,536	28,496	14,864

Table D.1: The number of water beads N_{W} and number of surfactant molecules N_{Mol} for each DPD micellar simulation case (for monodisperse solutions). Note that the number of beads in the surfactant molecule depends on n, ranging from 8 beads ($n = 0$) to 11 beads ($n = 3$). Box size defined by $L = 40$.

	N_W	N_Mol $n=0$	N_Mol $n=1$	N_Mol $n=2$	N_Mol $n=3$
30%	133,160	3,940	1,674	801	386
40%	112,136	5,348	2,272	1,087	524
50%	91,035	6,761	2,873	1,374	662
60%	77,566	7,663	3,256	1,557	751
65%	58,272	8,955	3,805	1,820	877
70%	46,634	9,736	4,135	1,978	953
75%	35,033	10,511	4,466	2,136	1,030
80%	23,379	11,291	4,798	2,295	1,106

Table D.2: The number of water beads N_W and number of surfactant molecules N_Mol of each type, for each DPD micellar simulation case (for polydisperse solutions representing AES). Box size defined by $L = 40$.

Appendix E

MD parameters for SDS molecule

Mass

Atom	Mass (gram/mol)
Oxygen	15.9994
Sulphur	32.0600
Carbon	12.0110
Hydrogen	1.0080
Sodium	22.9898

Table E.1: Summary of the mass values used in MD simulations.

Lennard-Jones interaction parameters

The oxygen and carbon atoms that are closest to the head group are treated slightly differently to the other atoms in the hydrocarbon chain. The definition of two different oxygen and carbon atoms are shown in Fig. E.1 and the values for ϵ_{ij} and σ_{ij} for each atom pair is given in Table E.2.
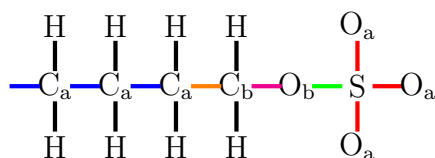

Figure E.1: Illustration of the two different oxygen atom and two different carbon atoms defined in the MD simulation. All subsequent carbon atoms in the hydrocarbon chain are C_a atoms. Note that hydrogen atoms are not shown.

Atom i	Atom j	ϵ_{ij}	σ_{ij}
O_a	O_a	4.122954462841457168E-01	2.625854035428913935E+00
O_a	C_a	1.653354984123153737E-01	3.066537799135407028E+00
O_a	H	1.080062726770026210E-01	2.496442138227286112E+00
O_a	S	3.575292004274581159E-01	3.057436901376735072E+00
O_a	C_b	3.178362756028405567E-01	2.717064020712530947E+00
O_a	O_b	1.038204303792348571E-01	3.238295444039348325E+00
C_a	C_a	6.630154972997068241E-02	3.581179283634555510E+00
C_a	H	4.331183156556572822E-02	2.915407359639444529E+00
C_a	S	1.433735664130799115E-01	3.570551028367321855E+00
C_a	C_b	1.274562198392401313E-01	3.173055093606844679E+00
C_a	O_b	1.015608295071512290E-01	3.259466857310918897E+00
H	H	2.829367882355780447E-02	2.373408142809749322E+00
H	S	9.365952658314305457E-02	2.906754988123776862E+00
H	C_b	8.326143729888541012E-02	2.583156954670584149E+00
H	O_b	6.634513912854232698E-02	2.653504030845614370E+00
S	S	3.100376933831125448E-01	3.559954315729227936E+00
S	O_b	2.756172800531233036E-01	3.163638072888010022E+00
S	C_b	2.196198790769573750E-01	3.249793383002357761E+00
C_b	C_b	2.450182241873804789E-01	2.811442217672497801E+00
C_b	O_b	1.952376598350860082E-01	2.888006183129844473E+00
O_b	O_b	1.194971397251269885E-01	3.100004256511835088E+00

Table E.2: Parameters for ϵ and σ in the Lennard-Jones potential (see Eq. 3.2).

Charge Distribution

The charge on each atom in the molecule is different. The distribution of charge across the whole molecule is shown in Fig. E.2.
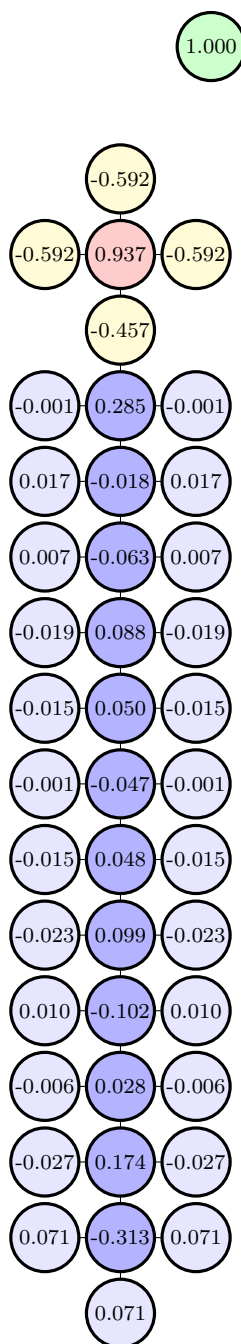

Figure E.2: The charge distribution on atoms making up an SDS molecule, as obtained from the Automated Topology Builder (ATB) and Repository [14]. Atoms are coloured by type: oxygen (yellow), sulphur (red), sodium (green), dark blue (carbon) and light blue (hydrogen).

Bond Interactions

The different types of bonds in the simulation are illustrated by the different colours in Fig. E.1. The parameters for each bond in Eq. 3.5 are listed in Table E.3.

Bond	k_{ij}	r_{ij}^0
S-O$_a$ (red)	2.999759082217973400E+02	1.4800000000E+00
S-O$_b$ (green)	2.031548757170172053E+02	1.6700000000E+00
C$_b$-O$_b$ (pink)	1.673040152963671190E+01	1.4400000000E+00
C$_b$-C$_a$ (orange)	2.998439770554493293E+02	1.5200000000E+00
C$_a$-C$_a$ (blue)	4.000342973231357746E+02	1.5300000000E+00
C-H (black)	3.492741395793498782E+02	1.0900000000E+00

Table E.3: Parameters for the bond interaction given in Eq. 3.5.

Angle Interactions

The atoms in the SDS molecule are labelled in Fig. E.3. The parameters for the angle interaction, see Eq. 3.6, between sets of these atoms are listed in Tables E.4 and E.5.
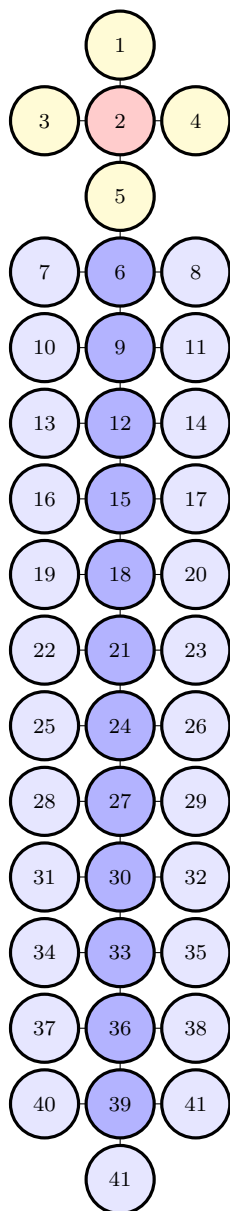

Figure E.3: Labelled atoms making up an SDS molecule, as obtained from the Automated Topology Builder (ATB) and Repository [14]. Atoms are coloured by type: oxygen (yellow), sulphur (red), sodium (green), dark blue (carbon) and light blue (hydrogen).

Atoms i,j,k	k_{ijk}	θ^0_{ijk}
1-2-3	1.569219096563931259E+02	1.1400000000E+02
1-2-4	1.569219096563931259E+02	1.1400000000E+02
1-2-5	1.922293393290815686E+02	1.0600000000E+02
3-2-4	1.569219096563931259E+02	1.1400000000E+02
3-2-5	1.922293393290815686E+02	1.0600000000E+02
4-2-5	1.922293393290815686E+02	1.0600000000E+02
2-5-6	4.480849815265150937E+01	1.1600000000E+02
5-6-7	1.804601961048520877E+02	1.0900000000E+02
5-6-8	1.804601961048520877E+02	1.0900000000E+02
5-6-9	5.512715332021083015E+01	1.0950000000E+02
7-6-8	4.750189404085062250E+01	1.0853000000E+02
7-6-9	5.511390518798809524E+01	1.1100000000E+02
8-6-9	5.511390518798809524E+01	1.1100000000E+02
6-9-10	1.804601961048520877E+02	1.0900000000E+02
6-9-11	1.804601961048520877E+02	1.0900000000E+02
6-9-12	5.511390518798809524E+01	1.1100000000E+02
10-9-11	5.502468723625295155E+01	1.0675000000E+02
10-9-12	3.017313270271808179E+01	1.1000000000E+02
11-9-12	3.017313270271808179E+01	1.1000000000E+02
9-12-13	4.763495597414375737E+01	1.0960000000E+02
9-12-14	4.763495597414375737E+01	1.0960000000E+02
9-12-15	5.511390518798809524E+01	1.1100000000E+02
13-12-14	1.922293393290815686E+02	1.0600000000E+02
13-12-15	3.017313270271808179E+01	1.0950000000E+02
14-12-15	3.017313270271808179E+01	1.0950000000E+02
12-15-16	1.804601961048520877E+02	1.0900000000E+02
12-15-17	1.804601961048520877E+02	1.0900000000E+02
12-15-18	5.511390518798809524E+01	1.1100000000E+02
16-15-17	1.922293393290815686E+02	1.0600000000E+02
16-15-18	3.017313270271808179E+01	1.0950000000E+02
17-15-18	3.017313270271808179E+01	1.0950000000E+02
15-18-19	3.017313270271808179E+01	1.0950000000E+02
15-18-20	3.017313270271808179E+01	1.0950000000E+02
15-18-21	5.511390518798809524E+01	1.1100000000E+02
19-18-20	1.922293393290815686E+02	1.0600000000E+02
19-18-21	3.017313270271808179E+01	1.0950000000E+02
20-18-21	3.017313270271808179E+01	1.0950000000E+02
18-21-22	1.804601961048520877E+02	1.0900000000E+02
18-21-23	1.804601961048520877E+02	1.0900000000E+02
18-21-24	5.511390518798809524E+01	1.1100000000E+02
22-21-23	1.922293393290815686E+02	1.0600000000E+02
22-21-24	1.804601961048520877E+02	1.0900000000E+02

Table E.4: Parameters for use in Eq. 3.6.

Atoms i, j, k	k_{ijk}	θ^0_{ijk}
23-21-24	1.804601961048520877E+02	1.0900000000E+02
21-24-25	3.017313270271808179E+01	1.0950000000E+02
21-24-26	3.017313270271808179E+01	1.0950000000E+02
21-24-27	5.511390518798809524E+01	1.1100000000E+02
25-24-26	1.922293393290815686E+02	1.0600000000E+02
25-24-27	3.017313270271808179E+01	1.0950000000E+02
26-24-27	3.017313270271808179E+01	1.0950000000E+02
24-27-28	1.804601961048520877E+02	1.0900000000E+02
24-27-29	1.804601961048520877E+02	1.0900000000E+02
24-27-30	5.511390518798809524E+01	1.1100000000E+02
28-27-29	1.922293393290815686E+02	1.0600000000E+02
28-27-30	1.804601961048520877E+02	1.0900000000E+02
29-27-30	1.804601961048520877E+02	1.0900000000E+02
27-30-31	3.017313270271808179E+01	1.0950000000E+02
27-30-32	3.017313270271808179E+01	1.0950000000E+02
27-30-33	5.511390518798809524E+01	1.1100000000E+02
31-30-32	1.922293393290815686E+02	1.0600000000E+02
31-30-33	1.804601961048520877E+02	1.0900000000E+02
32-30-33	1.804601961048520877E+02	1.0900000000E+02
30-33-34	3.017313270271808179E+01	1.0950000000E+02
30-33-35	3.017313270271808179E+01	1.0950000000E+02
30-33-36	5.511390518798809524E+01	1.1100000000E+02
34-33-35	1.922293393290815686E+02	1.0600000000E+02
34-33-36	1.804601961048520877E+02	1.0900000000E+02
35-33-36	1.804601961048520877E+02	1.0900000000E+02
33-36-37	1.804601961048520877E+02	1.0900000000E+02
33-36-38	1.804601961048520877E+02	1.0900000000E+02
33-36-39	5.511390518798809524E+01	1.1100000000E+02
37-36-38	1.922293393290815686E+02	1.0600000000E+02
37-36-39	3.017313270271808179E+01	1.0950000000E+02
38-36-39	3.017313270271808179E+01	1.0950000000E+02
36-39-40	5.511390518798809524E+01	1.1100000000E+02
36-39-41	5.511390518798809524E+01	1.1100000000E+02
36-39-42	5.511390518798809524E+01	1.1100000000E+02
40-39-41	5.247673834306662144E+01	1.0757000000E+02
40-39-42	5.247673834306662144E+01	1.0757000000E+02
41-39-42	5.247673834306662144E+01	1.0757000000E+02

Table E.5: Parameters for use in Eq. 3.6.